



HAL
open science

Optical nanoscopy of electrochemical growth in single entities

Paolo Ciocci

► **To cite this version:**

Paolo Ciocci. Optical nanoscopy of electrochemical growth in single entities. Analytical chemistry. Université Paris Cité, 2022. English. NNT : 2022UNIP7282 . tel-04468896

HAL Id: tel-04468896

<https://theses.hal.science/tel-04468896>

Submitted on 20 Feb 2024

HAL is a multi-disciplinary open access archive for the deposit and dissemination of scientific research documents, whether they are published or not. The documents may come from teaching and research institutions in France or abroad, or from public or private research centers.

L'archive ouverte pluridisciplinaire **HAL**, est destinée au dépôt et à la diffusion de documents scientifiques de niveau recherche, publiés ou non, émanant des établissements d'enseignement et de recherche français ou étrangers, des laboratoires publics ou privés.

Université Paris Cité

Ecole doctorale 388

*Laboratoire ITODYS (Interface, Traitements, Organisation et
Dynamique des Systèmes) – UMR 7086*

Optical nanoscopy of electrochemical growth in single entities

Par **Paolo Ciocci**

Thèse de doctorat de chimie physique et chimie analytique

Dirigée par **Frédéric Kanoufi**

Présentation prévue le 14/12/2022

Devant un jury composé de :

Pr. David PORTEHAULT

Professeure, *Sorbonne Université*

Examineur

Dr. Laurent BOUFFIER

Directeur de recherche, *Université de Bordeaux*

Rapporteur

Pr. Stefania RAPINO

Professeure, *Università di Bologna*

Rapportrice

Dr. Hilton Barbosa de AGUIAR

Chargé de recherche, *École Normale Supérieure Paris*

Examineur

Dr. Frédéric KANOUI

Directeur de recherche, *Université Paris Cité*

Directeur de thèse

Dr. Jean-François LEMINEUR

Maitre de conférences, *Université Paris Cité*

Co-encadrant

“I have often thought that we are wrong when we look at reality as a simple, elementary datum, whereas it is, in fact, the most convoluted, most layered, most organ-filled, resin-filled, tube-filled, fat and cartilaginous animal imaginable. The animal in which we live, the annelid worm with flesh made of infinite stardust.”

Solenoid, Mircea Cărtărescu

Acknowledgements

Optical nanoscopy of electrochemical growth of single entities

Abstract

Optical microscopy represents a powerful tool to probe *operando* electrochemical processes at the single nanoparticle (NP) level. The aim of this thesis is to push the limits of detection of such tool and the field of investigated phenomena. In this respect, this work is focused on different electrochemical situations involving the nucleation and growth of new phases on an electrode surface. It explores the dynamics of the electrodeposition or electrocrystallization of nanoparticles and the growth of gas nanobubbles during electrocatalytic activity.

These phenomena are studied by coupling a label-free optical microscopy named interference reflectance microscopy (IRM), to electrochemistry within micro/nanodroplet cells, also known as scanning electrochemical cell microscopy (SECCM). The latter electroanalytical technique allows confining electrochemical reactions within micrometric to nanometric areas of an electrode surface. Optical microscopy is used to probe *operando* the electrochemical processes with wide field of view and high spatial resolution, at high throughput, high sensitivity and minimal invasiveness.

This work focused on different electrochemical systems. First, the formation of hydrogen nanobubbles probed optically, is used as a nanoscale reporter of the local electrocatalytic activity of nanoparticles for the hydrogen evolution reaction, HER. It is particularly shown how the analysis of the optical features, based on an optical model, enabled extracting the size and shape evolution of individual nanobubbles. Secondly, IRM was used to unveil the extent of competitive electrochemical reaction during the HER. The methodology consists in discriminating different optical behaviors associated to different reaction products (gas or solid nanostructures). This allowed imaging the heterogeneities on indium tin oxide substrates and how they affect local electron transfer rates. Similarly, it was possible to discriminate the water reduction from the formation of Ni-based nanoparticles from the reduction of Ni²⁺ solutions.

In last instance, electrochemistry under confinement was investigated by studying optically sub-micrometric droplet electrochemical cells. Sub-droplet resolution imaging was demonstrated through the visualization of the droplet electrowetting, the probing of Ag electrodeposition for the growth of controlled number of NPs (1 to 4), and to investigate CaCO₃ crystallization electrochemically driven by pH variations.

Keywords: nanoparticles, operando optical microscopy, single entity electrochemistry, electrodeposition, electrocatalysis, competitive reactions, image processing, opto-electrochemistry, droplet cell

Nanoscopie optique de la croissance électrochimique d'entités uniques

Abstract en français

La microscopie optique est un outil puissant pour sonder les processus électrochimiques *operando* au niveau de la nanoparticule unique (NP). L'objectif de cette thèse est de repousser les limites de détection de cet outil et le champ de phénomènes étudiés. A cet égard, ce travail se concentre sur différentes situations électrochimiques impliquant la nucléation et la croissance de nouvelles phases à la surface d'une électrode. Il explore la dynamique de l'électrodéposition ou de l'électrocristallisation de nanoparticules et la croissance de nanobulles de gaz pendant l'activité électrocatalytique.

Ces phénomènes sont étudiés en couplant une microscopie optique sans marqueur, appelée microscopie à réflectance interférentielle (MRI), à l'électrochimie au sein de cellules électrochimiques formées par des micro/nanogouttes, également connue sous l'acronyme de SECCM. Cette dernière technique électroanalytique permet de confiner les réactions électrochimiques dans des zones micrométriques à nanométriques de la surface d'une électrode. La microscopie optique est utilisée pour sonder *operando* les processus électrochimiques avec un large champ de vision et une haute résolution spatiale, à haut débit, haute sensibilité et invasivité minimale.

Ce travail s'est concentré sur différents systèmes électrochimiques. Tout d'abord, la formation de nanobulles d'hydrogène, sondée optiquement, est utilisée comme un indicateur à l'échelle nanométrique de l'activité électrocatalytique locale des nanoparticules pour la réaction d'évolution de l'hydrogène, HER. Il est particulièrement montré comment l'analyse des caractéristiques optiques, basée sur un modèle optique, a permis d'extraire l'évolution de la taille et de la forme des nanobulles individuelles. Deuxièmement, la MRI a été utilisée pour dévoiler l'étendue de réactions électrochimiques compétitives pendant la réaction HER. La méthodologie consiste à discriminer les différents comportements optiques associés aux différents produits de réaction (gaz ou nanostructures solides). Cela a permis d'imager des hétérogénéités de réactivité sur les substrats d'oxyde d'indium et d'étain et la façon dont elles affectent les vitesses de transfert d'électrons locales. De même, il a été possible de discriminer la réduction de l'eau de la formation de nanoparticules à base de Ni de la réduction de solutions de Ni²⁺.

En dernier lieu, l'électrochimie sous confinement a été étudiée en étudiant des cellules électrochimiques de gouttelettes optiquement submicrométriques. L'imagerie à résolution sub-gouttelettes a été démontrée par la visualisation de l'électromouillage des gouttelettes, le sondage de l'électrodéposition de l'Ag pour la croissance d'un nombre contrôlé de NPs (1 à 4), et pour étudier la cristallisation du CaCO₃ électrochimiquement pilotée par les variations de pH.

Mots clés : nanoparticules, microscopie optique operando, électrochimie à entité unique, électrodéposition, électrocatalyse, réactions compétitives, traitement d'image, opto-électrochimie, cellule à gouttelettes.

Résumé

Bibliographie

Les méthodes de microscopie optique ont été le plus souvent utilisées en physique et en biologie, car elles permettaient de quantifier l'action des forces en suivant le mouvement des objets, ou d'identifier les fonctions biologiques des sous-entités des micro-organismes vivants. Les microscopies optiques ont été moins considérées en chimie ou en électrochimie. L'une des raisons est que le domaine visible de la lumière utilisée pour dessiner une image optique n'est généralement pas le domaine spectral le plus informatif pour identifier les structures ou les transformations chimiques. Ce point de vue a considérablement changé au cours des dernières décennies grâce aux progrès réalisés dans (i) la conception synthétique de molécules ou de nano-objets ayant des propriétés optiques commutables dans le domaine visible, (ii) le développement de photodétecteurs très sensibles et rapides, par exemple capables de détecter la limite ultime d'un seul photon, ou (iii) le développement de stratégies (instrumentales ou informatiques) permettant l'imagerie à plus haute résolution (comme la microscopie à super-résolution) et une détection plus sensible (même sans marquage).

L'électrochimie à l'échelle macroscopique n'est pas suffisante pour évaluer les performances électro-catalytiques d'électrodes nanostructurées car ces dernières sont rarement homogènes. En effet, les nanoparticules, contrairement aux molécules, sont produites au sein d'une distribution de taille, de structure (facettes cristallographiques) et donc au sein d'une même population de nanoparticules on s'attend à observer une grande variabilité dans l'activité électrocatalytique. Par exemple, cette variabilité qui est contenue dans l'ensemble du comportement électrochimique de milliards de NP déposées sur une électrode ne reflète pas nécessairement la caractéristique électrochimique intrinsèque d'une NP isolée dans le dépôt. Il faut alors combiner l'électrochimie à une seconde technique analytique pour sonder la nanostructuration de l'électrode au niveau de l'entité unique. L'objectif de cette thèse est donc de combler le fossé entre la réponse électrochimique globale d'une électrode et le comportement d'une entité unique par l'utilisation d'une imagerie optique très sensible capable de résoudre les NP dans l'espace et le temps. Pour ce faire, une interface électrochimique d'intérêt est amenée dans le champ de vision d'un objectif de microscope. Cet objectif collecte la lumière provenant de l'interface d'intérêt et la transmet à un photodétecteur. Si la transformation électrochimique modifie la lumière collectée par l'objectif, il en résulte un changement au niveau du détecteur. Dans les microscopes à grand champ de vue, une caméra, composée de millions de détecteurs, capture instantanément une image plein champ (millions de pixels) de

l'interface d'intérêt. Fondamentalement, les objets sont imagés à partir de la lumière qu'ils émettent ou de la lumière qu'ils absorbent ou diffusent. Les principes de l'imagerie à haute résolution sont présentés dans la figure 1. Ces techniques ont été utilisées pour étudier des systèmes *operando* de différentes natures.

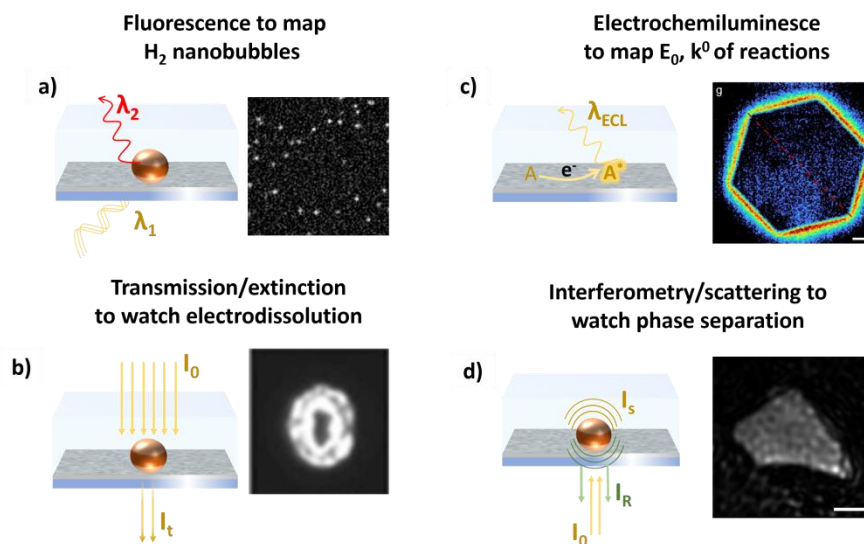


Figure 1 : types de détections basées sur les phénomènes répondant au processus d'imagerie des systèmes électrochimiques : a) fluorescence, b) microscopie de transmission c) electrochemiluminescence, d) interférométrie

Les stratégies de microscopie par émission couplées à une activation électrochimique ont été utilisées avec succès ces dernières années pour cartographier les processus de transfert d'électrons avec une très haute résolution spatiale. Elle permet de révéler l'hétérogénéité. La sensibilité et la résolution de cette méthode d'imagerie ont été poussées jusqu'à la limite du photon unique et donc de l'événement chimique unique. L'ECLM à photon unique a été utilisé pour résoudre spatialement et temporellement la réaction d'oxydation d'un complexe tris(2,2'-bipyridine)ruthénium(II) sur des électrodes, révélant que les sites les plus actifs d'un catalyseur de type microplaque d'or, caractérisés par des constantes de vitesse de réaction plus élevées, sont situés sur les bords de chaque plaque.

Les microscopies optiques sont idéales pour suivre de manière dynamique et dans des conditions *operando* la dynamique de formation et de croissance de nanobulles, NBs, sur des surfaces. Les réactions électro-catalytiques telles que les réactions d'évolution de l'hydrogène ou de l'oxygène produisent souvent des NBs à la surface de l'électrode qui nucléent et croissent une fois que l'environnement local est saturé de molécules de gaz. Ces bulles agissent comme des nano-reporters de l'activité catalytique. En utilisant cette méthodologie, le groupe de Zhang a imagé la diffusion surfacique d'hydrogène (hydrogen spillover) se produisant à l'électrode ITO supportée par une nano-plaque d'or pendant la réaction

d'évolution de l'oxygène et la production retardée de H₂ NBs à l'électrode AuPd pendant la réaction d'évolution de l'hydrogène qui pourrait être expliquée par la capacité du palladium à stocker l'hydrogène.

Les transferts d'électrons entraînent également un large éventail d'événements chimiques et physiques qui peuvent également être sondés par des approches optiques. La réaction électrochimique peut conduire à la création de nanostructures qui peuvent être imagées au stade précoce de leur formation par des microscopies optiques. Une étude de cas est le dépôt électrochimique de métaux nobles tels que Ag, Au ou Cu pour lesquels les mécanismes de nucléation et de croissance font encore l'objet d'une recherche intensive. L'observation optique de la cinétique de dissolution d'entités uniques par la même méthodologie est également possible. L'électrodissolution de NPs d'Ag individuelles est toujours activement étudiée. Une façon d'analyser la cinétique de dissolution de NPs uniques à partir d'images optiques consiste à évaluer la durée caractéristique de la diminution de la lumière diffusée par la DFM. Cette stratégie a été proposée pour imager la dissolution d'entités marines de carbonate de calcium de taille micrométrique (Coccolithes) déclenchée par l'électrogénération d'acide. Ce titrage opto-électrochimique régi par la limitation de la réaction de surface a permis de reconstruire en 3D le volume de l'entité en fonction de la cinétique de dissolution et de déterminer la masse initiale de CaCO₃, ainsi que d'étudier l'effet de certains adsorbats (Mg²⁺) sur la vitesse de dissolution.

La visualisation *operando* de différents contrastes ou caractéristiques optiques à une interface polarisée permet de concevoir la possibilité de processus électrochimiques parallèles ou concurrents. La conversion électrochimique ou les processus d'insertion d'ions pendant la charge ou la décharge des matériaux de stockage d'énergie peuvent s'accompagner d'une transformation physique considérable. L'expansion/rétrécissement du volume relatif d'un objet ne dépassant pas quelques % peut être détecté à partir de la super-localisation de ses bords pendant sa conversion électrochimique (par exemple, l'oxyde de cobalt) ou l'intercalation d'ions Li⁺. L'imagerie dynamique de l'état local de la charge (front d'avancement des ions Li⁺) dans une microparticule d'oxyde de NbW pendant la lithiation et la délithiation révèle des séparations de phases au sein de la particule.

La microscopie optique permet une observation complémentaire de nombreux phénomènes chimiques. Cependant, de nombreuses autres techniques de microscopie peuvent également être utilisées *operando* ou ex-situ pour caractériser spatialement les changements de surface de l'électrode, complétant ainsi la mesure du courant électrochimique. Par exemple, les expériences SEM ex-situ (post-mortem) peuvent être réalisées dans des régions identiques à

celles de l'imagerie optique, ce qui est communément appelé approches de microscopie multi-corrélative.

En effet, de plus en plus d'efforts sont déployés pour créer un trait d'union entre les techniques d'analyse locale, en combinant au moins une technique réalisée *operando*. Ceci est particulièrement intéressant, par exemple, lorsque les systèmes électrochimiques impliquent des réactions complexes produisant différents produits et intermédiaires. De toute évidence, cela crée des ensembles de données volumineux, multidimensionnels et interconnectés qui sont de moins en moins faciles à interpréter/analyser par des êtres humains.

Ces ensembles de données sont de plus en plus traités par des concepts de science des données, des procédures automatisées et des approches de machine learning, ML. Par exemple, des articles récents ont traité de l'introduction de ces approches pour identifier à partir d'images microscopiques les différents composants d'un matériau d'électrode dans une batterie, pour caractériser statistiquement la morphologie des NPs, pour prédire les propriétés optiques des NPs plasmoniques ou pour récupérer des informations chimiques à l'échelle nanométrique.

Dans cette thèse, nous avons utilisé des méthodologies d'imagerie optique *operando* en combinaison avec l'électrochimie pour étudier divers systèmes électroactifs. Les données recueillies ont donné accès à divers descripteurs à l'échelle nanométrique qui ont ensuite été exploités pour comprendre pleinement la réactivité des surfaces des électrodes.

Un système électrocatalytique modèle - la réaction d'évolution de l'hydrogène sur des NP de Pt uniques - a d'abord été étudié afin d'optimiser la méthodologie et d'extraire des descripteurs quantitatifs de l'activité des NP au niveau de l'objet unique.

Ensuite, l'effet des hétérogénéités de surface dans un substrat conducteur transparent a été étudié en sondant plusieurs régions du même substrat, afin de démontrer que les changements locaux de la conductivité de surface peuvent affecter localement la compétition entre différentes réactions.

Enfin, les réactions électrochimiques compétitives ont été étudiées optiquement dans une configuration SECCM. Cela a permis de tester la limite de détection et la résolution du suivi optique en milieu confiné et de révéler l'interaction entre l'interface liquide/air, le transport ionique et l'achèvement local dans des systèmes sensibles au pH tels que l'électro-cristallisation du CaCO₃ et le dépôt de NP.

De plus, l'analyse ML est un moyen prometteur pour aider à différencier les comportements à partir d'images optiques. J'ai initié une telle analyse ML à la fin de ma thèse et notamment lors d'un détachement à l'Université d'Aarhus. Le sujet de mon projet de recherche n'était pas

lié à l'électrochimie mais à l'assemblage d'origami d'ARN sur des surfaces de mica. Il s'agissait d'un système intéressant pour commencer à me familiariser avec le ML. Les algorithmes ML que j'ai développés sont actuellement utilisés pour analyser les images AFM du groupe d'Aarhus. Cette partie n'est donc pas abordée dans ce manuscrit.

Électrocatalyse au niveau des nanoparticules uniques - le cas de la réaction d'évolution de l'hydrogène au niveau des NPs de Pt

Une grande attention dans le domaine de l'(électro)catalyse est consacrée à l'estimation de l'activité intrinsèque pour des réactions spécifiques. Les protocoles courants suivis pour l'électrocatalyse de masse sont l'estimation de la densité de courant au potentiel de demi-vague ou dans des conditions de limitation par la diffusion, normalisée par la surface électroactive par des méthodes de stripping ou par la masse du principal métal électroactif. L'accès à l'électroactivité au niveau d'une entité unique permet d'évaluer la contribution provenant de l'interaction entre le catalyseur et le substrat et entre les NPs voisines, ainsi que l'effet de la taille et de la forme sur l'activité intrinsèque.

Dans ce document, la nucléation et la croissance de NPs unique pendant l'électrocatalyse sur des NPs de Pt adsorbés sur une électrode ITO ont été analysées par couplage entre microscopie optique (interférométrie par réflexion, IRM) et l'électrochimie, EC (couplage IRM/EC). Grâce à une approche de microscopie corrélative SEM/IRM, il est pour la première fois mis en évidence, par simple mesure de l'intensité optique des NPs, qu'un tel phénomène peut être étudié quantitativement et sélectivement sur une population spécifique de NPs, illustrée ici par des NPs de Pt individuelles. La figure 2a montre un exemple caractéristique de zoom sur une zone de $30 \mu\text{m}^2$ d'une région d'intérêt, ROI, de l'image optique de l'électrode peuplée de NPs individuelles. Elle contient des caractéristiques de contraste sombre résultant de la présence des NPs de Pt. Après 30 s d'activation de la par application d'un potentiel à l'électrode d'ITO, le contraste de quelques points optiques change et devient clair, tandis que l'intensité des autres points ainsi que du fond reste constante.

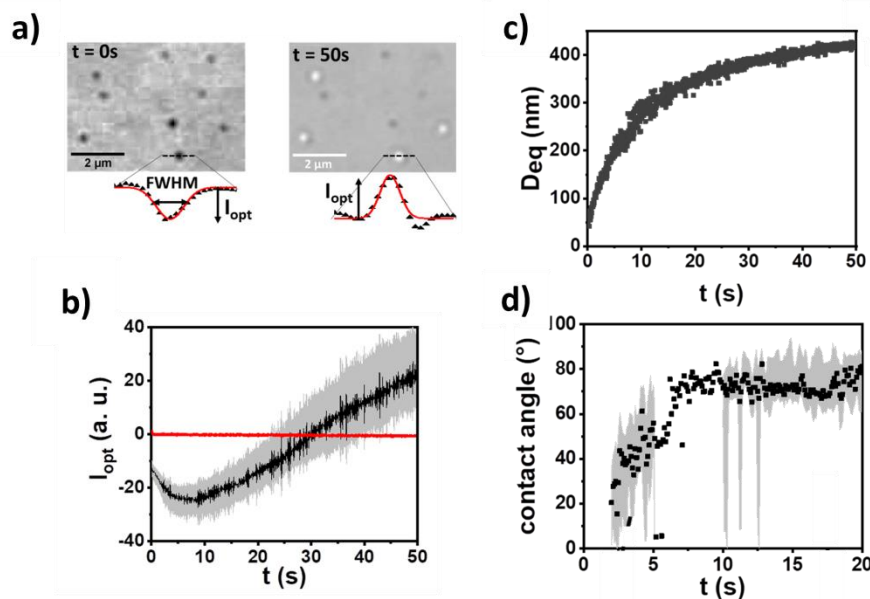


Figure 2 :a) images optiques avant et après CA ainsi que profils optiques le long d'une ligne, dans la même région, sur une NP évoluant ensuite vers un NB. b) Médiane (noir), premier et troisième quartiles (gris) de la variation de I_{opt} , définie en c, de $N > 100$ NP en fonction du temps de polarisation de l'électrode ; fluctuation du fond en rouge. c) Évolution de la taille apparente d'un seul NB généré à un seul NP en fonction du temps. d) Variations de l'angle de contact des NBs individuels ($N=12$, médiane et premier à troisième quartiles en noir et gris, respectivement)

L'évolution typique de la variation d'intensité soustraite du fond à ces points est présentée sur la figure 2b. À l'aide de la simulation d'images optiques, la croissance d'une seule NB a été suivie quantitativement par l'évolution à la fois de l'intensité optique et de la superlocalisation du motif de diffraction associé à l'image optique d'une NB. Le volume de chaque NB est proportionnel à l'intensité optique qui lui est associée. Un examen plus approfondi des images théoriques, à angle de contact constant, montre que le FWHM des caractéristiques des motifs optiques sombre varie également avec la taille de l'empreinte de la NB. Cela suggère que la variation du diamètre de l'empreinte, ΔD , peut être extraite de ces diagrammes de diffraction pour les NBs ayant une dimension D variant entre $200-250 \text{ nm} < D < 500 \text{ nm}$. Il convient de noter que la valeur de la limite inférieure est en fait cohérente avec la valeur de la fonction d'étalement du point $PSF \approx 1,22/2NA \approx 220 \text{ nm}$ du microscope modélisé avec l'ouverture numérique de l'objectif, $NA=1,4$, et la longueur d'onde de détection $\lambda=510 \text{ nm}$. Expérimentalement, les FWHM des motifs optiques ont ensuite été obtenus à partir d'une approche dynamique de super-localisation pendant la croissance des NBs individuelles. A partir de la variation du volume et du diamètre, il a donc été possible d'estimer l'angle de contact de chaque NB pendant sa croissance avec une sensibilité proche de 5×10^4 molécules d' H_2 . La tendance de la figure 2d, pour $N=12$ NBs, montre que la NB croît selon deux régimes de croissance. L'angle de contact de la NB augmente d'environ 30° à 75° pendant les

premières étapes de la croissance de la NB. Par la suite, la NB croît principalement avec un angle de contact constant de 75° et donc selon une augmentation de son empreinte sur la surface. Ces observations des modes de croissance avec l'augmentation de l'angle de contact sont en accord avec les théories actuelles sur la nucléation et la croissance des NBs.

L'analyse à haut débit du processus de croissance a également révélé sa corrélation avec la charge électrochimique. En outre, l'approche dynamique de la superlocalisation des NBs et des NPs met en évidence i) le possible, mais léger, mouvement à l'échelle nanométrique des NPs de Pt et, ii) la déconnexion électrique rapide d'une quantité substantielle de NPs de Pt provoquée par la croissance des NB. Néanmoins, la croissance des NBs a été suivie en continu même après que les NPs de Pt les plus actives aient été recouvertes par des NBs, ce qui suggère fortement la présence d'une diffusion d'hydrogène via la surface d'électrode entre NPs.

Il semble que l'électrogénération des NBs puisse rendre compte de l'activité des nanocatalyseurs mais il peut être difficile d'attribuer le rôle de chaque nanocatalyseur individuel sur la croissance d'un NB donné. Il était alors tentant de supprimer le rôle du catalyseur et d'observer l'électrogénération de NBs à l'électrode ITO en absence de catalyseur.

Différenciation des voies électrochimiques compétitives sur les surfaces d'électrodes optiquement transparentes (ITO)

Les réactions compétitives peuvent être définies comme deux ou plusieurs processus (électro)chimiques qui consomment les mêmes réactifs spécifiques dans la même interface ou région d'intérêt tout en formant deux ou plus produits de réaction différents. Les calculs théoriques et les preuves expérimentales basés sur les paramètres cinétiques et thermodynamiques aident généralement à établir l'ampleur de chaque réaction et les processus prédominants qui se produisent dans des conditions données. En solution, la meilleure façon d'obtenir une description dynamique de ces réactions est d'enregistrer un signal (spectroscopique, électrochimique, optique, en masse, ...) reflétant l'évolution temporelle de la concentration des espèces (aussi bien des réactifs que des produits).

Cela peut être compliqué pour une pléthore de systèmes non idéaux, y compris les surfaces d'électrodes. L'interaction entre la charge électrique de la double couche, les espèces ioniques, les limites de grains de la surface, les régimes de transport et les limites de phase peut conduire à des interactions non linéaires entre chaque contribution qui peut changer vers la

surface de l'électrode, ce qui entraîne une grande difficulté d'interprétation. L'approche de l'électrochimie par entité unique est donc un outil puissant pour évaluer à l'échelle nanométrique la contribution de chaque acteur, y compris les NPs, les frontières de phase et les substrats comme l'oxyde d'indium et d'étain (ITO).

Dans un premier temps, l'ITO nu a été sondé pour visualiser l'effet des hétérogénéités de surface sur la compétition entre la réduction des protons et l'électroréduction de l'ITO dans des gouttelettes micrométriques d'électrolyte acide. Deuxièmement, un processus profondément influencé par les changements de pH dans l'électrolyte - l'électrodéposition de Ni sur l'ITO - a été étudié. Comme pour les autres métaux du groupe du fer, les conditions de pH affectent fortement l'état d'oxydation des NP électrodéposées, conduisant à la formation de coquilles d'oxyde/hydroxyde autour des noyaux métalliques. L'étude de ces processus au niveau de l'entité unique permet de révéler des réactions compétitives locales sur un site de nucléation spécifique.

Le comportement de réduction des électrodes en ITO dépend de différents paramètres chimiques et physiques tels que la conductivité de l'électrode (liée à l'épaisseur du revêtement en ITO), le pH et la composition chimique de l'électrolyte, le rapport In:Sn, la porosité et la rugosité du revêtement.

L'ITO est généralement considéré comme un substrat inerte. Cependant, des processus de surface tels que la reconstruction du revêtement, la formation de défauts à l'échelle nanométrique (comme des NPs) ont été décrits et sont généralement détectés par imagerie SEM ex situ. La stabilité de l'ITO en milieu acide a été contrôlée optiquement comme étape préliminaire. Elle met en évidence une dégradation de l'ITO à environ 16 nm/min dans 1 M H₂SO₄ et seule une faible concentration d'acide (5 mM H₂SO₄) doit être utilisée pour assurer la stabilité de l'ITO pendant une durée suffisante.

Les mesures optiques réalisées sur l'ITO hautement conducteur, tout en balayant le potentiel vers des valeurs négatives, mettent en évidence la formation de deux ensembles distincts de caractéristiques correspondant à la formation de deux types de nano-objets. Ces deux populations sont attribuées à la formation de NBs H₂ et de NPs d'ITO réduits issus respectivement de l'HER et de l'électroréduction de l'ITO. Une analyse détaillée de leur réponse optique a permis de les discriminer en fonction de leurs caractéristiques optiques. La formation des NBs de H₂ se produit à un potentiel plus négatif dans des positions aléatoires avec une probabilité <2% de nucléer au même site entre des cycles de potentiel consécutifs. De plus, les positions du centre de masse des NBs peuvent varier au cours de la dynamique de leur croissance et de leur dissolution, attestant d'un processus de croissance asymétrique. Par

ailleurs, les NP d'ITO réduites apparaissent à un potentiel moins négatif et leur formation est confirmée par une analyse SEM ex situ. Contrairement aux NBs, >99% des NPs réapparaissent à la même position durant les cycles successifs de potentiel et l'analyse du déplacement du centre de masse prouve que les NPs sont statiques tout au long du processus de croissance/dissolution.

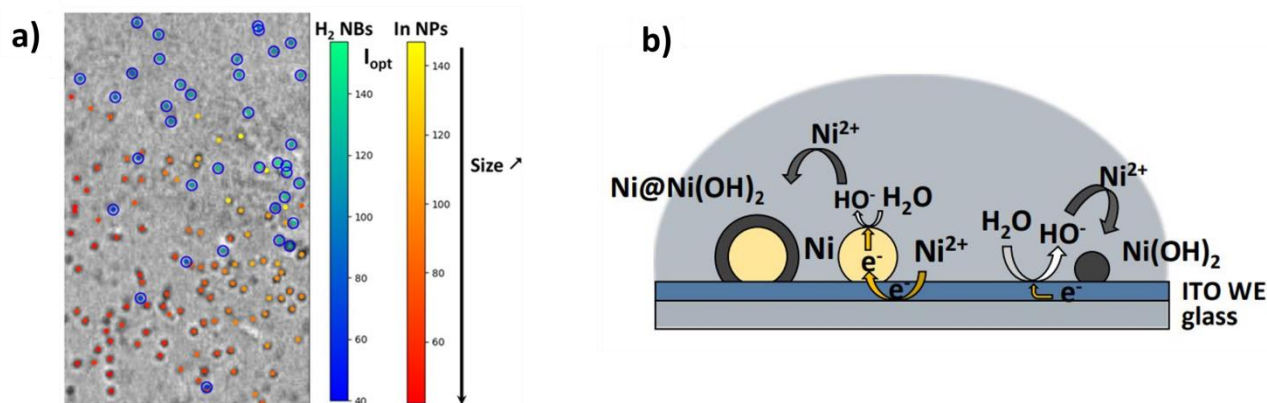


Figure 3 :a) Image reconstruite montrant comment chaque population de motifs se développe sélectivement sur différentes régions de l'électrode ITO, les barres de couleur fournissent une comparaison qualitative de la différence de taille des nanopatrons dans chaque population. b) Mécanismes d'électrodéposition du Ni sur l'électrode de ITO.

Enfin, le comportement de réduction des électrodes ITO dépend fortement de la résistance au transfert de charge locale de l'ITO, qui peut varier au sein d'un même substrat. Ceci est démontré en changeant la position de la gouttelette sur un même substrat ITO ou en changeant l'épaisseur du revêtement ITO. Le comportement électrochimique ainsi que les réponses optiques ont changé en fonction de la résistance de l'échantillon, montrant un déplacement du potentiel d'amorçage de la formation de NPs vers des potentiels moins négatifs quand la résistance au transfert de charge diminue alors que le potentiel d'amorçage de l'HER reste principalement le même. La présence d'hétérogénéités conductrices d'une taille > 50 μm est également mise en évidence par SECM en mode régénération (mode feedback) et explique la ségrégation entre les régions où prédominent des NBs ou celles où la formation de NPs prédomine (figure 3a). En fin de compte, l'imagerie optique de la dynamique de la formation locale de NPs d'ITO réduit ou de NBs peut être utilisée comme un moyen de rationaliser le vitesse de transfert d'électrons local de l'ITO et de prédire la présence de phénomènes compétitifs spatialement dépendants des hétérogénéités pour des systèmes plus complexes.

Ceci a été illustré dans le cas de la réduction de solutions de Ni²⁺, qui produit du Ni métallique et/ou des NP de Ni(OH)₂ (figure 3b). Deux types de NP sont identifiées sur la base

d'une différenciation optique in situ avec une sensibilité inférieure à 25 nm. La formation directe préférentielle des deux matériaux est généralement rationalisée sur la base de l'identification de la signature de la réduction du Ni^{2+} ou de la réduction de l'eau dans la trace électrochimique. La microscopie optique montre que cela est généralement plus complexe. En particulier, le Ni métallique peut toujours nucléer et croître, indirectement, même si la courbe électrochimique semble montrer la réduction de l'eau (même si la signature de réduction du Ni^{2+} est invisible). Ces mécanismes directs et indirects ont ensuite été décryptés in situ grâce à la capacité unique de la microscopie optique de différencier NPs métalliques et d'hydroxydes. L'importance de les étudier au niveau d'une seule entité plutôt qu'à partir de mesures d'ensemble est particulièrement mise en évidence. En effet, cette étude au niveau de l'entité unique montre que pour les deux mécanismes, les NPs de Ni sont formées par une croissance rapide et auto-inhibée, qui peut pourtant se traduire par une croissance graduelle d'un point de vue d'ensemble. Ceci est dû à la différence de dynamique de nucléation qui est liée à la compétition entre réduction de Ni^{2+} et réduction de l'eau. Globalement, cette compréhension permet de sonder, et à son tour de contrôler in situ, la taille et la densité de surface des NPs de Ni. La méthodologie peut être étendue à l'électrodéposition des nombreuses NPs dont la signature électrochimique manque de reproductibilité ou est difficile à identifier.

Observer l'électrochimie au sein de gouttelettes d'électrolyte

Une façon d'améliorer les signaux et la sélectivité dans les expériences d'électrochimie sur objet unique est de travailler dans des nano-environnements confinés. Cela consiste à utiliser des nanopores, des nanogouttes ou des nanocanaux comme réacteurs où une très petite quantité de nano-objets (< 10) est confinée. Cela permet de contourner les inconvénients de l'électrochimie sur objet unique résolue dans le temps, comme la nécessité de travailler avec des solutions ultra-diluées, et de limiter les effets de diffusion entre différentes NPs ou sites de nucléation. Le volume du réacteur est le paramètre fondamental pour déterminer les phénomènes de transport et le nombre d'entités réagissant simultanément. Ce dernier peut être exploité pour extraire différentes informations : alors qu'un nanoréacteur contenant une seule NP peut être utilisé pour sonder la relation entre sa structure et son activité pour une réaction spécifique sans contribution de diffusion moléculaire. Une zone confinée contenant 10 sites de nucléation peut être utilisée pour calculer le chevauchement entre chaque couche de

diffusion et comment les gradients ioniques peuvent affecter les nucléations/réactions au fil du temps. Des nano-gouttes formées dans une configuration SECCM c'est-à-dire à l'aide d'une pipette remplie d'électrolyte sont les systèmes les plus polyvalents pour générer de façon reproductibles des nanoréacteurs de taille contrôlée. Il est aujourd'hui facile de contrôler la taille de l'ouverture de la pipette, qui peut aller du micromètre à la dizaine de nanomètre en diamètre, et de l'utiliser pour confiner une région submicrométrique d'une surface d'électrode par la gouttelette qui sera formée à partir du ménisque du liquide. De plus, les pipettes ont été utilisées avec succès pour manipuler, compter et dimensionner des NPs individuelles confinées à l'embouchure de la pipette, et les caractériser électrochimiquement. L'instrumentation moderne permet de personnaliser des routines pour balayer et analyser (et donc imager en continu et à grande vitesse) plusieurs régions d'électrodes à l'aide de ces pipettes. Cela permet d'utiliser les gouttelettes générées par la pipette 1) pour la livraison et le dépôt contrôlés de divers types de nanocolloïdes et de NPs sur des emplacements spécifiques d'électrodes avec un contact électrique optimal, 2) pour révéler les propriétés hétérogènes de nombreuses caractéristiques de matériaux, y compris des matériaux 2D, des nanotubes, des joints de grain et les facettes cristallographiques d'électrodes ou électrocatalyseurs sous la forme de NPs uniques. La microscopie optique, sensible à la surface d'électrode, peut être couplée à cette configuration expérimentale. Elle permet d'ajouter des informations complémentaires et fondamentales pour tous ces systèmes. Tout d'abord, elle permettrait d'examiner la stabilité ou la déformation des gouttelettes dans le temps ou pendant un actionnement électrochimique. Ensuite, elle permet de voir à l'intérieur de la gouttelette et de visualiser les phénomènes électrochimiques dynamiques ou les phénomènes chimiques à l'intérieur de la gouttelette. Dans ce chapitre, deux systèmes ont été étudiés : l'électrodéposition d'Ag au sein de gouttelettes de diamètre $< 1 \mu\text{m}$ et la cristallisation de CaCO_3 à l'aide d'un ajustement électrochimique des équilibres de pH.

L'étude de l'électrodéposition de NPs uniques d'Ag est une preuve de concept démontrant la potentialité du SECCM à électrodéposer des NPs une par une (une par gouttelette) et donc à imprimer des réseaux de NPs sur surfaces d'électrodes. Pour explorer cette possibilité, une méthode de visualisation complémentaire est nécessaire. Elle doit être capable de résoudre les NPs individuelles immobilisées sur la surface. On montre ici que la microscopie optique est idéale pour observer les événements et des détails de dépôt localisé *operando* dans une cellule électrochimique. Le couplage de techniques optiques à l'électrochimie par pipette a notamment révélé des effets de taille, de composition, de structure ou de surface sur l'activité ou le mouvement de NPs individuelles. Dans ce document, la microscopie optique est utilisée pour observer de manière synchrone des événements uniques, se produisant à l'intérieur de la

cellule de gouttelettes du SECCM, et ce pendant l'étape d'électrodéposition de NPs d'Ag sur une électrode ITO.

Les processus se produisant à l'intérieur du ménisque en SECCM sont toujours déduits des tracés transitoires de courant électrochimique et d'observations ex situ post mortem. Nous avons proposé, en collaboration avec le leader dans ce domaine, le groupe de Patrick Unwin à l'Université de Warwick, de coupler cette technique avec la microscopie optique. Nous avons choisi la configuration IRM (microscopie interférométrique par réflexion), méthode sans marquage fluorescent, et montré qu'elle permet le suivi *operando* de la transformation du ménisque pendant l'électrochimie. Par des stratégies de super-localisation, nous avons également montré que l'IRM offre une résolution d'imagerie sub-gouttelettes permettant de suivre les processus redox locaux (figure 4a).

En utilisant une électrode ITO optiquement transparente, il a été possible d'imager et de suivre la stabilité de la taille du ménisque du SECCM pendant une expérience de voltampérométrie. Ceci permet de répondre à une question importante dans la communauté du SECCM : quelle est la stabilité de la gouttelette ? Ce point a jusqu'à présent été principalement abordée avec l'analyse ex situ des empreintes de gouttelettes ou l'analyse des images de gouttelettes de balayage du SECCM à un potentiel fixe. La possibilité de visualiser le ménisque in situ permet d'avoir une vision plus globale du contact entre le ménisque et la surface d'électrode. De plus, une analyse minutieuse des images IRM a montré sans ambiguïté la croissance de motifs optiques limitées par la diffraction au sein du ménisque.

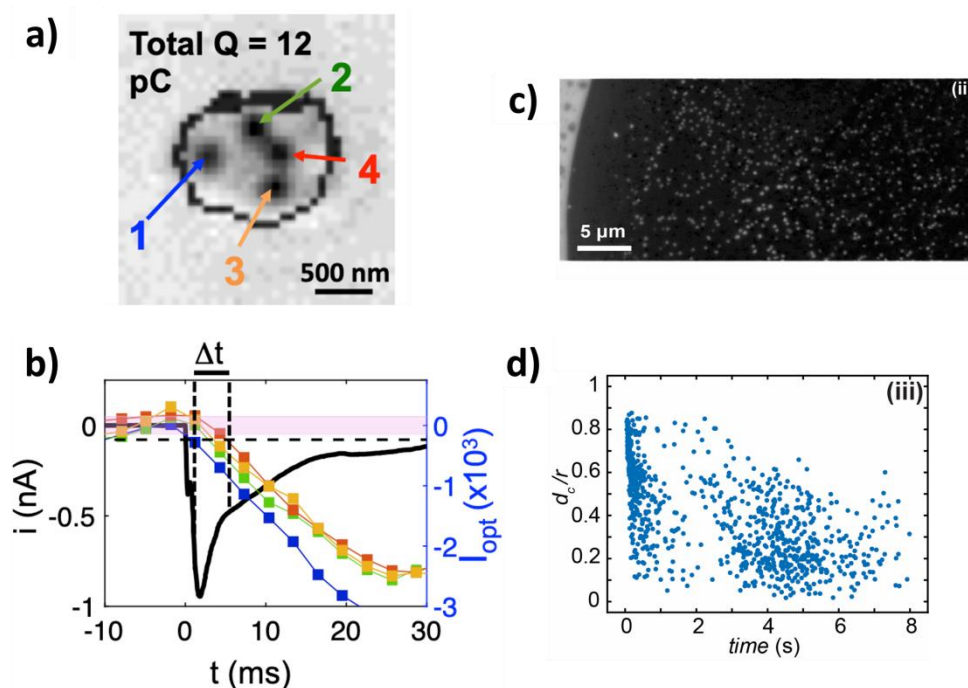


Figure 4 :a) Image optique traitée d'une cellule de gouttelettes plus grande (diamètre de 1.1 μm) montrant 4 NPs à la fin de l'électrodéposition d'Ag. b) Comparaison du courant électrochimique total et des traces d'intensité optique pour les quatre NPs qui se développent à l'intérieur de la cellule à gouttelettes. c), d) images IRM et position radiale normalisée de nouvelles caractéristiques optiques émergentes pour la précipitation de CaCO_3 induite par voie électrochimique à -1.0 V.

L'électrodéposition d'Ag a été suivie dans des gouttelettes d'un diamètre compris entre 500 et 1000 nm. Une à six NPs distinctes ont été détectées par gouttelette, avec une limite de taille de détection estimée à 60 nm en diamètre. La méthode hybride révèle en outre la dynamique de la croissance des NPs, mettant en évidence la formation différée de différentes NPs, une caractéristique qui n'apparaît pas dans les tracés de courant électrochimique. En effet, les NPs apparaissent progressivement sur la surface de l'électrode de travail dans les 5-15 premières ms de l'électrodéposition (figure 4b). Sur une échelle de temps plus longue, on peut observer le déplacement de leur centre de masse de 30-200 nm. Ces observations suggèrent, à partir d'une visualisation *operando*, que les NPs se développent à partir de la diffusion et de l'agrégation en surface de noyaux d'Ag instantanément électrogénérés (bien que non détectés optiquement). Ceci est en accord avec les modèles récents de croissance par nucléation-agrégation. Au-delà de l'aperçu mécanistique unique de l'électrodéposition, le couplage d'une cellule électrochimique nanométrique et d'un suivi optique constitue une plateforme prometteuse pour la production contrôlée de collections de NP sur des surfaces en vue d'une évaluation comparative de l'activité électrochimique de NPs uniques.

Dans un second temps, la précipitation de CaCO_3 est étudiée par une modulation électrochimique du pH de la solution et ainsi créer une solution localement sursaturée en CO_3^{2-} . L'imagerie *in situ* IRM a fourni des preuves du nombre et de la distribution spatiale des événements de cristallisation sur la surface d'électrode en contact avec le ménisque d'électrolyte. Il révèle en temps réel des modes de croissances distincts en fonction du différents potentiels d'électrode ou de la taille des pipettes utilisées. Les volumes de réaction plus petits ont montré une densité accrue de cristaux de CaCO_3 nanométriques répartis de manière assez uniforme (confirmée par spectroscopie Raman) aux potentiels cathodiques appliqués les plus élevés (i.e. à un taux de sursaturation locale élevée). Pour des volumes de réaction plus importants (embouts de micropipettes SECCM), l'emplacement des événements de cristallisation devient alors dépendant du potentiel appliqué, ce qui laisse supposer une interaction dynamique entre le transport de masse des réactifs au sein de l'électrolyte et dans la pipette, les vitesses de réactions de l'ORR à la surface de l'ITO et le transport de CO_2 et d' O_2 à travers l'interface air/ménisque (figure 4c-d). Des simulations multiphysiques (COMSOL) ont mis en évidence les origines mécanistiques de la cristallisation et nous avons

été en mesure de prédire le temps de début et, dans une certaine mesure, l'emplacement des événements de cristallisation.

En conclusion, ce travail s'est concentré sur différents systèmes électrochimiques. Premièrement, la formation de nanobulles d'hydrogène, sondée optiquement, est utilisée comme un indicateur à l'échelle nanométrique de l'activité électrocatalytique locale de nanoparticules pour la réaction d'évolution de l'hydrogène, HER. Il est particulièrement montré comment l'analyse des caractéristiques optiques, basée sur un modèle optique, a permis d'extraire l'évolution de la taille et de la forme des nanobulles individuelles. Deuxièmement, la microscopie optique a été utilisée pour dévoiler l'étendue de réactions électrochimiques compétitives à la réaction HER. La méthodologie consiste à discriminer les différents comportements optiques associés aux différents produits de réaction (gaz ou nanostructures solides). Cela a permis d'imager les hétérogénéités sur des substrats d'oxyde d'indium et d'étain et la façon dont elles affectent les vitesses de transfert d'électrons locaux. De même, il a été possible de discriminer la réduction de l'eau de la formation de nanoparticules à base de Ni de la réduction des solutions de Ni^{2+} .

Enfin, l'électrochimie sous confinement a été étudiée optiquement en cellule électrochimique miniaturisée, nanogouttelettes d'électrolyte submicrométriques. L'imagerie à résolution sub-gouttelettes a été démontrée par la visualisation de l'électromouillage des gouttelettes, le suivi optique dynamique de l'électrodéposition (croissance) d'un nombre contrôlé de nanoparticules (1 à 4) d'Ag, et pour étudier la cristallisation du CaCO_3 par contrôle électrochimique de variations locales de pH.

Most common abbreviations list

NPs	Nanoparticles
NBs	Nanobubbles
NN	Neural Network
ML	Machine Learning
DL	Deep Learning
AI	Artificial Intelligence
FM	Fluorescence microscopy
ECLM	Electrochemical luminescence microscopy
iSCATT	Interferometric scattering
IRM	Interference reflectance microscopy
SECM	Scanning electrochemical microscopy
SECCM	Scanning electrochemical cell microscopy
SEM	Scanning electron microscopy
SPRM	Surface plasmon resonance microscopy
ITO	Indium tin oxide
WE	Working electrode
QRCE	Quasi reference counter electrode

Summary

Acknowledgements	iii
Abstract	iv
Abstract en français	vi
Resumé	ix
Most common abbreviations list	xxiii
Summary	xxiv
1 General introduction	1
2 Optical microscopies in electrochemistry	5
2.1 Overview of operational principles	6
2.1.1 Operational principles	7
2.1.2 Methodologies for quantitative image analysis	8
2.1.2.1 Single object detection by super-localization	9
2.1.2.2 Background minimization and contrast maximization	11
2.1.2.3 From local optical information to electrochemical signals	12
2.2 Imaging single events	13
2.2.1 A great eye on electrode surface	15
2.2.1.1 Single electron transfer imaging	16
2.2.1.2 Probing concentration profiles	19
2.2.1.3 Growth and dissolution at the nanoscale	20
2.2.1.4 Electrochemically driven transformations	23
2.2.1.5 Catalysis and motion	25
2.2.2 Seeing competitive processes	27
2.2.2.1 Physical transformation versus electrochemistry	28
2.2.2.2 Competing electrochemical reactions	29
2.2.2.3 One vs. many	30
2.2.3 Large data collection in hyphenated techniques	31
2.3 Machine learning for imaging electrochemistry	32

2.3.1	Elements of machine learning	34
2.3.2	Unravelling hidden information by machine learning	36
2.3.2.1	Automated segmentation and phase boundary recognition	37
2.3.2.2	Tracking dynamically multiple phenomena	41
2.4	What this thesis is about	44
3	Electrocatalysis at single nanoparticles – the case of hydrogen evolution reaction at Pt	47
3.1	Introduction	47
3.2	NBs as hydrogen evolution reaction markers	49
3.3	Quantitative description of single NBs	53
3.3.1	Quantitative estimation of NBs size and shape	55
3.3.2	Suggestion of hydrogen spillover	61
3.4	Conclusions	65
4	Differentiating competitive electrochemical pathways at optically transparent (ITO) electrode	69
4.1	Introduction	69
4.2	Probing bare ITO in acidic conditions	71
4.2.1	Proton reduction vs. indium reduction	72
4.2.1.1	Hydrogen NBs nucleation on bare ITO	75
4.2.1.2	ITO reduction in acidic condition	78
4.2.2	Heterogeneity of surface reactivity	80
4.3	The complexity of Ni electrodeposition	84
4.4	Conclusions	89
5	Watching the electrochemistry within sub-micrometric electrolyte droplets	93
5.1	Introduction	93
5.2	Sub-droplet resolution to watch Ag electrodeposition	95
5.2.1	Multi NPs deposition monitoring	98
5.2.2	Centroid motion during NPs growth	102
5.3	Monitoring early stage nucleation for non-metallic CaCO ₃ crystals	103
5.3.1	Experimental approach	104
5.3.2	Real time imaging of pipette meniscus	104

5.3.3	Droplet size effect in nucleation and growth	107
5.3.3.1	Control experiment to evaluate ITO stability range	107
5.3.3.2	Controlled CaCO ₃ crystallization in a microscale meniscus	109
5.3.3.3	CaCO ₃ crystallization at large meniscus	114
5.3.4	FEM model of CaCO ₃ precipitation in the larger meniscus	116
5.4	Conclusions	120
6	Materials and methods	123
6.1	IRM experimental setup	123
6.2	Image processing	125
6.2.1	Background removal	125
6.2.2	Super-localization	127
6.2.3	Optical transients	128
6.2.4	Edge detection	128
6.2.5	Correlative SEM	130
6.3	Materials and chemicals	130
6.3.1	Chemical products	130
6.3.2	Pipettes fabrication	131
	Conclusions and perspectives	133
	Bibliography	137

Chapter 1

General introduction

Electrochemistry is a powerful analytical tool in materials science.

However, macro-scale electrochemistry alone is not sufficient for evaluating the electrocatalytic performances of nano-structured electrodes as the latter are rarely homogeneous. Indeed, nanoparticles, unlike molecules, are produced within a distribution of size, structure (crystallographic facets) and therefore within a same population of nanoparticles one expects to observe a wide variability in electrocatalytic activity. For instance, this variability which is contained within the ensemble electrochemical behavior of billions of NPs drop-casted on an electrode does not necessarily reflect the intrinsic electrochemical characteristic of one particular NP inside the deposit. It then requires combining electrochemistry to a second analytical technique for probing the electrode nano-structuration at the single entity level.

The aim of this thesis is therefore to bridge the gap between the global electrochemical response of an electrode and single entity behavior through the use of highly sensitive optical imaging capable of resolving NPs in space and time. The term “single entity” has been largely discussed and adopted by the electrochemists community for the first time in 2016, during the “Next Generation Electrochemistry” Faraday Discussions, indicating a novel methodological and experimental paradigm focused on one entity (active site, NP, single cell, ...) at the time.¹ This ambitious task led to the formation of the Single ENTity NanoElectrochemistry (SENTINEL) Consortium, a Marie Skłodowska Curie innovative training network founded by European Union which groups a multidisciplinary collaboration between 20 institutions oriented to different projects. Each project has been focused in exploring different ideas closely linked to single entity electrochemistry, from the design of new instruments to push electrochemical detection limit to early stage diagnosis through nanoprobes sensing.

My thesis is taking part of this consortium and consists in unraveling dynamic and simultaneous electrochemical phenomena at the nanoscale by coupling electrochemical measurement in a droplet cell to interference reflection microscopy that images the electrode interface. It has also been focused on optimizing the methodology to extract quantitative and reliable information from large volumes of structured data. Most of the results obtained during this thesis is contained in the present manuscript divided into 5 key Chapters.

Chapter 2 presents the state-of-the-art in the coupling of *operando* optical imaging for probing nanoscale electrochemistry and how to extract quantitative information insightful for electrochemists from an optical image sequence. More specifically, the chapter relates what are the fundamental experiments of the last five years and how these milestones can be considered as the starting point to improve the methodological aspect concerning *operando* microscopies in electrochemistry. The last part of the chapter discusses briefly what I think is a possible evolution of the field and which corresponds to the use of machine learning algorithms applied in electroactive materials imaging.

Chapter 3 is dedicated to the opto-electrochemical study of a widely used electro-catalyst, platinum NPs, in order to define activity descriptors for single NPs. It details how single entity approach can bring new, fundamental, information even for systems whose bulk electrochemical response is widely known.

Chapter 4 is dedicated to competitive processes in both electrode surface and *in situ* electrodeposited NPs. Original experiments have been designed to probe quantitatively the effect of substrate heterogeneities on local electroactivity, to demonstrate how these effects cannot be neglected and to decouple the contribution of simultaneous, competitive, reactions.

Chapter 5 takes a deeper look into the growth dynamic of Ag NPs, electrochemically driven within confined sub-microdroplets., It allowed to assess how transport phenomena can affect nucleation sites density and position, to investigate the droplet stability in SECCM configuration and to demonstrate how sub-droplet resolution can unravel the dynamic of these phenomena also for droplets of about 500 nm of diameter.

Technical aspects are presented in Chapter 6, where all the instrumentation, the materials and image processing methodology used can be found.

Finally, the SENTINEL program allowed me to complete two secondments intended to enhance collaboration during my Ph. D. work and so to combine different instrumental tools and single entity approaches. My first secondment has been in collaboration with Warwick University, in order to combine Scanning electrochemical cell microscopy (SECCM) expertise from Prof. Patrick Unwin with high resolution optical microscopy. The results of this collaboration are described in Chapter 5

My second secondment, in collaboration with Prof. Mingdong Dong from Aarhus University, focused on developing neural networks to analyze atomic force microscopy images of RNA origami. Although this project hasn't involved electrochemistry, it was the ideal system to test

this novel methodology. This project is still under investigation and its results are not included in this thesis.

Chapter 2

Optical microscopies in electrochemistry

This chapter will introduce the state-of-the-art of *operando* optical microscopies applied to electrochemical systems of interest such as electrosynthesis and electrodeposition, dynamic monitoring of single nanoparticles (NPs) chemical and structural changes and electrocatalysis. Milestones of last five years will be presented to delineate the aim of this thesis and the future perspectives for electrochemistry at the nanoscale. Results from hyphenation between high throughput visualization, multi-correlative microscopies and electrochemical characterization will be presented to better focus the next challenges in nanoelectrochemistry and advanced optical microscopies. The rapid acquisition of large volumes of data in a single experiment allows a deeper understanding of the system at different time and spatial scales. One of the rising challenges is therefore the necessity to minimize the time to extract this amount of quantitative information. For this reason, the last section is dedicated to the use of machine learning (ML) strategies in imaging electrochemical processes, a data-driven approach whose strength lies on the amount of data itself.

2.1 Overview of Operational Principles

Optical microscopy methods have provided insights in a broad range of disciplines for more than a century. They have been most commonly used in physics and biology, as they allowed quantifying the action of forces by monitoring the motion of objects, or identifying the biological functions of sub-entities of living microorganisms. Optical microscopy has been less considered in chemistry or electrochemistry. One of the reasons is that the visible range of light used to draw an optical image, is not usually the most informative spectral range for identifying chemical structures or chemical transformations. This view has considerably changed over the last decades thanks to progresses in (i) synthetic design of molecules or nanoobjects with switchable optical properties in the visible range, (ii) the development of highly sensitive and rapid photodetectors, e.g. able to detect the ultimate limit of a single photon, or (iii) the development of (instrumental or computational) strategies enabling imaging at higher resolution (such as super-resolution microscopy) imaging and higher sensitivity detection (even label-free).

Visible light has been used to visualize an electrochemical process for the first time in 1987.² The aim of R.C. Engstrom was to observe how heterogeneities in vitreous carbon electrodes were affecting the electrochemical transformation of a luminescent or fluorescent redox molecule, such as $\text{Ru}(\text{bpy})_3^{2+}$, at the scale of hundreds of microns. The use of optical microscopy remained mostly unexplored during the '90s, mostly because the scanning electrochemical microscope, SECM, invented in the meantime, was expanding much faster owing to its ability to provide faster and more quantitative electrochemical information.

The development of fast charged-couple device CCD cameras and other technological and methodological progress has re-activated the promise of optical microscopes as high throughput tools to image electrochemistry. For details about these progress and the operational principles and applications of optical microscopy for imaging electrochemical systems we refer to a number of recent reviews.³⁻⁶ Here it is rather presented a comprehensive discussion of the last three years research efforts using optical microscopy to image electrochemistry. This chapter focuses particularly on new methodologies able to unravel new level of complexity in terms of electrochemical processes/information, of simultaneous phenomena visualization, as well as new experimental and image processing methodologies.

2.1.1 Operational principles

Figure 1a presents a schematic of the strategy used to image an electrochemical system by an optical microscope. To do so, an electrochemical interface of interest is brought in the field of view of a microscope objective. This lens collects the light coming from the interface of interest and sends it through to a photodetector. If the electrochemical transformation alters the light collected by the objective it results in a change at the detector. In wide field microscopes, a camera, made of millions of detectors, captures instantaneously a full field image (millions of pixels) of the interface of interest. Confocal optical microscopy would rather focus on the photons coming from a single sub-micrometric region analysis (confined physically by a pinhole), defining the pixel of the image, and the full field imaging of the interface requires moving the observation region as in scanning probe microscopies. The interest in imaging electrochemical processes by wide-field optical microscopes is two-fold. First, they allow capturing within a few milliseconds timescale a single image snapshot (typically $50 \times 50 \mu\text{m}^2$) containing therefore thousands of localized optical information. When the light used to image a process is not too intense, the imaging process is not perturbing the electrochemical process, or, unlike in the different scanning local electrochemical probe microscopies, it is not required to account for the invasiveness contributions (electrochemical, geometrical confinement, or displacement) of the nearby local electrochemical probe (micro/nanoelectrode, nanopipettes, AFM tip, etc...). It then provides a unique means to observe operando and at high throughput electrochemical processes in conditions near to those of real electrochemical systems.

However, unlike for the latter scanning local electrochemical probes microscopies such as SECM, scanning ions conductance microscopy (SICM) or scanning electrochemical cell microscopy (SECCM), imaging electrochemical processes with an optical wide-field microscope consists in catching the optically visible footprint of the result/consequence of an electrochemical reaction. It is therefore an indirect imaging method where the local optical information collected at each pixel of the optical image carries (and may be converted) into local electrochemically relevant information.

Quantitative electrochemical imaging from optical images is therefore more demanding as it not only contains the chemical complexity of the systems but also requires the appropriate analysis or conversion of the optical image. For the former reason, optical microscopy has first tackled model (or simpler) systems and light detection principles. Some of them are recalled in Figure 1b, and basically objects are imaged from the collection of light they emit

or light they absorb or scatter. Emission-based microscopies, such as fluorescence (FM),⁷⁻⁹ electrochemical luminescence (ECLM)¹⁰ or Raman-based (RM) microscopies, usually require labelled tracers (fluorescent or Raman active molecules or quantum dots). Label-free microscopies are sensitive to the local change in refractive index associated to an electrochemical reaction. It was mostly addressed from the change in absorbance for an electrochromic object, or change in light extinction, for example for plasmonic NPs. For uncoloured dielectric objects variations in the refractive index can also be probed by interferometric imaging mode exploited for example by the interferometric scattering (iSCATT) or other equivalent microscopes.¹¹⁻¹³

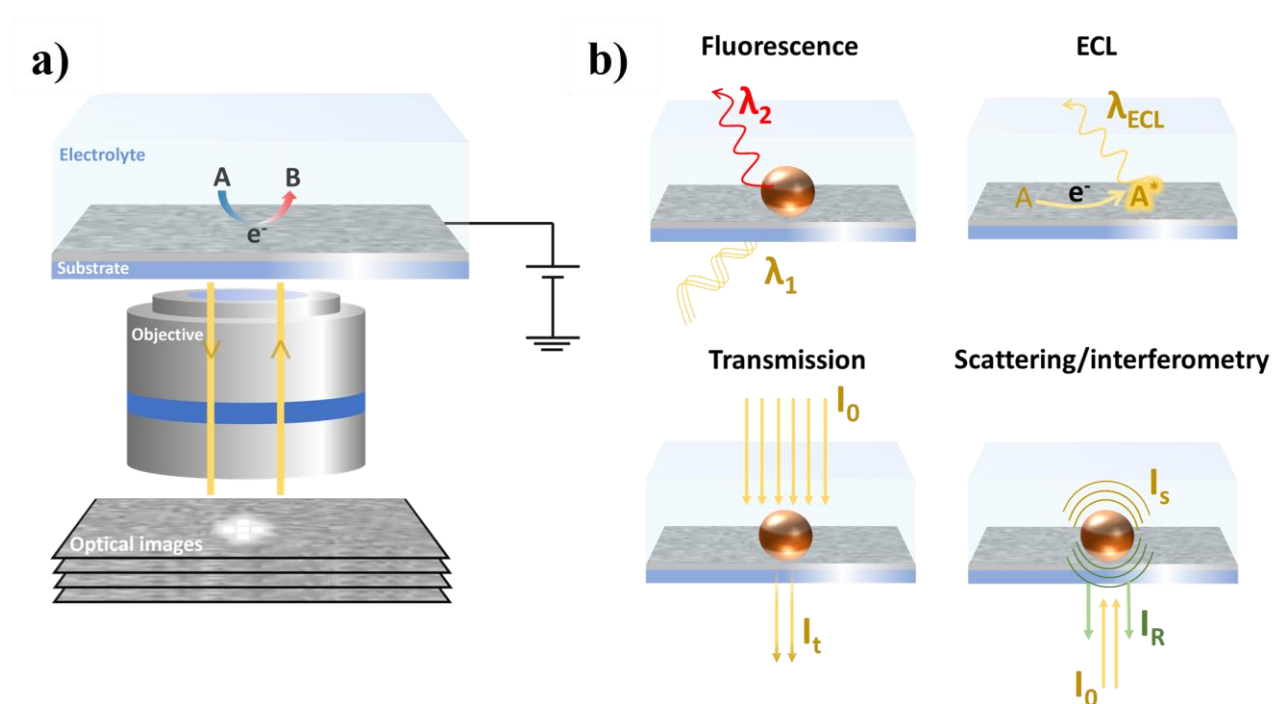


Figure 1. a) Basic principles of visible light microscopy; b) types of detections based on the phenomena responsive of the imaging process.

2.1.2 Methodologies for quantitative image analysis

Although each imaging technique has its own precautions and protocols, there are some methodologies which are common to obtain images where quantitative information can be underlined easily. The aims are mainly 1) to associate variations of local optical properties to changes in the nano-object and/or on its surface, 2) to reduce the background level in order to increase the signal-to-noise ratio and the sensitivity and 3) to increase the precision in

localizing and tracking dynamic events. This section presents an overview of the main methodologies, while specific protocols used for image acquisition and processing of this thesis will be detailed in Chapter 6.

2.1.2.1 Single object detection by super-localization

The image formation requires a significant change of the local optical properties relative to the background level. Sensitive detection and imaging then mostly rely on the ability to image a system with the lowest background level.

Removing the background incident light is usually obtained through oblique incidence illumination (obtained in dark-field illumination). The total internal reflexion (TIR) incidence allows observing with higher sensitivity the few 2-3 hundred nanometers adjacent the illuminated interface. Different single object studies rely on super-localizing in this illuminated region the position of single objects. The concept of super-localization (enabling super-resolution imaging¹⁴) consists in resolving the centre of mass or centroid, by a Gaussian fit procedure, of the optical feature representing the imaged object. This is showcased in Figure 2. An object physically smaller than the diffraction limit will appear in an image as diffraction limited spot. Figure 2a presents the theoretical or simulated representation, also known as the airy spot of such diffraction limited feature. This diffraction limit can be described by different mathematical functions, but more conveniently as shown in the 2D plots of Figure 2b, by a 2D Gaussian curve. Fitting the experimental optical feature by a 2D Gaussian allows defining for a given feature 4 descriptors: the position of the maximum of the Gaussian fit (x_0, y_0) , the width of the Gaussian curve σ (formally its width along the x - and y -axes may differ), and the intensity of the maximum, I_0 . By converting the experimental image by a mathematically treated image where only I_0 is plotted at the position (x_0, y_0) within the precision of their estimate is the concept of transforming an optical image into a super-resolution image (last 2D plot of Figure 2b). On the other hand one can only point the position of this optical feature (x_0, y_0) which is then the concept of super-localization.

Single fluorescent molecular probe sensitivity is reached by FM, in what is known as single molecule localization microscopy SMLM.⁹ SMLM was used to monitor the dynamics of molecular adsorption and electrochemical or catalytic processes at various nanointerfaces, such as NPs or nanobubbles (NBs).¹⁵⁻²¹

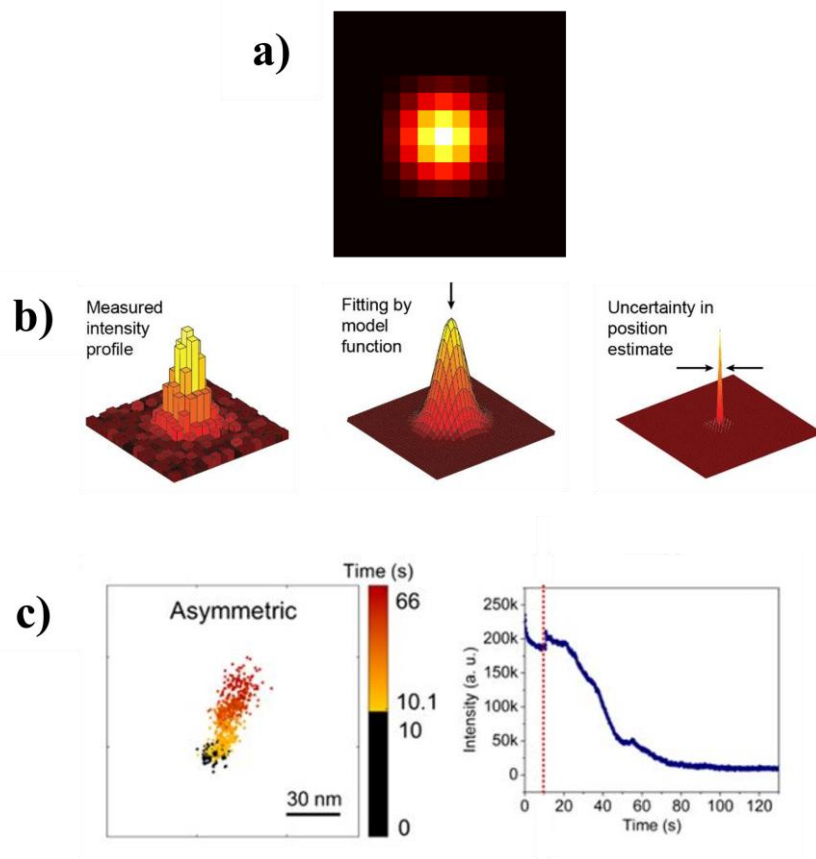


Figure 2. a) Simulated diffracted optical spot; b) scheme about the concept of super-localization with bidimensional Gaussian fit; c) example of optical centroid coordinates over time during single Ag NP dissolution monitored by dark field microscopy. *Adapted from references 14, 27.*

Noteworthy, the concepts of super-localization (see Figure 2c) and of high sensitivity TIR illumination have also been used with label-free microscopies. It enables the observation of any type of nanoobject deposited on or near a thin plasmonic Au electrode in the surface plasmon resonance microscopy SPRM configuration.^{5,22,23} At non-plasmonic (transparent) electrodes, TIR illumination allows super-localizing and tracking the growth of nanodendrites with nanometric spatial resolution.²⁴ Super-localization procedures are not only interesting to track physical motion or growth of objects in 3D. If the centroid position is changed by less than the physical size of the object monitored, it is more likely that the phenomenon observed is a reorganization (rotation or local transformation, or local charging^{25,26}) of the object. Figure 2c shows at first how the centroid motion of a Ag NP can be tracked with a precision in the order of 10 nm; secondly, the total displacement of the centroid was smaller than the particle size, so it was attributed to the anisotropic dissolution triggered by an electrochemical reaction.²⁷

2.1.2.2 Background minimization and contrast maximization

The last years have shown increased interest in interferometric-based strategies. They are exploited in different reflection-based microscopy configurations, the most popular being the interference scattering microscope (iSCATT).^{11,12} Visualization principle relies, as sketched in Figure 1b, on the collection by the photodetector of the interference between the light scattered by the object of interest and the beam reflected by the planar (electrode-electrolyte) interface where it is standing. While the reflected waves are planar, the ones scattered by the object are spherical and dependent on its dielectric properties. The intensity collected at each pixel of the detector can be described by the equation (1):

$$I(\mathbf{r}) = |E_{refl}|^2 + |E_{scatt}|^2 + |E_{refl}||E_{scatt}|\cos(\vartheta) \quad (1)$$

The term responsive of interference is the last term of the right hand side of the equation, composed by the product between the modulus of reflected electrical field and scattered electric field, also dependent on the phase between both fields, ϑ .

The optical images are made of interference fringes and the image of the objects can have either darker or brighter contrast compared to the background (i.e. the reflection from the naked interface). Even if the different contrasts in the images makes their interpretation less straightforward, this configuration allows pushing the limit of detection by several orders of magnitude compared to direct (dark-field for example) imaging. It has particularly been used to image the formation of electrochemical double layer at individual NPs.¹³

Recent efforts have also been devoted to push the detection limit by using ECLM since the light emission event is triggered by an electrochemical reaction, and therefore does not require an illuminating light source. ECLM is therefore operated under almost ideal dark conditions, though under the constraining conditions requiring producing reactive species at an electrode under strongly oxidative (or reductive) potentials.¹⁰ As it relies on the reaction-transport of electrogenerated species, ECLM is pertinent to image adhesion sites of single biological cells.²⁸⁻³³ The implementation of interferometric measurement is also possible.³⁴ Ultra-sensitive cameras are now capable of reaching the ultimate detection of single photons. ECLM is then ideal for imaging objects or reactions nearby an electrode region with single photon sensitivity.^{29,35}

2.1.2.3 From local optical information to electrochemical signals

The most straightforward information in an optical image is the object position, (from localization procedure) along its 2D or 3D trajectory towards a polarized electrode, which correlates to the electrochemical current in electrochemical nanoimpact studies.^{36–40} The changes in optical signature during an electrochemical experiment carry more valuable chemical information complementary to the electrochemical one. As detailed in Chapter 4 and 5, it is obtained first from the characteristic times (duration, onset, etc.) of the optical signature variations associated and correlated to different (electro)chemical transformations (see below, conversion, dissolution, growth etc.). Different quantitative strategies have also been proposed, to convert the optical signature variation into an optically-inferred electrochemical curve, such as an optical-voltammogram.^{3,6,25,41–43} Light absorbance or the extinction wavelength (for plasmonic NPs) are usually proportional to a local concentration or amount of electrochemically transformed material, i.e. an electrochemical charge.⁴⁴ The electrochemical current then often tracks the time derivative of local optical transients. Figure 3 reports lithiation/de-lithiation on LiCoO_2 single NPs and Ag underpotential deposition on Au NPs as representative phenomena which can be probed by optically inferred CVs.^{45,46} Optical CVs can be here inferred by the derivative optical footprints sensitive to variation of refractive index or from the spectral shift over time. Optical CVs on single objects can therefore either confirm the electrochemical signal associated to bulk measurement, or unravel hidden signatures as showed in figure 3b, where the optical CVs on single NPs shows how Ag electrodeposition occurs easily on (100) faceted Au NPs than on (111) ones.

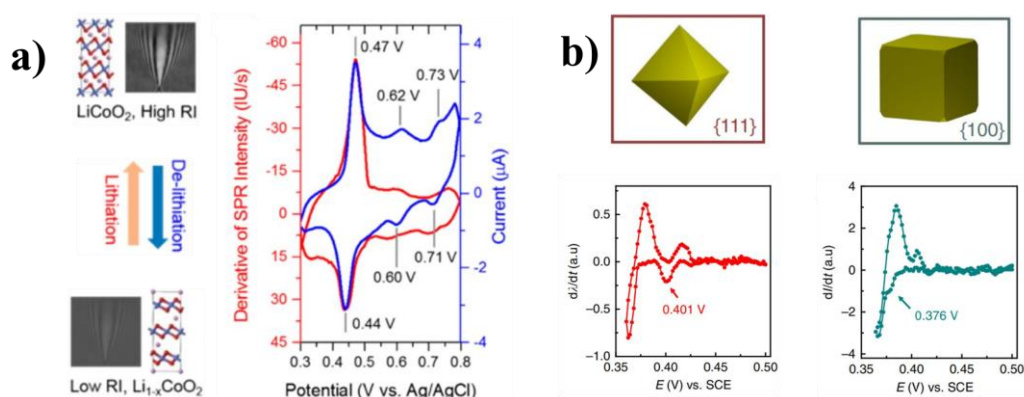


Figure 3. a) lithiation and de-lithiation probed *operando* by SPRM, with a comparison between an electrochemical CV and the optically inferred CV; b) growth monitoring of a single Co NP; the optically inferred CV allows to monitor Co(OH)_2 formation as consequence of the oxygen reduction reaction. *Adapted from ref 45, 46.*

For more complex situations, optical models have been developed to simulate the change in optical intensity associated to the electrogenerated growth of NPs,⁴¹ the conversion of NPs,^{47,48} or NBs from electrodes, or electrocatalytic processes at NPs. This will be detailed in Chapter 3.

Another means to extract quantitative information from optical images is to compare them to correlative complementary higher resolution microscopies, such as an electronic microscopy (or EDX) image in the same location. Even if such correlative imaging is obtained *ex situ* it provides a complementary imaging (sizing, structure, etc.) for a large number of imaged objects from which structure – optical response relationship can be obtained.

It requires a large amount of objects to be analysed and is obtained using automatized image analysis routines.⁴² These routines, often employing machine learning (ML) strategies, are now able to compare/recognize automatically images obtained from different microscopies, in order to find the same features, classify them according to their activity, shape or structure. As it will be detailed in the last section of this chapter, ML algorithms requires training dataset which must be carefully defined, in order to reach a sufficient efficiency in their tasks. In the context of opto-electrochemistry, this means the necessity to acquire optical footprints which have enough specificity to be the hallmark of specific single events. Therefore, the next section will detail the concepts behind single entity approaches in electrochemistry and how optical microscopies can add relevant additional information.

2.2 Imaging single events

The renewed interest in optical microscopy of the last decades is intimately related to the expansion of the field of single-entity electrochemistry.⁴⁹⁻⁵¹ While parameters reflecting the average electroactivity remains the most important indicator to evaluate performance of devices such as electrolyzers, fuel cells or batteries, the understanding of dynamic phenomena at the nanoscale has become a necessary pathway to design new strategies to push their performance. Although the first single entity experiments has been pioneered more than 60 years ago,⁵² the interest for single entity approach for close-to-real-life systems started growing from the meticulous examination of electrochemical transients associated to the reactive collision of individual nanoobjects onto an electrode, as showed in Figure 4 for Ag NPs.⁵³

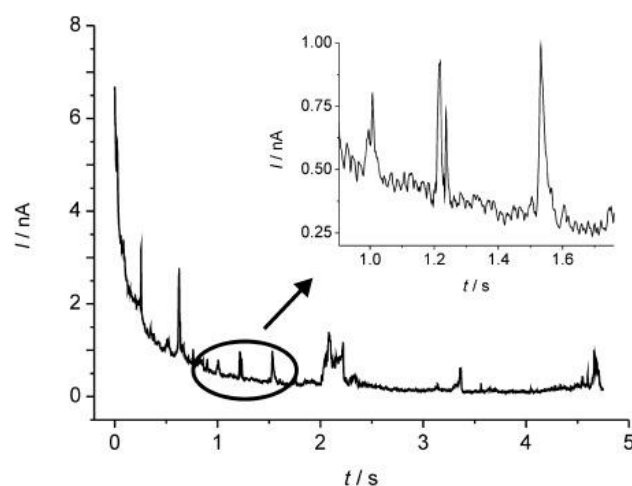


Figure 4. Chronoamperometric profiles showing oxidative Faradaic collisions of AgNPs in citrate solution. The inset shows detailed impact spikes. *Adapted from reference 53.*

By finding different statistical populations related to the shape of these transients, the assumption that the average response from millions of NPs was approximate to the sum of individual responses was no more sufficient to have a comprehensive understanding of electrode interfaces. The attractiveness of single entity approach in extracting quantitative statistical information from populations of single objects instead of a current/activity value related to the average response of billions of NPs drop casted into a macro electrode, therefore, pushed efforts in miniaturization of electrochemical probes, in parallel with the development of low current potentiostats capable to measure currents below the nA. Nowadays, the most commonly used nanopores can be divided into three groups.

Nanopores take inspiration from the Counter-Coulter experiment and are used especially for sensing application or to mimic biological processes. Briefly, it consists either into a metallic surface patterned laser etching or by controlled breakdown, or by biological membranes functionalized with pore-forming proteins. When the nanopore is polarized at a certain potential, a translocation current will be recorded everytime a specific object passes through the pore. The translocation current is therefore proportional to size, hydrodynamic properties and charging of each translocated object.^{54,55}

Micro- and nanoelectrodes gained popularity thanks to great advantage due to the minimization of capacitive contribution in the electrochemical reaction occurring at their surface. They can be used either as scanning probe to map, in the SECM configuration, the electroactivity for a specific reaction toward heterogeneous surfaces, grain boundaries or

patterned substrates. In single entity electrochemistry, they are used as NPs collector in diluted solutions to study temporally resolved electrochemical nanoimpacts.

Finally, nanopipettes are maybe at present the most popular tool to perform electrochemistry at the nanoscale. Nanopipettes are usually crafted using a laser puller on borosilicate capillaries. The size of the tip-end pipette can be reproduced easily controlling the laser heating and pulling force, although further fabrication procedure could be required to modulate the geometry at the extremity. Once filled with the electrolyte of interest, the great advantage of nanopipettes is their versatility of use. They can be used to probe surface topography of living cells and other soft systems, to map the local conductance in complex environment or to confine sub-micrometric or nanometric areas of larger electrode into picoliter droplet formed by the meniscus of the pipette.^{56,57} It is an ideal tool to perform single entity electrochemistry.

As sketched in Figure 5, optical observation has been implemented for all these configurations, in order to provide insightful complementary information about the dynamic of collisional events, of translocating objects in biological environment or to unravel the proximity effect on NPs growth/motion within confined droplets.

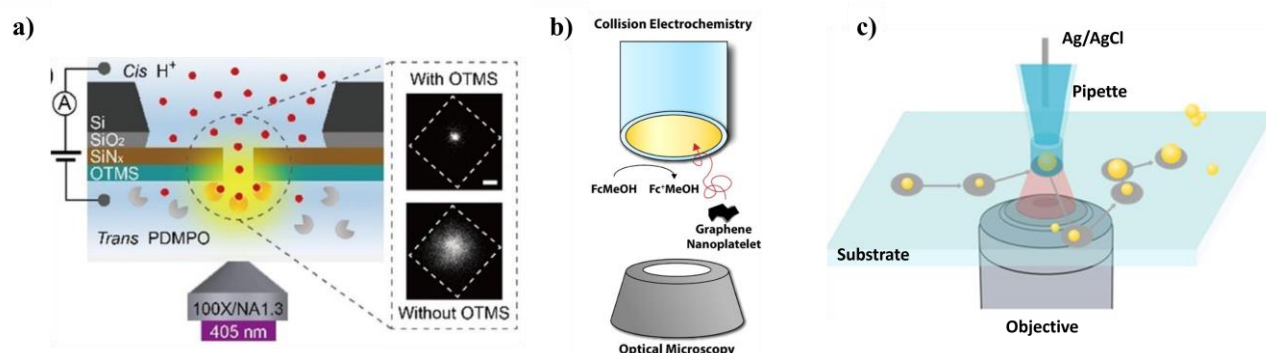


Figure 5. Schematic of optical microscopy coupled with a) nanopore sensor, b) a disk gold microelectrode used for nanoimpacts and c) a micropipette used in SECCM configuration. *Adapted from ref 55, 56 and 116.*

2.2.1 A great eye on electrode surface

Following the seminal works of Crooks⁵⁸ and Tao,⁵⁹ two types of information can be gathered by optical microscopy for single entity electrochemistry. Firstly, high-throughput, wide-field-of-view imaging of the electrode region allows seeing where and how nanoobjects encounter the electrode, i.e. the mass transport. Spatio-temporal localization of a wide variety of individual objects (from biological objects, to individual particles and molecules) has been

obtained with a large variety of microscopies, including those supplemented with spectroscopic interrogation,^{44,60,61} in 2D or more recently in 3D. Direct visualization of single objects trajectories at the proximity of polarized electrode surface unlocked the study of transport phenomena dependent on the applied potential, the electrode size and the distance of the object from the electrode, probing, for instance, to determine if a certain potential can overcome the Brownian motion contribution before the diffusion limited regime. Secondly, the optical signal associated to the individual objects is scrutinized as it provides further complementary information about the electrochemical transformation of the isolated object or in its surrounding environment.

2.2.1.1 Single electron transfer imaging

Emission based microscopy strategies coupled to electrochemical actuation have been successfully used over the past few years for mapping electron transfer processes with very high spatial resolution. It allows revealing the heterogeneity of electrode reactivity. Nanoscale or single molecule resolution imaging is reached by single fluorescent molecule localization, SMLM, which consists in observing the fluorescence blinking dynamics of single molecules upon their adsorption on surfaces.⁶² It allows evaluating, then mapping with nanometer resolution, the kinetic of different reactions. Particularly appealing to study catalytic mechanisms, the strategy has also been used to map electron transfer kinetics at single graphene layers⁶³ or demonstrating the importance of such processes through defects.⁶⁴ To circumvent the difficulty of evaluating such measurements for non fluorogenic species, a methodology taking advantage of competing adsorption between fluorogenic and non-fluorogenic compounds was proposed to image the photoelectrochemistry of quinones at the surface of a photovoltaic particle.¹⁷ To enable the imaging of electron transfer at non fluorogenic species, Zhang et al. also proposed a method using a bipolar electrode system to directly couple a conventional electrochemical (e.g. oxidation) reaction on one pole of the bipolar electrode, to the opposite electrochemical (e.g. reduction) conversion of a special fluorogenic species, on the opposite pole, as shown in Figure 6.⁶⁵

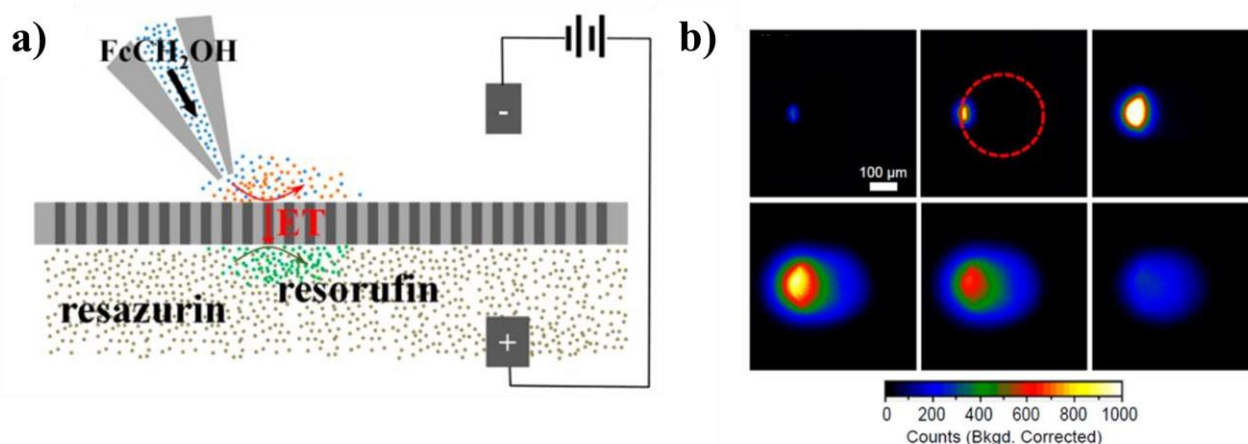


Figure 6. (a) Schematic diagram showing the setup to image release of FcMeOH from a glass micropipet with an array of carbon-fiber ultramicroelectrodes. The FcMeOH molecules are oxidized on the top surface of the carbon electrodes generating resorufin on the bottom surface of the carbon rods. (b) Fluorescence snapshots recorded from an experiment in which a solution of 2 mM FcMeOH with 0.1 M Na₂SO₄ was discharged from a 3 μm micropipette. *From reference 65.*

By observing optically the opposite pole electrode surface by fluorescence microscopy (Figure 6b), one can actually obtain an image of the reaction of interest with the non-fluorogenic species. The imaging strategy can be coupled with both electro-active or a pH-sensitive fluorogenic species that emit light upon (electro)chemical transformation, and the conversion of the fluorogenic species into a Faradaic current information was demonstrated.^{66,67} As photon detectors are much more sensitive than charge detectors, when a single-electron transfer results in a single photon emission, transducing electrochemical events into light emission can dramatically enhance the detection sensitivity up to the single electron-transfer event. Using an ECL reaction at the detection pole allows in principle a higher sensitivity (lower noise).⁶⁸ The strategy can be employed to image a wide range of electrochemical processes or serve as an indirect quantitative fluorescent sensor for non fluorogenic redox labels for cellular biomarkers,⁶⁹ or respiration.⁷⁰ The pixel in the image is given by the size and density of the bipolar electrode arranged in arrays. The micrometer-range resolution is sufficient to image biomarkers bound at cell membranes,⁷¹ while the use of nanoelectrode arrays allows reaching sub-micrometer resolution.⁷²

ECL microscopy was used at the level of single molecule or single event imaging. The advantage is the near-zero optical noise level imaging and absence of photobleaching usually encountered in single molecule fluorescence microscopy studies. Single molecule ECL

allowed imaging the adsorption sites of cells on an electrode surface from the blocking of the electron transfer reaction. The single molecule sensitivity allowed detecting and imaging the position of single protein at the cell membrane⁷³. Single molecule ECL imaging also considerably increases the spatial resolution of ECLM down to few 100 nm by applying the concepts of super-resolution microscopy. It helped detail the facet and defect-dependent electrochemical activity of Au nanorods and nanoplates.⁷⁴

The sensitivity and resolution of this imaging method was pushed down to single photon and therefore single chemical event limit. Single photon ECLM was employed to resolve spatially and temporally single tris(2,2'-bipyridine)ruthenium(II) complex oxidation reaction at electrodes. By using large excess of co-reactant to ensure a surface confined regime, collecting and counting single photons over time resulting from single reaction events, Dong et al. implemented such dynamic counting to draw super-resolved images of electrodes or cells.²⁹ Next, the strategy was used to map the $\text{Ru}(\text{bpy})_3^{2+}$ electron transfer kinetics and standard potential over a catalytic gold micro-plate catalyst surface. The super-resolution image of these descriptors are provided in Figure 7.³⁵ It revealed that the most active sites, characterized by higher reaction rate constants, are located at the edges of the catalyst. By comparing the Turn Over Frequency (TOF) mappings constructed at different potentials, they also highlighted the formation of Au oxide on the catalysts at higher over-potential resulting in the decreasing in reactivity.

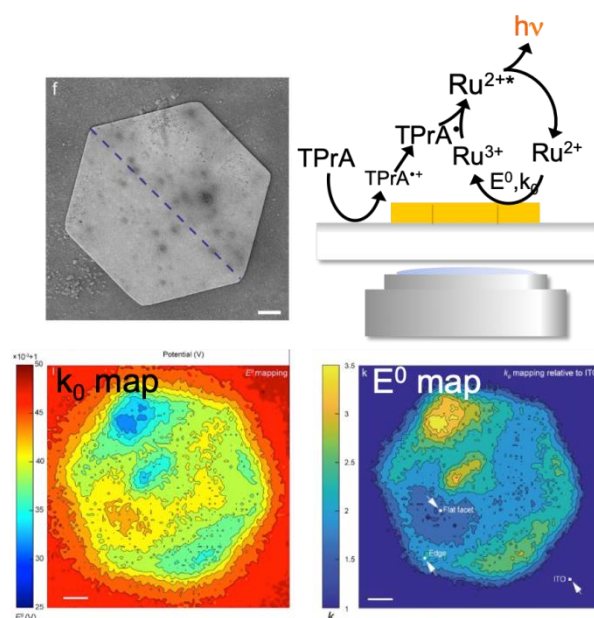


Figure 7. Kinetic and thermodynamic mapping of $\text{Ru}(\text{bpy})_3^{2+}$ oxidation on a gold plate by ECLM. Adapted from reference 35.

2.2.1.2 Probing concentration profiles

The heterogeneity of charge transfer is not just restricted to the polarized electrode or its electroactive domains but it propagates, through mass transfer, within diffusion distances. Optical microscopy methodologies have also been developed to map the transport of optically active species involved in electrochemical reactions. It is actually a unique, simple, instrument enabling imaging *operando* molecular transport from/to electrode regions. The most commonly imaged are the electroactive species engaged in the reaction: fluorogenic electroactive or pH sensitive species, light absorbing or refracting reaction products or substrates, scattering NPs,... Recent strategies are devoted to the transport of the electrolyte itself (ion fluxes) during the electrode reaction: from fluorogenic or Raman active electrolyte ions to fluorogenic electroinactive molecules or particles which are used to monitor the accessibility or flow of the solvent to porous electrodes.

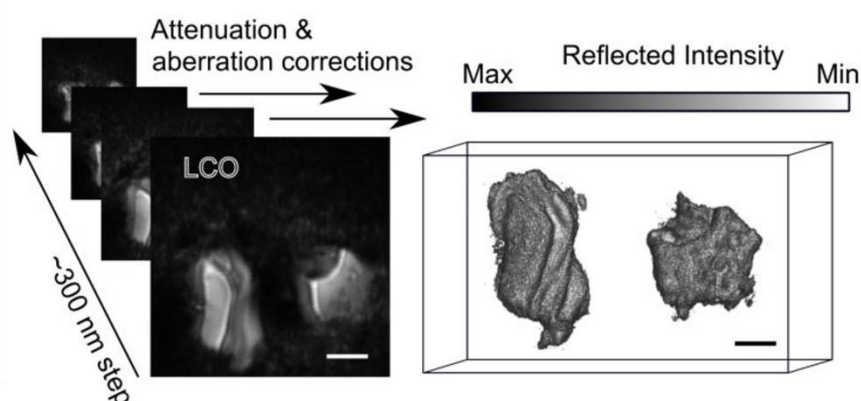


Figure 8. Stack of images acquired along z-axis by 2-photon fluorescence excitation and 3D optical reconstruction after aberration corrections. *From reference 82.*

3D mapping is also possible through confocal imaging (under pseudo steady-state electrochemical conditions), illustrated recently from the 3D diffusion layer build-up including more recently during enzymatic reactions.^{75–78} The instruments are mature enough to tackle the transport of active species in real energy storage or conversion systems, such as porous electrodes⁷⁹ for electrolyzers or battery^{80–82} under operation. Refractive index-based microscopy was recently used to image the local transport of Li^+ ions during (dis)charging currents within individual micrometric electroactive LiCo oxide or NbW oxide microparticles.^{80,81} Merryweather et al suggested from the dynamic analysis of these ions propagation, that the charge and discharge processes do not follow the same trajectory within

the particle. These differences are discussed based on the difference in conductivities in each state which is then manifested locally.⁸⁰ It was transposed to similar imaging in the presence of the usual electrode components (polymer binder and carbon paste) and improved to a 3D probing inside the particles using confocal visualization.⁸² Complemented with 2-photon fluorescence excitation the local distribution of the LiPF_6 electrolyte could be imaged around the particles, as shown in Figure 8. Close to the end of the charge, inhomogeneous electrolyte diffusion is revealed as a result of the geometry and porosity of the carbon/binder matrix surrounding the particles.

2.2.1.3 Growth and dissolution at the nanoscale

Electron transfers also result in a wide range of chemical and physical events that can be probed with optical approaches as well. EC reaction can lead to the creation of nanostructures that can be imaged at the early stage of their formation by optical microscopies. A case study is the electrochemical deposition of noble metals such as Ag, Au or Cu for which the nucleation and growth mechanisms are still under intensive investigation.⁸³

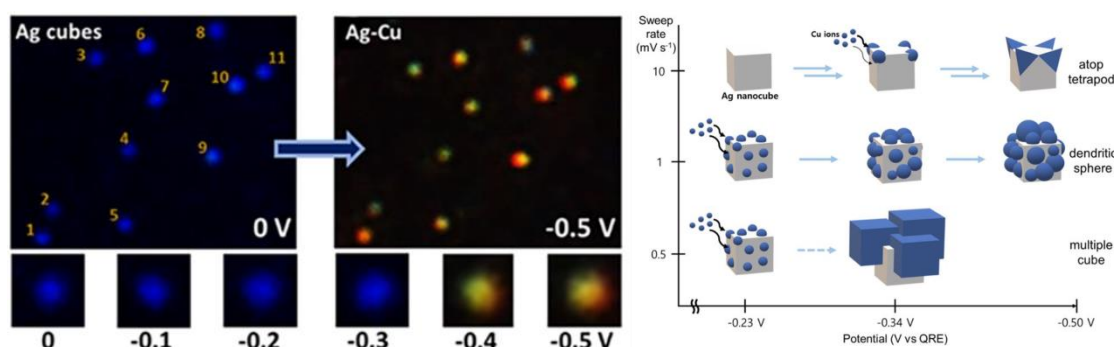


Figure 9. Visualization of Cu growing on Ag cubes by DFM, with a schematic of differences in growth mechanism observed varying applied potential and sweep rate. *Adapted from reference 84.*

Dark-field spectroscopic microscopy succeeded to detect the facet dependent deposition of atomic layers of silver on single gold NPs, as well as different growth mechanisms of Cu electrodeposited on Ag cubes, as reported in Figure 9.^{44,84} Visualizing *operando* deposition processes also gives access to the evolution of the surface nucleation density.^{85,86} As the local scattering intensity is linked to the NP volume, it also allows to size single NPs over time and to measure/control their growth dynamics.^{41,85,87,88} Then, by differentiating the NP volume

fluctuation, one can further calculate an optical current related to the growth of single NPs (see Chapter 4 and 5).⁴¹

Optical microscopy was also employed for imaging the electrodeposition of more complex materials such as Ni,⁴² Co,⁸⁸ Li,^{89,90} Mg,⁹¹ or Zn²⁴ as metal and/or as metal (hydr)oxides (Ni, Mn⁹² or Zn⁹²) with important implication in electro-catalysis and batteries as well as for studying the electro-crystallisation of metal oxides for energy conversion and storage. For instance, optical microscopy, employed as an “optical microbalance” evidenced the direct influence of zinc hydroxide sulphate precipitation/dissolution during the dissolution/deposition of MnO₂ electrode associated to its discharge/charge in aqueous Zn-MnO₂ battery environment.⁹² As shown in figure 10, Godeffroy et al. unravelled the complex, pH-sensitive interplay between oxygen evolution reaction, MnO₂ deposition and zinc hydroxide sulphate dissolution during the charge process. The oxidation of Mn²⁺ ions from solution results in the deposition of MnO₂ thin layers during charge. The thickness of the layer can be inferred from the change in optical reflectivity of the electrode surface. An optical image can then be converted into a map of relative deposition rate of MnO₂. The deposition is apparently faster around the ZHS particles (white features in the Figure 11b). This is because the deposition is associated to a local pH decrease. As H⁺ is released, the ZHS particle is dissolved enabling to locally buffer the pH. As the deposition is easier at less acidic pH, near ZHS particles the deposition is easier. After a longer charging period, the ZHS particles have completely dissolved and the pH cannot be buffered anymore. The pH decrease constantly along the charge to the point of favouring the water oxidation, which may impart the overall cyclability of the electrode material.⁹²

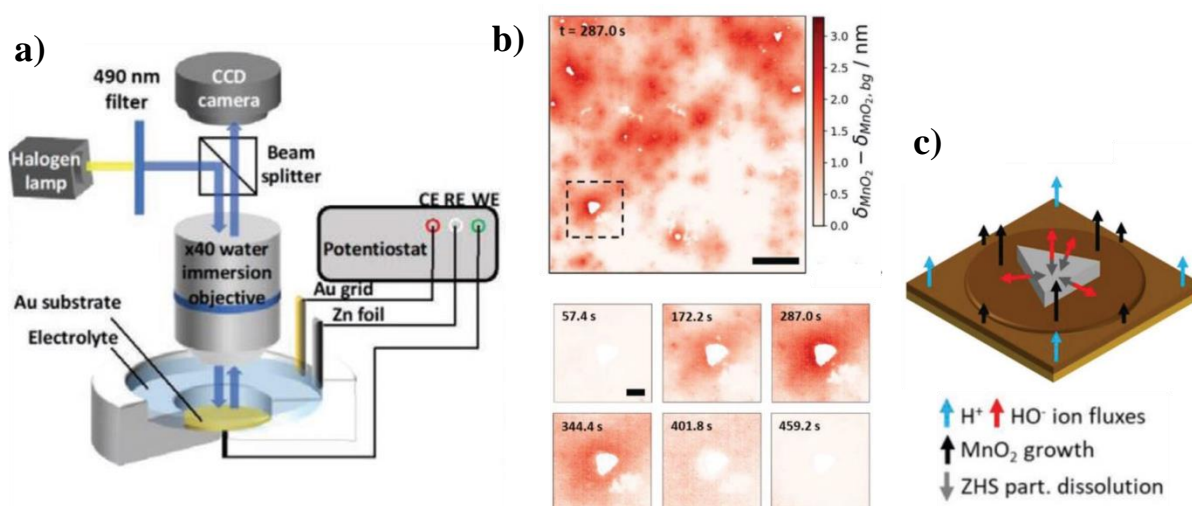


Figure 10. a) Scheme of the optical reflectometry setup used to probe b) in situ MnO_2 thickness in the proximity of zinc hydroxide sulphate particles during charge/discharge cycles. c) scheme of all the species involved in proximity of the same particle. *Adapted from reference 92.*

An optical visualization can also represent a helping hand in the elaboration of hetero-nanostructures as exemplified by monitoring the electrochemically assisted deposition of shell of various compositions around Au NPs. These studies take advantage of the sensitivity of the localized surface plasmon resonance spectrum of the NP to alteration of its surface composition. The electrodeposition is then tracked from the change in color of the NP observed by DFM. It was used to track amalgamation of Au with Hg,^{93–95} the electrodeposition of mono or bimetallic shells (Ag ,⁴⁴ or Pt, Pd, Rh, PtPd and PdRh⁹⁶) or semiconductor shells (CdS, CdSe and ZnS) around Au NPs.⁹⁷

Observing optically the dissolution kinetics of single entities by the same methodology is also possible. The electro-dissolution of single Ag NPs is still actively investigated.^{4,60,61,98} One way of analysing the single NP dissolution kinetics from optical images consists in evaluating the characteristic duration of the decrease of light scattered by DFM. The same strategy is proposed (Figure 11) to image the dissolution of single micron-sized marine entities of calcium carbonate (Coccoliths) triggered by the electro-generation of acid.^{99,100} This opto-electrochemical titration governed by surface reaction limitation allowed to reconstruct in 3D the entity volume based on dissolution kinetic and to determine the initial CaCO_3 mass, as well as to investigate the effect of some adsorbates (Mg^{2+}) on the dissolution rate. The strategy is sound as a means to evaluate the CO_2 storage capacity of biomineralizing algae.

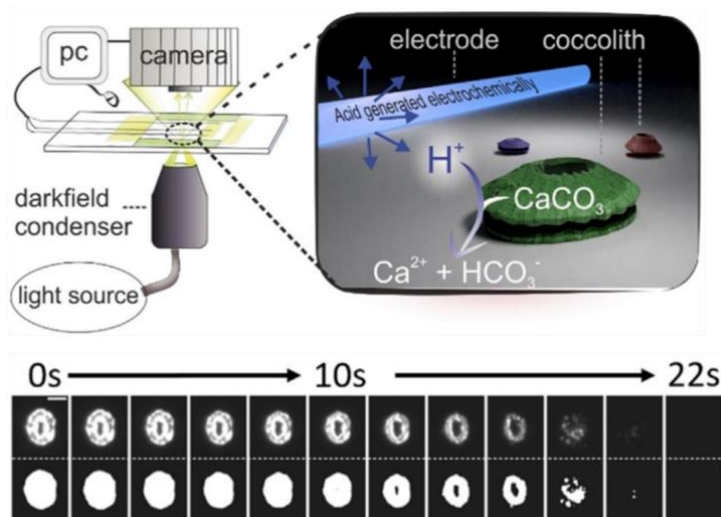


Figure 11. DFM setup used to probe coccolithophores calcification degree by electrogenerated dissolution. *Adapted from reference 99.*

2.2.1.4 Electrochemically driven transformations

As the electrochemical transformation of a single entity usually provokes a significant modification of its intrinsic optical properties, optical imaging can be employed to follow the conversion process, to identify reaction intermediate and to decipher mechanistic routes. Optical microscopy is currently used to track the redox conversion of different electrode materials or individual entities attached to electrodes. The conversion of electrochromic NPs is imaged from local absorbance imaging. For instance, Evans et al. exploited the change in optical density to optically monitor and quantify the conversion of single WO₃ NPs, i.e. indirectly the lithium ion intercalation process.¹⁰¹ From the experiments, it is concluded that the pseudo-capacitive charge storage depends on the NP morphology. The same methodology was also applied in a comprehensive series of studies from Wang's group on the (indirect) visualization of the mass transport of potassium ions inside single Prussian blue particle during their reversible electro-chromic conversion to Prussian white.^{25,43,102} Optical data suggested a less intuitive shell-to-core transformation mechanism²⁵ and evidenced partial conversion due to inactive zone inside some of the studied particles.¹⁰² The same material was further investigated by coupling optical visualization to electrochemical impedance spectroscopy (EIS) to probe the depth of surface charging layer during the same redox conversion.¹⁰³

Optical phase retrieval from SPRM allows a quantitative direct evaluation of refractive index variation at the single NP level. Variation in optical intensity can be used to investigate the

onset potential associated with the beginning of a redox reaction, such as from PB to PW in figure 12a and how fast the conversion occurs. This strategy also brings selectivity to label-free imaging for discriminating different types/chemistry of NPs.⁴⁸ The approach was also used to discriminate surface charging and compositional evolution during the electrochemical reaction conversion of Ag into AgCl NPs, previously imaged by interferometric reflection microscopy.^{38,47} Again, the conversion does not follow the same intermediates and dynamics during oxidation or reduction (Figure 12b). The reduction of the less conductive AgCl NP also starts with heterogeneous surface inclusion before a core-shell transformation operated. As the visualization also provided spatial information, the NPs were also shown to move on the electrode during multi-step charge injection of the electrochemical conversion. It was hypothesized that the local halide ions release during the conversion was propelling the NPs.⁴⁷

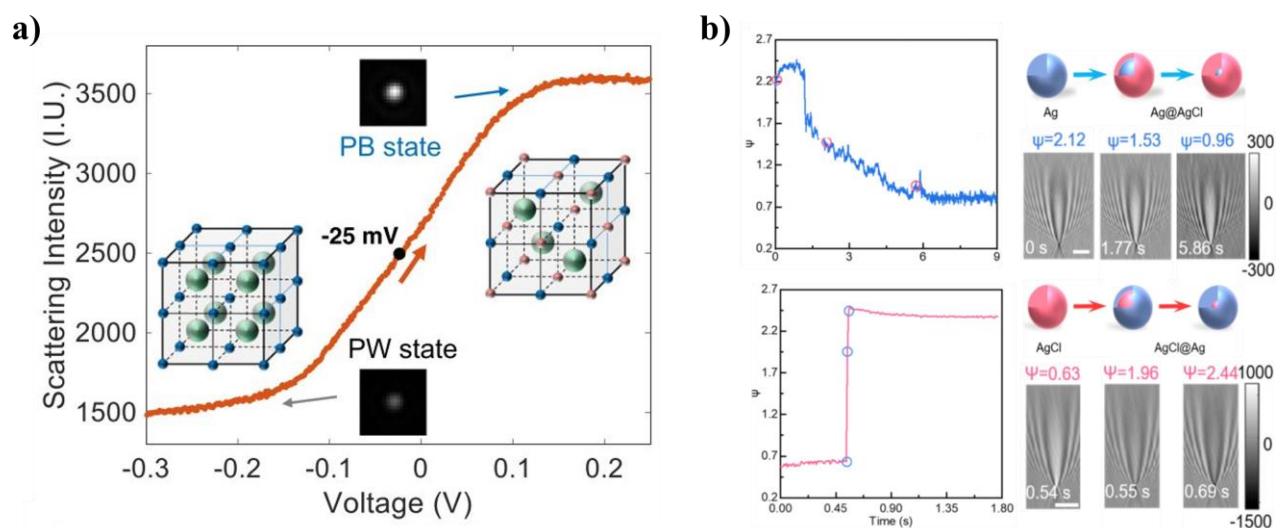


Figure 12. Electrochemical conversion of a) Prussian Blue into Prussian White and b) of AgCl into Ag and vice versa, probed by DFM and SPRM. *Adapted from reference 103 and 48.*

Refractive index based microscopy is also a pertinent technique to image the reversible oxidation and reduction conversion of graphene through local change in refractive index. The imaging technique enables identifying the role of defects in the structure.¹⁰⁴ Noteworthy, graphene layers are potential material for the fabrication of in situ TEM cell. The optical transparency and its possibility to image electrochemical changes by optical microscopy would be an asset for correlative *operando* optical and TEM imaging.

Battery electrodes are composed of electroactive particles whose charge/discharge is still operated below their theoretical capacity. As discussed above the de-

intercalation/intercalation of Li^+ ions was probed by iSCATT in 2D or 3D at the level of single micrometric LiCoO_2 particles. The label-free technique is sensitive to the local concentration of Li^+ ion enabling to reconstruct the evolution of the front of Li^+ intercalation or de-intercalation within the particle during, respectively, the charge or discharge of the particle.⁸⁰

2.2.1.5 Catalysis and motion

The accumulation of products at the vicinity of a nanoscale electro-catalyst sometimes provokes a change in the local refractive index of the surrounding medium that can further be detected by optical microscopy (see Chapter 3).⁵⁹

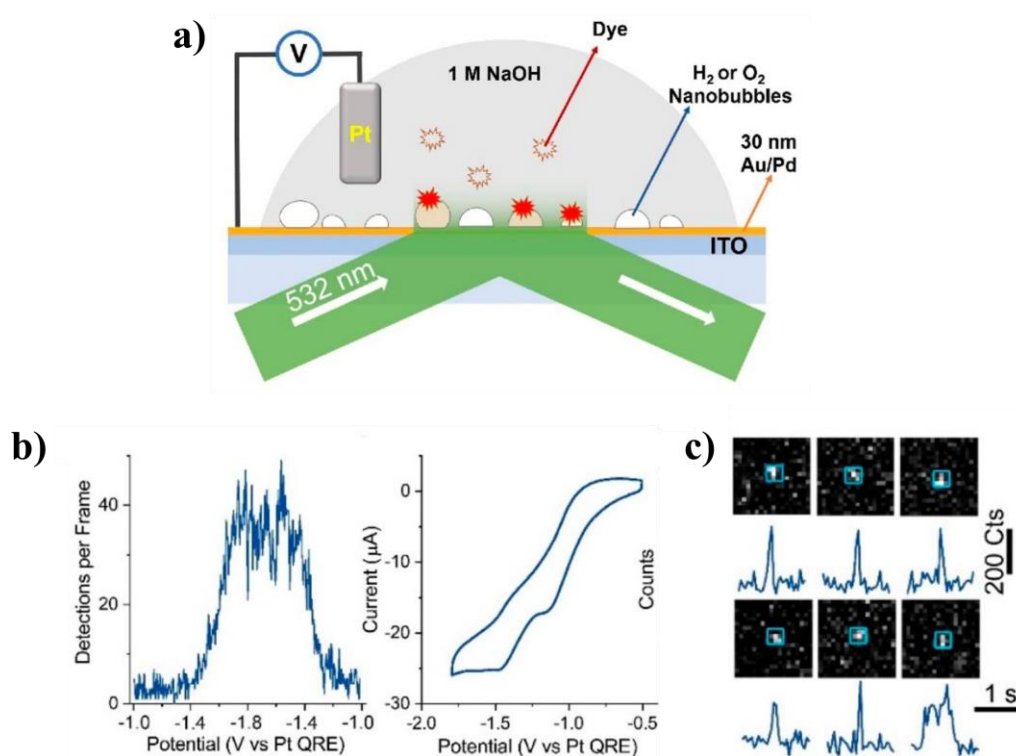


Figure 14. a) scheme of TIR setup used to label NBs formation; b) dependency of recorded NBs detection by potential during a CV; c) fluorescence image of six NBs with their intensity-time evolution. *Adapted from reference 108.*

Electro-catalytic reaction such as hydrogen or oxygen evolution reaction often produce NBs at the electrode surface that nucleate and grow once the local environment become saturated by gas molecules. It is believed that those bubbles act as nano-reporters of catalytic activity. Therefore, mapping their nucleation sites reveals the most active region of the electrode.¹⁰⁵

Optical microscopies are ideal to monitor dynamically and under operating conditions the dynamics of formation and growth of NBs on surfaces.^{106,107} Nano-bubbles were imaged by single molecule fluorescence microscopy using fluorescent probes that are trapped at the liquid-gas interface,¹⁸ even forming molecular aggregates.²⁰ Using this methodology shown in Figure 14a, the group of Zhang imaged the hydrogen spill-over occurring at gold nano-plate supported ITO electrode during OER²¹ and the delayed production of H₂ NBs at AuPd electrode during HER that could be explained by the ability of palladium to store hydrogen.¹⁰⁸ An alternative for imaging NBs is to rely on sufficiently sensitive scattering-based microscopy as NBs scatter light. The formation of NBs are directly monitored at NPs by interferometric or DF microscopies^{109,110} or at step edge of graphene by SPRM.¹¹¹ These microscopies are meant as a tool to investigate gas evolution mechanisms. For example graphene electrode polarized at negative potential is shown to produce O₂ gas bubble suggesting the graphene acts, during O₂ reduction reaction as a superoxidedismutase.¹¹¹ The growth of the electrogenerated gas bubble can also be tracked optically. As shown in Chapter 3, this growth is revealed as a transient increase of the optical intensity, confirmed by optical modelling. Coupled with super-localization the NBs were shown to sometimes disconnect the NPs from the electrolyte while they continued growing, revealing the existence of a possible cross-talk among the NPs.²¹ At high gas evolution rate, the image of the bubble is fading away with time which is attributed, taking advantage of the NP-distance vs scattering intensity dependence in TIRM, to the lift of the nanocatalyst above the bubble (Figure 15). Wang et al tracked the vertical motion of nanocatalysts (IrO₂, doped Ca₃Co₄O₉ and Pt decorated C₃N₄ nano-sheets) during OER caused by the formation of O₂ NBs in between the electrode and the catalysts and further used this hopping behaviour as an indicator of catalytic activity.¹¹⁰ By doing so, they highlighted the concept of motion-activity relationship that should be taken into account in many catalytic reactions.

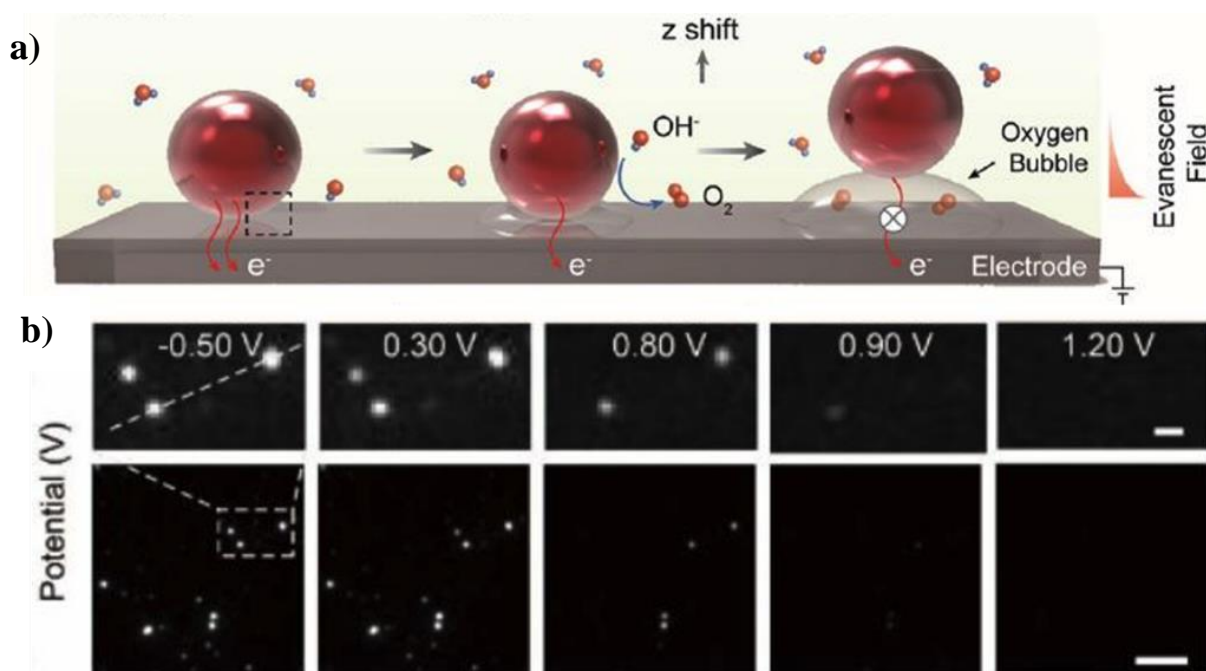


Figure 15. a) Schematic of IrO₂ hopping induced by oxygen NBs formation at the interface between NPs and electrode; b) optical images showing fluctuation in intensity in the potential region of oxygen evolution. *Adapted from ref 110.*

Motion is an important characteristic of NBs. At even higher gas evolution rates, NBs formation and leave from the electrode is detected through blinking events in DFM.¹¹² Blinking fluorescence events also allow reporting by ECLM single NB formation and motion.¹¹³ Motion along the electrode plane during the NB formation or dissolution is generally probed by super-localization principles (see Chapter 4.2).^{106,114,115} It is related to the weak adhesion of the bubble on the electrode surface until the contact line is pinned at strong adsorption sites.

The motion of nanoobjects near an electrode is also a central question in understanding the whole processes involved in electrochemical collisions studies.¹¹⁶ Various optical microscopy configuration are able to track the trajectory of individual nanoobjects towards their adsorption/reaction at an electrode.⁷⁴ They uniquely imaged the rotation and reorientation of individual graphene nanoplatelets during blocking nano-impact on microelectrode.^{39,117}

2.2.2 Seeing competitive processes

The operando visualization of different optical contrasts or features at a polarized interface allows devising the possibility of parallel or competing electrochemical processes. Beyond the

competition between mass transfer to and reaction at the electrode, or the observation of higher current densities at electrode edges, an electrochemical reaction is, by essence, bound to the local heterogeneous activity of the electrode. Different electrode reactions can then occur at the same electrode potential, and different reaction products can be formed. To identify their competitive formation (and to evaluate their Faradaic efficiency) it is necessary complementing the electrochemical current-potential curve by complementary characterizations. As detailed in Chapter 4, optical microscopy can be a unique mechanistic tool when different paths are revealed as distinct optical footprints. It allows evidencing the physical (or chemical) alteration of the electrode during or related to the electrochemical process or evaluating the competition between chemical routes in electrosynthesis.

2.2.2.1 Physical transformation versus electrochemistry

The electrochemical conversion or processes of ion insertion during energy storage material charge or discharge can be accompanied by considerable physical transformation. Relative volume expansion/shrinking as low as few % can be probed from the super-localization of individual microparticle edges during its conversion (e.g. cobalt oxide)¹¹⁸ or Li^+ ions intercalation (in NbW oxide).⁸¹ The dynamic imaging of the local state of charge (front of Li^+ ions) in NbW oxide microparticle during lithiation and delithiation reveals phase separations within the particle. Figure 16b presents the time series of the differential optical contrast images during the delithiation of a NbW oxide microrod. Initially, the particle darkening (delithiation) is rather homogeneous over the particle, except from the white lower part of the rod from which a front of different delithiation rate (red domains) propagates towards the upper end of the rod. This heterogeneous state of charge of the particle (observed both during charge and discharge) is related to the dependence of Li^+ diffusion coefficient with the state of charge. Beyond the separation of phases with different transport properties within the particle, charging the particle at extreme rates of de-lithiation (5 to 20 C) can even lead to the particle dislocation or rupture, detected also optically from the appearance of the dark dot at 283s and propagating later from the left to the right of the particle in Figure 16.⁸¹

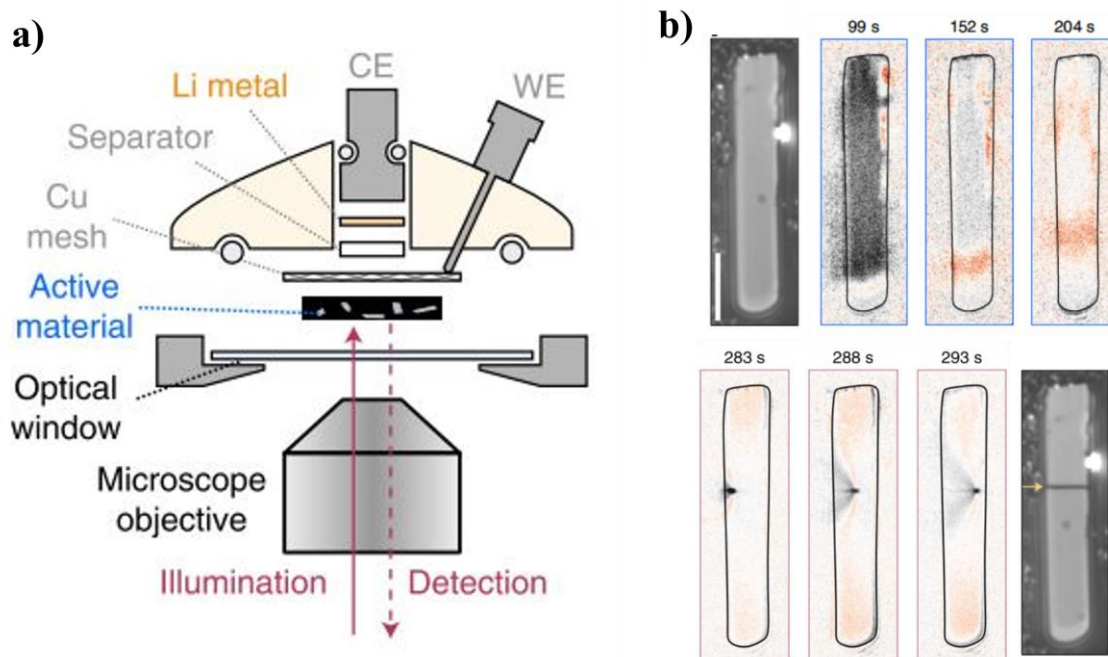


Figure 16. a) schematic of optical setup used to probe b) ion migration driven phase separation in NbW particles, leading to particle cracking. *Adapted from reference 81.*

2.2.2.2 Competing electrochemical reactions

Parallel or competing chemical reactions can also be imaged by optical microscopy. A typical example is the monitoring of electrochemical processes occurring within the potential regions associated to electrolyte discharge. This was for instance illustrated by Wonner et al. during the DFM monitoring of single silver NP oxidation in presence of chloride ions.¹¹⁹ First, optical images and local intensity variations showed the reversible transformation of Ag NPs into silver chloride and therefore proved that the NPs are not dissolved. At higher anodic potential, the electrochemical current is largely due to water and chloride oxidation, hiding the reaction of the NPs. However, analysis of the image sequence recorded during the electrolyte breakdown reveals the further transformation of the silver chloride NPs into silver oxide or chlorite.

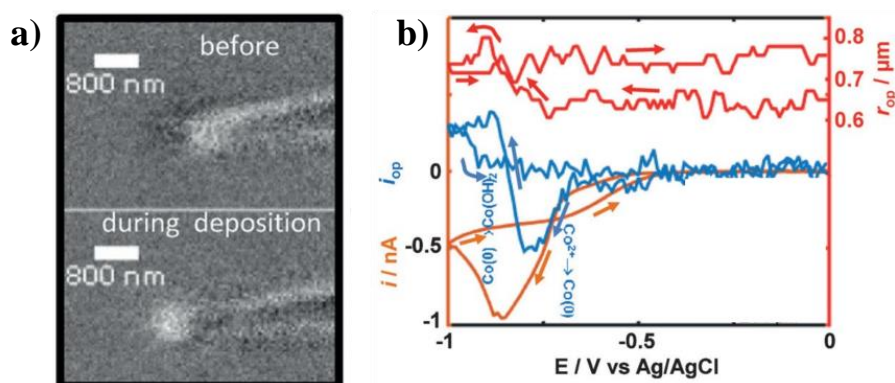


Fig 17. Growth monitoring of a single Co NP; the optically inferred CV (in blue) allows to monitor Co(OH)_2 formation as consequence of the oxygen reduction reaction. *From reference 88.*

A second example is the optical monitoring of the cathodic formation of single cobalt hydroxide NPs that grown at the tip-end of a nano-electrode (Figure 17a).⁸⁸ The reaction mechanism is deciphered by comparing the electrochemical current and the optical CV (described in Figure 17b). At low overpotentials, both EC and optical data indicate the reduction of the cobalt precursor into metallic cobalt. However, the optical monitoring revealed that metallic cobalt is further converted into Co(OH)_2 NPs which inhibit the reduction of Co^{2+} at higher cathodic potential. The purely chemical oxidation of metallic Co occurring at high anodic potential and traduced by a cathodic optical current present in Figure 17 (the blue curve), cannot be inferred solely from the electrochemical current and highlights the usefulness of the complementary optical monitoring.

2.2.2.3 One vs. many

The nucleation/growth of new phases, as in electrodeposition or electrocrystallization processes, is often associated with collective behaviors. These can be understood from high throughput imaging such as optical microscopy that allows seeing individuals and the ensemble. For example, inspection of the electrochemical curve recorded during electrodeposition can diagnose the progressive growth of NPs on an electrode. Optical observation would instead indicate faster growth of each individual NP, with the apparent progressive growth associated to the broad distribution of NP nucleation or onset times.^{41,85,86,120} Label free optical microscopies (dark field, interference reflection, or wide-field SPR) are now able to image NP densities up to 10^9 NPs per cm^2 . They allowed imaging

the dynamics of NPs onset during the electrodeposition of Ag,^{41,86,120} Cu,⁸⁵ or Ni (vs. Ni(OH)₂) NPs, or the electrocrystallization of CaCO₃ particles, as furtherly showed in Chapter 4 and 5.

Collective behaviors are related to the overlapping of the diffusion layers to sustain the NPs growth. This contribution could be evaluated from the distribution of sizes of the Voronoi (elemental) cell occupied by each NP during their growth.⁸⁶ Because of such overlapping, it is seen that the nucleation of NP is delayed close to existing ones, and its growth is slowed down.⁸⁵

The formerly discussed spatio-temporal distribution of NP nucleation/growth events could not be anticipated from the sole inspection of the, ensemble averaged, electrochemical response. On the other hand, individual object or domain activity is imaged optically. The sum of the optically-inferred activity of all the individual domains can then be compared to the ensemble electrochemical response. This optical-electrochemical correlative strategy was achieved in a number of situations, more recently for the electrodeposition of Ag,^{41,86,121} Ni NPs,⁴² the electrogeneration of H₂ NBs¹¹⁰ and the charging/discharging of MnO₂ electrode for Zn/MnO₂ batteries.⁹² It is particularly insightful when the optically-inferred information does not match the electrochemical one.

2.2.3 Large data collection in hyphenated techniques

Optical microscopy represents one example of complementary observation. However, many other microscopy techniques can also be used *operando* or *ex-situ* to spatially characterize electrode surface changes, thus completing the measurement of the electrochemical current. For instance, *ex-situ* (*post-mortem*) SEM experiments can be performed in regions identical to those of optical imaging, which is commonly referred to as multi-correlative microscopy approaches.

There is indeed increasing efforts towards the hyphenation of local analysis techniques, combining at least one performed *operando*.¹²² This is particularly interesting for instance when electrochemical system involve complex reactions yielding different products and intermediates. Obviously, this creates large, multidimensional and interconnected datasets that are less and less straightforward to interpret/analyse by human beings.

Those datasets are more and more handle by data science concepts, automatized procedures and ML approaches. For instance, recent papers discussed the introduction of these approaches for identifying from microscopy images the different components of an electrode material in battery, to statistically characterize the morphology of NPs,¹²³ to predict the optical properties of plasmonic NPs¹²⁴ or to retrieve nanoscale chemical information.¹²⁵ Those strategies are however still under-exploited in electrochemistry and the present thesis aims at introducing machine vision concept in *operando* and correlative microscopy experiments.

2.3 Machine learning for imaging in electrochemistry

With the rising popularity and availability of high throughput microscopy coupled with electrochemical devices,⁴ as well as SECCM,¹²⁶ SICM¹²⁷ and other electrochemical mapping techniques¹²⁸, the work of electrochemists have considerably changed over the past decade.¹²⁹ Indeed these imaging techniques give them access to a myriad of information and characterizations obtained from the nanoscale to the macroscale in complement to the usual electrochemical curve they were used to handle. Since they are not related a priori to the electrochemical curve, these raw images, which contain a lot of complementary and local information not organised in a relational database, are called unstructured data. By increasing such knowledge of a system by *operando* and complementary *ex situ* imaging techniques (SEM, EDX, etc, often operated in the same location) the dataset accompanying a simple CV curve (of few kb size) may rise up to several Gb.⁴

A single experimenter cannot handle all these data within a reasonable time and while a PhD student was able to analyse hundreds of CVs during his PhD, the new generation electrochemist working with high throughput high resolution electrochemical imaging will have to handle Tb of data generated during a PhD.

There is then an increasing need for those electrochemists to shift towards data science and adopt new methodologies based on artificial intelligence (AI) to automatize and postprocess the large datasets of complex, multiple and complementary unstructured data these techniques produce. It is a fundamental requisite in order (i) to apprehend the overall complexity these datasets offer, meanwhile to process them (ii) in a straightforward and reasonable time and (iii) reducing arbitrary, human-biased assumptions. In this section, we will illustrate why data-driven approaches will be fundamental for the next generation electrochemistry.

Many new challenges arise from a) the dataset size acquired during each experiment and b) the necessity of disentangling different imaging and electrochemical contributions related to simultaneous phenomena.

In this section, I will focus on the case of the *operando* imaging of electrochemical processes by an optical microscopy, although the discussion extends to the many other high resolution imaging strategies proposed to monitor electrochemical processes *operando* or *ex situ*.

A typical cyclic voltammetry monitored *operando* by optical microscopy with a high spatial resolution camera (e.g. using routinely >1000x1000 or 1 Mpixel) and a temporal resolution of about 3 ms can easily produce 3-4 Gb of raw unstructured data in form of images. With such camera it is possible to observe hundreds of features (such as individual nanoobjects). It is impossible to manually extract quantitative and statistically representative information about these hundreds of features from thousands of images. Indeed this strategy consists in analysing the information carried by each pixel of the image along a movie. This can be achieved by the most standard FIJI or ImageJ software, an easy-to-use platform for analysing images with multiple open source tools (i.e. protocols) enabling to extract pertinent parameters from images. These software packages allow handling information contained in images without programming skills, although their effectiveness is more limited. Common protocols on images processing are usually based on standard algorithms and routines (where each command can be associated to a mathematical operation) written in languages such as java for ImageJ, or for more specialized data scientist such as Python, R, C++ or MATLAB, to mention the most commonly used.

However, while these procedures can be sufficient when experimental and instrumental conditions are acceptable in terms of good signal-to-noise ratio, well-separated and immobilized objects and absence of simultaneous events or spatial drift, they are often not sufficient to disentangle and discriminate between simultaneous events occurring at the limit of resolution or detection and depending on multiple sets of parameters. AI is nowadays the best candidate to deal with such large volumes of raw unstructured data.

The structure of the section is the following. Some general considerations about AI are first described. Secondly, some of the last advances of ML algorithms applied to electrochemical systems are reported.

2.3.1 Elements of machine learning

The term “artificial intelligence” is used to define all the systems designed to mimic and even outperform the human skills in performing complex tasks. The ideas behind AI were raised and formalised by Alan Turing in 1950, in a seminal work on the edge between mathematics and philosophy.¹³⁰ However, it is only in the last decade, with the mass availability of calculators and computers with sufficient computational power and access to large amount of data, that AI systems have become commonplace in many research fields. AI covers a plethora of topics which goes from natural language processing to robotics. A comprehensive discussion of the state-of-the-art of AI is beyond the scope of this thesis and can be found in the dedicated literature.¹³¹ Herein, we will only consider ML and deep learning (DL) techniques applied to imaging of electrochemical systems.

ML is referred to specific algorithm which can optimize a performance criterion learning from past experience or previously acquired datasets without being explicitly programmed. The tasks performed by these algorithms go from solving regression problems to object classification and to predicting outcomes based on a set of parameters. DL is a subset of ML techniques which takes inspiration of learning mechanisms and architectures in biological brains. The core principle of DL is composed by collections of computing elements called nodes or neurons. The multilayer, interconnected architectures with which they are organized are called neural networks (NN). The connections between each node of different layers are encoded by specific *weights* which are responsive of the information processing. The training step is therefore the iterative process necessary to find the best set of weights to perform a specific task. After a proper training, NNs can be used¹³¹ to unveil hidden correlations and high-level features from raw data.

The power of NNs relies on the possibility to learn any specific task from a predefined dataset also called *training dataset*. For the unsupervised learning, the training dataset usually contains just raw unstructured data, which are used as input to find hidden correlation patterns. For the supervised learning, the training dataset rely on a pre-treated, well known dataset where the user defines certain parameters as output (*labels*) corresponding to specific input data. These labels can either be vectors univocally encoding for specific objects or phenomena (mainly used in classification tasks), either values corresponding to physical parameters. During the supervised training, each weight is updated in order to find values which minimize the difference between the so-obtained output and the labels defined in the training dataset. For this reason, NNs performance is strongly affected by how properly the

training dataset is defined. Poor quality data in terms of dataset volume, signal-to-noise ratio or under sampling can lead to insufficient performance or to overfitting (i.e. when the algorithm predictions fit too well on the training dataset and fails on new data).

If the dataset is composed by images, pre-processing can be pixels' intensity rescale and/or normalization and the image augmentation using space invariant transformations, if the amount of data is not enough.¹³² For these reasons, there are several ways to evaluate the consistence and the efficiency of each NN to perform a specific task. It is not always trivial to choose the more effective evaluation test, but an accepted methodology is to exclude the 20-30% of data in the training dataset from the training itself, in order to evaluate the NN performance on well-known, unused data. The evaluation metrics consist in choosing and evaluating statistical parameters such as the overall error associated to the weights, or the percentage of false negatives and false positives obtained on the test dataset (of which properties are already known, .

ML approach differs from *ab initio* and semi-empirical simulations because it is not necessary to know in advance the underlying physical laws or to decouple the effect of several, non-controllable parameters inextricably correlated, relying only on quality and large amount of data used for the training process. For example, bimetallic electrocatalysts are evaluated correlating relevant experimental parameters (chemical composition, synthesis temperature, surface area, etc) with their performance in terms of half-wave potential or specific activity.¹³³ Finding the best synthesis parameters to optimize the catalyst performance can be done using DL algorithms, although they will not give any hints on the physical and chemical phenomena which lead to performance enhancement.¹³³ Therefore, ML is not intended to substitute physics-based modelling or understanding, but 1) to fasten the discovery of new materials with a data-driven approach instead of repeating trial and error experiments and 2) to fasten and increase the amount of quantitative information that can be extracted from unstructured data. Therefore both data-driven approaches and physical understanding are necessary to produce consistent scientific knowledge.¹³⁴ Although DL and ML have been proved to efficiently perform a variety of tasks which goes from real time object detection to non-Gaussian noise reduction in poor quality signals and images, a synergistic approach can avoid a black-box use of these algorithms.

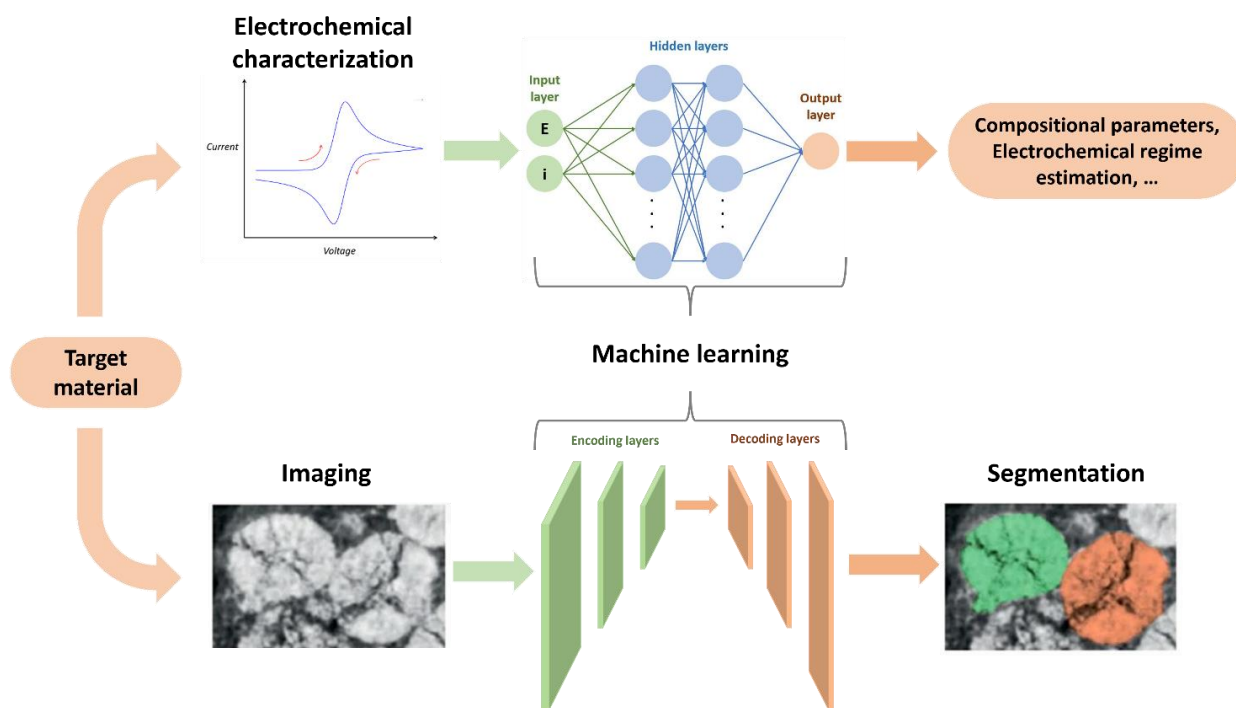


Figure 16. Schematic showing two applications of ML algorithm in electrochemistry, to find the unknown compositional parameters from CV and to perform automated segmentation tasks for features identification on complex images. Adapted from ref ¹³⁵, Copyright 2020, Nature group.

2.3.2 Unravelling hidden information by ML

While ML is becoming widely used in bioinformatics, astronomy and automation, their use in electrochemistry is still embryonal, even though the first pioneering works in the late ‘90s involving NNs on corrosion studies,^{136,137} intermetallic interference in voltammetric strippings¹³⁸ and polymer sensors.^{137,139,140} Figure 16 schematizes two tasks where ML has been used recently, the prediction of a set of parameters associated to a certain electrochemical response and segmentation to recognize electroactive material. Moreover, NNs have been exploited by A. Bond¹⁴¹ and R.G. Compton¹⁴² to classify the type of electrode reaction mechanism or to predict the voltammogram shape starting from an input dataset containing rate and equilibrium constants, formal potentials and diffusion coefficients of all the species taking part in the reaction.^{143,144}

When dealing with single entity electrochemistry with statistical relevance, one needs generating large volumes of data, supported with multiple complementary analyses. Finding quantitative relations between the electrochemical data and all the complementary analyses is usually time consuming and not straightforward, especially when microscopy or imaging

analyses are involved. I then detail herein some of the new advances in NNs applied to microscopy analyses of electrode surfaces, with the perspective for the electrochemical community of using these approaches also for *operando* data analysis.

2.3.2.1 Automated segmentation and phase boundary recognition

Segmentation consists in a series of tasks who aim at identifying the set of pixels belonging to a specific region in an image. The ultimate goal is to simplify the image representation in order to simplify its analysis. Segmentation algorithms are therefore fundamental to perform many computer vision tasks such as camera-assisted vehicle autopilot, face recognition or satellite imaging and can be easily applied to microscopy.^{145–147}

Whereas the segmentation task can be straightforward for model systems designed to be ideal, the quantitative identification of the different regions remains a non-trivial task. Classical algorithms are based (i) on pixel intensity thresholding, (ii) on automatized edge detection (such as Canny edge algorithm, Sobel filtering, watershed segmentation coupled with Euclidean distance transformation or the phase stretch transform) by finding discontinuities in intensity or surface orientation or on iterative unsupervised clustering. All these methods are sufficient for high quality images where the signal-to-noise ratio is good enough and no artefacts are present, while they fail in accuracy with complex multiphase electrode interfaces. Nowadays both *in situ*, *operando* and *ex situ*, *post mortem* high resolution imaging techniques are widely applied to electrochemical systems in order to identify and recognize active nanostructures from their support, heterogeneities and grain boundaries on polycrystalline electrodes as well as porosity geometry in batteries.¹⁴⁸ To analyse the collected images, researchers started to rely on ML and DL. For instance, such methodology allowed to obtain quantitative, unbiased information about the ratio between carbon-binder domain, active phase and porosity in 3D electrodes.^{135,149,150} A rigorous and univocal quantification is fundamental to model and understand transport phenomena in the porous phase and to design new battery materials, as illustrated by Demortière et al. for $\text{LiNi}_{0.5}\text{Mn}_{0.2}\text{Co}_{0.3}\text{O}_2$ (Li-NiMnCo or Li-NMC) electrodes. They evaluated different multiphase segmentation approaches on 3D battery electrode images obtained by X-ray computed tomography.¹⁴⁹ However, one needs to pay attention to the algorithms that are employed as they can lead to different outcomes, as shown in Figure 17.

Thresholding based on histogram intensity (fig 17c) is one of the simplest algorithms and does not involve ML. It consists in assigning, for each pixel, a different label based on three intensity intervals, each one ideally corresponding to one of the three electrode phases. K-means clustering (fig 17d) is an unsupervised ML algorithms. It consists in an iterative algorithm which tries to minimise the within-cluster variance assigning, for each pixel, a label corresponding to its nearest cluster centroid. The number of cluster must be known in advance and it does not work effectively for highly asymmetric samples. Convolutional NN (fig 17e) is probably the most common and powerful DL algorithm for image recognition and classification. It is composed of several layers performing space invariant operations in order to enhance important pixels and to generate feature maps corresponding to each hidden layers. These maps can be used to “rebuild” a segmented image. Histogram thresholding and K-means clustering lead respectively to an overestimation of the Carbon Binder Domain (CBD phase) and to rough definition of the phase boundaries, while the convolutional NN based segmentation allowed to refine the segmentation of the three phases.

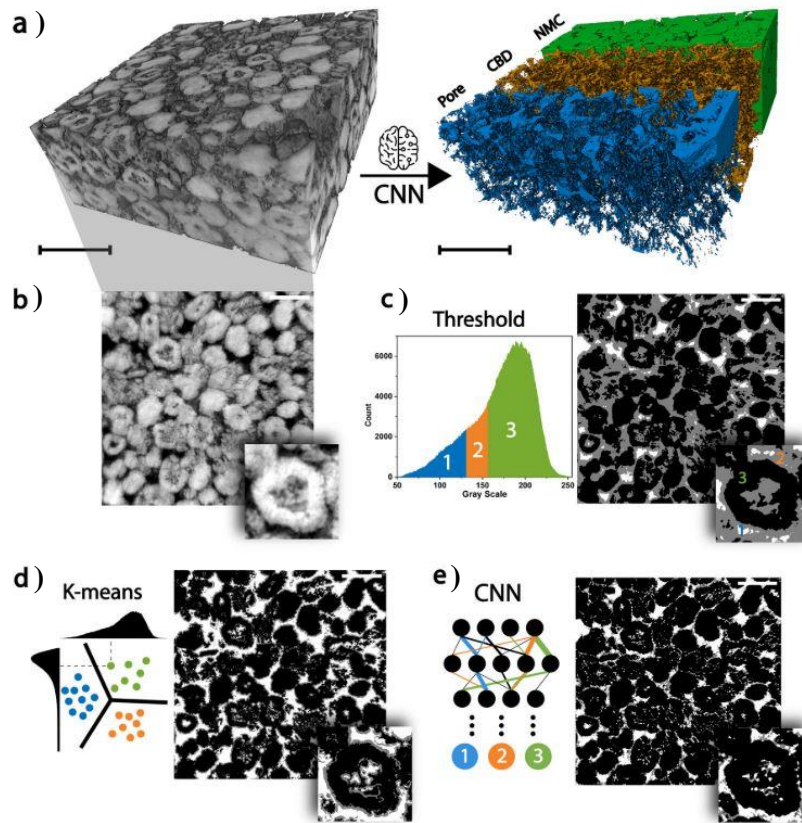


Figure 17. a) volume rendering illustrating the purpose of turning raw 3D volumes into multiphase segmented ones. b) selected 2D cross-section from the previous raw volume, with a zoom on a NMC particle and its surroundings. c) The histogram of distribution of the intensity of the pixel of the image in (b) and its classification into three categories, and resulting image reconstructed upon the different categories identified; the classification is established from the theoretical volume fractions, where the green, orange and blue categories (respectively black, gray, and white colours in the reconstructed image) represent respectively NMC, carbon- binder-domain, and pores. d) An illustration of segmentation applying automatic k-means on a map constructed by the gray level and Sobel filtered values of the raw tomogram. On the right, the result of this method. e) On the left, a schematic of artificial NN, and on the right the output of CNN. Reproduced from reference 149.

Moreover, if it is important to evaluate the bias of a given algorithmic method of identification, it is also important to evaluate the human bias in performing segmentation tasks on complex images. This is obtained by asking a group of different people to define the ground truth, finding a variation of at least 10% in segmentation. The conclusion pointed out that convolutional NN cannot eliminate completely the human bias. Performance and degree

of uncertainty reached with a specific dataset are therefore an indication of the experimenter's self-consistence in labelling images. The subjectivity in defining reactive boundaries and edges involved by a specific reaction has been underlined also in corrosion research.

A quantitative investigation of surfaces subjected to corrosion can be conducted using ML techniques. One reason for such interest is that many mechanistic schemes can be proposed to explain corrosion scenarios in real life and the understanding of such process often requires multiscale analytical approaches often composed of noisy, heterogeneous data preventing the possibility to build a universal experimental protocol. The ultimate goal is to identify and detect corroded areas, pixel by pixel, at their early stage from images and to predict where corrosion processes are more likely to happen considering the local environmental parameters and their random time scale. This approach is very versatile and can be applied to either high-resolution images such as those obtained by AFM¹⁵¹ or to real life photos.¹⁵²

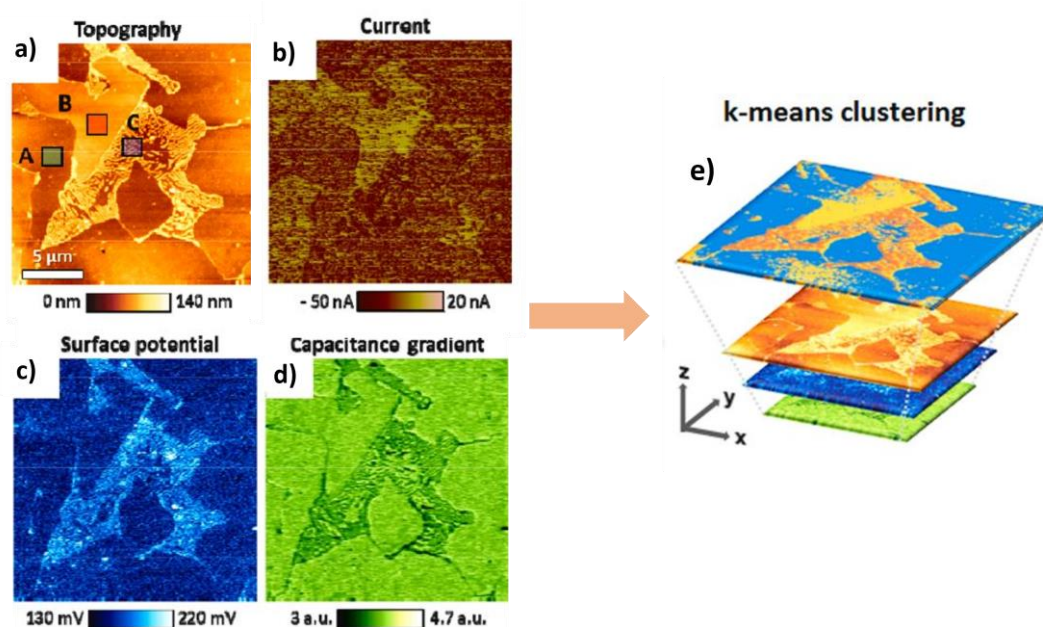


Figure 18. a) carbon steel topography with three structural phases; b-d) same location mapping of current, surface potential, and capacitance gradient; e) aggregation of the data implemented by k-means clustering. *Reproduced from ref 151.*

The complexity in identifying correlation between different microstructures and corrosion phenomena has been highlighted by Y. Kim and co-workers on commercial low carbon steel.¹⁵¹ This work, presented in Figure 18, shows how to apprehend structure-function or structure-activity relationships for the particular case of material corrosion based on the

aggregation and cross-correlation of multiple topographic, structural and functional imaging techniques (the multi-correlative strategy described in the previous section).

A corrosion analysis by SEM and topographic AFM at the microscale was first achieved. X-ray diffraction (XRD) analysis was also run to identify the local microstructure present in the polycrystalline steel sample. Then, they mapped the same surface location using different AFM based techniques, from magnetic force microscopy to Kelvin probe force microscopy to compute magnetization and surface potential images, respectively. Finally, the cross-correlation of these images is obtained by unsupervised k-means clustering (Figure 18e). The k-means clustering of the multi-dimensional images composed by the stack of images acquired with each technique allowed identifying three clusters corresponding not only to morphological variations, but also to different behaviours under corrosion conditions, taking into account of the local variation of the considered physical properties.

Identifying micrometric extended phase open up to the possibility to use the same approach for single NPs and single atoms. One effort in this direction has been done by V. P. Ananikov and co-workers, who developed a U-net architecture to detect automatically 5-10 nm Pd NPs on carbon microparticles from SEM images. The decorated carbon microparticle is further used as catalyst for Suzuki-Miyaura reaction.¹⁵³ The multi-level segmentation of the images allowed not only to extract quantitative statistical information about the size and shape of Pd NPs but also to unravel with unprecedented accuracy the correlation between the number of detected Pd NPs on a single carbon microparticle and the turnover frequency of the catalysis.

2.3.2.2 Tracking dynamically multiple phenomena

If one of the former example was showing how to cross-correlate images of samples obtained at equilibrium, several microscopies are also able to image dynamically the transformation of surfaces or nanostructures. This is a situation typical in electrochemistry, where the electro-active material is driven out of equilibrium during the imaging process by the application of a potential or current. The dynamic local change of the optical response of the material is captured in a movie, or stacks of images.

ML has already proven to be a powerful tool to analyse image sequences that are often more complex and therefore to track effectively micro- and nano-features motion and or alteration under non-equilibrium conditions. Different DL architectures can be used to pre-process images enhancing the signal-to-noise ratio or overlapping a probability map as output on the

original image. In this way it is possible to identify and highlight the features of interest and enable their subsequent tracking with standard localization algorithms.

If the latter standard algorithms are easier to implement but more demanding in computing time or less automatized, more complex DL architectures have been proposed to learn and take into account both the spatial and temporal information within stack of images. It is the case of the class of NN encoder-decoder using a long short-term memory (LSTM): these NNs memorized the information about the features of an image taking into account also their temporal evolution, so that it's easier to identify anomalous behaviours in dynamic phenomena. Although not yet used in electrochemical situations, these NNs have been showcased for tracking dynamically diffraction-limited features from optical microscopy images or biological samples with more complex (non-spherical) shapes such as zebrafishes or ants.^{154,155}

In these examples, the DL architectures outperformed human sensitivity in achieving dynamic localization tasks. However, their use is still embryonal in the multi-correlative microscopy *operando* imaging of electrochemistry. For example such experimental strategy could be used to extract multiple spatio-temporal descriptors of nano/micrometric regions of an electro-active material from images and to relate them to the electrochemical information. In the field of electro-catalysis, this could allow rapid identification of electro-catalysts based on univocal structure-function relationship at multiple scales.

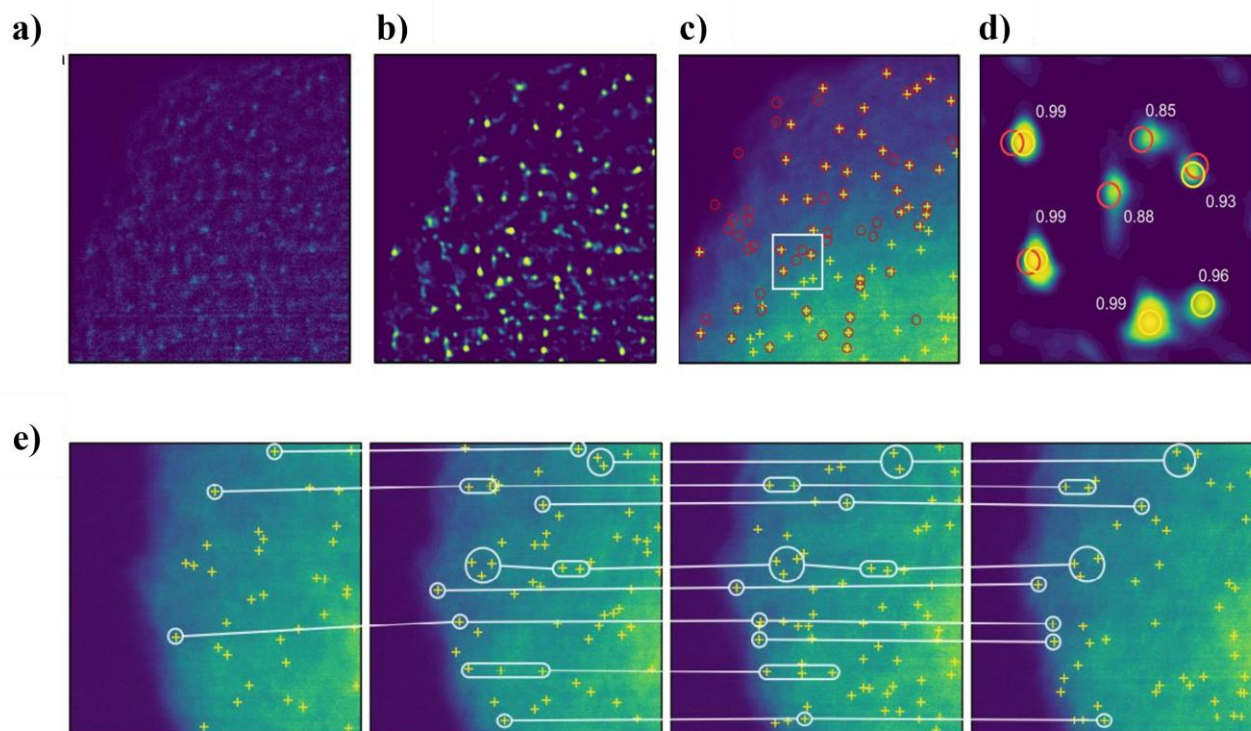


Figure 19. a) Typical background-subtracted and intensity-normalized STEM image of the Pt1/ NC catalyst ($15 \text{ nm} \times 15 \text{ nm}$, 34.3 px nm^{-1}) and b) corresponding likelihood map for atom detection generated by the CNN model; c) Processed AC-STEM image with the manually tagged (red circles) and CNN-detected (yellow crosses, yellow circles in (c, d)) single atoms overlaid. d) ($68 \text{ px} \times 68 \text{ px}$) region showing differences in; e) four consecutive frames showing a subset of motionless Pt atoms (white regions) and a subset changing their location. *Adapted from reference 156.*

N. Lopez and coworkers used a similar approach with Aberration Corrected Scanning Transmission Electronic Microscopy (AC-STEM) micrographs to track the dynamics single-atom catalysts consisting of Pt atoms and iron atoms on nitrogen doped carbon matrixes.¹⁵⁶ A STEM image with atomic resolution of the catalytic surface is provided in Figure 19a. Single atoms are visible as regions of higher contrast (green in Figure 19a) and their localization is possible simply by STEM contrast enhancement. However, the change in background intensity over the image makes the single atoms identification by human difficult as they do not exhibit a unique signature in terms of image contrast. They analyzed the STEM images using a NN composed by just 3 convolutional layers which enables enhancing the STEM images quality (Figure 19b). It was then possible to extract from each STEM images the

single atom coordinates (by standard localization algorithm like Trackpy from Python library or a second NN) and to compare the results obtained with and without image enhancement. As shown in Figure 19c and d, many features are not detected or incorrectly localized in the untreated images (red circles). By applying the same approach to the other frames contained in the sequence, it is also possible to define a subset of motionless features from other which change location. Although it was not possible to distinguish when this motion is provoked by the electron beam and when by differences in metal-host coordination strength (commonly observed for single atom catalysts¹⁵⁷), an implemented version of the algorithm here used could include a final classification step to distinguish the two cases.

In conclusion, this section showcased the promising performance of AI-based algorithms in complex, time-consuming tasks such as features localization and identification, surface segmentation or multi-particle tracking, and how these algorithms can be adapted to extract statistical, quantitative information in *operando* microscopies. Still little used, AI-based methodologies will be promising when coupled with electrochemical systems.

2.4 What this thesis is about

This chapter presented the state-of-the-art of nanoscale phenomena visualization by optical microscopy, focusing on the main milestones of last five years and on problems which can rise up to extract quantitative, statistical parameters from images crowded and rich in information.

So far, recent milestones showed how *operando* optical microscopies can now extract quantitative, reliable information from single NPs with single behavior, such as their coordinates during motion or changes in their structure translated into specific optical signatures. However, more complex situations in electrocatalysis are still poorly studied with a single entity approach, especially if competitive processes are involved. Also local geometrical effect at the phase boundaries between electrode and electrolyte, non-inert substrates interacting or competing with NPs and competitive redox reactions need to be addressed quantitatively.

In this thesis, we employed *operando* optical imaging methodologies in combination with electrochemistry to study various electroactive systems. The collected data gave access to various nanoscale descriptors that have further been exploited to fully understand the reactivity of the electrode surfaces.

A model electrocatalytic system – the hydrogen evolution reaction at single Pt NPs – has been studied at first, to optimize the methodology and to extract quantitative descriptors of NP activity at the single object level.

Then, the effect of surface heterogeneities in transparent conductive substrate has been investigated probing several regions of the same substrate, in order to demonstrate that local changes in surface conductivity can affect locally the competition between different reactions.

Finally, competitive electrochemical reactions were optically studied in an SECCM configuration. It allowed to test the limit of detection and resolution of the optical monitoring in confined environment and to reveal the interplay between the liquid|air interface, the ionic transport and local completion in pH sensitive systems such as CaCO_3 electro-crystallization and NP deposition.

Moreover, ML is a promising way to help differentiate between behaviors from optical images. I have initiated such ML analysis at the end of my thesis and particularly during a secondment at Aarhus University. The topic of my research project was not related to electrochemistry but to the assembly of RNA origami on mica surfaces. This was an interesting system for initiating my acquaintance with ML. The ML algorithms I developed are currently used to analyze AFM images from the Aarhus group. This part is therefore not discussed in this manuscript.

Chapter 3

Electrocatalysis at single nanoparticles – the case of hydrogen evolution reaction at Pt NPs

Reprinted with permission from *ACS Nano* 2021, 15, 2, 2643–2653. Copyright 2021 American Chemical Society.

This chapter will answer the following questions: can gaseous NBs always be used as nanoscale electroactivity indicators? If so, can we use optical microscopy to track and quantify the growth of NBs and in turn evaluate the local electroactivity of an individual nanocatalyst during a gas evolution reaction? What other information about electrochemical gas evolution reactions can be provided by optical monitoring?

3.1 Introduction

A lot of attention in (electro-)catalysis is devoted in estimating the intrinsic activity for specific reactions. Common protocols followed for bulk electrocatalysis are the estimation of current density at the half wave potential or in diffusion limited condition, normalized by electroactive area by stripping methods or by the mass of the main electroactive metal. Accessing the electroactivity at single entity level allows evaluating contribution coming from the interaction between catalyst and substrate and between neighbors NPs, as well as the size and shape effect on intrinsic activity.

During electrochemical gas evolution reactions, gaseous bubbles or NBs can be produced when the solution is saturated. In a sense, gaseous NBs then could be considered as nano-reporters in gas-generating reactions, at least at high gas (electro)-generation rates, or high current densities. In those conditions, NBs are generated through the formation of a gaseous phase between the electrolyte and the electroactive material, provoking large change in its

electroactive surface area. Hence, NBs formation is inferred and related to local catalytic activity,^{112,158,159} from severe current drops in many electrochemical devices. The necessity to establish when the detrimental effect is predominant¹⁶⁰ motivates the needs of studying NBs formation and stability at the single entity level.

Secondly, NBs is a physical system which differs from micro and macroscopic bubbles. Their dissolution should occur faster than for larger bubbles because of the large Laplace pressure within the bubble itself, but their lifetime can rise as the solution become super-saturated or in presence of ionic species which can alter their stability.¹⁶¹ The discrepancy behind theoretical studies and experiments still raises ambiguity in understanding what parameters affects NBs stability and formation/dissolution dynamics: according to Epstein-Plesset theory, NBs dissolution time should be in the order of magnitude of millisecond, while it has been observed from experiments that NBs can be stable for hours even in undersaturated environments.^{105,162} For this reason, the correlation between their geometry and their stability, both in terms of lifetime and substrate stability effect, have been studied mostly using atomic force microscopy (AFM). Although the high spatial resolution allows to observe *quasi* 3D NBs early stage growth at the nanoscale and high speed setup have been nowadays used also coupled with electrochemical actuation,¹⁶³ the use of AFM cantilever probes strongly affects NBs shape.

High spatial resolution optical techniques overcame this problem, adding also the possibility to monitor wide (tens or hundreds of microns) regions of interest of an electrode surface. For instance, the effect of charged bubbles and specific molecules such as surfactants and surface contaminants has been recently studied by Zhang and collaborators using a total internal reflection fluorescence microscopy, TIRFM, configuration with fluorophores such as rhodamine and Nile Red.¹⁸⁻²⁰ By tracking local intensity changes in optical images taken during cyclic voltammetry experiments at various conditions, it was possible to mimic the effects of contaminants and to infer the charging on hydrogen NBs as well as the contribution of H₂ migrating towards the electrode surface (spillover effect¹⁶⁴) induced by the hydrogen evolution reaction, HER, on gold nano-plate electrocatalysts. Although the number of fluorescent molecules has increased during last years, luminescent labels can hardly images the (nano)materials at the origin of the NBs. Label-free microscopy technique allows to acquire high-throughput images at high frequency without the risk of using fluorophores which can act as contaminant. If the gas electroactive generator is a metallic NP supporting localized surface plasmon resonance (LSPR), they can be imaged directly under dark field illumination.^{6,165,166} For instance, sensitivity of the LSPR to local charge and refractive index

variations has been used to identify, from individual NP extinction spectra, the role of H₂ spillover before NB formation.¹⁶⁷ Spillover toward electrode surface suggested an asymmetry in transport phenomena also for spherical NPs. This lead to maximize the gas generation especially at the 3-phase boundary NP|surface|electrolyte, as recently stated from pure electrochemical studies of gas NBs nucleation at nanoelectrodes by Henry White's group for single 35 nm Pt NPs.¹⁶⁸ The implications of asymmetric gas generation for electrocatalytic materials have been showed by J. Li and collaborators, showing how oxygen evolved NBs nucleates mostly at this 3-phase boundary, provoking the detachment of the NP itself and its motion along the z-axis.¹¹⁰

The issues presented in this overview make the characterization of NBs physical and dynamic properties still difficult. This chapter is therefore dedicated to the *operando* optical investigation of gas NBs as nano-reporters of hydrogen evolution reaction (HER) on single Pt NPs. Interference reflection microscopy already allowed to visualize nanoscale processes for a wide range of nanomaterials, such as Ag NPs down to ca. 10 nm in diameter as well as non-plasmonic materials (*i.e.* weaker scattering objects).^{47,169} Here, IRM has been used to track optically H₂ NBs electrogenerated by commercial 40 nm Pt NPs. Quantitative estimate of the size and shape of the NB has been obtained by coupling the optical evaluation of the optical footprints associated to each NBs with an optical model. In the end, the hypothesis of hydrogen spillover towards the surface is discussed.

3.2 Nanobubbles as hydrogen evolution reaction markers

Platinum NPs were first drop casted on ITO substrate. Their catalytic activity was locally investigated by approaching the tip-end of a micropipette of ca. 100 μm diameter^{56,170,171} positioned atop an inverted microscope, filled with sulfuric acid (5 mM) near the electrode surface, as shown by Figure 1a. ITO electrode is therefore used both as an optical sensor and as the working electrode (WE) of a ca. 200 μm diameter micro-electrochemical cell formed by the electrolyte droplet. A typical cyclic voltammogram obtained at the NPs-supported ITO WE delimited by the electrolyte droplet is shown in Figure 1b.

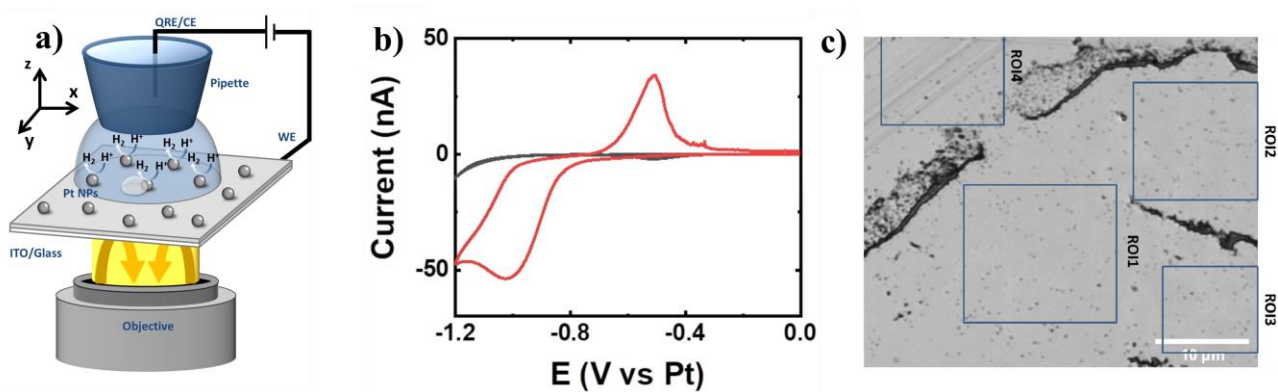


Figure 1. a) Schematic representation of the opto-EC setup used to study HER at single 40 nm Pt NPs deposited on an ITO surface; b) CV recorded in 5 mM of sulfuric acid on bare ITO (black curve) and on dropcasted Pt NPs (red curve) O surface. c) Optical image of dropcasted Pt NPs on a 50 micron wide area. The region of interest in blue is where single NBs growth has been monitored, avoiding the large aggregate of NPs.

The CV evidences a reduction peak with a maximum recorded at -1 V followed by an oxidation peak at ~ -0.5 V, whereas without NPs no current is detected at such potentials. It is characteristic of the catalytic reduction of H^+ followed by H_2 reoxidation at a large ensemble of Pt NPs. A droplet of the same electrolyte was positioned in another location of the NP supported ITO surface. The optical image of the center of the droplet within a ca. $55 \times 40 \mu m^2$ full image is shown in Figure 1b. The dropcasting of the NPs produced, from coffee-ring effect, a heterogeneous density of NPs over the surface with in some areas, μm^2 large regions of agglomerated NPs. Apart from these large agglomerates, different regions of interest, ROIs, within the imaged field of view were used to apprehend the formation of H_2 at individual NPs. The electrode was then biased, in a chronoamperometric experiment, CA, at a constant and sufficiently negative potential (-1 V vs Pt QRE) to ensure a mass transfer limited reduction of H^+ into H_2 at the Pt NPs, while both the electrochemical current (see Figure 2a) and the optical images are recorded at a frequency of 500 Hz and 20 Hz respectively. More specifically, on the recorded optical images, the optical signal (I_{opt} defined in Figure 2c) is a combination (interference) of the field reflected by the electrode interface and of the far-field back-scattered by the NPs. This interferometric mode imaging provides enhanced visibility of wide range of nanomaterials.¹⁰⁴

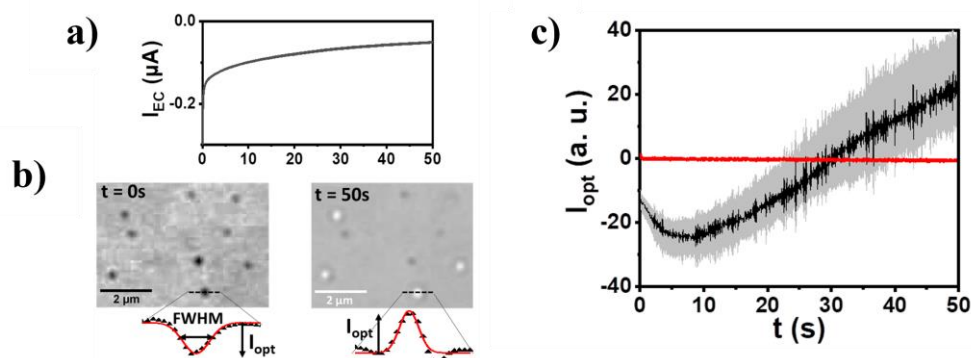


Figure 2. a) EC current recorded during a chronoamperometric, CA, experiment at the ITO surface polarized at -1 V vs Pt in 5 mM of sulfuric acid for 50 s. b) Optical images before and after CA together with optical profiles along a line, in the same region, over a NP evolving later a NB. c) Median (black), first and third quartiles (grey) of the variation of I_{opt} , defined in c, of $N > 100$ NPs as a function of the electrode polarization time; background fluctuation in red.

Figure 2b shows a characteristic example of a zoom over a $30 \mu\text{m}^2$ area of a ROI of the optical image of the electrode populated by individual NPs and immersed at $t=0$. It contains dark contrast features resulting from the presence of the Pt NPs. After 30 s of EC actuation, the contrast of few optical spots changes and becomes bright, while the intensity of the others ones as well as of the background remains fairly constant. Typical evolution of the background subtracted intensity variation at these spots is presented in Figure 2c. Based on image sequences covering areas $>250 \mu\text{m}^2$ and containing $N > 100$ Pt NPs, 30% of the latter generate a significant optical intensity fluctuation during the 50 s of electrode polarization at -1 V. If the latter fluctuation is due to HER, it can then be concluded that all the NPs do not possess an equivalent catalytic activity, which is probed here optically. It could be due to discrepancies in surface functionalization by citrate capping agent, sporadic sulfate adsorption, the presence of an oxide layer that passivates the NP surface, or a poor connection of the NPs with the current collector. To ensure that it is not related to NP aggregates that locally increase the HER electrode activity, the presence of aggregates was scrutinized by correlative *ex situ* SEM analyses.

As presented in Figure 3a, the SEM image in the same location as the optical images of Figure 2c reveals that the NPs are individual entities and are separated by a distance greater than the diffraction limit so that they are optically resolved. Over larger image areas, apart

from the few NP μm large agglomerates, NPs are also mostly dispersed as individual entities or are present as small aggregates.

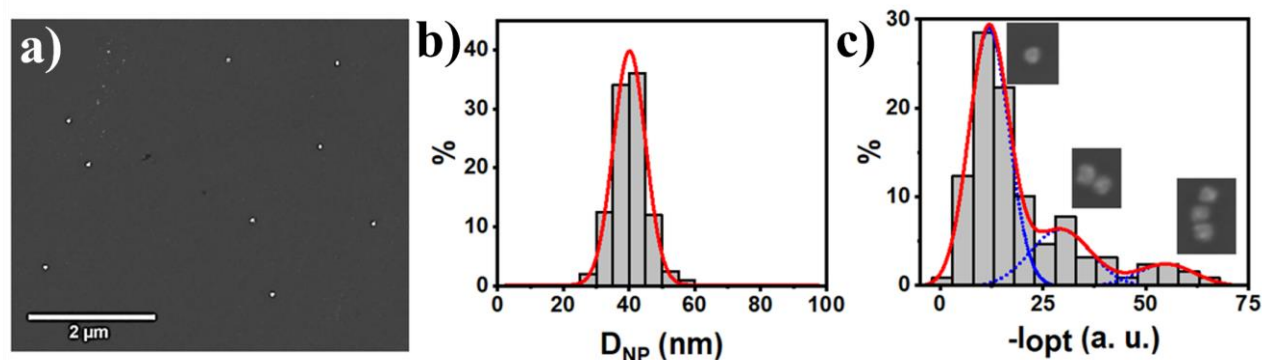


Figure 3. a) SEM microscopy image of Pt NPs (same location as in Figure 2c) immobilized at the ITO electrode surface. b) SEM deduced size distribution of the Pt NPs ($N > 200$). c) Distribution of the optical features intensity ($N > 200$) obtained from one optical image. SEM images of NP monomer, dimer and trimer are incrustated in c).

Based on SEM image analysis and the size distribution graph of Figure 3b, the mean NP size was estimated to 41 ± 5 nm in diameter. In contrast to the narrow SEM size dispersion, the distribution of NP intensities, I_{opt} , in Figure 3c, presents a trimodal distribution having a major mode with maximum centered at $I_{\text{opt}} \approx -11$ representing 68% of the population and two additional modes representing respectively 23% and 9% with local maxima centered at $I_{\text{opt}} \approx -28$ and $I_{\text{opt}} \approx -54$. From same location SEM/optics imaging analysis of the different populations, the latter two modes correspond to NP dimers and trimers, as those imaged in SEM and shown in Figure 3c. If individual NPs within these aggregates cannot be spatially resolved optically, the aggregates can be easily discriminated by measuring the intensity, I_{opt} , of the diffraction limited spots, as shown in Figure 4. Based on this result, only the HER activity of the most abundant population (the individual Pt NPs) was investigated.

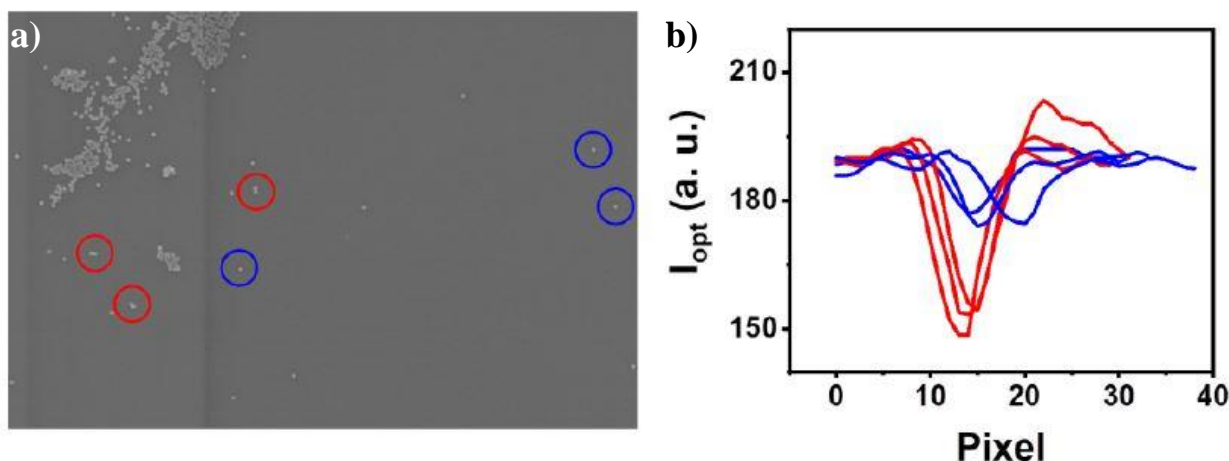


Figure 4. a) SEM microscopy image of Pt NPs immobilized at the ITO electrode surface. b) optical intensity associated to monomers (in blue) and dimers (in red) of the same NPs in a).

The changes in optical intensity at the location of NPs during HER are attributed to H_2 evolution. If the earliest label-free imaging of HER at Pt NPs by surface plasmon resonance microscopy, SPRM, suggested I_{opt} changes were due to local molecular H^+ or dissolved H_2 concentration gradient around catalytic NPs,⁵⁹ we believe such change results from H_2 gas NB formation, as demonstrated later by White *et al.*, who showed that single gas NBs can nucleate and grow from electrochemical reactions at nanoelectrodes.¹⁷² The optical visualization of NBs on surfaces was further confirmed (i) from fluorescence imaging (rigorously of the NB-solution interface) during HER at electrode surface or NPs, or (ii) from label-free imaging of gas NBs, either by SPRM at heated surfaces^{106,114} or dark field microscopy for qualitative benchmarking of NPs electrocatalytic activity.^{109,112}

3.3 Quantitative description of single nanobubbles

It is explored here the possibility of analyzing quantitatively the NBs formation from the variations of the local optical intensity, I_{opt} , recorded by IRM. The optical transients of single NBs at single Pt NPs were extracted by computerized image treatment from the video recorded during the 50 s of the electrode polarization at -1 V vs Pt. The variation with the polarization time, t , of the median I_{opt} value, as well as of its first and third quartile values, recorded over $N > 100$ single NPs is presented in Figure 2c and compared to the background

intensity. I_{opt} decreases up to ca. 8 s and subsequently increases to the point of showing a contrast inversion (features brighter than the background) at ca. $t > 25$ s. These fluctuations are attributed to the formation of single surface NBs, pinned at individual Pt NPs during HER. For a NB to nucleate at an active site and then grow, there is first a condition for the local concentration of electro-generated molecular H_2 precursors, which should locally supersaturate the solution according to the classic nucleation and growth theories, *e.g.* following the Epstein-Plesset theory.¹⁷³ This is likely occurring at the most reactive NPs, which ensure the highest local H_2 concentration at the earliest stage of the EC actuation. In this respect, the footprint of a NB formation is expected to reveal the most active region of an electrode, or here the most active Pt NPs. The production of NBs at only a fraction of the NPs may, at first sight, indicate that only this fraction of NPs is active.

Noteworthy, the EC current trace recorded in the CA experiment suggests the electrolyte droplet is saturated by H_2 during the whole experiment, at least in the optically imaged area. Indeed, the H^+ reduction current density, estimated from the CA curve assuming a $200 \mu\text{m}$ diameter electrolyte droplet, steadily decreases from ca. 0.76 mA/cm^2 at the start of the CA to 0.16 mA/cm^2 at $t = 50$ s. The pseudo steady current at long times suggests a pseudo constant flux of H_2 production. If NPs were considered as independent individual nanosources of H_2 , *e.g.* nanoelectrodes, within $t > 1$ s each one should operate under steady-state H_2 hemispherical mass transfer regime. However, 40 nm nanosources cannot be considered as independent when separated by $< 10 \mu\text{m}$.^{174,175} Both the inter-NP and inter-NB distance distributions, are below $5 \mu\text{m}$, suggesting the occurrence of H_2 diffusion cross talk between NPs. The dynamic tracking of the dimension and position of each NB during its growth suggests that most nanosource NPs are rapidly switched off by the NB they generate. The continuous growth of the NBs must then be sustained from other cross-talk sources. The μm large coffee-ring agglomerates sporadically distributed over the ITO surface resulting from the drop casting of the Pt NPs are likely such sources of H_2 homogenization over the ITO surface. Typically, in the $55 \times 40 \mu\text{m}^2$ region optically monitored within the electrolyte droplet, 3 of them are clearly detected, which all show an optical intensity variation and then H_2 gas evolution during the CA experiment. If the catalytic activity of these agglomerates is not discussed herein, from the same computation arguments,^{174,175} such HER active agglomerates are expected to afford after few seconds and over a much wider region (several tens of micrometers) a homogeneous H^+ and H_2 concentration over the ITO surface. This implies they will sustain a local saturation of the solution by H_2 homogeneously over the ITO surface, and therefore conditions for sustaining a long time growth of H_2 bubbles.

After few seconds both H^+ and H_2 diffusion is then operated through a linear diffusion regime, along the vertical z-axis, from the electrode surface to the micropipette opening. The expansion of the H^+ and H_2 diffusion layer along the vertical axis explains the current density decrease with time. Owing to the finite geometry of the droplet, this current decrease corresponds to the exhaustive electrolysis of H^+ into H_2 , enforcing a saturation of the droplet by H_2 . This saturation is further attested by the high stability and the unusually long lifetime of the NBs. Such stability is verified here by optical monitoring through the >140 s long NBs dissolution time after the CA was stopped.^{176,177}

3.3.1 Quantitative estimation of NBs size and shape

As in the first instant of the NB growth the NP signal dominates, the optical transients, $I_{opt}(t)$ in Figure 2d, recorded during HER were subtracted from the signal related to the NP. To rationalize such NB growth, the interferometric optical images of NBs at an ITO aqueous solution interface were modelled by boundary element method, as in previous studies related to NPs growth published by our research group.^{47,169} It is hypothesized here that NBs grow from surfaces as spherical caps characterized by two geometrical parameters defined in Figure 5a, namely, D the diameter of the footprint of the NB on the surface and θ the contact angle formed with the electrode surface and measured through the gas phase. The volume of such spherical cap NB is given by:

$$V_{NB} = \frac{\pi}{24} \frac{D^3}{\sin^3 \theta} (2 + \cos \theta)(1 - \cos \theta)^2 \quad (1)$$

so that the geometry of a NB is fully determined by only 2 independent parameters among D , θ and V_{NB} . Henceforth, for the sake of dimension homogeneity, one defines an apparent NB size, D_{eq} , as a descriptor of the NB volume,

$$D_{eq} = \left(\frac{12}{\pi} V_{NB} \right)^{1/3} \quad (2)$$

which corresponds, for a given NB volume, whatever D and θ , to the diameter of the hemisphere, dashed in Figure 5a, having the same volume V_{NB} as the original spherical cap. It ensues from (1) and (2) that for $\theta=90^\circ$, $D_{eq}=D$. Henceforth, the geometry of a given NB is now fully determined by only 2 independent parameters among D , θ and D_{eq} .

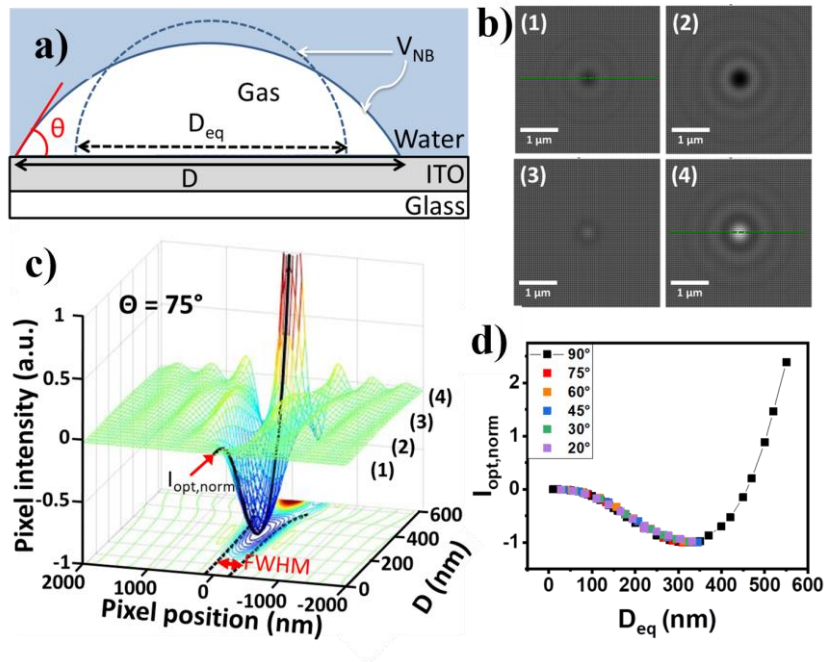


Figure 5. a) Schematic representation of the optically simulated configuration: a NB sphere cap surface is generated at the interface between the glass coated ITO electrode surface and an aqueous electrolyte. The NB sphere cap is defined by the diameter and contact angle (D, θ) of its footprint on the ITO, and by an apparent diameter, D_{eq} , of an equivalent (dashed) hemisphere with same volume, V_{NB} . b) Simulated optical images of hemispherical NBs of different sizes (127, 238, 373, 412 nm, from 1 to 4) located on top of an electrode (70 nm thick ITO layer). b) Theoretical variation of optical intensity profile along cross section (e.g. dashed green lines in b) as a function of the NB diameter, D , showing the variations of I_{opt} (black line) and FWHM (dashed black line) with D ; $\theta = 75^\circ$. d) Evolution of I_{opt} as a function of D_{eq} for a single NB for contact angles ranging from 20° to 90° .

The theoretical optical images were then computed for NBs of various volumes, meaning for various couples of D and θ values. The examples of theoretical images in Figure 5b for hemispherical NBs and for NBs with smaller contact angle (not shown) present the same general trends: small NBs appear as negative contrast features in the center of the calculated images and the larger the NB the darkest the feature (e.g. for hemispherical NB of diameter $D < 250$ nm). This trend is reverted as the optical contrast feature is becoming brighter for further NB increase, until the NB can be observed as bright contrast feature (e.g. for $D > 380$ nm for hemispherical NBs). In a first approximation and following the methodology used in

Figure 2c for experimental contrast features, the modeled contrast features were fitted by a Gaussian peak characterized by its intensity I_{opt} (the equivalent of the experimental I_{opt} values) and its full width at half maximum, FWHM.

As both D and θ influence the I_{opt} and FWHM characteristics (see Figure 5c, 5d), for the sake of simplicity, we first consider that NBs grow with constant contact angle. The hemispherical case $\theta=90^\circ$ was first chosen based on the macroscopic evaluation of the contact angle $\theta_M=90^\circ$ of water droplets or gas bubbles in water on the ITO surface. The theoretical normalized I_{opt} variations as a function of D_{eq} (note that $D=D_{eq}$ for $\theta=90^\circ$) are presented in Figure 5d. The calculations not only reproduce the contrast inversion but also the minimum of intensity observed in the experimental optical transients of Figure 2c.

Figure 5d also overlays the I_{opt} - D_{eq} variations for other contact angles $90^\circ > \theta \geq 20^\circ$. The good overlap of these variations for small enough NBs, $D_{eq} < 350$ nm, demonstrates that I_{opt} only depends on the NB volume for $V_{NB} < 1.6 \times 10^{-2} \mu\text{m}^3$. One can use such quantitative simulation of I_{opt} - D_{eq} variations to extract, from the experimental optical transients, the dynamics of NBs growth without prior knowledge of the real NB geometry. It is illustrated in Figure 6a, where an I_{opt} transient is transformed, into an apparent growth curve ($D_{eq}(t)$) for a single NB appearing over a single NP region, by inversion of the modelled I_{opt} - D_{eq} curve from Figure 5d.

The amount of H_2 gas contained inside such a NB, $n_{\text{H}_2\text{g}}$, was then estimated from both the NB volume and the gas internal pressure, P_{gas} , assuming an ideal gas,

$$n_{\text{H}_2\text{g}} = V_{NB} P_{gas} / k_B T \quad (3)$$

where k_B is the Boltzmann constant and T the temperature, while the internal pressure is obtained from the Young-Laplace equation:

$$P_{gas} = P_0 + \frac{4\gamma \sin\theta}{D} \quad (4)$$

with $P_0=1$ atm, the ambient pressure and $\gamma=72.8$ mN/m, the aqueous solution surface tension. For the case of a hemispherical NB, $\theta=90^\circ$, $D_{eq}=D$ and $P_{gas}=P_0+4\gamma/D$.

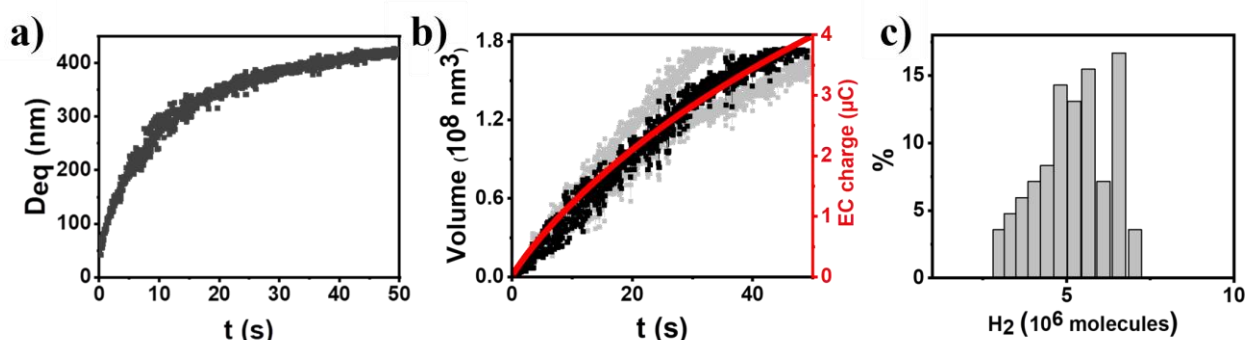


Figure 6. a) Evolution of the apparent size of a single NB generated at a single NP as a function of time. b) Correlation between the NB volume (median in black, first to third quartile in grey) and the measured total EC charge (in red). c) Distribution of the estimated amount of hydrogen molecules inside single gas NBs after 30 s of EC actuation.

The latter equations then allow a quantitative estimate of n_{H_2g} along the CA experiment at the single NB level. As in electrodeposition processes, it can be compared to the overall electrochemical charge exchanged for the electro-generation of nanomaterials at an electrode surface. This was indeed evidenced for NB growth on longer timescale allowing an *in situ* AFM monitoring.¹⁷⁸ Such growth dynamics fits with the Epstein-Plesset theory for gas NB growth.¹⁷³ It is further confirmed here by a $t^{1/2}$ growth law during the first ~20 s. More pertinent from the point of view of the Faradaic yield of the electrochemical reaction, the plot of Figure 6b shows that the average NBs volume (roughly equivalent to n_{H_2g} for $t > 3$ s, $P_{gas} \approx 7 \pm 1$ atm) correlates to the charge passing through the EC cell. Finally, one can also construct a distribution of the amount of hydrogen molecules trapped in single NBs at any arbitrary time of the EC experiment and at high throughput.

Such a quantification, illustrated in Figure 6c for $N > 100$ single NBs formed after 30 s of EC actuation, is interesting for benchmarking, since it provides a quantitative mapping of the catalytic activity of individual NPs towards HER, as qualitatively suggested earlier.^{109,112} Owing to the strong interaction of H_2 gas with Pt NPs, it is expected that the latter act as nucleation sites for H_2 NB growth. At first sight, it seems also reasonable that the most catalytically active NPs produce the highest H_2 local concentrations and therefore grow NBs. As a further information brought by such quantitative analysis, the limit of optical detection, L.O.D., of gas NB was evaluated, in terms of equivalent diameter, to $D_{lod,eq} \sim 50$ nm, yielding for $\theta = 90^\circ$ a L.O.D of $\sim 5 \times 10^4$ H_2 molecules, a sensitivity equivalent to that of SPRM.¹¹⁴

A closer examination of the theoretical images, at constant contact angle, shows that the FWHM of the dark contrast features also varies with the NB footprint. Figure 5c presents the cross section of the predicted contrast features for different D values and a constant contact angle of 75° . The values of the FWHM extracted from these cross sections are reported in the lower plane of Figure 5c. Interestingly, the variations of the FWHM with D hold whatever the NB contact angle, as long as it is detected as a dark feature and roughly as long as I_{opt} is sufficiently different from the background (sufficient signal to background ratio, *i.e.* $D < 500$ nm in Figure 5c). It suggests that the footprint diameter variation, ΔD , can be extracted from such diffraction patterns for NBs with $200\text{-}250\text{nm} < D < 500$ nm. Noteworthy, the lower bound value is actually consistent with the value of the point spread function $\text{PSF} \approx 1.22 \lambda / 2\text{NA} \approx 220$ nm of the modeled microscope with objective's numerical aperture, $\text{NA} = 1.4$, and detection wavelength $\lambda = 510$ nm.

Experimentally, the FWHMs of the optical patterns were then obtained from a dynamical super-localization approach during the growth of individual NBs (*i.e.* while I_{opt} varies). Examples of such FWHM variations during the CA experiment for $N = 10$ NBs, indeed show an increase of the FWHM for $t > 2$ s. These variations attest that, as soon as $t > 2$ s, the NB footprint diameter, D , is above the ca. 250 nm of the microscope PSF.

Therefore, from the same strategy as that used for I_{opt} , the experimental evolution of ΔD of an individual NB during its growth was inferred from the experimentally measured ΔFWHM along the CA experiment, with the help of the predicted FWHM- D curve.

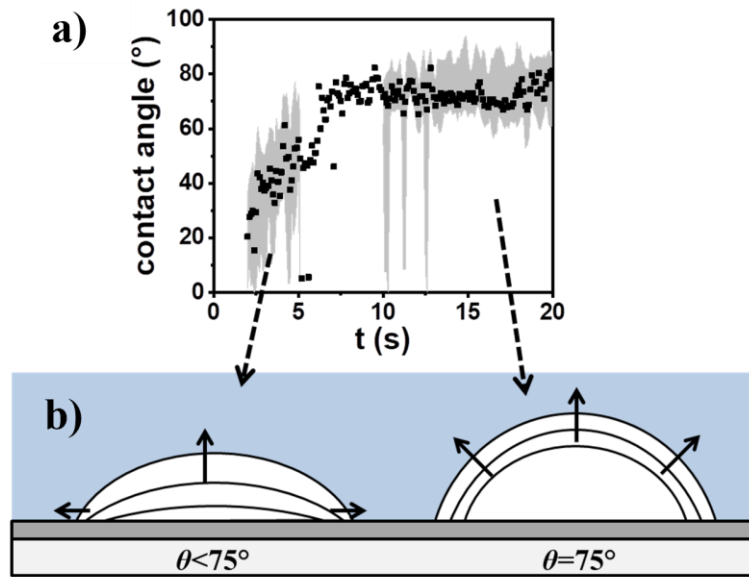


Figure 7. a) Single NBs contact angle variations (N=12, median and first to third quartiles in black and grey, respectively) estimated from D_{eq}/D . b) Schematic representations of the two NBs growth regimes at short and long times (with an increase of the contact angle or at constant contact angle).

Overall, such inspection of the optical model then suggests that the monitoring of both FWHM and I_{opt} of the optical feature yields two complementary information, respectively the footprint, D , and the volume of the NB, V_{NB} (or equivalently D_{eq}). From equations (1) and (2), it can be shown that the D_{eq}/D ratio is a decreasing function of θ , allowing then from both independent and complementary optically inferred parameters to evaluate the NB contact angle on the surface. This analysis was tested on the experimental optical images at the early stage ($t < 20$ s) of a NB growth. The resulting variation of the evaluated NB contact angle is shown in Figure 7a.

The trend in Figure 7a, for N=12 NBs, demonstrates that the NB grows according to two growth regimes schematized in Figure 7b. The NB contact angle increases from ca. 30° to 75° during the earliest stages of the NB growth. Later, the NB mostly grows at a constant contact angle of 75° by an increase of its footprint on the surface. These observations of growth modes with increasing contact angle agree with current theories on NB nucleation and growth.^{176,179}

Indeed, formally, owing to the intervention of the gas internal pressure in (3), the growth dynamics of gas NBs on surfaces differs from that of solid NPs. If the latter most often operates at constant contact angle, it is less likely for gas NBs, which could be pinned to

surfaces enforcing a growth at almost constant footprint on the surface while the contact angle of the NB increases at the first instants of the growth.

Our results agree with the previous AFM imaging of NB growth/dissolution processes,¹⁷⁸ and the later theories proposed to explain that at the nanoscale, the contact angle of gas NBs decreases with decreasing NB size.^{176,179} There is a further energy minimization argument, as with a small contact angle during its nucleation stage, a NB presents a radius of curvature, $r_{curv} = D/2\sin\theta$, much larger than its footprint on the surface, D . It allows, based on Laplace pressure equation (4), the NB to nucleate and grow with a considerably decreased gas internal pressure.

3.3.2 Suggestion of hydrogen spillover

The smallest NB contact angle that could be evaluated here (25-30°) strongly suggests that NBs may nucleate on surfaces with smaller contact angle than their macroscopic value. Moreover, contact angles as low as 24-34° for <10 nm H₂ nucleating NBs at Pt surface have recently been reported.^{180,181} Taking into account that macroscopically, Pt has a wettability comparable to that of ITO ($\theta_M=90^\circ$), the contact angle values are also in agreement with those reported herein.

However, the measured NB footprint is significantly higher (D up to 300 nm) for $\theta=30^\circ$ in the present work than the reported 10 nm nuclei on Pt nanoelectrode. This difference might be explained by the difference of H₂SO₄ concentration used (5 mM herein vs >1 M in other works). Indeed, at best, the mass transfer limited reduction of the 5 mM H₂SO₄ solution would provide a growth of NBs with a maximum 5 mM concentration of dissolved H₂. From Henry's law describing the equilibrium between the saturation of the solution at the NB surface, $C_{H_2,s}$, and the internal H₂ NB pressure through Henry's constant $K_{H_2}=0.78$ mM/atm:

$$C_{H_2,s}=P_{gas}K_{H_2} \quad (5)$$

the 5 mM upper limit of dissolved H₂ imposes an upper limit for $P_{gas,M}= 7.4$ atm in the NB during the whole CA experiment, much lower than those employed at higher concentration during single NBs electro-generation at nanoelectrodes.^{172,180-185} It imposes from (4) a nucleation and growth of NBs with lower bound curvature radius $r_{curv,m}=266$ nm. Typically, within the reported values of ca. $\theta=30^\circ$ contact angle, the smallest NB nucleus that could be produced under our conditions should then be a spherical cap of footprint diameter $D=2r_{curv}\sin\theta=266$ nm, a value close to those reported experimentally, and height

$h=r_{curv}(1-\cos\theta)=35$ nm. The consistent predicted and observed dimensions (D and θ) of the NB in its earliest optical detection support that IRM provides a pseudo-3D analysis of such dynamic process, as would do AFM,^{178,186} but at a higher throughput and image acquisition rate, and without possible tip-NB contact perturbation.

The optical detection of the NP, along with the NB, prevents a sensitive detection of the first instant of the NB nucleation, which usually takes place within < 100 ms.^{106,180} However, the optical imaging further allows mapping H_2 evolution at the NP supported ITO. Figure 8 provides a map of the characteristic time needed to grow individual $D_{eq}=350$ nm NBs within two different ROIs.

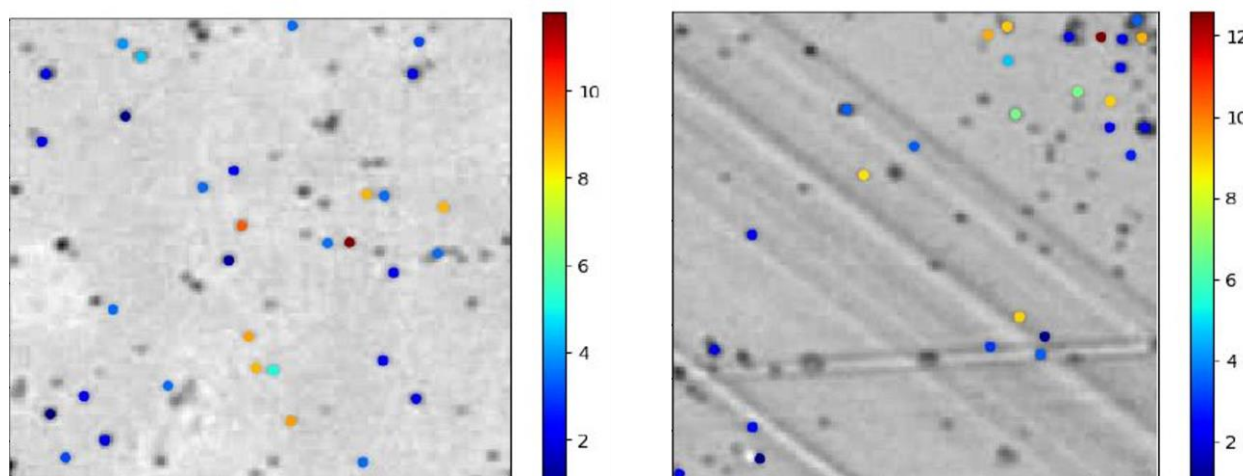


Figure 8. Two representative ROIs reporting characteristic time (in seconds) necessary to grow individual NBs with $D_{eq}=350$ nm.

These characteristic times are widely distributed, as the n_{H_2} estimated at 30 s in Figure 6c, and range between 2 and 15 s, though with no apparent dependence on spatial localization: they are neither related to the proximity of a neighbouring NP or NB or to the μm large agglomerates. Such variability is then mostly related to the NB nucleation, which has different origins, relative to either the gas nucleation activation barrier or the electrochemical process activation barrier. The importance of nucleation activation barrier has been modelled or experimentally measured for the nucleation of NBs of different gases at nanoelectrodes¹⁸⁰ or under thermal activation at SPR surfaces.¹⁰⁶ Although the nucleation of NBs occurs on the sub-100 ms range, not explored here, gas nucleation rates for mass transfer limited electrochemical processes show a much narrower distribution than the growth times experimentally observed here. The wider distribution observed here could be related to the influence of the surface roughness and/or chemistry of the NP or ITO on the nucleation

activation barrier (*i.e.* the wetting of the NP).¹⁰⁶ As investigated more in details in Chapter 4, surface chemistry could play similarly a significant role in the overall electrochemical activity of the NP. The capping agent of the NP is expected to control both the electrical contact between the NP and the electrode and the electron transfer rate for HER at the NP-solution interface. Recent works have also demonstrated the importance of the control of NP-electrode contact resistance in single entity electrochemistry.⁴³ Considering these latter effects predominate, the NB growth activity suggests that the H₂ NBs nucleation occurs at first on Pt NPs, which possess higher apparent activity toward proton reduction. It is then tempting to suggest that the most active NPs will grow the largest NBs.

However, owing to the 3D optical reconstruction of the NB during its growth, the geometrical situation is schematically depicted, at scale and considering a slight off-centering of the NB and the NP, in Figure 9a and b for different instants of the growth of a NB, employing the contact angles evaluated in Figure 7a. It can be concluded that during the NB growth, the NB may cover the whole NP, disconnecting it from the electrolytic solution, typically for $t > 3-5$ s. The catalytic reaction may then be halted and the NB should stop growing, unlike what is observed in Figure 6a.

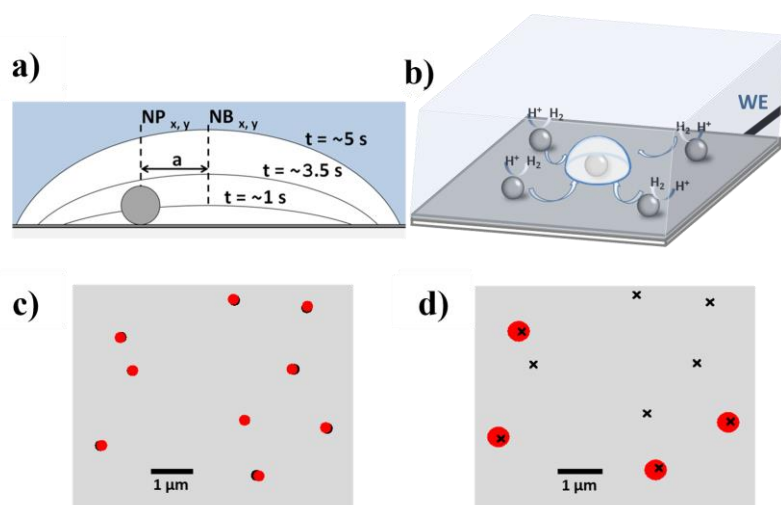


Figure 9. a) and b) Two schematic representations (side and perspective view, respectively) of a H₂ NB disconnecting a Pt NP during HER. c) Pt NPs positions located by Gaussian fits before (black dots) the NBs generation and after (red dots) the complete NB dissolution. d) Pt NPs positions before the electrode polarization (black crosses) and H₂ NBs positions (the red disks represent to scale the electrode area covered by the NBs) after 50 s of EC actuation. The electrode region is the same as that presented in Figures 2b and 3a.

One possibility though to prevent the NP disconnection could be that the NP is pinning the NB and both are strongly off-centered. Because IRM is label-free, both the NP and NB can be detected separately. Their respective positions over the reaction were also monitored by super-localization, as illustrated in Figure 9c and d for the very same electrode region shown in Figures 2b and 3a. We used the same dynamical super-localization approach to record the precise location of the centers of mass of the Pt NPs in the absence of NB. Subsequently, when the NB signal dominates (dark or bright) its center of mass is located by employing the post-treatment proposed by Zhang and co-workers.¹⁵⁸

The possible alteration of the electrode nanostructure caused by the EC actuation was first investigated by comparing the NPs positions before the NBs nucleation and after their subsequent dissolution (black and red dots in Figure 9c, respectively). According to Figure 9c, most NPs are weakly bonded to and migrate through the ITO surface, 40 nm in average, the tracking precision being ~ 10 nm.⁴⁷ Even if the NP motion could be induced by the electrode polarization, recent works suggest that it would be due to non-uniform chemical fluxes generated during the EC reaction at the NPs surface.¹⁸⁷ It could also be related to asymmetric NBs growth at the side of the NPs, propelling them by the same mechanism as for micro-motors.^{188–190} After 50 s of actuation, the center of mass of the NBs detected in the same area as in Figure 2b (N=4 NBs with N=9 NPs) are located within an average perimeter estimated to <70 nm starting from the center of mass of their corresponding NPs. NPs and NBs are represented to scale as black crosses and red disks respectively in Figure 9d. NBs have also been found to be roughly stationary during the growth, as no significant lateral motion is measured during the time scale of the EC experiment.

Therefore, owing to this short-range motion of the nucleating NPs, summarized in Figure 6C, NBs should disconnect the Pt NPs once entirely covering them at $t \sim 3.5$ s. However, no sharp EC current drops are observed in the EC current-time transients, while NBs continue growing. This observation could be explained by the H_2 feeding from other neighbouring sources. Solution or surface diffusion of H_2 could be equally invoked, the latter corresponding to the spillover, recently imaged on ITO surface by TIRFM visualization.¹⁰⁸

Once the surface of the catalysts is saturated, the growth of NBs remains possible even if the catalyst is isolated from the solution by the covering NB, fed by the other non-blocked Pt catalysts, including the μm large agglomerates. Indeed, the NPs remaining apparently optically inactive can produce H_2 that diffuses in solution or hydrogen atoms that migrate out onto the ITO surface toward the existing NBs as schematized in Figure 9b. Through such phenomena, NBs can continue growing, even if the (most active) catalysts are rapidly

electrically isolated. The EC current transient suggests an exhaustive electrolysis of H^+ and therefore saturation of the droplets by H_2 over the whole experiment duration. This means that the non-nucleating NPs and the presence of other large agglomerates would strongly contribute to such H_2 production, while the activity of the former cannot be probed optically here. Noteworthy some of these optically inactive NPs are also subjected to motion, which could suggest their electrochemical activity. This points to the necessity of complementary or multi-correlative electrochemical microscopies for deeper insight. Definitely, local electrochemical probings,^{191,192} operated at the nanoscale, as those using nano-electrochemical cells, nanoelectrodes or nanopipettes^{193,194} would allow unveiling such aspect.

3.4 Conclusions

In (electro-) catalysis, NBs are frequently employed as nano-reporters that have been associated to the presence of local catalytic activity.^{112,158} Together with their detrimental effect in devices efficiency, it motivates the needs of studying them at the single object level. Herein, the nucleation and growth of single surface NBs during electrocatalysis on single Pt NPs adsorbed on ITO electrode have been analyzed through IRM/EC coupling. Thanks to a SEM/IRM correlative microscopies approach, it is first evidenced simply through NPs optical intensity measurement that such a phenomenon can be quantitatively investigated selectively on a specific population of NPs, exemplified here from individual Pt NPs. With the help of optical images simulation, single NBs growth was quantitatively followed through the evolution of both the optical intensity and super-localization of the diffraction pattern associated to the NB optical image. With a sensitivity close to 5×10^4 H_2 molecules, gas NBs were imaged, in pseudo-3D owing to the estimation of the footprint, the volume and the contact angle of the NB. The high throughput analysis of the growth process also revealed its correlation with the EC charge. In addition, the dynamic super-localization approach of both the NBs and the NPs evidences i) the possible, yet slight, *operando* nanoscale motion of the Pt NPs and, ii) the rapid electrical disconnection of a substantial amount of Pt NPs provoked by the NBs growth. Still, the NBs growth was continuously tracked even after the most active Pt NPs have been covered, strongly suggesting the presence of hydrogen crosstalk from less active NPs to the most active ones.¹⁶⁷

It seems that NB electrogeneration may report the activity of nanocatalysts but it may be difficult to attribute the role of each individual nanocatalyst on the growth of a given NB. It

was then tempting to remove the role of the catalyst and observe the electrogeneration of NBs at ITO electrode (Chapter 4) free from catalysts.

Chapter 4

Differentiating competitive electrochemical pathways at optically transparent (ITO) electrode surfaces

Reprinted with permission from *Electrochimica Acta* **2021**, 386, 138498. Copyright 2021 Elsevier.

This chapter will reply the following questions: is it possible to optically discriminate competitive processing occurring at the same potential? How much surface heterogeneities can affect the local electrochemical response? What is the role of the substrate during an electrochemical reaction?

4.1 Introduction

Competitive reactions can be defined as two or more (electro-)chemical processes which need for the same specific reagent(s) within the same interface or region of interest. Theoretical calculations and experimental evidences based on kinetic and thermodynamic parameters usually helps to establish the extent of each reaction and predominant processes occurring at given conditions. In solution, the best way to obtain a dynamic description of these reactions is to record a signal (spectroscopic, electrochemical, optical, in mass, ...) reflecting the temporal evolution of concentration of species (both reactants and products).

This can be complicated for a plethora of non-ideal systems, including electrode surfaces. Interaction between electric double layer charging, ionic species, surface grain boundaries, transport regimes and phase boundaries can lead to nonlinear interplays between each contribution which can change toward the electrode surface, leading to great difficulty in

interpretation. Single entity approach to electrochemistry is therefore a powerful tool to evaluate at the nanoscale each actor, including NPs, phase boundaries and substrates as indium tin oxide (ITO).

In the context of *operando* microscopies coupled with electrochemistry, ITO is widely popular thanks to its combination of high transparency, good electronic conductivity^{195,196} and poor electrocatalytic properties. In this respect, ITO has been used as a WE to optically track and detect the electrochemical collision,^{6,119,197,198} the displacement,¹⁹⁹ deformation,¹¹⁸ chemical conversion or transformation^{27,43,47,116,119,120,200} of individual various objects subjected to an electrochemical reaction. The same properties have made of ITO an important material also in application related to photovoltaics,²⁰¹ electrochromism,^{202,203} fuel cells,²⁰⁴ or electrocatalytic devices.^{205,206}

ITO is often considered as chemically stable and inert in mild conditions, although its chemical and electrochemical stability strongly depends on the pH of the adopted electrolyte,²⁰⁷ as reported by many researchers for hydrochloric acid²⁰⁸ and other common acids typically used as electrolytes.^{209,210} Most of systematical studies^{209,211} about ITO degradation under various reduction and oxidation conditions probed its surface at macroscopic level and for extreme pH conditions: the chemical degradation provokes decreasing in transmission and conductive properties. Although SEM and XPS showed ITO can be reduced into arrays of metallic NPs composed of In and Sn,²⁰⁹ there were no *operando* studies at micro- or nanoscale until recently. SECCM analyses on bare ITO found, for instance, difference in electron transfer kinetic of 1,1'-ferrocenedimethanol of about three order of magnitude toward the surface, confirmed also by biphasic responses recorded by spectroelectrochemical characterization.^{212,213}

The implication of such variations in electron transfer kinetic can potentially affects electrodeposition, electrocatalysis and any electrochemical process at local level. *Operando* microscopy at the single entity level is therefore necessary not only to unravel different subpopulation hidden in an average electrochemical response, but also to understand if statistical variability is due to the intrinsic stochasticity of a substrate activity or competition between NPs/substrate or between two redox reactions. This has recently been shown by probing electrodisolution of gold NPs on different ITO surfaces. Different populations of dissolution times were found, although SEM and X-ray spectroscopy revealed no structural differences in NPs. The different outcomes has been therefore attributed to substrate heterogeneities rather than to NPs itself.²¹⁴

The aim of this chapter is therefore to explore with IRM the heterogeneities in electrochemical responses in terms of competitive processes in the region of HER. Two levels of complexity have been investigated. At first, bare ITO has been probed to visualize the effect of surface heterogeneities in affecting the competition between proton reduction and ITO electro-reduction in micrometric acidic electrolyte droplets. Secondly, a process deeply influenced by pH changes in electrolyte - electrodeposition of Ni on ITO - has been probed. Like other earth-abundant metals from the iron group, pH conditions strongly affects the oxidation state of electrodeposited NPs, leading to formation of oxide/hydroxide shells around metallic cores. The study of these processes at the single entity level allows revealing local competitive reactions on a specific nucleation site.

4.2 Probing bare ITO in acidic conditions

In the context of the visualization of HER at ITO electrodes one first needs considering the stability of ITO substrates under acidic conditions. A degradation process, usually irreversible, occurs in extremely acidic conditions ($\text{pH} < 1$), without need of applied potential. It consists of the chemical dissolution of oxides, In_2O_3 and SnO_2 , recognizable from uniform variations in optical properties such as the substrate absorbance or, as detected by IRM or other optical microscopies, from variations in the background intensity, I_{bkg} . In standard lithographic techniques >1 M HCl solutions are generally used to etch and pattern ITO coatings with etching rates of the order of several nm/min.²¹⁵ Solutions of other acids at lower concentration may be used to operate the dissolution of ITO. If often unsuspected because undetected *in situ* by optical techniques, the enhanced optical sensitivity of IRM allows monitoring such subtle variations in the optical transparency of ITO coatings. In this respect, Figure 1 shows the evolution of the light reflected by the ITO|electrolyte interface collected by IRM with the time of contact of droplets composed of 5 mM to 1 M H_2SO_4 electrolyte.

These measurements were performed for a 70 nm thick ITO coating in the absence of electrode polarization. They correspond to the time evolution of I_{bkg} that would be recorded *in situ* during typical IRM monitoring of an electrochemical reaction. The action of acidic solution on I_{bkg} is characterized by a two-step process. In the first instants I_{bkg} decreases slowly until, in a second period, it vanishes abruptly, suggesting the ITO coating gets completely removed. The overall process takes ca. 250 s in a 1 M H_2SO_4 solution, which is in

the range of the approx. 16 nm/min etching rate observed in 2 M HCl solutions.²¹⁵ Decreasing the acid concentration decreases the slopes of the first and second stages of I_{bkg} variations. For 5 mM H₂SO₄, indeed I_{bkg} does not change by less than 1 % within 20 min, suggesting that the ITO surface can be considered stable during most electrochemical studies in such conditions. Noteworthy, when HER reactions are considered, such low H⁺ content limits the amount of H₂ that can be evolved and therefore the number of gas bubbles that can be generated at the surface.

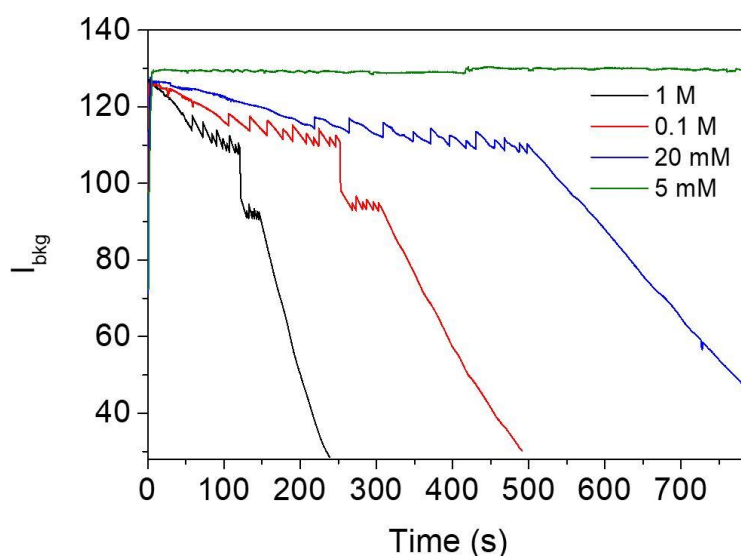


Figure 1. Evolution with time of the background intensity, I_{bkg} , recorded by IRM for a 70 nm ITO layer contacted with micrometer size droplet of H₂SO₄ solutions.

4.2.1 Proton reduction vs. indium reduction

The reduction behavior of ITO electrodes depends on different chemical and physical parameters such as the electrode conductivity (related to the ITO coating thickness),²¹⁶ the pH²¹⁰ and chemical composition of the electrolyte,²¹⁷ the In:Sn ratio, the coating porosity and roughness.¹⁹⁵ ITO is usually considered as an inert substrate. However, surface processes such as coating reconstruction, nanoscale defects formation (such as NPs) have been described²¹⁸ and are usually detected by *ex situ* SEM imaging. We propose herein to probe *operando* the reduction behavior of ITO coating using IRM monitoring during cyclic voltammetry experiments. As it will be discussed later, by using three ITO substrates named ITO_l, ITO_m and ITO_h of increasing coating thickness and therefore increasing conductivity, this behavior depends on the conductivity of the ITO coating. The general overview of the situations

encountered and of the experimental methodology used is first described, in Figure 2, in the case of the most conductive one, ITO_h.

Figure 2a shows the cyclic voltammogram of the ITO_h electrode contacted with a ca. 200 μm diameter droplet of 5 mM H₂SO₄ electrolyte confined by a micropipette equipped with a Pt wire used as both QR and counter electrode. A first quasi-reversible system enlarged in the inset of Figure 2a is detected. It corresponds to two bell-shaped reduction and oxidation peaks of equivalent charges, respectively at E_{c1} and E_{a1} , assigned to sulfate ions adsorption/desorption. This quasi-reversible system is present on all CVs, and its apparent $E^0 = (E_{c1} + E_{a1})/2$ is unchanged, whatever the ITO conductivity compared to an external potential reference such as the E^0 of FcMeOH. All CVs are then rescaled vs the E^0 of this quasi-reversible system. Towards more negative potentials, two other reduction processes are detected with onset potential at respectively -0.8 and -1.05 V.

Optical images of the ITO|electrolyte interface were recorded with a 20 Hz frequency synchronously with the CV; some examples images obtained at 0.3, -0.95 and -1.2 V are given in Figure 2b. Compared to the first image at 0.3V, optical patterns have appeared on the latter two images concomitantly to the onset of the cathodic current flows.

A dynamic super-localization approach in every image frame allowed counting the number of patterns, N , per image along the electrode potential evolution (see Figure 2c) and characterizing every optical pattern through the position (x,y) and optical intensity, I_{opt} , of its center of mass (see Experimental section). On the negative scan, N , as for the CV, presents two successive onsets of pattern appearance: a sharp increase in N occurs around -0.83 V, followed by a second increase at -1.19 V. On the reverse oxidation potential scan two sharp decreases in N are also detected at -1.14 and -0.49 V respectively.

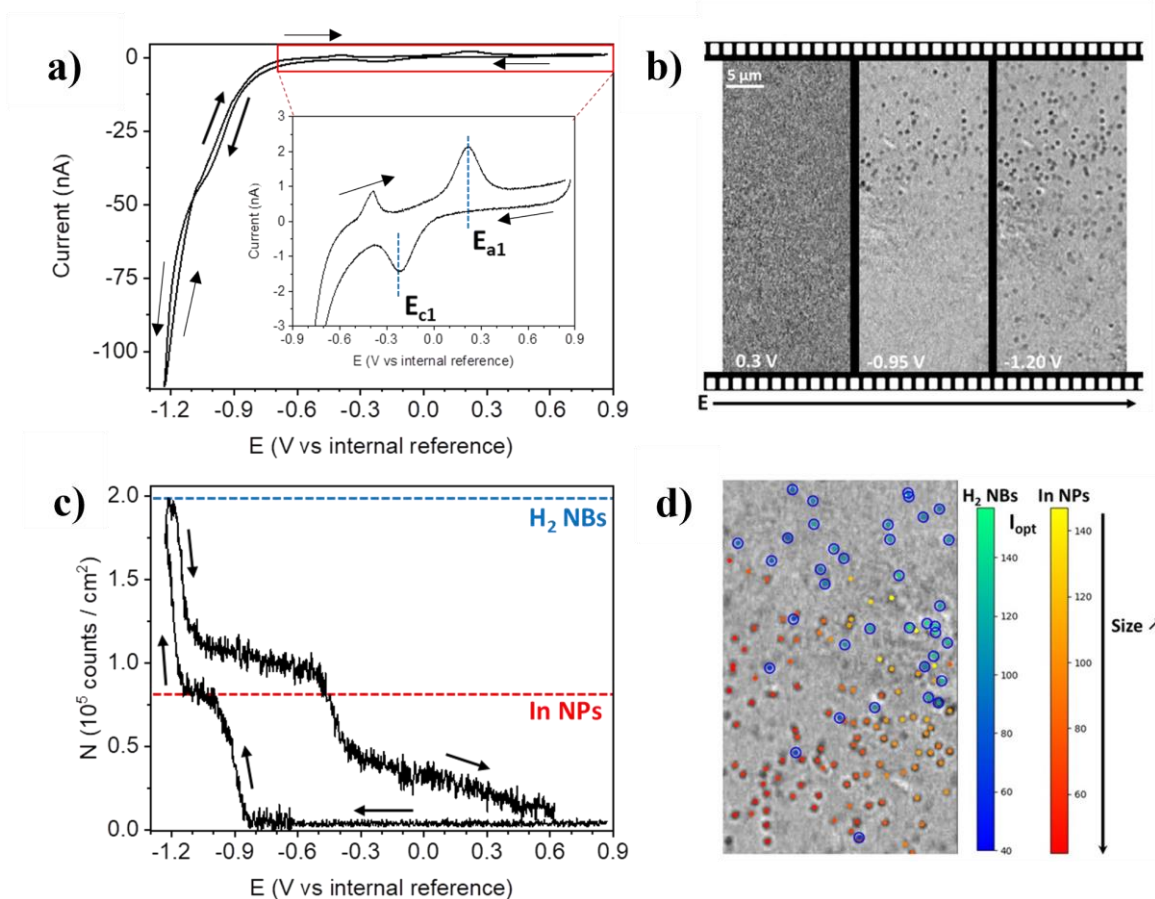


Figure 2. Illustration of the opto-electrochemical investigation of the electrochemical behavior of an ITO electrode contacted with a 5 mM H_2SO_4 micrometric electrolyte droplet confined at the tip of a micropipette. a) Cyclic voltammogram of a ca. 200 μm diameter droplet of electrolyte recorded when in contact with the ITO_h substrate ($v = 50 \text{ mV/s}$). b) Examples of sequential optical images recorded at different electrode potentials showing the successive formation of optical patterns. c) The number N of optical patterns detected at each image along with electrode potential identifies two regions of potentials and the formation of two populations of patterns associated, respectively, to the reduction of ITO into $\text{In}(0)$ and the formation of H_2 NBs. d) Reconstructed image showing how each pattern population grows selectively on different regions of the ITO_h electrode, the colorbars provide a qualitative comparison of the difference in size of the nanopatterns in each population.

The optical spots observed on the different images are all characterized by diffraction-limited patterns, suggesting they correspond to the formation of sub-wavelength objects whose

footprint on the electrode is <300 nm based on previous modeling, described in Chapter 3, of the optical response of sphere cap-type nanoobjects. The appearance and disappearance of these features in two different potential regions suggests that two populations of nanoobjects are formed on the ITO with two different chemical compositions and natures.

These two nanoobjects populations were further discriminated based on their optical features (see Figure 2d). Indeed, it has been noted that the two populations are distinct when considering i) their optical transients, ii) their characteristic (median) onset potentials of patterns appearance during the forward potential scan and disappearance during the reverse scan and, iii) nanoscale motion. The characteristics and identification of each of these populations are discussed in the next sections. They are associated to either the reduction of ITO into metallic NPs of In(0) and the evolution of H₂ NBs from HER.

4.2.1.1 Hydrogen NBs nucleation on bare ITO

Tracking the steps and mechanisms of hydrogen NBs nucleation and growth on a large variety of interfaces and NPs is fundamental for validating theoretical models related to heterogeneous nucleation and gaining insights on how NBs can affect the efficiency of devices' catalysts. Quantifying and following *operando* the hydrogen NBs growth on bare ITO is interesting not only to distinguish NBs optical footprint from the one related to ITO reduced NPs, but also to gain a statistically significant reference signal in order to compare kinetic parameters of non-catalyzed H₂ nucleation from catalyzed one. The growth mechanism of H₂ bubbles can be investigated with a high throughput quantitative analysis thanks to IRM high sensitivity probing (< 20 nm), as previously achieved in Chapter 3 for H₂ NBs nucleation on Pt NPs under similar conditions in 5 mM H₂SO₄ electrolyte.

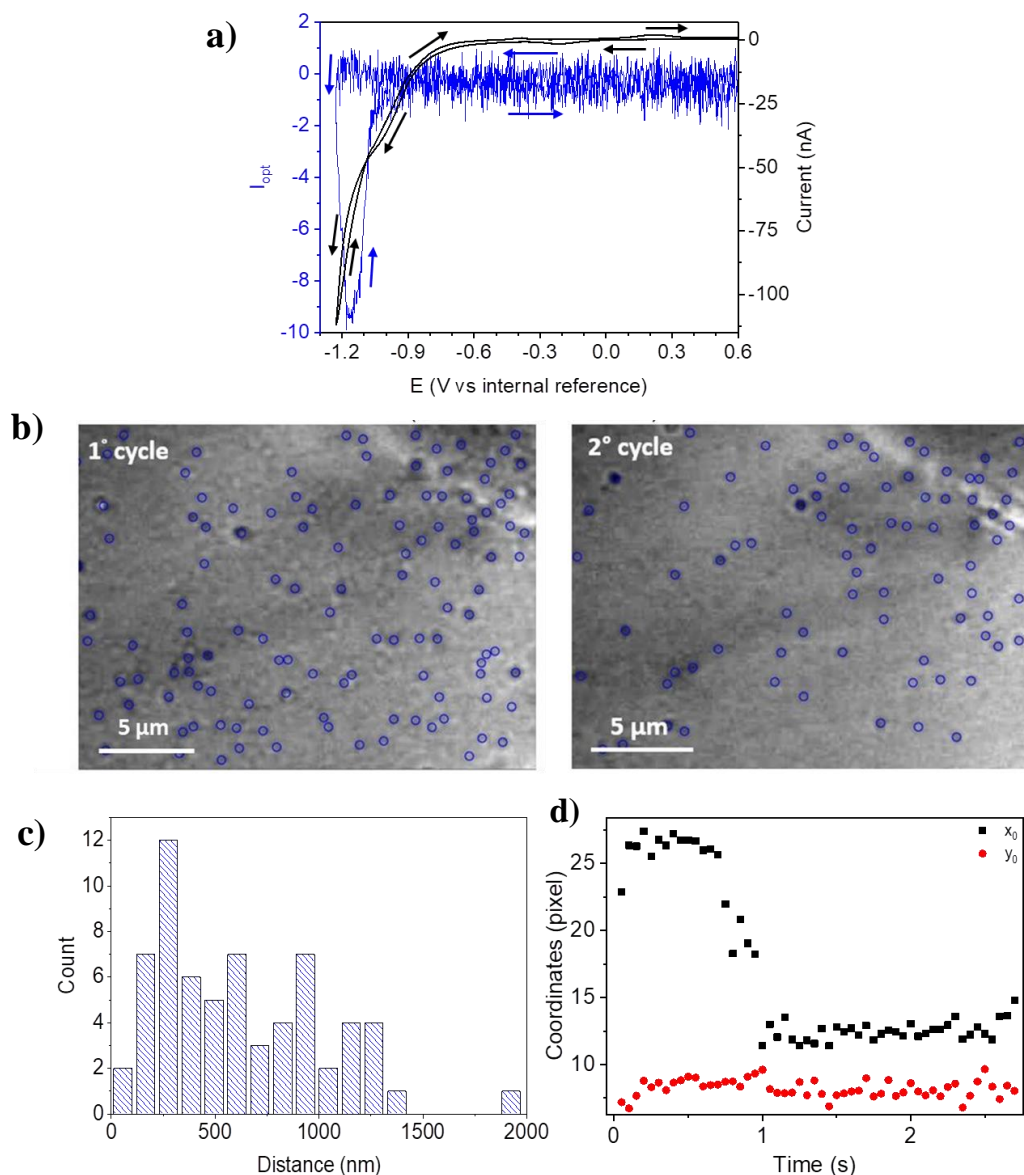


Figure 3. a) Median of the distribution of optical voltammograms, $I_{\text{opt}}-E$ curves, recorded from the patterns appearing at $E < -1.1$ V and corresponding to the formation of H_2 NBs in a 5 mM H_2SO_4 confined electrolyte droplet together with CV at 50 mV/s. b) Positions related to H_2 NBs along two consecutive voltammetric cycles. c) Histogram of the distribution of distances between the NBs patterns along consecutive images. d) Evolution with time of the position of a single H_2 NB (grown during the CV experiment).

Figure 3a shows the median optical transients, presented as opto-voltammograms *i.e.* $I_{\text{opt}}-E$ curves, of the distribution of >100 patterns appearing in the $E < -1.1$ V region. This electrochemical signature is related to the proton reduction and the formation of H_2 NBs upon

HER. In the absence of Pt nanocatalysts, even if ITO is not a catalyst of HER, H₂ NBs were also produced here directly at the ITO electrode by HER, but at a more negative potential, E < -1.19 V (E < -1.42 V vs FcMeOH⁺/FcMeOH).

Despite the high sensitivity of IRM for gas bubbles detection, the onset of detection of NBs is shifted compared to the onset potential observed electrochemically in the CV for proton reduction. Indeed, while the latter starts around -1.05 V, no bubbles are observed until overcoming a local critical concentration of dissolved H₂. This corresponds to conditions to reach the saturation of the electrode surface with H₂ in order to initiate the nucleation of NBs on the ITO surface, as demonstrated in different systems related to HER from Pt nanoelectrodes or other catalytic NPs.^{181,219} It is then expected that NBs are produced under H₂ mass transfer control, while the formation of ITO reduced NPs is rather driven by a surface transformation process.

Besides the longer delay between the onsets of the electrochemical current and of the corresponding optical patterns expected for the formation of NBs compared to solid NPs, the optical patterns related to H₂ NBs can be distinguished from ITO reduced NPs based on the different dynamics of their positions on the ITO surface.

These differences can be related to difference in the nucleation and growth of gas NBs or solid NPs on surfaces. On one hand, contrary to the formation of metallic NPs that produces rather immobile nuclei when their size is >5 nm,²²⁰ the nucleation of gas NBs implies more mobile molecules with much higher surface diffusion. On the other hand, these processes differ from the energetics of their activation barrier. For NBs nucleation, this is mostly governed by the formation of the gas/liquid/solid triple-interface, *i.e.* the wetting of the ITO surface by the electrolyte. The activation barrier^{106,180,219} is then much smaller than that required for solid phase transformation. While the former is influenced by rather low surface energy variations (chemical defects),¹⁰⁶ the latter requires larger energies usually controlled by the electrode potential. Overall, NBs present higher mobility than NPs.

The dynamics of the nano-objects was revealed *in situ* by optical microscopies,¹¹⁶ in the first instance by comparing the positions of the optical patterns formed at the ITO surface along different cycles of a same CV, as shown for NBs for two consecutive cycles in Figure 3b. When comparing the images recorded in the same region at the same potential NBs appear in random positions and at different locations between consecutive potential cycles, as expected for low activation barrier energy process. This is best described quantitatively by evaluating from such images the position of any given optical pattern observed during the second CV

and comparing it to the position of the closest pattern detected in the same region but on the first CV. The histogram provided in Figure 3c shows the distribution of distances between these patterns along consecutive images. From such distribution, the distance between NBs along consecutive cycles are >100 nm for 98 % of detected NBs and yield a <2 % probability to find a NB on the same nucleating site along two successive cycles.

In the second instance, the pinning of NBs relies on the presence of geometrical defects on surfaces¹⁷⁶. Henceforth during its growth, a NB may find a site of higher pinning energy. It is then expected that growth and dissolution of NBs are not symmetric processes,¹¹⁴ unlike for the growth/dissolution of NPs; indeed, the position of the center of mass of the NB may vary during the dynamics of its growth and dissolution. An example of such trajectory of the center of mass of NB during its growth/dissolution is presented in Figure 3d. It shows that during this stage the NB center of mass can move by ca. 13 pixels, *i.e.* by ca. 700 nm.

4.2.2.2 ITO reduction in acidic condition

The onset of appearance of the other population of patterns observed in Figure 1 and highlighted in Figure 4a is associated to a decrease of I_{opt} at $E \sim -0.8$ V. It is followed by a return of I_{opt} to the background level in the reverse scan, which occurs concomitantly to a bell-shaped oxidation peak at -0.39 V. Owing to its surface-limited electrochemistry, this optical transient behavior is attributed to the reduction of In(III) into metallic In(0) NPs. Indeed, the electroreduction of In_2O_3 and SnO_2 can be described by two possible reactions (2) and (3) yielding to the formation of metals NPs:



However, previous works²⁰⁹ demonstrated from *ex situ* analysis by SEM and X-ray Photoemission Spectroscopy (XPS) that ITO reduced NPs are composed mainly of In(0). This process is partly reversible, the oxidation peak at -0.39 V in Figure 4a being assigned to the reoxidation of In(0) into In(III), even if its reduction counterpart cannot be clearly identified on the CV.

The formation of metallic NPs upon ITO reduction is also demonstrated by *ex situ* SEM analysis performed in regions where the reduction exploration was stopped at $E \sim -1.0$ V. As shown in Figure 4b, ITO reduced NPs were detected by SEM; they have an average diameter

of ca. 120 nm from the dispersion size graph in the inset. Surface morphology of untreated ITO film was evaluated from high magnification SEM images (not shown). The bare ITO surface is composed by grains with an average diameter ~ 20 nm and is completely exempt of NPs. A consistent amount of few particles ($< 0.7/\mu\text{m}^2$) aggregates is also present, as well as non-spherical NPs after sweeping the potential.

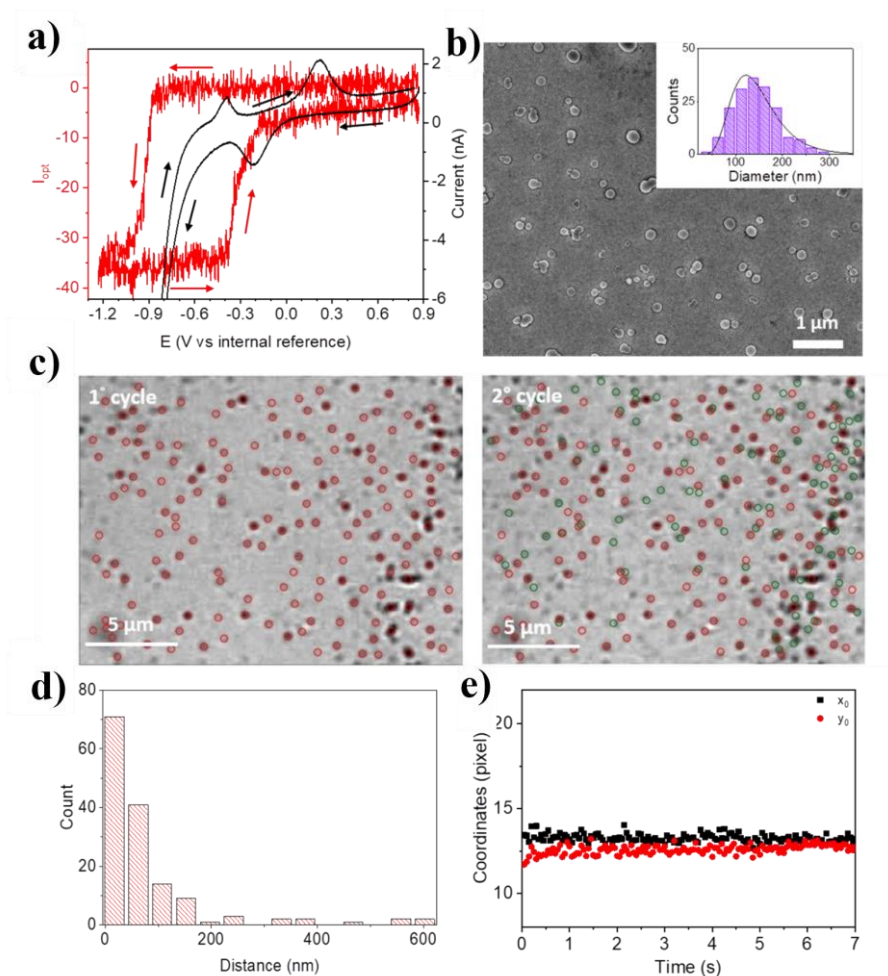


Figure 4. a) Median of the distribution of optical voltammograms, $I_{\text{opt}}-E$ curves, recorded from the patterns corresponding to the reduction of ITO into metal In(0) NPs (red trace) during the cyclic voltammogram recorded in Figure 3A (black trace). b) SEM image of ITO reduced NPs with the corresponding particle size distribution. c) Optical images related to ITO reduced NPs along two consecutive voltammetry cycles; the green spots correspond to ITO reduced NPs appearing only during the second cycle. d) Histogram of the distribution of distances between the NPs patterns along consecutive images. e) Evolution with time of the position of a single ITO reduced NP recorded during the CV experiment.

The dynamics of the NP formation, monitored by IRM, evidences further differences between the NPs and NBs formation. Indeed, as seen in the optical images of Figure 4c, when running successive potential cycles, most NPs appear on reduction scans and disappear on the reverse oxidation scans in exactly the same positions and new NPs (in green) appear on new positions in the second cycle. The reappearance of NP at identical position along successive cycles is quantitatively demonstrated from the same parameter evaluating the distance between NPs along cycles (see Figure 4d). On the contrary to NBs this distribution is narrowed towards zero. On the basis of the observed distribution $> 84\%$ NPs are reallocated on the same positions within < 100 nm error. Additionally, the analysis of the displacement of the NPs center of mass during their growth/dissolution, as exemplified in Figure 4e, confirms that the NPs are rather static all along the process, which is not the case for the NBs (see Figure 3d).

Besides, the optical transients show that a small percentage of the patterns associated to ITO reduced NPs does not re-oxidize (and vanish) during the reverse potential scan. This could be due to the chemical dissolution of some of these NPs, in agreement with previous works.²⁰⁹ In this case, a hole is left in place of the previously formed ITO reduced NP, eventually useful for electrodeposition in such positions. Optically, these holes are detected, as for the H^+ -induced dissolution of ITO, as regions of lower intensity (darker contrast) than the original surface.

4.2.2 Heterogeneity of surface reactivity

As also demonstrated by previous XPS analysis,^{209,221,222} ITO surface consists of a complex non-stoichiometric microstructure: parameters such as local variation of In:Sn ratio, surface and near-surface density defects (*e.g.* oxygen vacancies, substitutional Sn^{4+} or interstitial In) and grain boundaries orientation can influence locally the ITO electrochemical response. In this respect, the onset potential related to the ITO surface reduction can be shifted depending on surface heterogeneities, and is therefore expected to be strongly dependent on the ITO surface conductivity.

Such effect of the ITO conductivity, summarized in Table 1, was first investigated by depositing electrolyte droplets in the SECCM-like configuration over different regions of the same most conductive ITO_h substrate. The opto-electrochemical monitoring of their reduction behavior shows variety in the opto-electrochemical responses. As an example, Figure 5a presents the CV and overlaid opto-voltammogram of one of the most reactive regions

explored. The electrochemical response shows that the ITO reduced NPs formation is associated to a reversible surface process with reduction and oxidation peaks at -0.58 and -0.25 V, respectively. Optical patterns also appear on the IRM images, as those presented in Figure 4c, with onset of appearance and of disappearance in correspondence with the ITO reduction and re-oxidation peaks, respectively. Unlike in Figure 4, the I_{opt} values in Figure 5a exhibit a positive contrast compared to the optical background suggesting that on this explored region, larger NPs are formed.⁴¹ Indeed, the sign of the optical contrast is related to the refractive index and size of the nanoobject and owing to the interferometric nature of the IRM small nanoobjects appear as dark (negative contrast) optical patterns while larger nanoobjects appear as bright patterns (positive contrast).

The heterogeneous electroactivity of ITO substrates was further confirmed by SECM in unbiased feedback mode using FcMeOH as a redox probe and a $\sim 10 \mu\text{m}$ diameter disk Pt ultramicroelectrode (UME). Such experiment actually probes the ability of the ITO surface to drive a reduction reaction (the reduction of the tip-electrogenerated FcMeOH^+) and thus reflects its electroactivity. It is shown in first instance that the ITO activity increases with the macroscopic conductivity of the samples. The $200 \times 200 \mu\text{m}^2$ area SECM image acquired at $\sim 5 \mu\text{m}$ distance from the ITO_h electrode (Figure 5b) shows a contrasted feedback current due to the inhomogeneous regeneration of FcMeOH^+ at the ITO_h surface. In regions 1 and 2 (Figure 5b), these variations were quantitatively analyzed by SECM approach curves (Figure 5c). The latter indicate the coexistence between regions with negative feedback close to or surrounded by areas with positive feedback with adimensional charge transfer, K , extracted from the theoretical fit,²²³ which varies ~ 5 times from one region to another one. These results confirm that ITO may show relatively large regions ($>50 \mu\text{m}$) of contrasted electron transfer rates. Moreover, these heterogeneities can also explain the segregation of the NBs and NPs regions that can be observed in Figure 1.

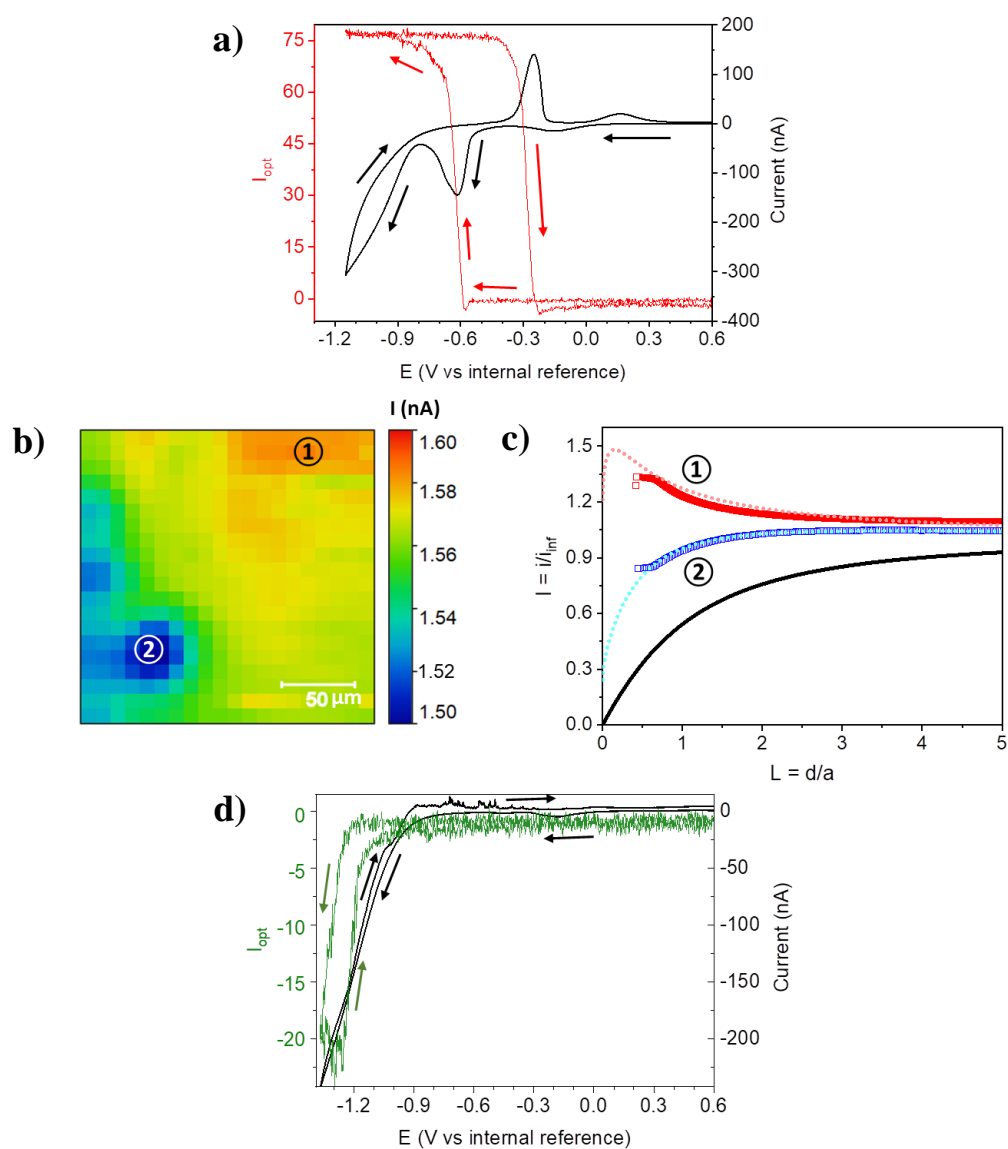


Figure 5. a) Cyclic voltammetry at 50 mV/s in a 5 mM H_2SO_4 confined electrolyte droplet (black trace) with median optical intensity variation related to a population of ITO_h reduced NPs ($N > 100$, red trace). b) SECM image and c) approach curves on the ITO substrate using FcMeOH as redox probe. The image was obtained with a scan rate of 100 mV/s at a $\sim 5 \mu\text{m}$ tip-substrate distance and the approach curves at $1 \mu\text{m/s}$. The best theoretical fits (dot traces) of the approach curves were found using for the dimensionless charge transfer constant: $K=1.4$ ① and $K=0.3$ ②; the black trace is the theoretical curve for the pure negative feedback. d) Cyclic voltammetry (black trace) and corresponding optical voltammetry ($N > 100$, green trace) as in a) performed at a lower conductive ITO substrate, ITO_l .

This effect was further investigated on a less conductive ITO₁ electrode (resistance of 500 Ω). The CV of the 5 mM H₂SO₄ droplet solution on the ITO electrode and the associated median optical transient are provided in Figure 5d. Interestingly, no ITO reduced NPs were detected and the onset potential of NBs formation, ca. -1.25 V, was shifted only 100 mV towards more negative potentials than on the more conductive ITO_h electrode (compare with Figure 3a). Even pushing the reduction scan at -1.7 V vs internal reference did not lead to the appearance of new optical patterns, but it provoked a uniform irreversible degradation of the substrate, recognizable by the decrease in the background intensity. These observations suggest that the formation of NPs is encouraged at higher conductive ITO electrode whereas the onset potential of the HER remains roughly independent of the ITO conductivity.

The dependence of the electron transfer rate on the formation of the NPs can be related to the nature of the ITO. Indeed, Sn in ITO films is commonly present in Sn(II) and Sn(IV) oxidation states whose concentrations rule the film electronic conductivity.²²⁴ The *n*-type electronic conductivity strongly depends on free electrons by the higher valent dopant Sn(IV) centers within the In₃O₂ metal oxide. On the other hand, Sn(II) centers can act as local traps of electronic conductivity, decreasing the electron transfer rate with In(III) centers and with electrolyte. This suggests that regions with locally high surface density of Sn(IV) will be more likely to form metallic In NPs at lower potential and simultaneously to consume H⁺ ions, disfavoring the H₂ NBs formation in regions where In(0) NPs are formed.²¹⁷ Therefore, it suggests that more conductive ITO contains higher concentration of Sn(IV). The competing role in H⁺ consumption between HER and the NPs formation also explains the absence of NPs formation on ITO₁ (Figure 5d) since the H⁺ are most likely entirely involved in the HER reaction, also disfavoring the formation of NPs.

Finally, the quantitative kinetics information obtained by SECM and IRM is collated in Table 1 for the different ITO substrates investigated. If the SECM in the feedback mode provides an estimate of the local electrochemical activity of the ITO and of its local resistance to charge transfer, the IRM imaging during a CV experiment provides, at higher throughput, similar information. Indeed, monitoring the onset of ITO reduced NP formation also likely probes the local resistance to charge transfer and electroactivity of ITO surface. Interestingly the process of NB formation seems quite insensitive to the heterogeneity of electroactivity for such non-catalytic support.

Table 1. Comparison of the optical monitoring of the onset of NBs or In(0) NPs formation with macroscale film resistance and SECM feedback.

Sample	Resistance (Ω)	K^a	$E_{\text{onset NP}} \text{ (V)}^b$	$E_{\text{onset,NB}} \text{ (V)}^b$
ITO _h	40	1.4 / 0.3 ^c	-0.6 / -0.8	-1.2
ITO _m	150	0.1	-1.05	-1.2
ITO _l	500	0.02	n.a. ^d	-1.2

^a Dimensionless finite kinetics rate from SECM with FcMeOH; ^b Optically inferred onset potentials (vs internal reference); measurements correspond to the median of >100 optical transients, the standard deviation estimated from the interquartile onset potentials distributions and internal reference potential fluctuation is $\pm 50\text{mV}$; ^c Extreme values evaluated on the same sample from SECM feedback and optical detection of In(0) NP; ^d No NP formed.

4.3 The complexity of Ni electrodeposition

Reprinted with permission from *Angew. Chemie - Int. Ed.* **2021**, 60 (31), 16980–16983

Typically, the electrodeposition of Ni-based materials yields a variety of electrochemical responses, depending on the electrolyte composition (pH, buffer strength,...) and electrode (nature and preparation). Owing to its competition with water reduction, the signature of Ni²⁺ reduction may be absent from the electrochemical curve.^{225–229} Such competition produces either Ni or Ni-hydroxides, and the diversity of electrochemical responses makes the composition and electroactivity of the deposited material quite challenging to anticipate.²²⁹

Herein, the cathodic nucleation and growth of individual Ni-based NPs on ITO substrate, used as optical sensor and electrode, has been scrutinized by interference reflection microscopy, IRM.

Multiple areas of ITO surface has been screened by confining a droplet of 1 to 5 mM NiCl₂ + 0.1 M KCl electrolyte on the ITO with the tip end of a micropipette, and imaging this

microelectrochemical cell during linear sweep voltammetry (LSV), in reflection mode, by IRM. The experiment is depicted in Figure 6.

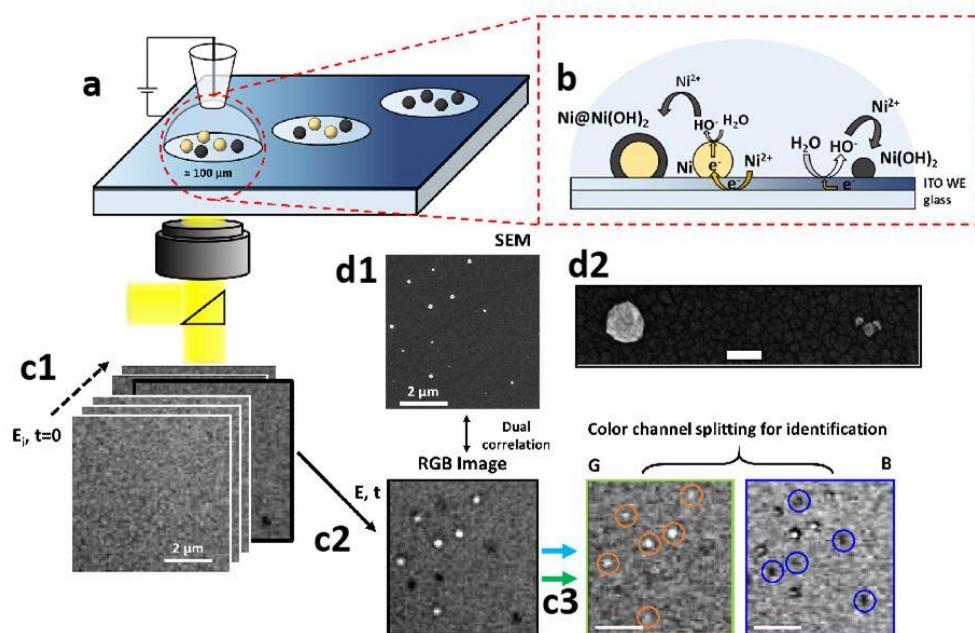


Figure 6. Experimental set-up (a) used for probing the variability in Ni electrodeposition mechanisms (b) by *operando* optical microscopy (c1) and identical location *ex situ* SEM (d1). Schematic description of the differentiation of NP populations by splitting the color channels (c3) of each raw RGB image (c2).

Owing to their contrasted refractive index, the presumed Ni and Ni(OH)₂ NPs should be distinguished by the IRM image analysis depicted in Fig. 6c1-c3. Briefly, each recorded RGB image of the ITO is split along its three color channels, respectively red, R, green, G, and blue, B (Fig. 6c3). The less sensitive G channel detects the most scattering NPs as bright-contrasted features. Then, this population is subtracted from the more sensitive B image, revealing a new population of NPs detected as dark-contrasted features.

Figures 7a and b show the two representative LSVs obtained for the reduction of a 1 mM Ni²⁺ microdroplet, along with the ensemble-averaged I_{opt} variations for the two populations of optical features detected on the ITO surface. At first sight, these experiments differ, respectively, from the presence or absence of a sharp reduction peak at -1.45 V, and the formation of either the two populations of bright- and dark-contrasted features or of only one population of dark-contrasted features.

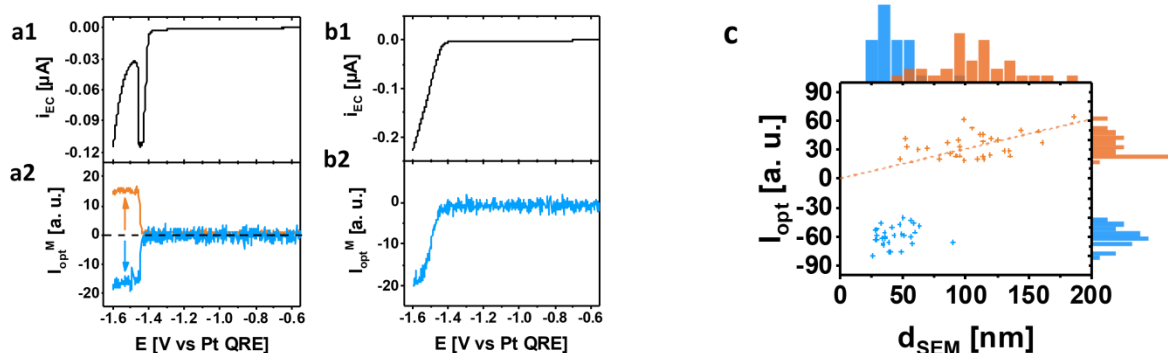


Figure 7. Representative examples of (a1, b1) LSVs of 1 mM NiCl₂ + 0.1 M KCl (scan rate: 50 mV/s) and (a2, b2) ensemble-averaged optical transients of the two different NP populations (orange: bright-contrasted NPs, N = 170 in (a2); light blue: dark-contrasted NPs, N = 31 in (a2) and 430 in (b2)). c) Identical location IRM-SEM: I_{opt}^M , defined in (a2), vs size plots for bright-contrasted (a) and dark-contrasted NPs (b). Dashed line provides a linear regression ($I_{opt}^M = \alpha d_{SEM}$) for the bright-contrasted NPs.

More specifically, the sharp reduction peak in the LSV of Fig. 7a1 ($\approx 70\%$ incidence from 20 LSVs) corresponds, according to Ritzert and Moffat,^{226,227} to the deposition of a Ni film and concomitant water reduction. The latter results in the growth, by precipitation, of a Ni(OH)₂ layer, which is allowed as it is a better catalyst than bare Ni^{230,231} for water reduction, until it completely blocks further charge transfer. The sharp current decay accounts for such self-terminating deposition.^{227,232}

If the electrodeposition of a Ni film was indeed confirmed when the reduction of Ni²⁺ was conducted in a pH ≈ 6 phosphate buffer, in the absence of pH buffer, the optical images of the ITO surface, Fig. 6c2, suggests the formation of NPs. The I_{opt} transient in Fig. 7a2 shows the ensemble-averaged response extracted from these images for each NP population. Both bright- and dark-contrasted NPs appear and evolve, until an optimum value of I_{opt}^M is reached, in a very narrow potential range correlated with the sharp Ni²⁺ reduction peak. The I_{opt} transients of both NP populations suggest a fast terminated growth, supporting the self-terminated growth mechanism and its attribution to the electrochemical peak.

Identical-location SEM imaging of the ITO electrode was performed at the end of the LSV (Fig. 6d1). Unfortunately, the dimmer bright-contrasted NPs and many more dark-contrasted one were lost or moved during the surface rinsing process. The bright-contrasted NPs are almost spherical (Fig. 6d2) with a 110 ± 50 nm size distribution (Fig. 7c). Their size roughly

increases with the final value of their optical intensity, I_{opt}^M ($r^2 = 0.88$), providing a ≈ 20 nm l.o.d. From their regular spherical shape, these bright-contrasted NPs should be mostly composed of metallic Ni.

The few dark-contrasted NPs that could be co-localized by SEM have a more fractal shape (Fig. 6d2, right side) and are also smaller (diameter of 40 ± 15 nm) than their bright-contrasted counterparts. Their morphology resembles that of $\text{Ni}(\text{OH})_2$ NPs obtained by cathodic electrosynthesis.²³³ Moreover, similar fractal NPs were preferentially produced, and detected as the unique population of dark-contrasted NPs, in the experiments showing LSVs resembling Fig. 7b1. The absence of the Ni^{2+} reduction signature and the concomitant appearance of NPs with the water reduction wave, suggest that they could only result from the precipitation of $\text{Ni}(\text{OH})_2$. Despite the lack of size- I_{opt}^M correlation (Fig 7c), the IRM l.o.d. for $\text{Ni}(\text{OH})_2$ NPs is again ≈ 25 nm.

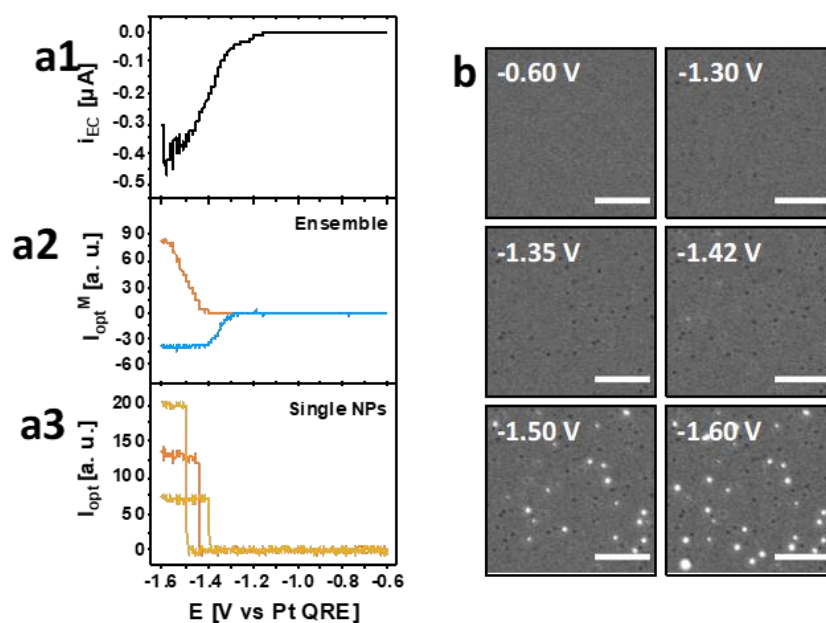


Figure 8. (a1) LSV at 50mV/s of 5 mM NiCl_2 + 0.1 M KCl, (a2) ensemble-averaged optical intensity of both NPs populations (orange: bright-contrasted NPs, $N = 354$; blue: dark-contrasted NPs, $N = 427$), and (a3) single NP optical transients of the median, first quartile and third quartile representative NPs. (b) Optical images recorded at different times during the LSV (scale bars: 5 μm).

When the Ni^{2+} concentration was increased to 5 mM, the same variability in electrochemical responses was observed, showing either the self-terminating Ni^{2+} reduction peak, or only water reduction. An example of the latter case is presented in Fig. 8a. The optical images (Fig 8b) show the appearance of dark-contrasted $\text{Ni}(\text{OH})_2$ NPs shortly after the onset of water

reduction, like in Fig. 7b. However, bright-contrasted Ni NPs also appear at more negative potentials.

Unlike in Fig. 7, it seems that even if water reduction was easier than Ni^{2+} reduction on this particular area, metallic Ni NPs were still able to nucleate without showing the Ni^{2+} reduction signature. This agrees with Penner *et al.*²²⁵ who demonstrated, by *ex situ* SEM, the indirect electrodeposition of pure Ni NPs on carbon electrodes even though water reduction was predominant. The same indirect Ni NP growth is demonstrated here *in situ* by a complementary optical monitoring. It further allows discussing the change from direct to indirect Ni NP growth. This is first evidenced from the difference in the ensemble-averaged I_{opt} transients (Fig 7a2 vs Fig 8a2): the fast limited growth at 1 mM becomes more gradual at 5 mM. Interestingly, at the single NP level, the I_{opt} transients (Fig 8a3) still present a sharp rise of intensity, suggesting the self-terminating growth of individual NPs is still operative. As pointed out for galvanic replacement at single Ag NP,^{234,235} the individual behavior is totally obscured in the ensemble response which then reflects the difference in the onset of appearance (nucleation) of each NP.

The latter is evaluated from the onset potential of individual NPs presented along with their $I_{\text{opt}}^{\text{M}}$ value, i.e. equivalently their final size, in Fig. 9 for both Ni^{2+} concentrations.

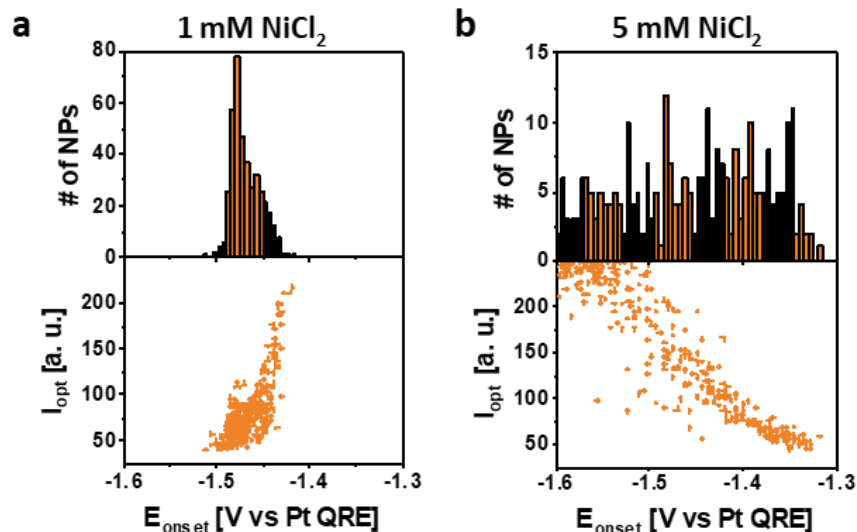


Figure 9. Onset potential distribution of Ni NPs and corresponding maximum optical intensity for 1 mM (a, $N = 170$) and 5 mM Ni^{2+} (b, $N = 334$).

For 1 mM NiCl_2 (Fig. 9a) the onset potential distribution presents a narrow peak, mimicking the sharp self-terminating Ni^{2+} reduction peak in the LSV (Fig. 7a1). The sudden drop in nucleation events highlights the increased predominance of water reduction at potentials

below -1.5 V. Moreover, the final NP size decreases as its onset potential becomes more negative: the earlier a NP nucleates, the larger it will be at the end of the LSV, as time and reduction goes on. This situation is generally encountered in progressive electrochemical nucleation processes, e.g. NPs electrodeposition⁴¹ or gas NBs generation, as shown in Chapter 3. The same behavior is detected for the duration of the sharp Ni²⁺ reduction peak. It suggests that the self-limited growth is related to a pH increase over the ensemble of the NPs. Overall, water reduction limits the Ni²⁺ reduction not only by limiting the growth of already nucleated Ni NPs, but also by limiting the formation of new nuclei on the ITO substrate.

For 5 mM NiCl₂ (Fig. 9b), on the contrary, the nucleation frequency of new NPs is rather constant over the explored potential range. As mentioned above, the growth of individuals is still self-terminating (Fig. 8a3), the sum of all the sharp (<0.3 s) individual events at a constant frequency of nucleation event rationalizes the observed ensemble-averaged optical response of Fig 8a2. Meanwhile, the final size of the NPs increases as their onset potential becomes more negative. This seemingly counter-intuitive behavior shows the influence of the electrode potential on the competition between water and Ni²⁺ reduction processes. If the initial formation of Ni(OH)₂ NPs suggests water reduction dominates, the competition turns in favor of Ni²⁺ reduction at more negative potentials, the growth rate of Ni NPs increasing with overpotential. Moreover, during the first 100 mV of the overall indirect deposition (Fig. 9b), NPs with a rather narrow size distribution (I_{opt}^M) are produced, at least much narrower than for their direct deposition (Fig. 9a), in agreement with Penner et al.²²⁵

4.4 Conclusions

This chapter demonstrates how IRM coupled to electrochemistry helps elucidating complex competitive mechanisms associated to surface heterogeneities and/or during electrodeposition of NPs in acidic and neutral conditions.

ITO stability in acidic media was monitored optically as preliminary step. It evidences a degradation of the ITO at approx. 16 nm/min in 1 M H₂SO₄ and only low concentration of acid (5 mM H₂SO₄) must be used to ensure the ITO is stable long enough.

The optical measurements performed at highly conductive ITO, while sweeping the potential toward negative values, evidence the formation of two distinct ensembles of features corresponding to the formation of two types of nanoobjects. These two populations are ascribed to the formation of H₂ NBs and of ITO reduced NPs issued respectively from HER

and the ITO electroreduction. A detailed analysis of their optical response allowed discriminating them based on their optical characteristics. The formation of H₂ NBs occurs at more negative potential in random positions with a <2% probability to nucleate at the same site between consecutive potential cycles. Moreover, the positions of the center of mass of the NBs may vary during the dynamics of their growth and dissolution, attesting of an asymmetric growth process. Besides, the reduced ITO NPs appear at less negative potential and their formation is confirmed by *ex situ* SEM analysis. On the contrary to NBs, >99 % NPs reappear on the same position during successive potential cycles and the center of mass displacement analysis evidences that the NPs are static all along the growth/dissolution process.

Finally, the reduction behavior of ITO electrodes strongly depends on the ITO electron transfer rate, which may vary within a same substrate. This is demonstrated by changing the position of the droplet on a same ITO substrate or by changing the resistance of the ITO coating. The electrochemical behavior as well as the optical responses changed accordingly with the sample resistance, showing a shift in the onset potential of the formation of NPs toward less negative potentials whereas the onset potential of the HER remains mainly the same. The presence of conductive heterogeneities of a size > 50 μm is further evidenced by SECM in unbiased feedback mode and explains the segregation between the NBs and the NPs formation generally observed. Ultimately, the optical imaging of the dynamics of the local formation of either reduced ITO NPs or NBs can be used as a means to rationalize local ITO electron transfer rate and to predict the presence of competitive phenomena spatially dependent to heterogeneities for more complex systems.

This has been illustrated in the case of the reduction of Ni²⁺ solutions, which yields metallic Ni and/or Ni(OH)₂ NPs. Both NPs are identified based on *in situ* optical differentiation with sub-25 nm sensitivity. The preferential direct formation of both materials is usually rationalized based on the identification of the Ni²⁺ reduction or water reduction signature in the electrochemical trace. Optical microscopy shows that this is generally more complex. In particular, metallic Ni can still nucleate and grow, indirectly, below the water reduction wave, even though the Ni²⁺ reduction signature is invisible. These direct and indirect mechanisms were then deciphered *in situ* by the unique differentiating potential of optical microscopy. The importance of investigating them at the single entity level rather than from ensemble measurements is particularly highlighted. Indeed, this single-entity study shows that for both mechanisms, Ni NPs experienced a fast self-terminating growth, which can yet result in a gradual growth from an ensemble point of view. This is due to the difference in nucleation

dynamics which is related to the competition between Ni^{2+} and water reduction. Overall, this understanding allows probing, and in turn controlling *in situ*, the size and surface density of Ni NPs. The methodology can be extended to the electrodeposition of the many NPs whose electrochemical signature lacks reproducibility or is difficult to identify, as presented in the next chapter.

Chapter 5

Watching the electrochemistry within sub-micrometric electrolyte droplets

Reproduced from Faraday Discussion 2022 (<https://doi.org/10.1039/D1FD00063B>) with permission from the Royal Society of Chemistry.

The results in this chapter come from collaboration with the group of electrochemistry and interfaces led by Patrick R. Unwin at Warwick University, UK, according to the PhD exchange European program, Marie Skłodowska Curie International Training Network, SENTINEL. The goal of the exchange between Warwick University and our group was to transfer the knowledge of our group in optical microscopy monitoring of electrochemical processes while the knowledge on scanning electrochemical cell microscopy was transferred from Warwick to Paris. The experiments summarized in this chapter are the results of this collaboration. Owing to the pandemic, I was not able to visit Warwick but I could implement SECCM in Paris. Meanwhile the PhD student in Warwick, Dimitrios Valavanis, has implemented an optical microscope in their SECCM set-up. He performed the experiments discussed in this chapter. I've discussed with him the experiments and I have fully performed the image processing and data analysis.

This chapter will reply the following questions: in SECCM the imaging resolution is provided by the size of the nanodroplet of electrolyte spreading on a surface. But what really happens inside this meniscus? Is this electrochemical process homogeneous over the wetted electrode surface? Can we use optical microscopy to image these phenomena and reach a sub-meniscus resolution? With what sensitivity and what complementary information could it provide?

5.1 Introduction

One way to enhance signals and selectivity in single entity electrochemistry experiments is to work in confined nano-environments. It consists in using nanopores, nanodroplets or

nanochannels as reactors where a very small amount of nano-objects (< 10) is confined. This allows bypassing drawbacks in temporally resolved single entity electrochemistry, such as the necessity to work with ultra-diluted solutions, and to limit the cross-talk effects between different NPs or nucleation sites. The reactor volume is the fundamental parameter in determining transport phenomena and the number of entities reacting simultaneously. The latter can be exploited to extract different information: while a nanoreactor containing only one single NP can be used to probe the relation between its structure and its activity for a specific reaction without cross-talk contributions, a confined area containing 10 nucleation sites can be used to compute the overlap between each diffusion layer and how ionic gradients can affect nucleations/reactions over time. Nanodroplets from SECCM setup constituted of a pipet filled with electrolyte are the most versatile systems to generate reproducible nanoreactor. Tuning pipette opening size ranging from micrometres to nanometres in diameter is nowadays easy, and can be used to confine a sub-micrometric region of electrode surface within the droplet from its meniscus. Moreover, pipettes have been successfully used to manipulate, count and size individual NPs confined within the pipette opening, and characterise them electrochemically.^{171,236,237} Modern instrumentation allows to customize routines to scan in sequence multiple electrode regions. This enables the use of pipette generated droplets 1) for the controlled delivery and deposition of various types of nanocolloids and NPs onto specific locations of electrodes with optimal electrical contact,^{42,238–246} 2) for revealing heterogeneous properties of many features of materials including 2D materials,^{171,247–250} nanotubes,^{251,252} grain boundaries and crystallographic facets in electrodes and electrocatalysts^{253–255} and single NPs.^{256–260} Surface sensitive optical microscopy coupled with this setup allows adding further, fundamental information for all these systems. First it would allow discussing the droplet stability or deformation over time or during an electrochemical actuation. Then it would allow seeing within the droplet and then visualizing dynamic electrochemical, or from competitive processes discussed in Chapter 5, chemical phenomena within the droplet. In this chapter, two systems have been investigated: the Ag electrodeposition within droplets $< 1 \mu\text{m}$ of diameters and the crystallization of CaCO_3 driven by electrochemical swing in pH equilibria.

The study of Ag NP electrodeposition is a proof of concept showcasing the potentiality of the SECCM to electrodeposit NPs one by one (one per droplet) and therefore to print arrays of NPs on electrode surfaces. To explore this possibility, a complementary visualisation method is required, capable of resolving individual NPs immobilised on the surface. Optical microscopy is ideal for observing *operando* events and details within an electrochemical cell.

Coupling optical techniques to pipette electrochemistry^{3,4,42,261} have notably revealed size, composition, structure or surface effects on the activity or motion of individual NPs. Herein, IRM is used to synchronously observe single events, occurring inside the SECCM droplet cell, during the electrodeposition step of Ag NPs onto an ITO electrode.

5.2 Sub-droplet resolution to watch Ag electrodeposition

The first system investigated is Ag electrodeposition in sub-micrometric droplets. A pipette is filled with an electrolytic solution containing 5 mM AgNO₃ in 0.1 M KNO₃ and a Ag/ QRCE is loaded from the back-end. The pipette (SECCM tip) is approached to the ITO-coated glass substrate, which is connected at the WE. A 0.2 V bias is applied between the WE and the QRCE, such as no Ag⁺ reduction (Ag electrodeposition) would occur upon landing (meniscus contact) at the WE. Landing is detected by a charging spike in the current trace and the approach is halted. At this point, a short 0.3 s rest period at the same approach potential allows the meniscus to stabilize on the surface and for a series of optical images to be recorded, which will be used as a control for the image analysis routines. The WE is then polarized at -0.8 V for 0.7 s to drive the reduction of Ag⁺ ions. The switch to the reducing potential is marked as time 0 s throughout this study. The whole procedure has been repeated at 8-20 different location with a “writing speed” in the order of one deposition site per 4s, as depicted in Figure 1a. The electrodeposition of Ag at the WE surface, defined by the SECCM meniscus, results in a current transient, as portrayed in Figure 1b. At the end of the deposition period, the WE is polarized back to 0.2 V while the pipette is retracted from the surface. Although previous studies of nucleation/growth of NPs with optical microscopy monitoring could optically isolate a single event, the electrochemical information (current) associated to such event was recorded for the entire electrode, averaged over the ensemble of NPs, as seen in Chapter 4.^{41,86,120} In contrast, with SECCM-IRM, the current is confined to the small SECCM meniscus, allowing the synchronous electrochemical monitoring and optical imaging of a single event.⁵⁶

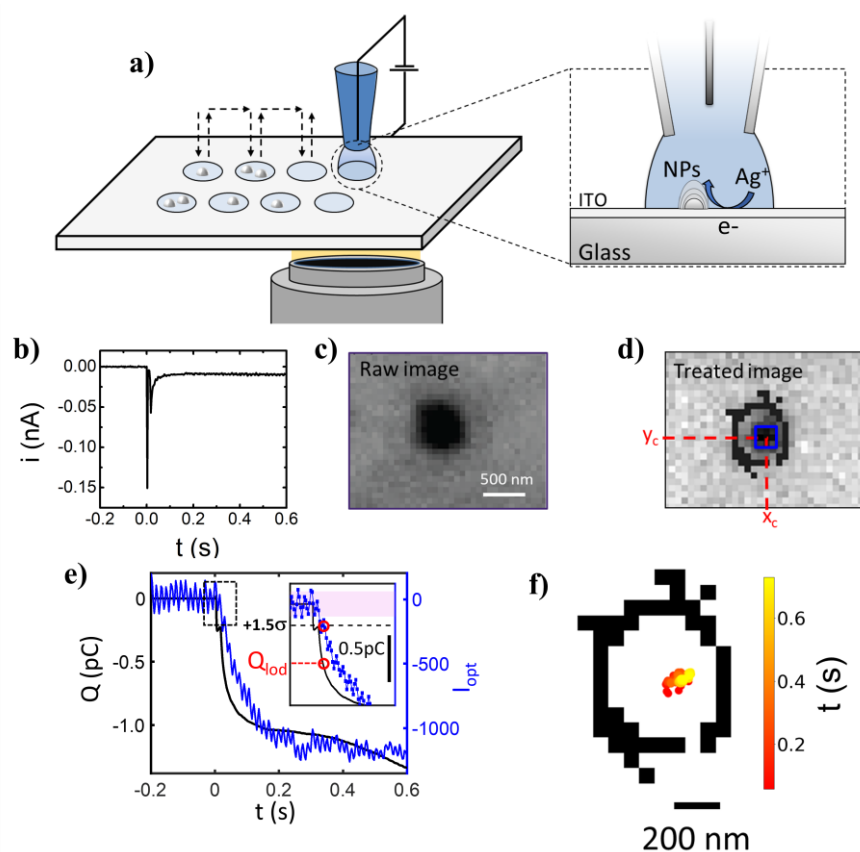


Figure 1. Experimental set-up a) used for electrodeposition in individual nanoelectrochemical cells a single Ag NP synchronously monitored *operando* by reflection-based optical microscopy. b) Current time trace recorded during Ag electrodeposition. c) Image of the ITO coated glass coverslip upper interface showing the footprint (dark region) of the nanoelectrochemical cell wetting the ITO. d) After image treatment, diffraction limited dark-contrasted optical feature is revealed within the edges of nanodroplet. e) Electrochemical charge and optical intensity traces comparison, enabling LOD to be estimated (inset). The pale red rectangle in the inlet corresponds to the standard deviation of the optical signal. f) Displacement of the optical feature centroid during its growth; the feature integrated intensity is evaluated over the blue square and its centroid super-localized.

To limit the deposit to a single or few NPs per landing site, the SECCM wetted area should be selected according to the density of nucleation sites. For Ag NP electrodeposition on ITO surface, although dependent on the electrodeposition overpotential, the NP density σ_{NP} is reported in the 10^8 to $5 \cdot 10^9$ NPs per cm^2 range.^{262,263} Hence, a single NP would be nucleating over a 160 to 1100 nm diameter disc electrode, well within the range of pipette fabrication

possibilities. Importantly, these dimensions are also compatible with the imaging resolution of optical microscopes. Using a high numerical aperture objective, such as a 63× magnification oil immersion objective, with a NA=1.4, it is theoretically possible to resolve objects separated by $\lambda/(2NA)=168$ nm for a $\lambda=470$ nm wavelength illumination. Optical microscopy can then image the presence of an individual NP within an individual nanodroplet. This is accomplished with IRM by acquiring images of the upper interface of the glass coated ITO substrate, while operating the inverted microscope in reflection mode. Temporal resolution is achieved by recording those images at a rate of up to 330 frames per seconds (3 ms resolution), Figure 1c shows a typical IRM image of the SECCM meniscus, recorded at the end of the electrodeposition procedure. The meniscus is detected optically in the raw image as a region of intensity darker than the surrounding background. This is related to the difference in refractive index between the electrolyte ($n\approx 1.33$) and the air ($n=1$), making, from Fresnel formalism of the reflection at optical interfaces, the wetted region of ITO less reflective than the ITO/air interface. Observation of the landing spot by itself is useful in understanding the dynamics of the meniscus in contact with the surface.

Image processing algorithms are used to visualize, *operando*, the Ag electrodeposition processes over time, with sub-droplet resolution.^{42,56} After background subtraction (using the initial control images), time domain intensity averaging, and droplet edge identification, the treated image in Figure 1d reveals the presence of a dark contrasted feature, optically resolved within a ca. 650 nm diameter droplet. This suggests that the electrodeposition produced a single Ag NP rather than a homogeneous metal coating over the landing area. Moreover, several descriptors of the produced NP and its evolution over time can be derived. On each image of the time series, the optical feature is super-localized: its centroid coordinates (x,y) are obtained, with ~ 10 nm precision, from a 2d Gaussian fit of the image intensity values. The lateral motion of the feature's centroid can be tracked and, in this event, the single NP remains motionless, with < 100 nm movement in the centroid position across the deposition period. The movement is represented in Figure 1F, where the NP centroid position in the meniscus over time is plotted. The lack of measurable NP movement could suggest a strong NP-electrode interaction. It is worth noting that centroid motion can be a proxy for NP motion, but does not actually measure it as for diffracted-limited objects, such as small NPs, the optical spots size doesn't reflect its real size. Also, changes in centroid position could, for instance, be an indicative of asymmetric NP growth mechanisms and not motion itself.

Integration over a 4x4 pixel region of interest (ROI) centred at the NP centroid (Figure 1D) provides the feature's optical intensity trace, I_{opt} . Figure 1e shows I_{opt} overlaid with the

evolution of the electrochemical charge trace, Q , calculated from Figure 1d by integration. Before the potential step, I_{opt} is stable, within the noise level. With the potential switching to -0.8 V, the dark contrasted feature appears and progressively darkens (decrease in I_{opt}). The optical intensity is usually a descriptor of the locally deposited mass (or a power law of the mass, depending on the optical microscopy used³). Its evolution, in Figure 1e, indeed tracks that of Q . From the final accumulated charge $Q_f = 1.45$ pC, the final diameter (d_{NP}) of the NP can be estimated from:

$$d_{\text{NP}} = 2 \left(\frac{3Q_f V_{\text{m,Ag}}}{2\pi FN} \right)^{\frac{1}{3}} \quad (1)$$

assuming N hemispherical NPs are deposited and using $V_{\text{m,Ag}} = 10.27$ cm³ mol⁻¹ the molar volume of Ag, and F the Faraday constant. From equation (1), for $N=1$ NP detected, the final NP diameter is estimated to be 83 nm.

As both charge and optical read-out are synchronized, the optical movie provides a real time and *in situ* monitoring of the NP evolution. We can estimate an optical limit of detection from the accumulated charge at the point where the optical intensity is different from the background value. This is depicted in the insert of Figure 1E. It corresponds to an accumulated charge of ~0.6 pC or equivalently, from equation (1), an NP diameter of 63 nm.

The experiment was performed in an array of $n=7$ different deposition locations. The SECCM meniscus formation was rather reproducible across the array, with an average footprint area, estimated from the IRM images, of 0.39 ± 0.06 μm² while the average electrodeposition charge was $Q_f = 2 \pm 0.6$ pC. Even within these nanometric droplets, it was possible to resolve between $N=0, 1$ or 2 NPs. Concerning this size of active electrode area, the σ_{NP} (in the case of detection of at least $N=1$) is estimated at 4.1 ± 1.0 NPs per μm²; and their average diameter estimated at $d_{\text{NP}} = 82 \pm 5$ nm.

5.2.1 Multi NPs deposition monitoring

Electrodeposition experiment, with the same experimental parameters but performed using a SECCM tip with a larger opening resulted in a wetted area of ca. 1.1 μm in diameter – approximately double the previous size. While Figure 2A corresponds to the treated optical image recorded at the end of the electrodeposition step for one of the 12 landing sites in this experimental array. Four different NPs are clearly resolved in this image and marked in the figure. The distribution of the number of NPs optically resolved at a landing site for this 12 spots array is provided in Figure 2B. An average of 5 NPs is detected per landing site, giving

an average σ_{NP} of 5 ± 1 NPs per μm^2 . The average NP diameter, estimated from the final charge for each electrodeposition spot and using equation (1), with N derived from the number of optical features, is 95 ± 10 nm. Both of these values agree with those obtained with the smaller pipette.

SEM images, recorded *post mortem*, of electrodeposition events using an even larger SECCM tip, resulting in a droplet of ca. $4 \mu\text{m}^2$, were compared with their corresponding IRM images as depicted in Figure 3. A larger droplet was used to ensure a correct identification of the NPs constellation and therefore the accuracy of the multi-microscopy cross-correlation.⁴² Both IRM and SEM images give a $\sigma_{\text{NP}} \sim 6$ NPs per μm^2 in good agreement with the values observed in smaller droplets. This average NP density suggests that the growth of a single Ag NP can be confined, on average, into a single nanodroplet if its footprint diameter is approximately 400 nm. This average NP density value was further used to calculate from (2) a theoretical Poisson distribution $P(N)$ representing the probability of finding $N=0,1, 2\dots$ Ag NPs into a droplet of surface area A_d .²⁶⁴

$$P(N) = \frac{(A_d \sigma_{\text{NP}})^N e^{-A_d \sigma_{\text{NP}}}}{N!} \quad (2)$$

The calculated Poisson distribution is superimposed in Figure 2b (shaded red bars) on the experimental histograms obtained for the 0.65 and 1.1 μm diameter droplets. For both cases, the number of NPs detected per droplet experimentally matches nicely the calculated distribution. This analysis supports that the highest probability (36.7% chance) of growing a single NP is found within a 450 nm diameter droplet, close to the droplet size we studied.

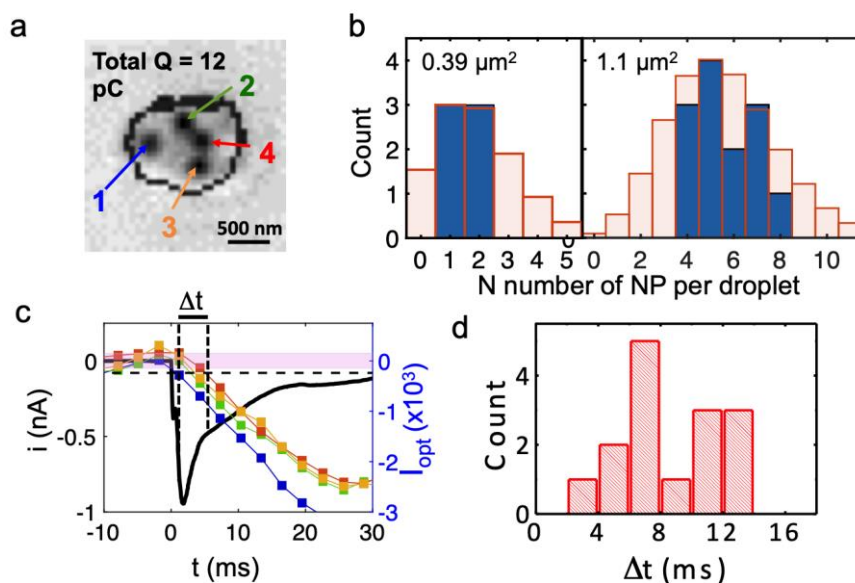


Figure 2. a) Treated optical image of a larger droplet cell (diameter of $1.1 \mu\text{m}$) showing 4 NPs at the end of the Ag electrodeposition. b) Calculated Poisson probability to find N NPs in a droplet of size 0.4 or $1.1 \mu\text{m}^2$ (light red bars, left and right panel, respectively) together with the number of NPs experimentally counted (blue bars). c) Comparison of the total electrochemical current and the optical intensity traces for the four NPs that grow inside the droplet cell. The pale pink rectangle and the dotted lines correspond to 1 and 1.5 times the standard deviation of the optical signal, respectively, the latter being used to evaluate the detection delay Δt . d) Distribution of detection delays between first and last NPs detected in different droplet cells

The use of the $1.1 \mu\text{m}$ droplets (and growth of multiple NPs per droplet) provides further insights into the electrodeposition process. The optical intensity traces of each NP in Figure 2a follow a similar pattern of I_{opt} decreasing with time, and tracking the electrochemical charge. It suggests that the four NPs have a very similar growth dynamics and grows to a similar final size. This is consistent with earlier electrodeposition of Ag NPs within nanoelectrochemical cells onto highly oriented pyrolytic graphite²³⁸ which pointed out the NPs nucleation was instantaneous, within less than a ms, and their growth limited by the mass transport of Ag^+ ions from the pipette to the droplet. This mass transfer regime is most likely explaining the electrochemical current trace of Figures 1d and 2c. It further highlights that for

such fast nucleation/growth processes, the electrochemical current trace is not sufficient by itself to investigate individual NP growth dynamics.

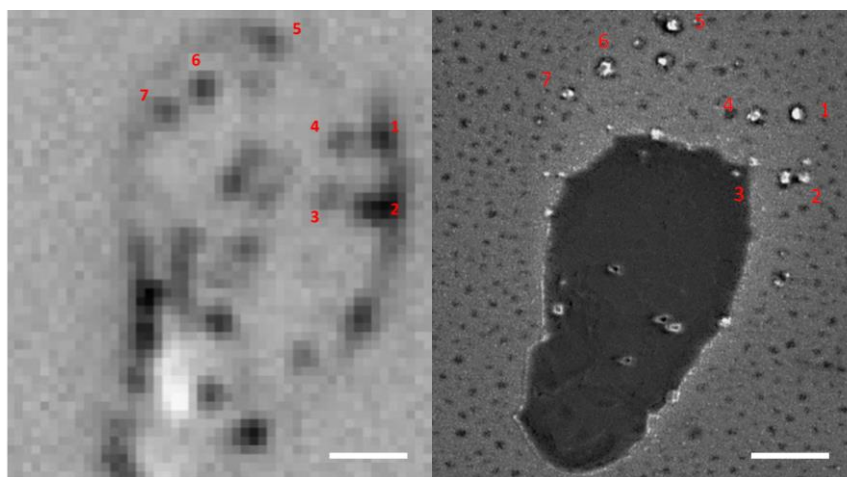


Figure 3. Comparison between *post mortem* images acquired by IRM (left) and SEM (right) for a $4 \mu\text{m}^2$ (scalebar: $1 \mu\text{m}$).

The synchronous optical monitoring of NP growth can elucidate early-stage evolution (Figure 2c). The onset of detection for each NP could be evaluated from their individual optical trace, using the same criterion that was used to evaluate the limit of optical detection in Figure 1E. The four NPs in Figure 2c are then detected sequentially within $\Delta t \approx 5$ ms. The distribution of NP detection onset delay, evaluated for all the experiments, is given in Figure 2d, and ranges from 3 to 13 ms. The difference in NP onset time could be related to an induction period, reflecting the formation of measurable NPs by aggregation of smaller, undetectable ones.²³⁸ This could not be discerned from the electrochemical current traces and the two approaches – electrochemical and optical – provide complementary information. If the electrochemistry points out to an instantaneous formation of multiple Ag nuclei on the electrode surface, and an aggregated NP growth, the optical monitoring is then revealing the dynamics of surface diffusion (with characteristic time in the 5-10 ms range). The above are in agreement with the revisited nucleation-aggregation mechanisms of electrodeposition.^{220,240} Similar conclusions and the characteristic nuclei motion dynamics were also previously captured in atomic-level detail by co-located high resolution transmission electron microscopy imaging.²⁶⁵

5.2.2 Centroid motion during NPs growth

Even if optical microscopy cannot reach such atomic resolution, it provides further insight into the growth regime, when focusing on the optical feature centroid position over time for individual NPs. As depicted in Figure 4a for a 1.1 μm diameter droplet containing 4 NPs, the centre of mass corresponding to topmost and leftmost NPs are clearly moving radially outwards, while the other 2 are apparently drifting around the same position. The range of NP displacement across all experiments, including all SECCM tip sizes, is depicted by the distribution in Figure 4b. The maximum displacement seen was about 210 nm. Most of the displacement seen is smaller than the NP dimension, and earlier single NP optical motion studies^{26,27,47,102,266} suggest that this centroid motion is most likely not associated to physical motion of the NP; but rather to an asymmetric growth of the NP.

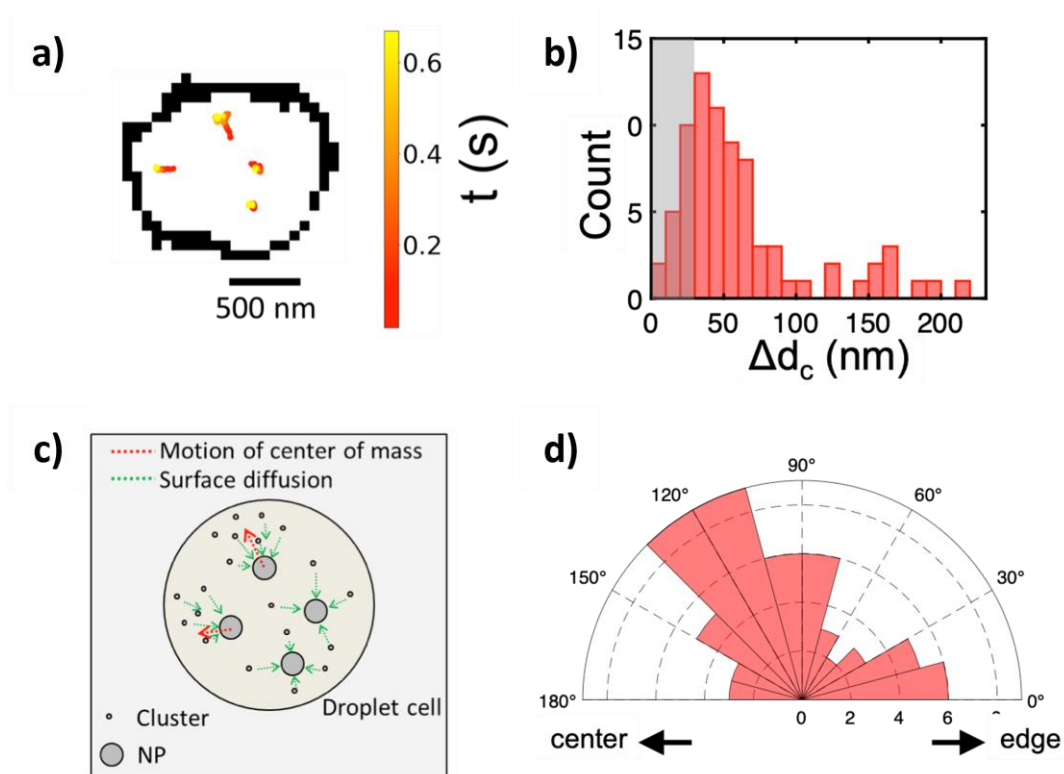


Figure 4. a) Displacement of the optical features centroid during the NPs growth for the droplet of Figure 2A. b) Distribution of NP displacement length Δd_c for all the experiments ($n=17$) monitored optically; the grey area ($\Delta d_c < 30$ nm) corresponds to immobile optical features. c) Scheme depicting the aggregative (asymmetric vs symmetric) growth mechanism that induces the motion of the optical features centroid. d) Polar distribution of angles reflecting the motion direction from the center of the droplet for the same experiments depicted in b).

As the growth of the NP is limited by mass transport of Ag^+ ions from the pipette to the SECCM meniscus, asymmetric growth of single individual NPs is very unlikely. However, the centroid motion observed agrees with the aggregative growth mechanisms, and the NP centroid motion would reveal the asymmetric surface transport of the Ag nuclei forming a larger NP. Proposed cases of nuclei surface diffusion and NP asymmetric growth by aggregation are drawn in Figure 4c. Outwards radial growth for NPs close to the meniscus perimeter, as observed in Figure 4a, is reasoned to result from a local slower mass transport rate (local confinement) at the SECCM meniscus edge, with further NP growth at these locations driven by aggregation, rather than also electrodeposition.

The direction of the asymmetric growth of the NP (centroid displacement) is evaluated from a growth angle (see Chapter 3). An angle of 0° indicates a displacement towards the edge of the droplet, while an angle of 180° , a displacement towards the centre respectively. The polar histogram of the NP growth angle, given in Figure 4d for all experiments, shows that most NP growth happens biased towards the centre of the droplet, which is the region with the faster mass transport rate. A portion of the NPs' growth direction happens towards the SECCM meniscus edge, which we attribute to those particles already at the outskirts of the droplet.

5.3 Monitoring early stage nucleation for non-metallic CaCO_3 crystals

This second study concerns the optical microscopy monitoring of droplet confined electrocrystallization of non-electroactive materials, i.e. particles of CaCO_3 . These crystals can be precipitated from the electrogeneration of alkali by cathodic polarization of an electrode. As the material formed is non-electroactive, the yield of the precipitation reaction and the amount of material formed is difficult to apprehend from the sole electrochemical current. To apprehend the extent of this reaction, it is imperative having a complementary *in situ* monitoring of the reaction. Optical microscopy (IRM) is again used to image the formed crystals at meniscus surfaces of different sizes and therefore to understand the crystallization process. Again showcased in the case of a model crystal such as CaCO_3 , the strategy should extend to other molecules of pharmaceutical interests.

5.3.1 Experimental approach

To probe CaCO_3 electrochemically driven crystallization, the pipette has been loaded with electrolyte solution (50 mM KNO_3 , for the study of ITO; and 5 mM CaCl_2 and 5mM NaHCO_3 (pH 2.7 HCl) for the crystallisation experiments). The SECCM QRCE potential was controlled during the experiments, while the ITO substrate (WE) was held at a virtual ground. The resulting current was measured at the WE with a custom-built current follower. For ease of interpretation, all potentials reported are for the WE electrode, which is the negative value of the SECCM QRCE potential. Final tip approach was performed by applying a small bias between the QRCE and WE (+0.2 V for ITO studies and - 0.1 V for the crystallisation experiments). The probe movement stopped automatically as soon as the current was above a threshold, set at the noise level (ranging between 100 fA and 30 pA, depending on the sensitivity of the current follower that was appropriate for each probe size).

Once the meniscus had landed on the WE (no contact from the pipette itself), a short pause allowed monitoring of the meniscus stability and provided a background for later image treatment (*vide infra*). The potential was then swept or stepped to drive ORR (and water reduction) at the WE, with synchronous IRM visualization of the meniscus footprint region. Once the potential sweep or step was finished, the potential was switched back to the approach value. The probe was then retracted, to detach the meniscus from the surface, and the WE shifted laterally and the approach recommenced. In this way, the experiment could be repeated on a fresh ITO region, allowing replicates of the experiment. IRM images were acquired synchronously throughout the entire experiment.

5.3.2 Real time imaging of pipette meniscus

The use of IRM opens up the possibility of real-time, *in situ*, tracking of the SECCM meniscus, allowing monitoring of its size and shape during experiments and the (electro)chemical phenomena occurring within. This opens the possibility of important phenomena such as the wetted area dependence on potential (electrowetting) to be studied. Although the wetted area may have little impact on the SECCM currents for steady-state transport-limited measurements,²⁶⁷ it is of great importance for new applications where current density is essential, such as in energy storage/conversion materials.²⁶⁸

Previously, the meniscus contact area and size has been deduced or inferred from a variety of means, including: (i) scanning sharp electroactive features on surfaces, such as individual single walled nanotubes, the border between an electrode and insulator, or step edges, and tracking the resulting current-lateral distance profiles with nm-resolution;^{171,251,269–271} (ii) measuring droplet footprints or line tracks left on a surface, with SEM or AFM, after SECCM scanning under certain conditions;^{171,268,272} (iii) AFM analysis of surface patterns after SECCM molecular-grafting, polymerization or adsorption;^{273–277} (iv) AFM analysis of SECCM etch features;^{278,279} (v) in-situ visualization of the meniscus and nanopipette with laser scanning fluorescence microscopy;²⁶⁷ (vi) analysis of dual-channel ion conductance tip approach curves.^{171,267,280} Nonetheless, as we show herein, IRM provides unprecedented views of the SECCM meniscus dynamics under operation.

To demonstrate IRM SECCM-meniscus imaging in real-time, we repeatedly approached a 50 mM KNO₃-loaded 200 nm diameter nanopipette to an ITO substrate and recorded cyclic voltammograms between +0.2 V and -1.6 V at 1.7 V s⁻¹ while IRM images were synchronously recorded at a rate of 325 frame per second (FPS). This procedure was repeated at 17 different locations over the ITO substrate. Figure 5A shows IRM images of the meniscus (dark contrasted area), which has a diameter of ca. 400 nm, at selected potentials. The voltammograms (Figure 5B) show no faradaic contribution before solvent breakdown at the extreme cathodic potential. The evolution of the dimension of the meniscus footprint was monitored during each voltammogram. The area of the meniscus was evaluated either from the surface area (in pixels) of the dark region in the center of the images, or from the super-localization of its edges along two orthogonal directions.

The meniscus was rather reproducible among the 17 different experiments with an overall ± 5 % variation in area, measured during the short pause after meniscus landing. Figure 5C gives the evolution of the ensemble-averaged surface area of 17 menisci during the potential cycle. The meniscus was rather stable during the forward potential scan from 0 V to -1.47 V, but its surface area increased when faradaic current flowed, in the solvent breakdown region. On the reverse scan, the meniscus did not retract to its original dimension. Note that the sudden increase in the meniscus size to a stable value at the start of the scan is associated with meniscus landing that we will analyze in detail elsewhere.

The inset of Figure 5C shows the evolution (in a narrower potential region from -1 V to -1.6 V) of the width of an individual meniscus estimated from the FWHM of the intensity profile. If the surface area provides an estimate with a quantum pixel resolution, the edge localization procedure allows sub-pixel resolution, here the individual meniscus diameter increases by

0.31 pixel, 20 nm, above the usual 5 nm resolution of the procedure.^{118,281} The observed electrowetting is not attributed to double layer charging effects since it rather occurs in the solvent electrochemical decomposition. However, the observed phenomena are in general agreement with the Young-Lippmann equation.

$$\cos \theta(V) = \cos \theta_0 + \frac{C}{2\gamma} V^2 \quad (3)$$

where θ is the contact angle depending on the applied potential (V), θ_0 is the contact angle at the point of zero charge, C is the capacitance per unit area and γ is the liquid|gas interfacial tension. The equation predicts a decrease of the droplet contact angle (and therefore increase in its footprint) with applied voltage.^{282–284}

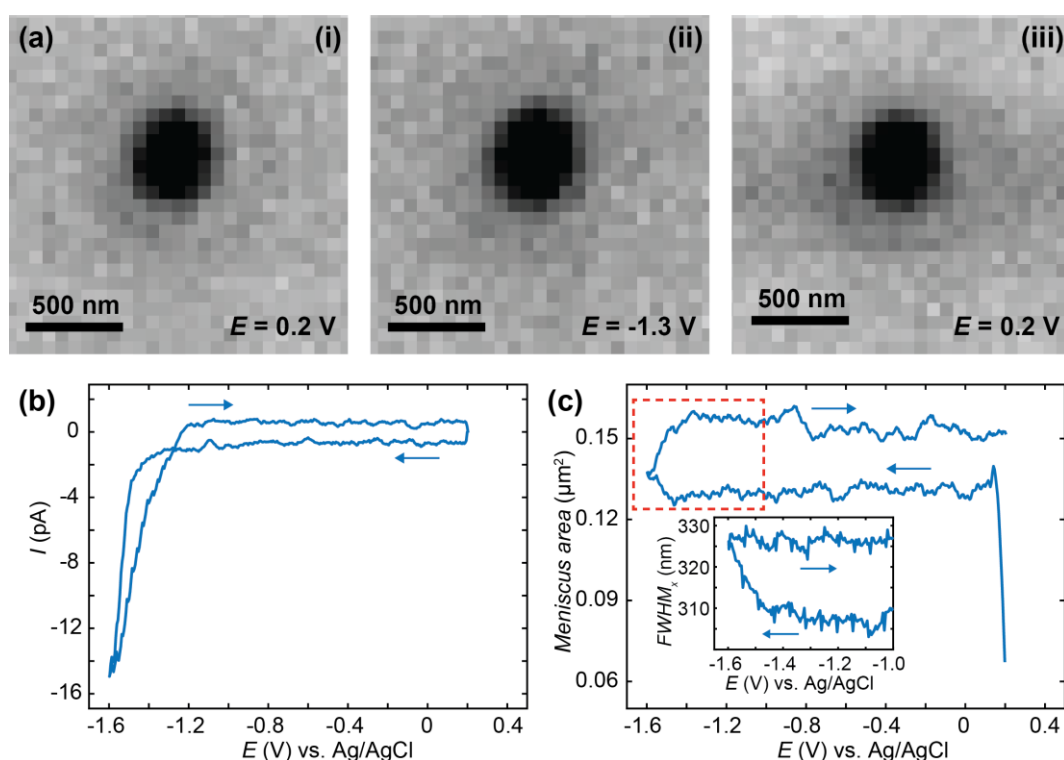


Figure 5. a) IRM images of an SECCM meniscus (200 nm diameter tip) at selected potentials during cyclic voltammetry (scan rate 1.7 V s^{-1}) at ITO with 50 mM KNO_3 solution. b) Representative cyclic voltammogram recorded at one of the 17 spots of the experiment array. c) Mean SECCM meniscus area (averaged over the 17 spots) as a function of the electrode potential as calculated from the corresponding IRM images. Inset in c) shows the evolution of the FWHM of the meniscus, in the selected potential window, evaluated from its edge-tracking along the horizontal axis, during the cyclic voltammogram corresponding to b). Arrows denotes potential scan direction. IRM imaging recorded at 325 FPS (ca. 5 mV potential resolution). Light source: mercury metal halide white light, filtered around the wavelength of 480 nm.

5.3.3 Droplet size effect in nucleation and growth

The faradaic current flowing at the most cathodic potentials can be attributed to solvent breakdown, and there may also be the reduction of ITO producing surface confined In NPs. This process has been evidenced by *ex situ* SEM images of the electroreduced NPs for a variety of electrolyte composition and pH.²⁰⁹ The dynamics of the NP formation and its competition with H₂ nanobubble electrogeneration during the hydrogen evolution reaction (HER) was reported in Chapter 5.

Thus, in principle, the confined region on the ITO WE accessed by SECCM facilitates the study of a *single* NP formation and growth event. Following the Poisson statistics discussed for Ag NP electrodeposition, within a meniscus of diameter, $d < 500$ nm, such as the one monitored in Figure 6a, the probability of finding one nucleation site is below 1 for an average nucleation site density lower than $4/\pi d^2 = 5 \times 10^8$ cm⁻².

5.3.3.1 Control experiment to evaluate ITO stability range

A treated version of the IRM snapshots at 0.2, -1.3 and -1.5 V for the forward scan and 0.2 V for the reverse scan can be seen in Figure 6a, with an indicative delimitation of the meniscus border (red dashed circle). These images can be compared to the raw images for 0.2, -1.3 (forward) and 0.2 V (reverse) in Figure 5a. The image is featureless during the forward scan until the potential reaches -1.5 V, or until a significant cathodic current is flowing (as in Figure 5b). Once cathodic current flows, an optical feature is clearly visible inside the meniscus perimeter, which was not visible in the untreated data (Figure 6a), and this feature remains during the whole reverse scan (at 0.2 V in Figure 6a). By inspecting the intensity (Figure 6b) of the region of interest (ROI) within the meniscus (red dashed circle in Figure 6b) throughout the entire image series, a decrease in the intensity was initiated at -1.5 V and is maintained over the cycle. Assigning $t = 0$ to the onset of the potential cycle, the intensity of the ROI is also plotted vs. time in Figure 6c. These data show that the intensity decreases over time after the feature appears on the image, indicating that the feature is growing in size with time, alongside the electrode plane.⁴⁷ Furthermore, by integrating the current over the cyclic voltammogram, one obtains the charge flowing through the ITO. The variation of the ROI intensity profile is remarkably similar to the morphology of the charge-time transient in Figure 6c.

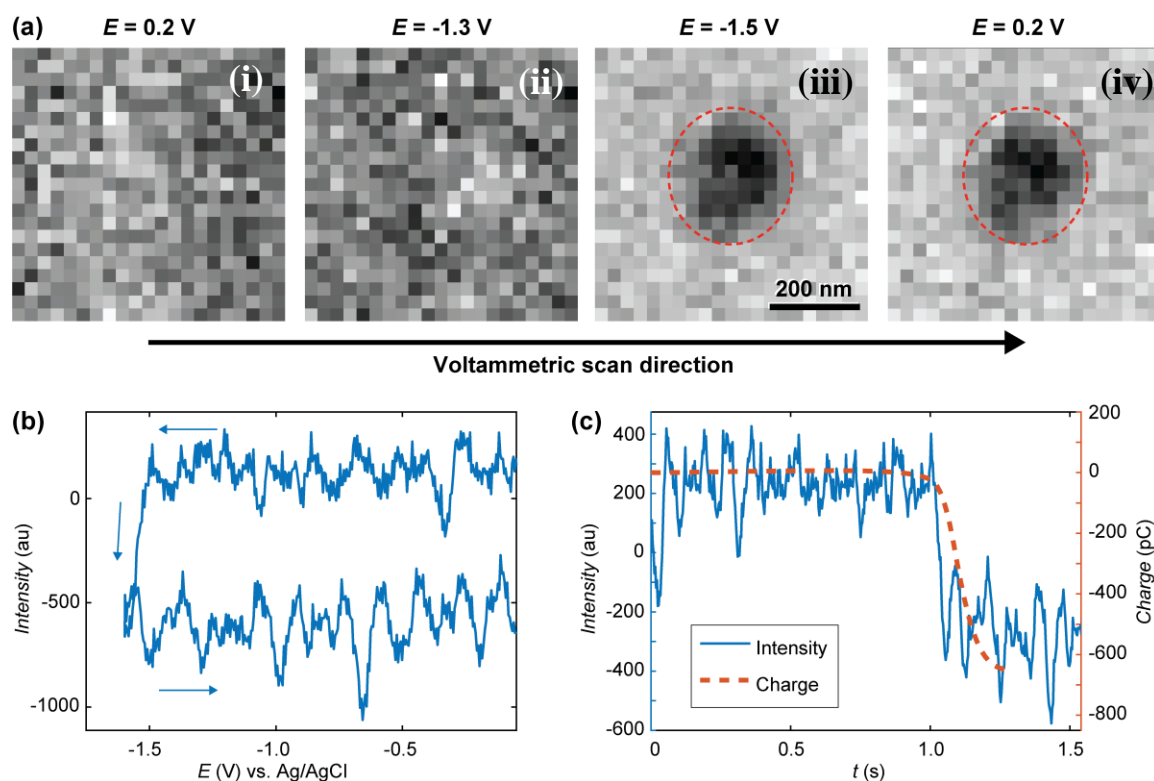


Figure 6. a) Treated IRM images recorded during the cyclic voltammetry in Figure 2a, showing the presence of a feature inside the SECCM meniscus after -1.5 V was reached on the forward scan b) Opto-voltammogram showing the intensity in the corresponding ROI (red circle in part a) over the applied potential range. c) Charge transient (calculated from integrating the current in Figure 5a) compared to the optical intensity transient ($t = 0$ at the onset of the cyclic voltammetry).

The feature may have two possible chemical origins. It could be related to HER and NB formation or the reduction of ITO into In NP. The formation of a NB at such a small volume would likely block the pipette opening which would be detected by a sudden drop in electrochemical current.¹⁸¹ Also, once HER had stopped (in the reverse scan) the nanobubble would dissolve back into solution quickly, which would be discerned by the IRM intensity.^{172,285} The current magnitude increases along the forward potential cycle and a crossing of the forward trace is detected on the reverse. Such crossing is often observed during the electrodeposition of metals and is usually attributed to the formation of a material with increased electroactive area (and electroactivity). From the electrowetting analysis, in Figure 4c, one could evaluate the variation in current density during voltammetry, knowing the dynamic meniscus surface area, obtained from Figure 5c. When this is done, the same voltammetric shape presenting the crossing branches is observed, indicating that the crossing

is not related to the change in meniscus surface area. It is then due to the formation of a material with higher electrochemical activity than the ITO, as would most likely be the metal In formed during ITO reduction. The ability to visualize, track and record the current flow for a single sub-diffraction limited event corresponding to ITO reduction into In NP with high temporal resolution of better than 5 ms, confirms the capabilities of SECCM-IRM for single entity opto-electrochemical dynamic measurements.

Moreover, from observations of both the meniscus surface area and surface degradation, we conclude that ITO is optically stable for IRM during electrochemical experiments ($E > -1.5$ V in KNO_3 at neutral pH), enabling us to monitor the electrodeposition of various nanomaterials in a rather large potential window. However, any interference or influence from possible ITO instability has to be considered for each particular set of conditions, as illustrated in the next section.

5.3.3.2 Controlled CaCO_3 crystallization in a microscale meniscus

We now turn to the electrochemically-induced deposition of insulating materials on ITO. For this we take CaCO_3 as our model system and use the slightly larger volumes provided by the meniscus of a few μm (1 - 8 μm) diameter SECCM probe. The use of a larger meniscus allows us to probe dynamics within a population of nano-entities within the electrolyte.

CaCO_3 is found throughout the natural world where it exists in a variety of structural forms (polymorphs) and morphologies. Many biological systems utilize CaCO_3 in their structural, defensive and optical structures, and have the ability to control and even switch between different polymorphs.²⁸⁶ The product of crystallisation is also heavily dependent on the reaction volume, with small (micron-size) volumes stabilizing early-stage, less stable forms (e.g. amorphous calcium carbonate, ACC).²⁸⁷ The early stages of CaCO_3 precipitation remain hotly debated,^{288–290} although it is known to proceed via rapid formation of ACC at moderate supersaturations.

To control the precipitation of CaCO_3 we modify the *local* supersaturation, S :

$$S = \sqrt{\frac{a_{\text{Ca}^{2+}} a_{\text{CO}_3^{2-}}}{K_{\text{SP}}}} \quad (4)$$

where a_i is the activity of species i , and K_{SP} is the solubility product of calcite, by changing the pH.^{291–293} Starting with an acidified (ca pH 2.7, therefore undersaturated, Figure 6a)

mixture of CaCl_2 and NaHCO_3 , a cathodic current at the ITO consumes H^+ and produces OH^- by reduction of O_2 (ORR), increasing the pH, converting HCO_3^- to CO_3^{2-} and causing the initially undersaturated solution to become supersaturated (Figure 7B), although far from stoichiometrically (i.e. $[\text{Ca}^{2+}] \gg [\text{CO}_3^{2-}]$). At this low starting pH most of the solution carbonate is in the form of CO_2 (Figure 7A) and the solution buffer capacity and pH is expected to drift over time towards less acidic (due to CO_2 loss to the atmosphere). Polarizing the ITO at different potentials allows us to tune the rate at which the supersaturation is changed and therefore to probe the heterogeneous nucleation/precipitation mechanism *in situ*. The Chapter 4 has demonstrated that different electrochemical activity emerges from different compositional surface heterogeneities on ITO and that SECCM-IRM coupling allows simultaneous events to be detected at the nanoscale within the meniscus. Here, for example, the formation of crystals at certain locations on ITO may serve as a useful marker of local electrochemical activity.

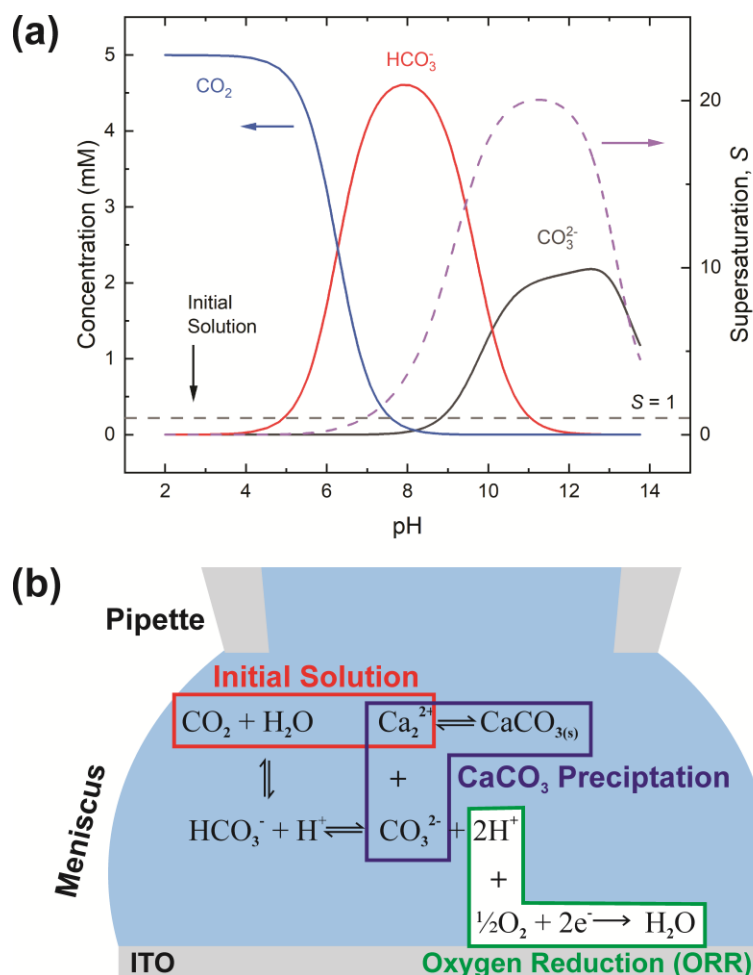


Figure 7. The principle of electrochemically-induced CaCO_3 precipitation. a) Speciation diagram (left axis) and supersaturation (right axis) for the $\text{CaCO}_3(\text{aq})$ system as a function of pH. Only principal species are shown, with the remaining mass balance made up of ion pairs (not shown). b) Equilibria relating O_2 reduction with CaCO_3 precipitation.

Electrochemically-induced CaCO_3 precipitation was investigated across a series of applied potentials at the ITO electrode starting from the same initial solution. In each case a small potential (-0.1 V) was used to approach the SECCM probe to the surface. This potential was held for 2 s to allow the SECCM meniscus to stabilize before being switched to the potential of interest for 10 s, and then back to -0.1 V while the probe retracted, ensuring a constant reaction time in each case. To maintain the pipette solution conditions over the course of several depositions, on alternate approaches of the probe to the surface, the potential was not switched, so as to allow the solution to re-equilibrate and any precipitate within the tip to be removed by deposition via meniscus contact with the ITO surface. This procedure was

repeated by means of successive approaches at different location of the ITO surface to form an array of points, typically with 5-8 repeats at each potential.

Whole, ca. 8 μm wide, meniscus IRM images, after 10 s of polarization at three different potentials, are shown in Figure 8, along with the current-time ($I-t$) traces recorded (Figure 8a). The dark contrasted area delineates the meniscus region. At less negative potential (Figure 8bi), the current was negligible and only a few bright spots are observed by IRM. At -0.7 V (Figure 8bii), however, a more significant current was recorded, and multiple spots, now dark, are observed in the images. This trend continues at -0.8 V (Figure 8biii), but at -0.85 V (not shown), although the current magnitude was still increasing, no clear spots inside the meniscus were seen. Feature detection was hampered by a general darkening of the spot area at this potential and below. The $I-t$ traces in all cases where $E < -0.5$ V shows non-monotonic behavior. An initial spike to negative currents is followed by a rapid decay, and the onset of a sustained increase towards more negative currents. This is unexpected for an ORR pulse at ITO and could suggest that either the crystallization events or a separate process at the ITO, possibly the formation of In NPs, are increasing the surface activity.

The size of the optical features seen in the IRM images can be estimated by their FWHM intensity, which is calculated by fitting a Gaussian function to the intensity profiles. The smallest FWHM associated with the dark features in Figure 7bii and 7biii are 185 ± 25 nm (from 30 spots – with an example shown in Figure 8bii). Optical features characterized by this low limit value of FWHM can be considered as diffraction-limited, suggesting that nanometric particles (< 200 nm) have been generated. The bright features observed at -0.5 V (Figure 8) increase in intensity with time, in contrast to a decrease observed for the lower potentials. Such behavior is attributed to the difference in size of the particles formed, as was demonstrated in Chapter 3 for gas NBs: bubbles larger than ca. 300 nm appeared brighter than the background, those smaller appeared darker. Despite a difference in the shape and refractive index of the CaCO_3 deposits, we might expect a similar behavior. Indeed, the bright features also show two-fold larger FWHM (365 nm – see example in Figure 8bi), indicating a particle > 300 nm in size at $E = -0.5$ V, while the FWHM remains diffraction-limited during the whole course of experiments at the other potentials.

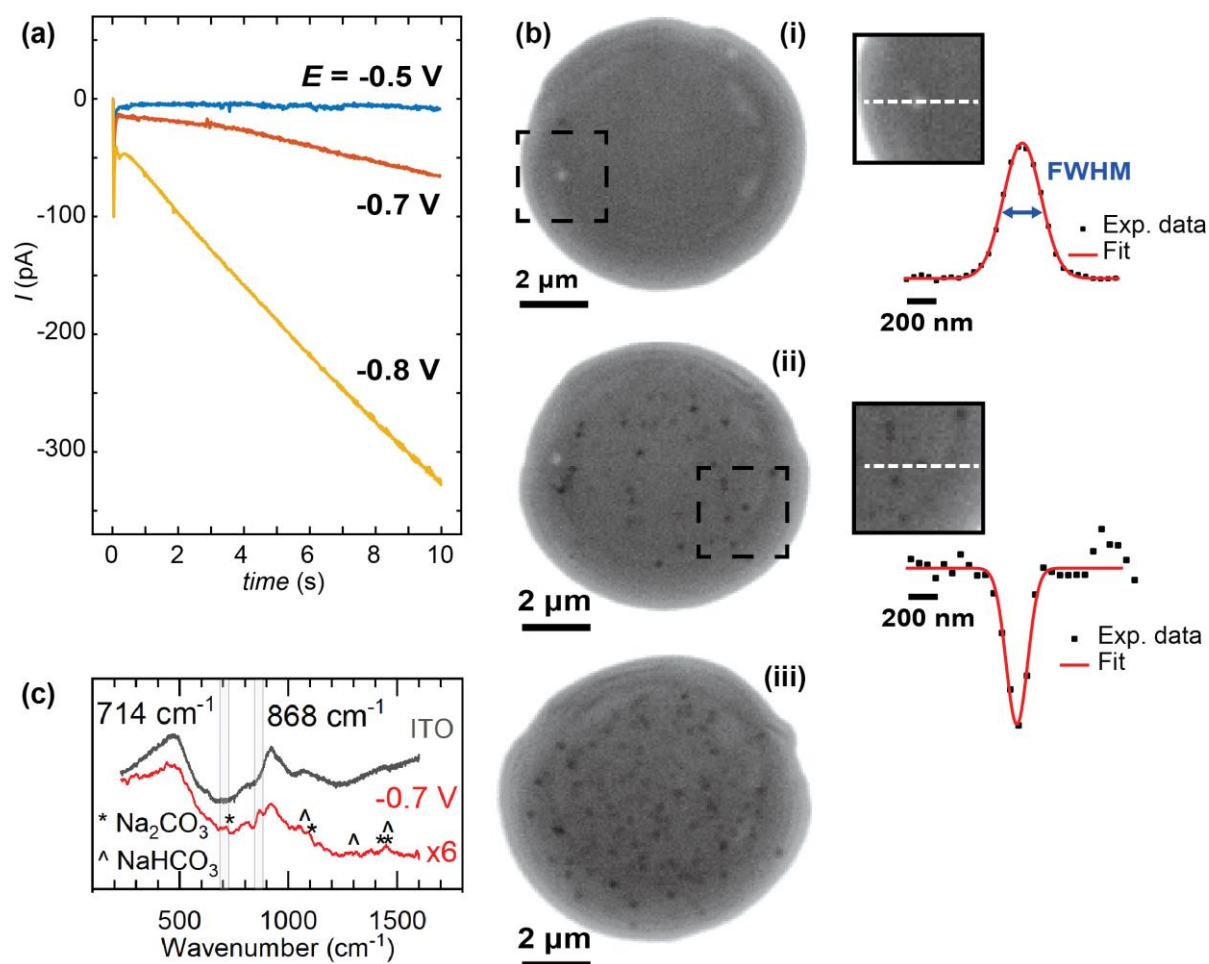


Figure 8. a) SECCM current and b) IRM images for the electrochemically-induced precipitation of CaCO_3 at different applied potentials with a ca. $8 \mu\text{m}$ diameter SECCM meniscus. Applied potentials, E , (i) -0.5 V , (ii) -0.7 V and (iii) -0.8 V . Insets of bi and bii show optical intensity line profiles of typical bright and dark features respectively, along with the corresponding Gaussian fits. IRM images recorded at 50 FPS and shown at the end of the potential pulse (10 s). Light source: blue LED (wavelength of 470 nm). c) Raman spectrum from a dried meniscus deposited at -0.7 V (with the spectrum from bare ITO subtracted). The bare ITO spectrum is also shown.

For $E < -0.85 \text{ V}$, in addition to the formation of NPs, a homogeneous decrease of the optical intensity was observed over the entire meniscus area (no change detected for the outer ITO/air interface region). This can be explained if a homogeneous decrease of the reflective properties of the ITO/electrolyte interface is considered, and most likely results from the deposition of a homogeneous layer of CaCO_3 , or a highly dense array of nanoobjects separated by $< 500 \text{ nm}$ such that they cannot be resolved by the optical visualization, onto the ITO surface. These large negative driving potentials will lead to more rapid formation of the supersaturation

condition,²⁹² and faster nucleation generally results in more nuclei and hence particles. Dense layers of ACC are also known to form at interfaces at appropriately high supersaturations.²⁹⁴ At such negative potentials and low pH, the reductive degradation of ITO may also occur. The formation of CaCO₃ crystals is supported by ITO background-subtracted Raman microspectroscopy of a dried meniscus deposited at -0.7 V, which reveals spectra with peaks consistent with the presence of CaCO₃ particles (Figure 8c). A broad peak at 868 cm⁻¹ is consistent with either the ν_3 mode of amorphous CaCO₃ (863 cm⁻¹) or calcite (873 cm⁻¹), while a small feature at 714 cm⁻¹ is also consistent with calcite.²⁹⁵

5.3.3.3 CaCO₃ crystallization at large meniscus

Using pipette probes of tens of μm in diameter allows investigation of even larger areas and the production of a population of hundreds or thousands of electrochemically-induced crystallization events. At this length scale surface heterogeneities, concentration gradients over the meniscus volume and localized fluxes may contribute to the SECCM-IRM observations. Figure 9 shows example IRM images taken after 8 s for two different applied potentials at the ITO electrode.

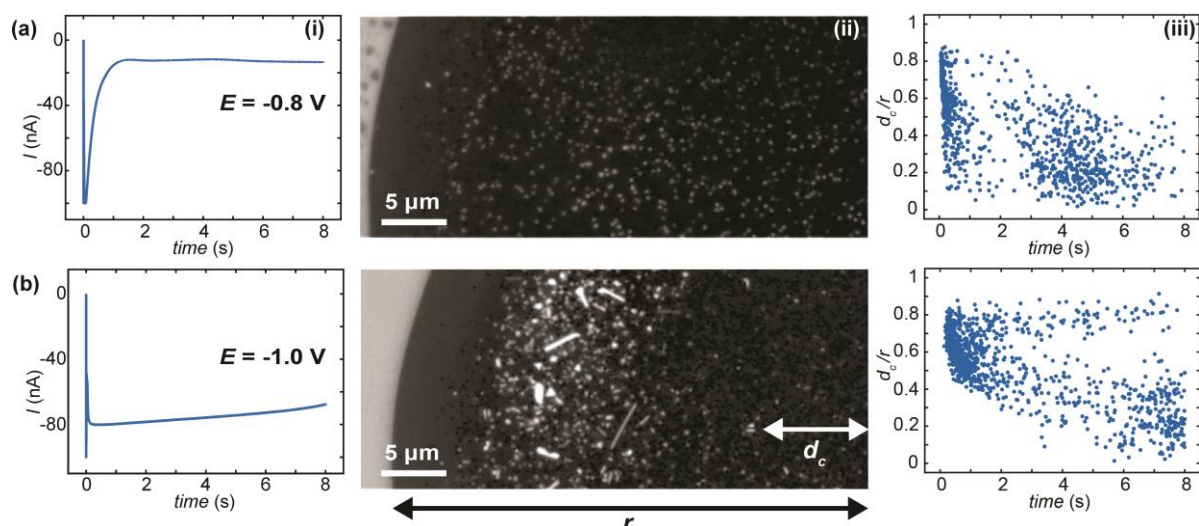


Figure 9. (i) SECCM current-time traces, (ii) IRM images and (iii) normalized radial position of new emerging optical features for the electrochemically-induced precipitation of CaCO₃ at different applied potentials, within a ca. 75 μm wide meniscus. Applied potentials, E , a) -0.8 V and b) -1.0 V. IRM recordings captured a rectangular section of the meniscus (half of that shown here) at 200 FPS. Light source: blue LED (wavelength of 470 nm).

When the applied potential is -0.8 V (Figure 9a_{ii}), a number of features, are observed. Most features show bright contrast and we observe a few aggregates, where neighboring features coalesce. Experiments at -1.0 V (Figure 9b) show no homogeneous drop in optical intensity over the meniscus: a much large amount of nanometric features are observed at the beginning of the potential pulse (Figure 9b_{iii}) which quickly grow to form a variety of μm -sized crystals with different size and shape, formed from the aggregation of nanometric deposits. For both -0.8 V (Figure 9a_{ii}) and -1.0 V (Figure 9b_{ii}) dark contrasted features are also detected. This behavior is similar to that in the small meniscus and, as suggested by the background experiments and cyclic voltammograms in acidic media (*vide infra*), the features could be associated with indium oxide reduction into metallic indium.

Further spatiotemporal analysis of the crystallization events show that the position of emerging new optical features in the meniscus, plotted as the radial position (d_c) divided by the meniscus radius (r), as a function of time, has a non-stochastic trend with the onset time of crystallization for -0.8 V (Figure 9a_{iii}) and -1.0 V (Figure 9b_{iii}). In the first 0.5 s after the potential was applied, a large percentage of the events initiate in a circular crown between $0.4 < d_c/r < 0.9$ for $E = -0.8$ V and between $0.5 < d_c/r < 0.8$ for $E = -1.0$ V. Other crystals start to be formed in areas closer to the meniscus center only at longer times.

When the experiment was repeated without CaCl_2 present in the solution (Figure 10a) a few spots were observed in the IRM images for $E \leq -1.0$ V. For more negative potential, and for the considered acidic pH, it is known that ITO is unstable (with respect to reduction of In to metallic NPs), which has been observed, along with H_2 NBs, by IRM previously. The features observed here (Figure 10a) are different in shape and appear in much small numbers than those observed when Ca^{2+} is present. To assess the effect of possible ITO degradation to the overall intensity change seen in IRM, cyclic voltammetry in acid media (HCl solution, pH 2.7) was carried out for aerated and deaerated (with nitrogen) solutions and over 2 different potential windows. Figure 10b shows the voltammograms recorded from 0.8 to -0.8 V. From this experiment it is clear the SECCM current is predominantly carried by ORR as a clear cathodic wave at around -0.4 V, present in aerated solution, is absent when the solution is deaerated. No other voltammetric feature alludes to ITO degradation, although the relatively large capacitive current might obscure some features. In contrast, for a larger potential window (Figure 10c), from 1.2 V to -1.2 V, a clear anodic peak at around -0.55 V is observed in the reverse scan, for both the aerated and deaerated solutions. This suggests that under the pH conditions for the CaCO_3 studies ITO reduction (leading to the re-oxidation peak at -0.55 V) only starts to become significant at potentials more negative than -0.8 V and that at less

cathodic potentials, many (if not all) of the diffraction-limited optical spots can be attributed to CaCO_3 particles.

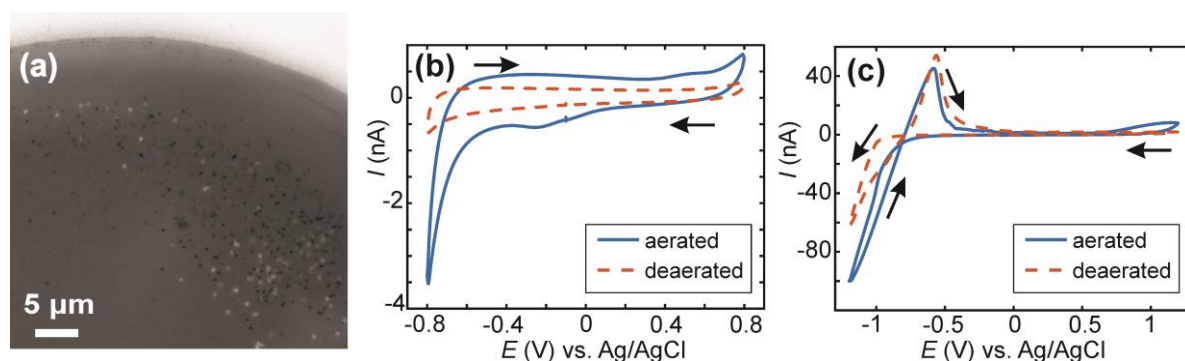


Figure 10. SECCM-IRM in a 5 mM NaHCO_3 solution (pH 2.7). Snapshot a) after $E = -1$ V was applied for 10 s for a series of IRM images recorded at 10 FPS. Light source: blue LED (wavelength of 470 nm). b) and c) cyclic voltammograms recorded with an aerated and a deaerated 5mM CaCl_2 , 5 mM NaHCO_3 (pH 2.7) solution for a ca. 80 μm diameter SECCM meniscus with different potential windows. Voltammetric scan rate = 0.2 V s^{-1} . Arrow denotes potential scan direction.

5.3.4 FEM model of CaCO_3 precipitation in the larger meniscus

To understand the differences observed when applying -0.8 V and -1.0 V to the larger menisci, reactive transport modelling of the pipette and meniscus was carried out. The model used an axisymmetric geometry based on microscopic characterization of the pipette and the wetted area observed with IRM. Two approach distances (meniscus heights - d_{app}) corresponding to the outer radius of the micropipette (31 μm), and half of this value, were modelled. This is because the meniscus thickness impacts O_2 transport at the air-water interface (and hence the current distribution).²⁸⁰ We did not measure the meniscus thickness in this work, but for this size pipette it should be achievable in the future through the use of laser scanning confocal microscopy and an appropriate fluorophore.²⁶⁷ Indeed, the use of a pH-sensitive fluorophore would also confirm the pH distribution in these types of experiments.²⁹⁶

To achieve a realistic estimate of the supersaturation we consider the 12 most significant species in the solution (the ions Ca^{2+} , Cl^- , Na^+ , HCO_3^- , CO_3^{2-} , H^+ and OH^- , the ion pairs

NaCO₃⁻, CaCO₃⁰, NaHCO₃ and Ca(HCO₃)⁺ and the gas phase species O₂ and CO₂) based on prior modelling with the PHREEQC speciation code.²⁹⁷ We solved the diffusion equation (5) for the flux of the *i*th species, *J_i*, at concentration, *c_i*, and time, *t*. Equilibria between the species was maintained by the continuity equation (Eq. 6), where *R_i* is the reaction flux necessary to maintain equilibrium (although deviations of up to 400% in equilibrium constants at long times were observed as there was a limitation on the rate of HCO₃⁻ dissociation that could be applied for reasonable computational efficiency, which would lead to an underestimate of supersaturation). Equilibrium constants were based on the local species activity *a_i* (Eq. 7), calculated from the activity coefficient *γ_i* based on the local ionic strength, *I* (Eq. 8) using the Davies equation (Eq. 9) with *A* = 1.82×10⁶ (ε*T*)^{-3/2}, where ε is the solution permittivity. For charged species *b* = 0.3, for uncharged species *b* = 0.1. Note that direct capture of CO₂ by OH⁻ to form HCO₃⁻ (as opposed to equilibration with H₂O to form HCO₃⁻ and H⁺ based on the local pH) was not considered, based on modelling of similar systems where the rate was negligible on these timescales due to the low OH⁻ concentrations.²⁵³

$$j_i = -D_i \nabla c_i \quad (5)$$

$$\frac{\partial c_i}{\partial t} + \nabla \cdot j_i = R_i \quad (6)$$

$$a_i = \gamma_i c_i \quad (7)$$

$$I = \frac{1}{2} \sum z_i^2 c_i \quad (8)$$

$$\log_{10} \gamma_i = -Az_i^2 \left(\frac{\sqrt{I}}{1 + \sqrt{I}} - bI \right) \quad (9)$$

The equilibrium concentrations given by the PHREEQC code were applied as the boundary condition at a plane 3500 μm inside the micropipette. Given the apparent importance of spatial variation across the wetted area, we imposed atmospheric equilibrium concentrations of O₂ and CO₂ at the air/meniscus interface (273 μM and 13.6 μM, respectively). A consequence of this approximation is that the total concentration of carbon species in the meniscus is depleted relative to that in the micropipette. We note that the alternative limiting treatment of CO₂ (no exchange with the atmosphere) would result in greater buffering and therefore longer timescales for the pH swing.

Using the simplifying assumptions that all current arises from the ORR, and that for a given potential, ORR is first order in O_2 , we imposed an inwards flux, of O_2 and an outwards flux of OH^- at the ITO surface:

$$J_{OH^-, ITO} = -4J_{O_2, ITO} = k_{ORR}[O_2] \quad (10)$$

where we chose k such that the simulated current over the ITO area, A , ($i = F \int \mathbf{n} \cdot \mathbf{J}_{OH^-} dA$) matched the experimental current. For all other boundaries and species not mentioned, a no flux boundary condition was used.

The expected evolution of pH and supersaturation, for fluxes corresponding to the current observed at -0.8 V and -1.0 V, are shown in Figure 11a. At $d_{app} = r$, both pH and S change much earlier at -1.0 V than at -0.8 V, with the -1.0 V case reaching saturation ($S = 1$) in less than 0.5 s, while -0.8 V takes closer to 4 s. These timescales correspond well with appearance times of new features presented in Figures 9(aiii) and 9(biii), with a clustering of new features around 1 s in the -1.0 V case, and a similar clustering at 4 s in the -0.8 V case. The effect of a closer approach ($d_{app} = r/2$) was examined and found to shift the observed changes to earlier times, (ca. 2 s at -0.8 V, Figure 11(a), black line, and ca. 0.4 s at -1.0 V, data not shown for clarity) and corresponding lower values of S . Electroneutrality was also considered and found to be violated as OH^- flux into the meniscus is not counter balanced by inward diffusion of cations; however, including electroneutrality (via the coupled Poisson-Nernst-Planck equations, data not shown) led only to minimal changes in timescale, with a slight increase in time taken to reach supersaturation.

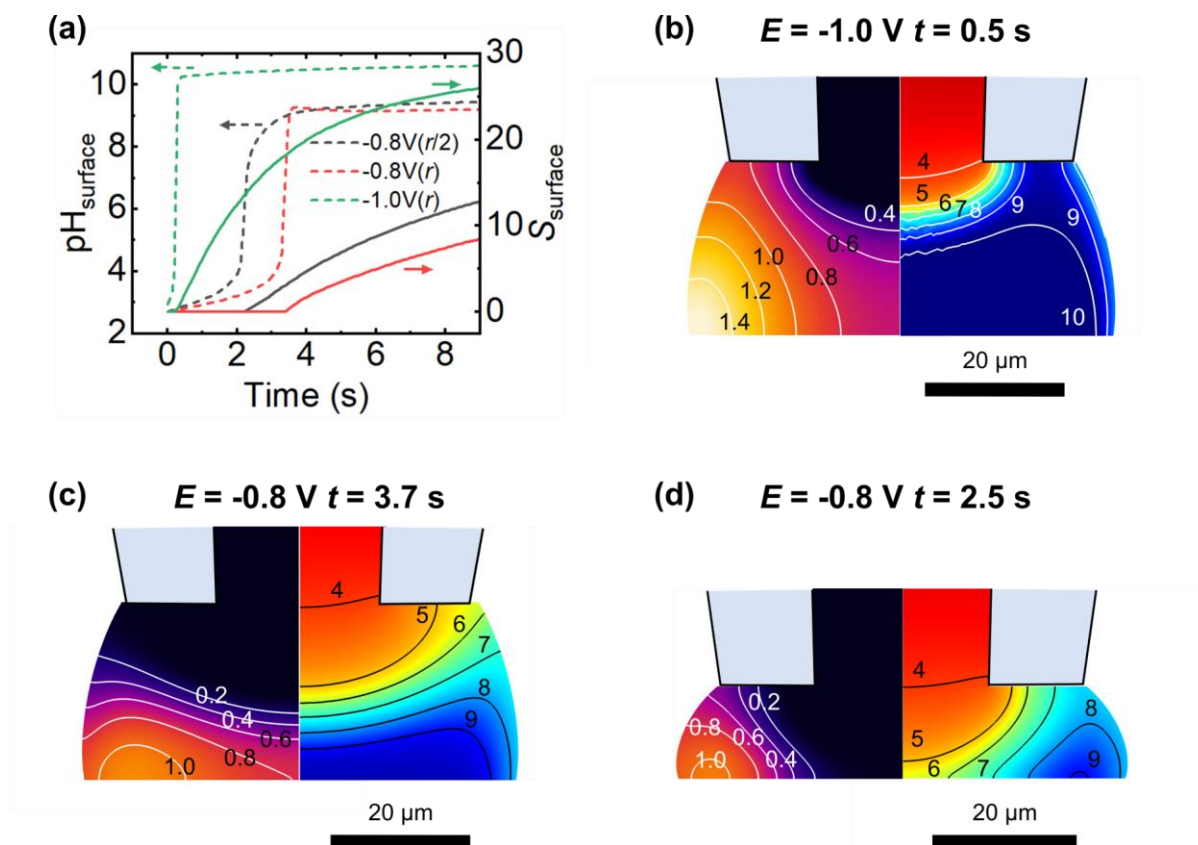


Figure 11. Reactive transport modelling of $\text{CaCl}_2 + \text{NaHCO}_3$ (5 mM, pH 2.7) droplets at the surface of ITO during oxygen reduction. a) The time-dependence of the average surface pH (left axis, dashed lines) and average surface supersaturation (right axis, solid lines) for a 62 μm diameter pipette for 2 different applied potentials (ORR rates; see text) and approach heights ($d_{\text{app}} = r$ or $r/2$). b) Profile of the supersaturation, S (left half, and contour lines) and pH (right half) at the first time point where supersaturation with respect to calcite was achieved with an ORR rate corresponding to -1.0 V for $d_{\text{app}} = r$. c) Same as b) but for an ORR rate corresponding to -0.8 V . d) Same as for c) but with $d_{\text{app}} = r/2$.

The spatial distribution of pH and S at the first timepoint where saturation is observed for both -1.0 V and -0.8 V cases, at $d_{\text{app}} = r$, are shown in Figures 11b and 11c, respectively. Both parameters have a strong spatial dependence, with change starting at the meniscus/air interface where the O_2 flux is greatest. Combined with the buffering action at the center of the droplet due to diffusion from inside the micropipette, this explains the experimentally observed preference for nucleation to occur around the edges of the meniscus rather than at its center. The pH buffering by atmospheric CO_2 may also contribute to the absence of particles at the very edge in the -1.0 V case (Figure 7bii). At longer times, at -1.0 V the pH of the

meniscus rapidly equilibrates and the spatial variation in S and pH is lost, however at -0.8 V slight variation in S and pH across the surface is observed to persist. Closer approaches (to $d_{\text{app}} = r/2$, Figure 11d) show a larger degree of spatial variation in pH and S . This simplified model is able to rationalize the timescale over which new features are observed and, to some extent, their spatial variation, emphasizing the importance of FEM modelling in interpreting SECCM deposition experiments.

5.4 Conclusion

In summary, it has been confirmed that the use of SECCM offers a versatile approach to characterize the electrochemical activity of surfaces. It is used here to pattern electrode surfaces with a controlled number of NPs (metal or inorganic crystals). However, the processes occurring within the meniscus in SECCM is always inferred from the electrochemical current traces and post mortem *ex situ* observations. We proposed in collaboration with the leader in this field, the group of Patrick Unwin at Warwick University, to couple this technique with optical microscopy. We chose the label-free IRM configuration and showed it allows the *operando* monitoring of meniscus transformation during electrochemistry. By super-localization strategies we also showed that IRM offers a sub-droplet imaging resolution enabling to track local redox processes.

Making use of an optically-transparent ITO electrode, it has been possible to image and track the stability of the SECCM meniscus size during voltammetry, resolving an important question in SECCM, which has hitherto mainly been addressed with *ex situ* analysis of droplet footprints or the analysis of SECCM scanning droplet images at a fixed potential. The ability to view the meniscus *in situ* provides a more holistic view of meniscus contact. Moreover, careful analysis of processed IRM images unambiguously showed the growth of diffraction-limited features within the meniscus.

Ag electrodeposition has been monitored in droplets ranging in diameter between 500 to 1000 nm, one to six distinct NPs were detected per droplet, with a detection size limit estimated to 60 nm in diameter. The hybrid method further reveals the dynamics of NP growth, pointing to the delayed formation of different NPs, a feature not clear in the electrochemical current traces. Indeed, NPs progressively appear on the WE surface within the first 5-15 ms of the electrodeposition. On a longer timescale, the displacement of their centroid by 30-200 nm is seen. These observations suggest, from *operando* visualization, that the NPs are grown from the surface diffusion and aggregation of instantaneously electrogenerated Ag nuclei (although

undetected optically), in agreement with recent nucleation-aggregation growth models. Beyond the unique mechanistic insights into electrodeposition, coupling a nanometric electrochemical cell and optical monitoring is a promising platform for the controlled production of collections of NPs on surfaces towards further single NP electrochemical activity benchmarking.

Secondly, precipitation of CaCO_3 by electrochemically changing the solution pH to create locally supersaturated solution. IRM *in situ* imaging provided evidence of the number and spatial distribution of crystallization events over the SECCM meniscus in real-time, revealing striking patterns for different driving potentials and tip sizes. Smaller reaction volumes showed increased density of fairly evenly distributed nanoscale CaCO_3 crystals (confirmed by Raman spectroscopy), with increased applied cathodic potential, which created high supersaturation. For larger reaction volumes (SECCM pipette tips), the location of the crystallization events become dependent on the driving potential hinting at the dynamic interplay between the pipette mass transport, ORR rates at the ITO surface, and CO_2 and O_2 transport across the air/meniscus interface. FEM simulations have highlighted the origins of the crystallization patterns and we were able to predict the onset time and, to an extent, the location of the crystallization events.

Chapter 6

Materials and methods

This chapter groups the materials used for each experiment and the images processing methods.

6.1 IRM experimental setup

The experiments have been performed using a motorized microscope (Zeiss Axio Observer 7) in an inverted configuration. A polychromatic unpolarized white light source illuminates from the backside a glass substrate covered by a thin film of ITO ($22 \times 22 \text{ mm}^2$, 0.15 mm of thickness) used as optical sensor. The light is focused through a 63x oil immersion objective with high numerical aperture (1.4). As described in section 2.1.2.2, part of the incident light is reflected by the ITO substrate towards an 8-bit CMOS color camera (Zeiss) or towards a sCMOS high resolution monochrome camera (C11440-42U30, Hamamatsu Photonics). The camera is synchronized with a low current potentiostat from CH 760 Instruments (figure 1). The pipette holder used for experiments in chapter 3 and 4 consists on a manual 3-axis stepper device. The pipette approach close to the substrate surface was monitored using a long-view connected to a second camera to avoid crashing the tip-end of the pipette. For the experiment in chapter 5, coarse pipette probe positioning was performed using a 3 axis micropositioner, while high resolution approaches were performed using a Z axis piezoelectric actuator. A 150 μm diameter Pt wire inserted in the capillary was used both as the counter and quasi-reference (QR) electrodes in a two-electrode-based electrochemical cell.

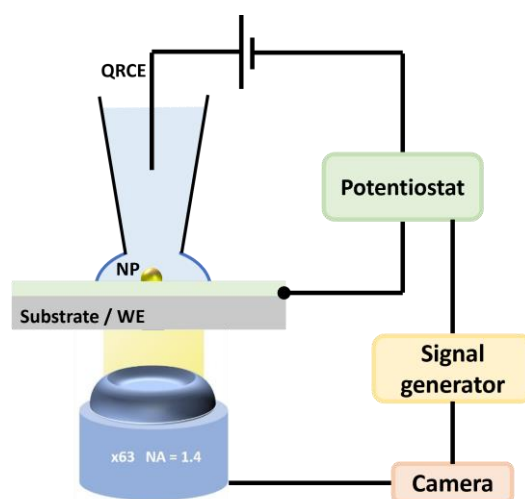


Figure 1. Schematic of the IRM experimental setup synchronized with a potentiostat.

For all the experiments, the camera and the potentiostat were triggered using a signal wave generator. Images acquisition framerate is limited by the transmission rate from the camera to the computer and by the region of interest size. The acquisition rate in Chapter 3 and 4 has been of 20 FPS, as the regions of interest were about 100 μm wide. The acquisition rate in Chapter 5 has been of 325 FPS. Image contrast depends also on diaphragm aperture. As showed in figure 2, an opening of about 50-70% of the whole diaphragm is a common choice to have both a wide field of view and a high signal-to-noise ratio.²⁹⁸

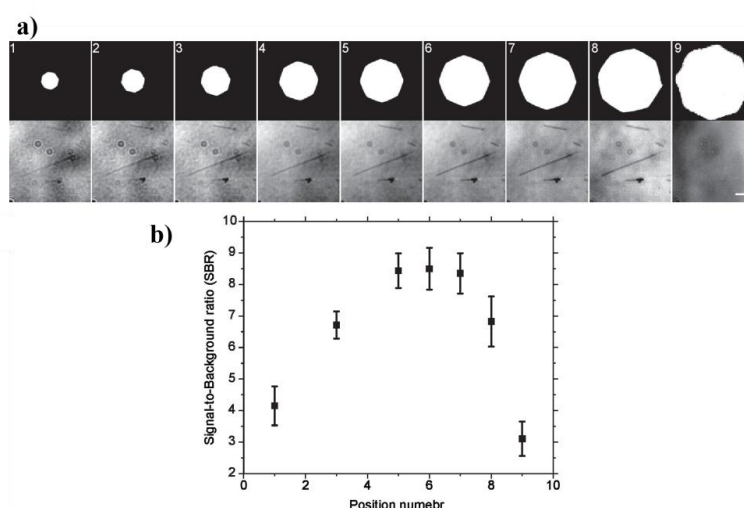


Figure 2. a) Images acquired with different diaphragm opening at the same region of interest (scalebar: 3 μm); b) signal-to-noise variation with diaphragm opening. *From reference 298.*

For the results presented in Chapter 4, the CVs were rescaled vs. an internal potential reference assigned to the quasi-reversible ITO surface transformation. This quasi-reversible system corresponds to the adsorption/desorption of sulfate ions at the ITO coated glass surface. After the ITO reduction experiments and recording blank experiments, a CV is performed in a solution of 1 mM FcMeOH used as a molecular potential reference. The CV shows the same ITO surface quasi-reversible system and the FcMeOH oxidation, allowing to rescale the apparent E_0 value of the quasi-reversible system, estimated from the median between the anodic, E_{a1} , and cathodic, E_{c1} , peak potentials, $E_0 = (E_{a1} + E_{c1})/2 = -0.23 \pm 0.02$ V vs the E_0 of the reversible FcMeOH⁺/FcMeOH couple.

For all the experiments, the camera and the potentiostat were triggered using a signal wave generator.

6.2 Image processing

6.2.1 Background removal

Raw electrochemical movies are saved as stacks of uncompressed .tiff images. Each image can be read as a rank 3 matrix $[A]_{x,y,c}$, where x and y are the two spatial direction which define the region of interest where the images are recorded and c is the “color” dimension, equal to 3 for images recorded with a RGB (Red, Green, Blue) camera. It is common practice to split the three channels and process them separately rather than process the RGB image. The signal-to-noise ratio can in fact change from channel to channel, depending on the light source used and on the chemical nature of scatterers and substrate. Some features can therefore be more contrasted on a specific channel, as showed in Figure 3. In this simulated example, dark contrasted optical features are visible only in the blue channel, while the bright contrasted ones can be detected only in the green channel. The red channel doesn't detect any signals. A similar example can be found in Chapter 5.3 of this thesis.

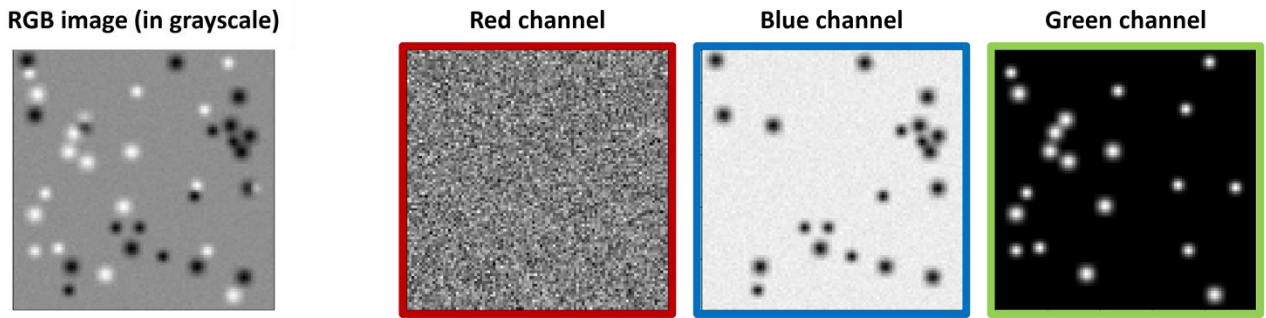


Figure 3: Simulated representation of an RGB image with both dark contrasted and bright contrasted features with the 3 colors channels splitted.

Channels can be split using Fiji software or using Python functions. The library Images can be processed in Python as 2 dimensional arrays. The library used to open the whole stacks of images in Python is called PIMS, a loading interface to wrap up sequential data.

The first processing step concerns background intensity. In experiments performed on regions of interest larger than tens of microns, it can be defined as the intensity extracted on a large (> 10 pixels) area without any optical features. Although this background definition can be useful to observe how background intensity changes over time, it doesn't take into account of fluctuation intensity along space due to geometric distortion, i.e. slight defocus along x and y directions, inhomogeneous contrast, and by light scattered by other objects or interfaces such as the perimeter of the droplet cell. For this reason, a common practice is to subtract to each pixel its corresponding intensity value in the first frame. Mathematically, the operation is the equivalent of a matrix subtraction, $[I]_{x,y,c} - [I_{bkg}]_{x,y,c}$.

Signal-to-noise can be improved also using contrast enhancement algorithms, as showed in Figure 4. The simplest method is to equalize the intensity histogram, so that intensities related to the object of interest are “stretched” within the full range of values allowed by the image format. An improved version of this algorithm is the adaptive histogram equalization, which consists in performing equalization on several histograms, each corresponding to different crops of the image, in order to takes into account spatial variation of the contrast in different regions.

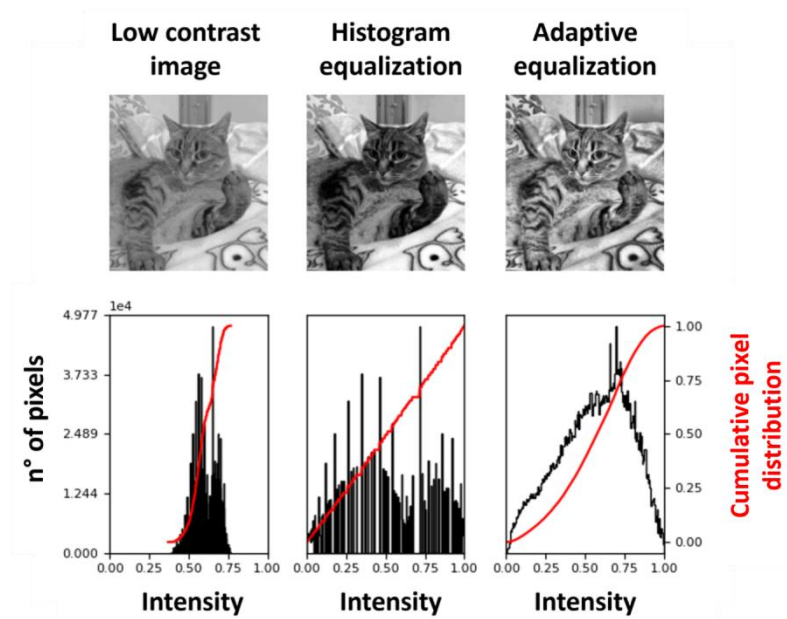


Figure 4: Difference between histogram equalization and adaptive equalization on a low contrast image, with their associated histogram intensity distribution and (in red) cumulative fraction of pixels.

6.2.2 Super-localization

Super-localization principles have been described also in section 2.1.2.1. The dynamic analysis of NPs and other scatterers have been made using homemade Python routines based on Trackpy, an open-source library which groups tools to track NPs motion. The super-localization procedure used for all the results is based on the Crocker-Grier algorithm.²⁹⁹ Assuming that the diffracted optical spot is centered on the NP position, the algorithm evaluates if a pixel can be chosen as local maximum/minimum. In particular, a pixel is selected as centroid scatterer if no other pixel within a certain distance is brighter. After that, a bidimensional Gaussian-like profile is fit in correspondence of each isolated scatterer. In this way, the centroid position associated to each NP can be estimated with a sub-pixel resolution ($\sim 1/10$ pixel accuracy). The spatial resolution depends therefore also on the pixels size. The localization precision strongly depends on signal-to-noise ratio and on how crowded is the image. With the Trackpy package, parameters tuning based on minimum integrated brightness and on minimum separation between two scatterers allows reducing the number of artifacts detected, but it is usually limited for noisy images. The same algorithm is used also to track the trajectory of each NP, using the function ‘trackpy.link’. To avoid artifacts, it is possible to assign the maximum distance one feature can move between two frames and/or the “memory”

which is the maximum number of frames a NP can disappear and reappear nearby. These two parameters can therefore be useful to take into account, for instance, out-of-focus frames or NPs tracking with low signal-to-noise ratio. NPs centroid coordinates can be indicative not only of real motion, but also of electrochemical processes occurring on the nano-object. As the size of the diffracted optical spots don't reflect the real size for objects smaller than the diffraction limit, centroid displacements smaller than the full width half maximum could also correspond to growth/dissolution and to reveal charging processes.^{27,102}

6.2.3 Optical transients

The optical intensity is obtained either from the value at the peak from the Gaussian fitting or from the average of optical intensity over several pixels. All the optical intensity footprints reported in this thesis are a pixel intensity average calculated over 4 x 4 pixel square centered to the maximum of fit. Extracting this value from all the frames of a movie allows obtaining the variation of intensity over time and/or over potential. As described in section 2.2, changes in optical spot intensity can be indicative of changes in dielectric properties of the associated nano-object. Its derivative can be useful to detect the onset time/potential of electrochemically triggered processes. Quantitative sizing can be performed by optical footprint if the optical information is associated with correlative electron microscopy and/or with simulations based on physical principles behind imaging processes. Finally, FWHM can be extracted along x and y directions from a 2D Gaussian fit, and it can be indicative of the growth of objects above the diffraction limit or of aggregation of 2 or more objects.

6.2.4 Edge detection

Another useful procedure used in this thesis (Chapter 5) is the edge detection. It consists on several mathematical methods to compute intensity discontinuities in images. The simplest algorithm used is the threshold masking (figure 3), which consists in selecting only the pixels with an intensity which is intermediate between the I_{bkg} and I_{max} . This method presents several limitations, as it can be applied only when signal-to-noise ratio is high enough to avoid artifacts and when the edge intensity is consistently different from the internal region intensity. For this reason, many algorithms are based on matrix operations. For instance, Sobel-Feldman filter replaces each pixel with an approximation of directional gradient at the corresponding position.

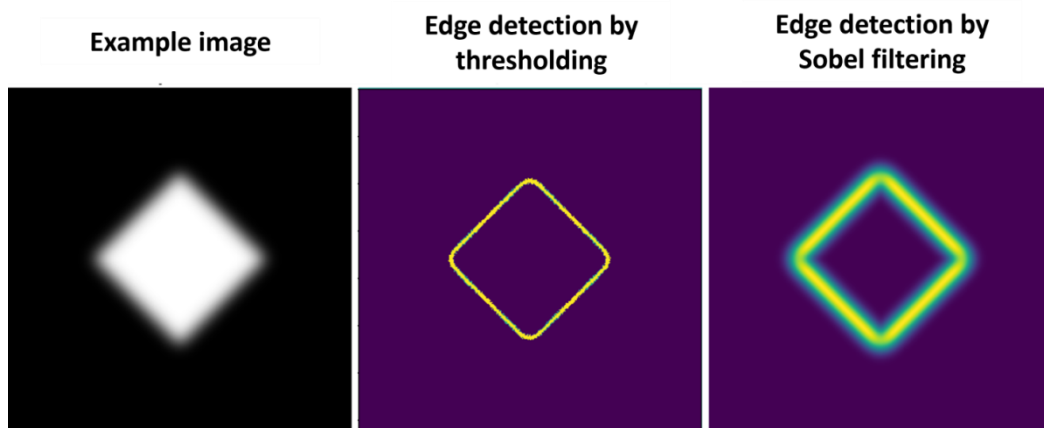


Figure 4: Simulated representation of an RGB image with both dark contrasted and bright contrasted features with the 3 colors channels split.

These algorithms are also affected by noise. For some of the results in Chapter 5, Savitzky-Golay algorithm³⁰⁰ has been used to smooth the temporal evolution of each pixel. It consists in fitting successive sub-sets of points with a low-order polynomial function, estimating the smoothed signal at the central point of each sub-set, as shown in figure 5. Each software has its own implementation of Savitzky-Golay algorithm, where the polynomial order and the subset length can be defined by the user.

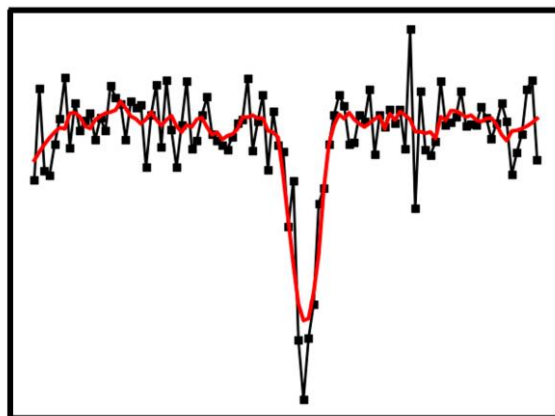


Figure 5: Noisy signal before (black curve) and after smoothing with a 2 order polynomial applied to a 5-point moving window.

Any other mathematical or statistical operation has been automatized using python libraries such as Numpy, Scipy (which provides a large variety of mathematical functions) and Pandas (to create tables and to manipulate data structures).

6.2.5 Correlative Scanning Electron Microscopy

SEM micrographs were acquired using an SEM microscope (Zeiss Supra 40), with an electron beam of 3 kV and a secondary electrode detector as collector. It was possible to find the same electrode location, previously visualized by IRM, thanks to the marks left by droplet cells after evaporation. In alternative, a common practice is to scratch carefully the ITO surface using a scalpel, in order to have a landmark for both IRM and SEM imaging.

6.3 Materials and chemicals

6.3.1 Chemical products

The experiments presented in chapter 4 for have been carried out with commercial citrate-capped Pt NPs dispersed in 2 mM sodium citrate from Nanocomposix. Sulfuric acid of analytical grade was purchased from Merk. The 22 x 22 mm ITO-coated glass coverslip substrates with a nominal resistivity of 70-100 Ω /square were purchased by 2SPI, USA.

The experiments presented in chapter 5 for have been carried out using three types of ITO coated glass coverslips (22 x 22 mm²) with three different macroscale resistances, namely ITO_h, ITO_m and ITO_l in order of increasing resistance ITO_h < ITO_m < ITO_l. The ITO substrates resistances, R, were estimated by a 2-point measurement with an ohmmeter over a constant 2 cm distance of the samples. Unless otherwise stated, the experiments were performed with ITO_h. ITO_h was purchased from ACM Villiers, France, (140 nm thickness with R = 40 Ω), while ITO_m and ITO_l were purchased from 2SPI, USA, respectively with indicated 30-60 Ω /square and 70-100 Ω /square sheet resistance (corresponding to ITO coating thickness of 140 and 70 nm, respectively) and respective measured resistance of R = 150 and 500 Ω . The substrates were thoroughly rinsed with ethanol and dried under argon flux before characterization. Sulfuric acid of analytical grade and ferrocenemethanol, FcMeOH, 97% were purchased from Merk and were used without any further purification. Experiments concerning Ni electrodeposition have been performed on 2SPI ITO-coated coverslips with 15-30 Ω /square. KCl (ACS reagent) was purchased from Acros Organics. NiCl₂.6H₂O (ReagentPlus), NaH₂PO₄ (>99.0%) and NaH₂PO₄ (>98.5%) were purchased from Sigma-Aldrich.

The results presented in chapter 6 have been carried out using potassium nitrate (KNO₃, Sigma), hydrochloric acid (HCl, 37 %, Honeywell Fluka), anhydrous calcium chloride

(CaCl₂, 96 %, Acros Organics), and sodium bicarbonate (NaHCO₃, 99+ %, Acros Organics), used as supplied by the manufacturer. Silver nitrate (AgNO₃, Sigma) and potassium nitrate (KNO₃, Sigma) were used for Ag electrodeposition as supplied by the manufacturer.

All the experiments have been performed using ultrapure water with a minimal resistivity of 18 MΩ.cm

6.3.2 Pipettes fabrication

All the pipettes have been prepared by pulling borosilicate glass capillaries (outer diameter = 1 mm, inner diameter = 0.5 mm) with a laser puller (P2000 Sutter). It consists in a CO₂ laser reflected by a gold retro mirror. The capillary is secured at its endings and it is heated orthogonally by the laser beam. By adjusting parameters such as the pulling force, the laser temperature or the scanning pattern of laser beam, reproducible pipettes with a diameter < 100 nm can be obtained. The used parameters are the following:

- Heat: it specifies the output power of the laser. The value used was 410
- Filament (FIL): it specifies the scanning pattern of the laser beam and the corresponding scan length on the capillary. The value used was 4, corresponding to a scanning length of about 6.5 mm.
- Velocity (VEL): it specifies the pulling velocity as the pipette glass starts to soften and to deform. The value used was 15.
- Pulling force (PULL): it defines the pulling force at the capillary extremities. The value used was 120.
- Delay (DEL): it controls the time delay between when the heat is turned off and the pull is activated. The value used was 120.

Although it is a common practice to report the parameters used to set the laser puller, external conditions such as temperature and humidity can affect the procedure. In particular, as the retro mirror is close to the capillary, it must be cleaned regularly in order to avoid asymmetric pipette manufacture and loss in reproducibility.

A homemade scratcher was used to furtherly tune the pipette diameter. It consists in a holder where the pipette is fixed perpendicular to an aluminum oxide polishing tape (Precision Surfaces International). The approach at the surface is conducted with a long view camera to avoid crashing the pipette and to monitor the tip-end opening during the whole process. The polishing tape is wet with ultrapure water and can rotate with constant velocity.

Conclusions and perspectives

Nanoscale phenomena are responsible of macro-scale electrochemical performance of nanostructured electrodes extensively used in energy conversion devices, batteries and sensors. For this reason, it is crucial to access nanoscale electrochemical descriptors of those electrified interfaces. However, it cannot be reach solely by classical electrochemistry.

Among the single entity approaches that emerged very recently, this thesis focuses on high resolution optical microscopies hyphenated with electrochemical characterization. During the three years of this thesis, I used interferometric reflection microscopy in combination with electrochemistry to study local variation in electrochemical response cause by electrode substrate heterogeneity, droplet confinement effects on diffusion and transport phenomena and competition mechanisms between concomitant electrochemical reactions.

Operando optical microscopy monitoring during electrochemical actuation allowed collecting large volumes of data. If properly processed, quantitative electrochemical information and various nanoscale descriptors for single entities can be accessed and further allows bridging the gap between local electrochemical response and global electrode activity. Moreover, optical inspection of nanostructured interfaces possesses several advantages to other methodologies. The first one is their experimental versatility. *Operando* optical microscopy can be synchronized with many instruments used to investigate electrochemical processes at the nanoscale, such as SECCM configuration and sub-micrometric droplet cells. Secondly, the possibility to probe wide fields of view allows correlating the global electrochemical response of thousands of NPs with statistical, single entity information, granting highly statistical investigations. Third, the possibility to extract optical intensity variations for each NP or scatterer represent an easy and effective way to identify different sub-population behaviors along the electrode surface. Lastly, no invasive procedures are required, as the visible light affect the most of materials less than electron beams.

In Chapter 3, H₂ NBs are used as nanoscale reporters of electrochemical activity for Pt NPs toward HER as they tend to grow first on the most active nanoparticles. For local optical transients extracted for ~100 NBs, the evolution of size and shape of NBs can be quantitatively evaluated with the help of optical simulation. This allowed also collecting evidences of neighbors Pt NPs cross-talk phenomena in form of hydrogen spillover toward the surface, as H₂ NBs growth continues even after the complete coverage of its corresponding NP. In conclusion, H₂ NBs can be used as descriptors of local electroactivity, but only if neighbors effects are considered too.

In Chapter 4 it has been demonstrated how surface heterogeneities effects on local electroactivity cannot be neglected. Although, every electrochemist knows that roughness and 2D/3D morphology affects transport phenomena, the electron transfer rate is often assumed as uniform towards the electrode surface. As we have demonstrated that this is not true also for electrodes considered as inert such as indium tin oxide, one needs to probe the effect of these heterogeneities in all that devices where the control of micro- and nanoscale is mandatory to push performance and lifetime. *Operando* IRM showed how these heterogeneities are traduced into different dominant electrochemical reactions at different regions of the electrode. IRM allows unraveling competitive processes also when they are not spatially separated, as demonstrated by Ni electrodeposition monitoring. Competition between Ni²⁺ reduction into metallic Ni and water reduction directly on ITO has been probed thanks to the different optical signature of the two processes. Moreover, it has been possible to verify how the electrochemical signal related to global Ni²⁺ electroreduction is less step-like than the signal associated to single NPs.

Finally, in Chapter 5 it has been investigated the effects of confinement in sub-micrometric droplets for both Ag electroreduction and CaCO₃ crystallization in SECCM configuration. It has been demonstrated how image processing allow to verify droplets stability of about 500 nm in diameter and to look within their perimeter in order to visualize multiple growth phenomena. In this way, growth events have been probed for direct electroreduction phenomena and for non-metallic crystallization electrochemically driven by pH changes. For the latter system, nucleation and growth have been visualized for droplets of different size, demonstrating how nucleation events over time are not stochastic, but reflects the interplay between oxygen transport from air|liquid interface and its reduction at electrode surface.

In conclusion, the results of this thesis demonstrate how it is actually possible to take into account of all the actors affecting electrochemical interfaces at the nanoscale without using ultra-high vacuum or invasive techniques. This is possible thanks to versatility of high resolution optical microscopies. Therefore, next future will bring a further increase in the spread of hybrid setups involving optical techniques, such as optical nanopores, spectroscopic tracking or hybrid SICM-optics. For instance, a reflective nanopore electrode has been used very recently to probe local morphological changes in zinc dendrites and to reveal the entity of competition between zinc deposition and the passivation layer formation.³⁰¹ Further imaging methods can also be explored in order to enhance more the selectivity to structural and chemical changes during electrochemical actuation. For instance, microscopies which can

assure both a spatial and a spectral resolution of the point spread functions can facilitate the acquisition of this information.³⁰²

In this sense, another aim is to push more the optical sensitivity to chemical and structural transformation. Recent developments already demonstrated the possibility to probe optically particle charging layer or NPs conversion with shrinking-core mechanism with a precision around 10 nm. Pushing this limit of another order of magnitude could unlock the possibility to have access to dynamic monitoring of phenomena such as deformation and relaxation of crystal lattice parameters.

Lastly, hybrid techniques can acquire large volume of images (see section 2.4.2) associated to electrochemical processes. In parallel, libraries with pre-trained machine learning algorithms are nowadays user friendly and are spreading fast, as they are showing great power in finding hidden correlations and in predicting mechanistic processes from images and CVs. Data-driven tools will not be in substitution of theoretical modelling, considering that their outcomes don't say anything about physics underlying specific responses, but they will be fundamental for novel methodologies in bridging single entity and bulk electrochemical analyses.

Bibliography

- (1) Crooks, R. M. Concluding Remarks: Single Entity Electrochemistry One Step at a Time. *Faraday Discuss.* **2016**, *193*, 533–547. <https://doi.org/10.1039/c6fd00203j>.
- (2) Engstrom, R. C.; DesJarlais, S.; Johnson, K. W. Characterization of Electrode Heterogeneity with Electrogenerated Chemiluminescence. *Anal. Chem.* **1987**, *59* (4), 670–673. <https://doi.org/10.1021/ac00131a028>.
- (3) Kanoufi, F. *Electrochemistry and Optical Microscopy*; 2021. <https://doi.org/10.1002/9783527610426.bard030108>.
- (4) Lemineur, J.-F.; Wang, H.; Wang, W.; Kanoufi, F. Emerging Optical Microscopy Techniques for Electrochemistry. *Annu. Rev. Anal. Chem.* **2022**, *15* (1), 57–82. <https://doi.org/10.1146/annurev-anchem-061020-015943>.
- (5) Wang, W. Imaging the Chemical Activity of Single Nanoparticles with Optical Microscopy. *Chem. Soc. Rev.* **2018**, *47* (7), 2485–2508. <https://doi.org/10.1039/C7CS00451F>.
- (6) Hoener, B. S.; Kirchner, S. R.; Heiderscheidt, T. S.; Collins, S. S. E.; Chang, W. S.; Link, S.; Landes, C. F. Plasmonic Sensing and Control of Single-Nanoparticle Electrochemistry. *Chem* **2018**, *4* (7), 1560–1585. <https://doi.org/10.1016/j.chempr.2018.04.009>.
- (7) Sojic, N.; Bouffier, L. Interplay between Electrochemistry and Optical Imaging: The Whole Is Greater than the Sum of the Parts. *Curr. Opin. Electrochem.* **2022**, *34*, 101007. <https://doi.org/10.1016/j.coelec.2022.101007>.
- (8) Doneux, T. Visualisation of Electrochemical Processes by Coupled Electrochemistry and Fluorescence Microscopy. *Current Opinion in Electrochemistry*. Elsevier B.V. 2022, p 101013. <https://doi.org/10.1016/j.coelec.2022.101013>.
- (9) Hao, R.; Peng, Z.; Zhang, B. Single-Molecule Fluorescence Microscopy for Probing the Electrochemical Interface. *ACS Omega* **2020**, *5* (1), 89–97. <https://doi.org/10.1021/acsomega.9b03763>.
- (10) Zhang, J.; Arbault, S.; Sojic, N.; Jiang, D. Electrochemiluminescence Imaging for Bioanalysis. *Annu. Rev. Anal. Chem.* **2019**, *12* (1), 275–295. <https://doi.org/10.1146/annurev-anchem-061318-115226>.
- (11) Taylor, R. W.; Sandoghdar, V. Interferometric Scattering Microscopy: Seeing Single Nanoparticles and Molecules via Rayleigh Scattering. *Nano Lett.* **2019**, *19* (8), 4827–4835. <https://doi.org/10.1021/acs.nanolett.9b01822>.

- (12) Young, G.; Kukura, P. Interferometric Scattering Microscopy. *Annu. Rev. Phys. Chem.* **2019**, *70* (1), 301–322. <https://doi.org/10.1146/annurev-physchem-050317-021247>.
- (13) Namink, K.; Meng, X.; Koper, M. T. M.; Kukura, P.; Faez, S. Electric-Double-Layer-Modulation Microscopy. *Phys. Rev. Appl.* **2020**, *13* (4), 044065. <https://doi.org/10.1103/PhysRevApplied.13.044065>.
- (14) Gahlmann, A.; Moerner, W. E. Exploring Bacterial Cell Biology with Single-Molecule Tracking and Super-Resolution Imaging. *Nat. Rev. Microbiol.* **2014**, *12* (1), 9–22. <https://doi.org/10.1038/nrmicro3154>.
- (15) Chen, P.; Zhou, X.; Shen, H.; Andoy, N. M.; Choudhary, E.; Han, K.-S.; Liu, G.; Meng, W. Single-Molecule Fluorescence Imaging of Nanocatalytic Processes. *Chem. Soc. Rev.* **2010**, *39* (12), 4560–4570. <https://doi.org/10.1039/B909052P>.
- (16) Chen, T.; Dong, B.; Chen, K.; Zhao, F.; Cheng, X.; Ma, C.; Lee, S.; Zhang, P.; Kang, S. H.; Ha, J. W.; Xu, W.; Fang, N. Optical Super-Resolution Imaging of Surface Reactions. *Chem. Rev.* **2017**, *117* (11), 7510–7537. <https://doi.org/10.1021/acs.chemrev.6b00673>.
- (17) Mao, X.; Liu, C.; Hesari, M.; Zou, N.; Chen, P. Super-Resolution Imaging of Non-Fluorescent Reactions via Competition. *Nat. Chem.* **2019**, *11* (8), 687–694. <https://doi.org/10.1038/s41557-019-0288-8>.
- (18) Suvira, M.; Zhang, B. Single-Molecule Interactions at a Surfactant-Modified H₂Surface Nanobubble. *Langmuir* **2021**, *37* (47), 13816–13823. <https://doi.org/10.1021/acs.langmuir.1c01686>.
- (19) Suvira, M.; Zhang, B. Effect of Surfactant on Electrochemically Generated Surface Nanobubbles. *Anal. Chem.* **2021**, *93* (12), 5170–5176. <https://doi.org/10.1021/acs.analchem.0c05067>.
- (20) Peng, Z.; Zhang, B. Nanobubble Labeling and Imaging with a Solvatochromic Fluorophore Nile Red. *Anal. Chem.* **2021**, *93* (46), 15315–15322. <https://doi.org/10.1021/acs.analchem.1c02685>.
- (21) Hao, R.; Fan, Y.; Howard, M. D.; Vaughan, J. C.; Zhang, B. Imaging Nanobubble Nucleation and Hydrogen Spillover during Electrocatalytic Water Splitting. *Proc. Natl. Acad. Sci. U. S. A.* **2018**, *115* (23), 5878–6588. <https://doi.org/10.1073/pnas.1800945115>.
- (22) Nizamov, S.; Sazdovska, S. D.; Mirsky, V. M. A Review of Optical Methods for Ultrasensitive Detection and Characterization of Nanoparticles in Liquid Media with a Focus on the Wide Field Surface Plasmon Microscopy. *Anal. Chim. Acta* **2022**, *1204*,

339633. <https://doi.org/10.1016/j.aca.2022.339633>.
- (23) Zhou, X.; Yang, Y.; Wang, S.; Liu, X. Surface Plasmon Resonance Microscopy: From Single-Molecule Sensing to Single-Cell Imaging. *Angew. Chemie* **2020**, *132* (5), 1792–1801. <https://doi.org/10.1002/ange.201908806>.
- (24) Ye, X.; Saqib, M.; Mao, J.; Li, G.; Hao, R. Spatiotemporally Super-Resolved Dendrites Nucleation and Early-Stage Growth Dynamics in Zinc-Ion Batteries. *Cell Reports Phys. Sci.* **2021**, *2* (5), 100420. <https://doi.org/10.1016/j.xcrp.2021.100420>.
- (25) Wang, W.; Yuan, T.; Wei, W.; Jiang, W. Vertical Diffusion of Ions within Single Particles during Electrochemical Charging. *ACS Nano* **2021**, *15* (2), 3522–3528. <https://doi.org/10.1021/acsnano.1c00431>.
- (26) Willets, K. A. Supercharging Superlocalization Microscopy: How Electrochemical Charging of Plasmonic Nanostructures Uncovers Hidden Heterogeneity. *ACS Nano* **2019**, *13* (6), 6145–6150. <https://doi.org/10.1021/acsnano.9b04062>.
- (27) Sundaresan, V.; Monaghan, J. W.; Willets, K. A. Visualizing the Effect of Partial Oxide Formation on Single Silver Nanoparticle Electrodissolution. *J. Phys. Chem. C* **2018**, *122* (5), 3138–3145. <https://doi.org/10.1021/acs.jpcc.7b11824>.
- (28) Ding, H.; Guo, W.; Su, B. Imaging Cell-Matrix Adhesions and Collective Migration of Living Cells by Electrochemiluminescence Microscopy. *Angew. Chemie Int. Ed.* **2020**, *59* (1), 449–456. <https://doi.org/10.1002/anie.201911190>.
- (29) Dong, J.; Lu, Y.; Xu, Y.; Chen, F.; Yang, J.; Chen, Y.; Feng, J. Direct Imaging of Single-Molecule Electrochemical Reactions in Solution. *Nature* **2021**, *596* (7871), 244–249. <https://doi.org/10.1038/s41586-021-03715-9>.
- (30) Ding, H.; Guo, W.; Su, B. Electrochemiluminescence Single-Cell Analysis: Intensity- and Imaging-Based Methods. *Chempluschem* **2020**, *85* (4), 725–733. <https://doi.org/10.1002/cplu.202000145>.
- (31) Voci, S.; Goudeau, B.; Valenti, G.; Lesch, A.; Jović, M.; Rapino, S.; Paolucci, F.; Arbault, S.; Sojic, N. Surface-Confined Electrochemiluminescence Microscopy of Cell Membranes. *J. Am. Chem. Soc.* **2018**, *140* (44), 14753–14760. <https://doi.org/10.1021/jacs.8b08080>.
- (32) Han, D.; Goudeau, B.; Manojlovic, D.; Jiang, D.; Fang, D.; Sojic, N. Electrochemiluminescence Loss in Photobleaching. *Angew. Chemie - Int. Ed.* **2021**, *60* (14), 7686–7690. <https://doi.org/10.1002/anie.202015030>.
- (33) Wang, Y.; Jin, R.; Sojic, N.; Jiang, D.; Chen, H.-Y. Intracellular Wireless Analysis of Single Cells by Bipolar Electrochemiluminescence Confined in a Nanopipette. *Angew.*

- Chemie Int. Ed.* **2020**, *59* (26), 10416–10420. <https://doi.org/10.1002/anie.202002323>.
- (34) Wang, Y.; Guo, W.; Yang, Q.; Su, B. Electrochemiluminescence Self-Interference Spectroscopy with Vertical Nanoscale Resolution. *J. Am. Chem. Soc.* **2020**, *142* (3), 1222–1226. <https://doi.org/10.1021/jacs.9b12833>.
- (35) Dong, J.; Xu, Y.; Zhang, Z.; Feng, J. Operando Imaging of Chemical Activity on Gold Plates with Single-Molecule Electrochemiluminescence Microscopy. *Angew. Chemie - Int. Ed.* **2022**, *61* (14), 6–11. <https://doi.org/10.1002/anie.202200187>.
- (36) Noël, J.-M.; Miranda Vieira, M.; Brasiliense, V.; Lemineur, J.-F.; Combellas, C.; Kanoufi, F. Effect of the Driving Force on Nanoparticles Growth and Shape: An Opto-Electrochemical Study. *Nanoscale* **2020**, *12* (5), 3227–3235. <https://doi.org/10.1039/C9NR09419A>.
- (37) Lemineur, J.-F.; Stockmann, T. J.; Médard, J.; Smadja, C.; Combellas, C.; Kanoufi, F. Optical Nanoimpacts of Dielectric and Metallic Nanoparticles on Gold Surface by Reflectance Microscopy: Adsorption or Bouncing? *J. Anal. Test.* **2019**, *3* (2), 175–188. <https://doi.org/10.1007/s41664-019-00099-8>.
- (38) Lemineur, J.-F.; Noël, J.-M.; Combellas, C.; Kanoufi, F. Revealing the Sub-50 Ms Electrochemical Conversion of Silver Halide Nanocolloids by Stochastic Electrochemistry and Optical Microscopy. *Nanoscale* **2020**, *12* (28), 15128–15136. <https://doi.org/10.1039/D0NR03799K>.
- (39) Pendergast, A. D.; Deng, Z.; Maroun, F.; Renault, C.; Dick, J. E. Revealing Dynamic Rotation of Single Graphene Nanoplatelets on Electrified Microinterfaces. *ACS Nano* **2021**, *15* (1), 1250–1258. <https://doi.org/10.1021/acsnano.0c08406>.
- (40) Sun, L.; Jiang, D.; Li, M.; Liu, T.; Yuan, L.; Wang, W.; Chen, H.-Y. Collision and Oxidation of Single LiCoO₂ Nanoparticles Studied by Correlated Optical Imaging and Electrochemical Recording. *Anal. Chem.* **2017**, *89* (11), 6050–6055. <https://doi.org/10.1021/acs.analchem.7b00649>.
- (41) Lemineur, J.-F.; Noël, J.-M.; Ausserré, D.; Combellas, C.; Kanoufi, F. Combining Electrodeposition and Optical Microscopy for Probing Size-Dependent Single-Nanoparticle Electrochemistry. *Angew. Chemie Int. Ed.* **2018**, *57* (37), 11998–12002. <https://doi.org/10.1002/anie.201807003>.
- (42) Godeffroy, L.; Lemineur, J.; Shkirskiy, V.; Miranda Vieira, M.; Noël, J.; Kanoufi, F. Bridging the Gap between Single Nanoparticle Imaging and Global Electrochemical Response by Correlative Microscopy Assisted By Machine Vision. *Small Methods* **2022**, *n/a* (n/a), 2200659. <https://doi.org/10.1002/smtd.202200659>.

- (43) Wei, W.; Yuan, T.; Jiang, W.; Gao, J.; Chen, H. Y.; Wang, W. Accessing the Electrochemical Activity of Single Nanoparticles by Eliminating the Heterogeneous Electrical Contacts. *J. Am. Chem. Soc.* **2020**, *142* (33), 14307–14313. <https://doi.org/10.1021/jacs.0c06171>.
- (44) Hu, S.; Yi, J.; Zhang, Y.-J.; Lin, K.-Q.; Liu, B.-J.; Chen, L.; Zhan, C.; Lei, Z.-C.; Sun, J.-J.; Zong, C.; Li, J.-F.; Ren, B. Observing Atomic Layer Electrodeposition on Single Nanocrystals Surface by Dark Field Spectroscopy. *Nat. Commun.* **2020**, *11* (1), 2518. <https://doi.org/10.1038/s41467-020-16405-3>.
- (45) Jiang, D.; Jiang, Y.; Li, Z.; Liu, T.; Wo, X.; Fang, Y.; Tao, N.; Wang, W.; Chen, H. Y. Optical Imaging of Phase Transition and Li-Ion Diffusion Kinetics of Single LiCoO₂ Nanoparticles during Electrochemical Cycling. *J. Am. Chem. Soc.* **2017**, *139* (1), 186–192. <https://doi.org/10.1021/jacs.6b08923>.
- (46) Hu, S.; Yi, J.; Zhang, Y. J.; Lin, K. Q.; Liu, B. J.; Chen, L.; Zhan, C.; Lei, Z. C.; Sun, J. J.; Zong, C.; Li, J. F.; Ren, B. Observing Atomic Layer Electrodeposition on Single Nanocrystals Surface by Dark Field Spectroscopy. *Nat. Commun.* **2020**, *11* (1), 1–7. <https://doi.org/10.1038/s41467-020-16405-3>.
- (47) Lemineur, J. F.; Noël, J. M.; Courty, A.; Ausserré, D.; Combellas, C.; Kanoufi, F. In Situ Optical Monitoring of the Electrochemical Conversion of Dielectric Nanoparticles: From Multistep Charge Injection to Nanoparticle Motion. *J. Am. Chem. Soc.* **2020**, *142* (17), 7937–7946. <https://doi.org/10.1021/jacs.0c02071>.
- (48) Wu, G.; Zhou, X.; Lv, W. L.; Qian, C.; Liu, X. W. Real-Time Plasmonic Imaging of the Compositional Evolution of Single Nanoparticles in Electrochemical Reactions. *Nano Lett.* **2022**, *22* (11), 4383–4391. <https://doi.org/10.1021/acs.nanolett.2c00831>.
- (49) Baker, L. A. Perspective and Prospectus on Single-Entity Electrochemistry. *J. Am. Chem. Soc.* **2018**. <https://doi.org/10.1021/jacs.8b09747>.
- (50) Wang, Y.; Shan, X.; Tao, N. Emerging Tools for Studying Single Entity Electrochemistry. *Faraday Discuss.* **2016**, *193*, 9–39. <https://doi.org/10.1039/c6fd00180g>.
- (51) Unwin, P. Concluding Remarks: Next Generation Nanoelectrochemistry – next Generation Nanoelectrochemists. *Faraday Discuss.* **2022**. <https://doi.org/10.1039/D2FD00020B>.
- (52) Coulter, W. H. Means for Counting Particles Suspended in a Fluid. US Patent, 2656508. *United States Pat. Off. Patentiert am* **1953**, *20*, 1953.
- (53) Zhou, Y. G.; Rees, N. V.; Compton, R. G. The Electrochemical Detection and

- Characterization of Silver Nanoparticles in Aqueous Solution. *Angew. Chemie - Int. Ed.* **2011**, *50* (18), 4219–4221. <https://doi.org/10.1002/anie.201100885>.
- (54) Fried, J. P.; Wu, Y.; Tilley, R. D.; Gooding, J. J. Optical Nanopore Sensors for Quantitative Analysis. *Nano Letters.* **2022**, pp 869–880. <https://doi.org/10.1021/acs.nanolett.1c03976>.
- (55) Yang, J.; Lu, Y.; Jin, L.; Zhao, C.; Chen, Y.; Xu, Y.; Chen, F.; Feng, J. Dynamic Optical Visualization of Proton Transport Pathways at Water–Solid Interfaces. *Angew. Chemie - Int. Ed.* **2022**, *61* (2). <https://doi.org/10.1002/anie.202112150>.
- (56) Saha, P.; Hill, J. W.; Walmsley, J. D.; Hill, C. M. Probing Electrocatalysis at Individual Au Nanorods via Correlated Optical and Electrochemical Measurements. *Anal. Chem.* **2018**, *90* (21), 12832–12839. <https://doi.org/10.1021/acs.analchem.8b03360>.
- (57) Tognoni, E. High-Speed Multifunctional Scanning Ion Conductance Microscopy: Innovative Strategies to Study Dynamic Cellular Processes. *Curr. Opin. Electrochem.* **2021**, *28*, 100738. <https://doi.org/10.1016/j.coelec.2021.100738>.
- (58) Fosdick, S. E.; Anderson, M. J.; Nettleton, E. G.; Crooks, R. M. Correlated Electrochemical and Optical Tracking of Discrete Collision Events. *J. Am. Chem. Soc.* **2013**, *135* (16), 5994–5997. <https://doi.org/10.1021/ja401864k>.
- (59) Shan, X.; Díez-Pérez, I.; Wang, L.; Wiktor, P.; Gu, Y.; Zhang, L.; Wang, W.; Lu, J.; Wang, S.; Gong, Q.; Li, J.; Tao, N. Imaging the Electrocatalytic Activity of Single Nanoparticles. *Nat. Nanotechnol.* **2012**, *7* (10), 668–672. <https://doi.org/10.1038/nnano.2012.134>.
- (60) Wonner, K.; Evers, M. V.; Tschulik, K. The Electrochemical Dissolution of Single Silver Nanoparticles Enlightened by Hyperspectral Dark-Field Microscopy. *Electrochim. Acta* **2019**, *301*, 458–464. <https://doi.org/10.1016/j.electacta.2019.01.129>.
- (61) Wonner, K.; Rurainsky, C.; Tschulik, K. Operando Studies of the Electrochemical Dissolution of Silver Nanoparticles in Nitrate Solutions Observed With Hyperspectral Dark-Field Microscopy. *Front. Chem.* **2020**, *7*. <https://doi.org/10.3389/fchem.2019.00912>.
- (62) Chen, P.; Zhou, X.; Andoy, N. M.; Han, K.-S.; Choudhary, E.; Zou, N.; Chen, G.; Shen, H. Spatiotemporal Catalytic Dynamics within Single Nanocatalysts Revealed by Single-Molecule Microscopy. *Chem. Soc. Rev.* **2014**, *43* (4), 1107–1117. <https://doi.org/10.1039/C3CS60215J>.
- (63) Chen, T.; Zhang, Y.; Xu, W. Observing the Heterogeneous Electro-Redox of Individual Single-Layer Graphene Sheets. *ACS Nano* **2016**, *10* (9), 8434–8442.

- <https://doi.org/10.1021/acsnano.6b03327>.
- (64) Xiao, Y.; Su, Y.; Liu, X.; Xu, W. Defect-Driven Heterogeneous Electron Transfer between an Individual Graphene Sheet and Electrode. *J. Phys. Chem. Lett.* **2019**, *10* (18), 5402–5407. <https://doi.org/10.1021/acs.jpcllett.9b02134>.
- (65) Guerrette, J. P.; Percival, S. J.; Zhang, B. Fluorescence Coupling for Direct Imaging of Electrocatalytic Heterogeneity. *J. Am. Chem. Soc.* **2013**, *135* (2), 855–861. <https://doi.org/10.1021/ja310401b>.
- (66) Djoumer, R.; Anne, A.; Chovin, A.; Demaille, C.; Dejous, C.; Hallil, H.; Lachaud, J.-L. Converting Any Faradaic Current Generated at an Electrode under Potentiostatic Control into a Remote Fluorescence Signal. *Anal. Chem.* **2019**, *91* (10), 6775–6782. <https://doi.org/10.1021/acs.analchem.9b00851>.
- (67) Djoumer, R.; Chovin, A.; Demaille, C.; Dejous, C.; Hallil, H. Real-time Conversion of Electrochemical Currents into Fluorescence Signals Using 8-Hydroxypyrene-1,3,6-trisulfonic Acid (HPTS) and Amplex Red as Fluorogenic Reporters. *ChemElectroChem* **2021**, *8* (12), 2298–2307. <https://doi.org/10.1002/celec.202100517>.
- (68) Anderson, T. J.; Defnet, P. A.; Zhang, B. Electrochemiluminescence (ECL)-Based Electrochemical Imaging Using a Massive Array of Bipolar Ultramicroelectrodes. *Anal. Chem.* **2020**, *92* (9), 6748–6755. <https://doi.org/10.1021/acs.analchem.0c00921>.
- (69) Tian, Z.; Wu, Y.; Shao, F.; Tang, D.; Qin, X.; Wang, C.; Liu, S. Electrofluorochromic Imaging Analysis of Glycan Expression on Living Single Cell with Bipolar Electrode Arrays. *Anal. Chem.* **2021**, *93* (12), 5114–5122. <https://doi.org/10.1021/acs.analchem.0c04785>.
- (70) Ino, K.; Yaegaki, R.; Hiramoto, K.; Nashimoto, Y.; Shiku, H. Closed Bipolar Electrode Array for On-Chip Analysis of Cellular Respiration by Cell Aggregates. *ACS Sensors* **2020**, *5* (3), 740–745. <https://doi.org/10.1021/acssensors.9b02061>.
- (71) Tian, Z.; Mi, L.; Wu, Y.; Shao, F.; Zou, M.; Zhou, Z.; Liu, S. Visual Electrofluorochromic Detection of Cancer Cell Surface Glycoprotein on a Closed Bipolar Electrode Chip. *Anal. Chem.* **2019**, *91* (12), 7902–7910. <https://doi.org/10.1021/acs.analchem.9b01760>.
- (72) Qin, X.; Li, Z.-Q.; Zhou, Y.; Pan, J.-B.; Li, J.; Wang, K.; Xu, J.-J.; Xia, X.-H. Fabrication of High-Density and Superuniform Gold Nanoelectrode Arrays for Electrochemical Fluorescence Imaging. *Anal. Chem.* **2020**, *92* (19), 13493–13499. <https://doi.org/10.1021/acs.analchem.0c02918>.
- (73) Liu, Y.; Zhang, H.; Li, B.; Liu, J.; Jiang, D.; Liu, B.; Sojic, N. Single Biomolecule

- Imaging by Electrochemiluminescence. *J. Am. Chem. Soc.* **2021**, *143* (43), 17910–17914. <https://doi.org/10.1021/jacs.1c06673>.
- (74) Chen, M.-M.; Xu, C.-H.; Zhao, W.; Chen, H.-Y.; Xu, J.-J. Super-Resolution Electrogenerated Chemiluminescence Microscopy for Single-Nanocatalyst Imaging. *J. Am. Chem. Soc.* **2021**, *143* (44), 18511–18518. <https://doi.org/10.1021/jacs.1c07827>.
- (75) Tassy, B.; Dauphin, A. L.; Man, H. M.; Le Guenno, H.; Lojou, E.; Bouffier, L.; De Poulpiquet, A. In Situ Fluorescence Tomography Enables a 3D Mapping of Enzymatic O₂ Reduction at the Electrochemical Interface. *Anal. Chem.* **2020**, *92* (10), 7249–7256. <https://doi.org/10.1021/acs.analchem.0c00844>.
- (76) Bouffier, L.; Doneux, T. Coupling Electrochemistry with in Situ Fluorescence (Confocal) Microscopy. *Curr. Opin. Electrochem.* **2017**, *6* (1), 31–37. <https://doi.org/10.1016/j.coelec.2017.06.015>.
- (77) Kankla, P.; Luksirikul, P.; Garrigue, P.; Goudeau, B.; Bouffier, L.; Kuhn, A. Site-Selective Bipolar Electrodeposition of Gold Clusters on Graphene Oxide Microsheets at a 3D Air|Liquid Interface. *Adv. Mater. Interfaces* **2022**, *9* (21), 3–10. <https://doi.org/10.1002/admi.202200304>.
- (78) Knezevic, S.; Bouffier, L.; Liu, B.; Jiang, D.; Sojic, N. Electrochemiluminescence Microscopy: From Single Objects to Living Cells. *Current Opinion in Electrochemistry*. Elsevier B.V. 2022, p 101096. <https://doi.org/10.1016/j.coelec.2022.101096>.
- (79) Wong, A. A.; Rubinstein, S. M.; Aziz, M. J. Direct Visualization of Electrochemical Reactions and Heterogeneous Transport within Porous Electrodes in Operando by Fluorescence Microscopy. *Cell Reports Phys. Sci.* **2021**, *2* (4). <https://doi.org/10.1016/j.xcrp.2021.100388>.
- (80) Merryweather, A. J.; Schnedermann, C.; Jacquet, Q.; Grey, C. P.; Rao, A. Operando Optical Tracking of Single-Particle Ion Dynamics in Batteries. *Nature* **2021**, *594* (7864), 522–528. <https://doi.org/10.1038/s41586-021-03584-2>.
- (81) Merryweather, A. J.; Jacquet, Q.; Emge, S. P.; Schnedermann, C.; Rao, A.; Grey, C. P. Operando Monitoring of Single-Particle Kinetic State-of-Charge Heterogeneities and Cracking in High-Rate Li-Ion Anodes. **2021**. <https://doi.org/10.1038/s41563-022-01324-z>.
- (82) Pandya, R.; Valzania, L.; Dorchie, F.; Xia, F.; Hugh, J. M.; Mathieson, A.; Tan, J. H.; Parton, T. G.; De Volder, M.; Tarascon, J.; Gigan, S.; de Aguiar, H. B.; Grimaud, A. Three-Dimensional Operando Optical Imaging of Single Particle and Electrolyte

- Heterogeneities inside Li-Ion Batteries. **2022**, 1–29. <https://doi.org/10.48550/arxiv.2207.13073>.
- (83) Lemineur, J.-F.; Noël, J.-M.; Ausserré, D.; Combellas, C.; Kanoufi, F. Combining Electrodeposition and Optical Microscopy for Probing Size-Dependent Single-Nanoparticle Electrochemistry. *Angew. Chemie* **2018**, *130* (37), 12174–12178. <https://doi.org/10.1002/ange.201807003>.
- (84) Oh, H.; Park, Y.; Song, H. Tracking Underpotential Deposition of Copper on Individual Silver Nanocubes by Real-Time Single-Particle Plasmon Scattering Imaging. *J. Phys. Chem. C* **2020**, *124* (37), 20398–20409. <https://doi.org/10.1021/acs.jpcc.0c05258>.
- (85) Laurinavichyute, V. K.; Nizamov, S.; Mirsky, V. M. Real Time Tracking of the Early Stage of Electrochemical Nucleation. *Electrochim. Acta* **2021**, *382*, 138278. <https://doi.org/10.1016/j.electacta.2021.138278>.
- (86) Lemineur, J.-F.; Noël, J.-M.; Combellas, C.; Kanoufi, F. Optical Monitoring of the Electrochemical Nucleation and Growth of Silver Nanoparticles on Electrode: From Single to Ensemble Nanoparticles Inspection. *J. Electroanal. Chem.* **2020**, *872*, 114043. <https://doi.org/10.1016/j.jelechem.2020.114043>.
- (87) Brasiliense, V.; Park, J. E.; Chen, Z.; Van Duyne, R. P.; Schatz, G. C. Nanopipette-Based Electrochemical SERS Platforms: Using Electrodeposition to Produce Versatile and Adaptable Plasmonic Substrates. *J. Raman Spectrosc.* **2021**, *52* (2), 339–347. <https://doi.org/10.1002/jrs.5974>.
- (88) Brasiliense, V.; Clausmeyer, J.; Dauphin, A. L.; Noël, J. M.; Berto, P.; Tessier, G.; Schuhmann, W.; Kanoufi, F. Opto-Electrochemical In Situ Monitoring of the Cathodic Formation of Single Cobalt Nanoparticles. *Angew. Chemie - Int. Ed.* **2017**, *56* (35), 10598–10601. <https://doi.org/10.1002/anie.201704394>.
- (89) Cheng, Q.; Wei, L.; Liu, Z.; Ni, N.; Sang, Z.; Zhu, B.; Xu, W.; Chen, M.; Miao, Y.; Chen, L.-Q.; Min, W.; Yang, Y. Operando and Three-Dimensional Visualization of Anion Depletion and Lithium Growth by Stimulated Raman Scattering Microscopy. *Nat. Commun.* **2018**, *9* (1), 2942. <https://doi.org/10.1038/s41467-018-05289-z>.
- (90) Bai, P.; Li, J.; Brushett, F. R.; Bazant, M. Z. Transition of Lithium Growth Mechanisms in Liquid Electrolytes. *Energy Environ. Sci.* **2016**, *9* (10), 3221–3229. <https://doi.org/10.1039/C6EE01674J>.
- (91) Kwak, J. H.; Jeoun, Y.; Oh, S. H.; Yu, S.; Lim, J.-H.; Sung, Y.-E.; Yu, S.-H.; Lim, H.-D. Operando Visualization of Morphological Evolution in Mg Metal Anode: Insight

- into Dendrite Suppression for Stable Mg Metal Batteries. *ACS Energy Lett.* **2022**, *7* (1), 162–170. <https://doi.org/10.1021/acsenergylett.1c02486>.
- (92) Godeffroy, L.; Aguilar, I.; Médard, J.; Larcher, D.; Tarascon, J.-M.; Kanoufi, F. Decoupling the Dynamics of Zinc Hydroxide Sulfate Precipitation/Dissolution in Aqueous Zn–MnO₂ Batteries by Operando Optical Microscopy: A Missing Piece of the Mechanistic Puzzle. *Adv. Energy Mater.* **2022**, *n/a* (n/a), 2200722. <https://doi.org/10.1002/aenm.202200722>.
- (93) Wang, J.-G.; Fossey, J. S.; Li, M.; Xie, T.; Long, Y.-T. Real-Time Plasmonic Monitoring of Single Gold Amalgam Nanoalloy Electrochemical Formation and Stripping. *ACS Appl. Mater. Interfaces* **2016**, *8* (12), 8305–8314. <https://doi.org/10.1021/acsami.6b01029>.
- (94) Schopf, C.; Wahl, A.; Martín, A.; O’Riordan, A.; Iacopino, D. Direct Observation of Mercury Amalgamation on Individual Gold Nanorods Using Spectroelectrochemistry. *J. Phys. Chem. C* **2016**, *120* (34), 19295–19301. <https://doi.org/10.1021/acs.jpcc.6b04668>.
- (95) Alizar, Y. Y.; Ha, J. W. Single-Particle Spectroelectrochemistry: Electrochemical Tuning of Plasmonic Properties via Mercury Amalgamation in Mesoporous Silica Coated Gold Nanorods without Structural Deformation. *Analyst* **2022**, *147* (10), 2035–2039. <https://doi.org/10.1039/D2AN00559J>.
- (96) Wang, H.; Zhao, W.; Zhao, Y.; Xu, C.-H.; Xu, J.-J.; Chen, H.-Y. Real-Time Tracking the Electrochemical Synthesis of Au@Metal Core–Shell Nanoparticles toward Photo Enhanced Methanol Oxidation. *Anal. Chem.* **2020**, *92* (20), 14006–14011. <https://doi.org/10.1021/acs.analchem.0c02913>.
- (97) Wang, H.; Zhao, W.; Xu, C.-H.; Chen, H.; Xu, J. Electrochemical Synthesis of Au@semiconductor Core–Shell Nanocrystals Guided by Single Particle Plasmonic Imaging. *Chem. Sci.* **2019**, *10* (40), 9308–9314. <https://doi.org/10.1039/C9SC02804H>.
- (98) Little, C. A.; Batchelor-McAuley, C.; Ngamchuea, K.; Lin, C.; Young, N. P.; Compton, R. G. Coupled Optical and Electrochemical Probing of Silver Nanoparticle Destruction in a Reaction Layer. *ChemistryOpen* **2018**, *7* (5), 370–380. <https://doi.org/10.1002/open.201800048>.
- (99) Yang, M.; Batchelor-McAuley, C.; Barton, S.; Rickaby, R. E. M.; Bouman, H. A.; Compton, R. G. Opto-Electrochemical Dissolution Reveals Coccolith Calcium Carbonate Content. *Angew. Chemie - Int. Ed.* **2021**, *60* (38), 20999–21006. <https://doi.org/10.1002/anie.202108435>.

- (100) Yang, M.; Batchelor-McAuley, C.; Barton, S.; Rickaby, R. E. M.; Bouman, H. A.; Compton, R. G. Single-Entity Coccolithophore Electrochemistry Shows Size Is No Guide to the Degree of Calcification. *Environ. Sci. Adv.* **2022**, *1* (2), 156–163. <https://doi.org/10.1039/d2va00025c>.
- (101) Evans, R. C.; Nilsson, Z.; Balch, B.; Wang, L.; Neilson, J. R.; Weinberger, C. R.; Sambur, J. B. Quantifying Capacitive-Like and Battery-Like Charge Storage Contributions Using Single-Nanoparticle Electro-optical Imaging. *ChemElectroChem* **2020**, *7* (3), 753–760. <https://doi.org/10.1002/celec.201902011>.
- (102) Jiang, W.; Wei, W.; Yuan, T.; Liu, S.; Niu, B.; Wang, H.; Wang, W. Tracking the Optical Mass Centroid of Single Electroactive Nanoparticles Reveals the Electrochemically Inactive Zone. *Chem. Sci.* **2021**, *12* (24), 8556–8562. <https://doi.org/10.1039/d1sc01623g>.
- (103) Niu, B.; Jiang, W.; Jiang, B.; Lv, M.; Wang, S.; Wang, W. Determining the Depth of Surface Charging Layer of Single Prussian Blue Nanoparticles with Pseudocapacitive Behaviors. *Nat. Commun.* **2022**, *13* (1). <https://doi.org/10.1038/s41467-022-30058-4>.
- (104) Li, W.; Wojcik, M.; Xu, K. Optical Microscopy Unveils Rapid, Reversible Electrochemical Oxidation and Reduction of Graphene. *Nano Lett.* **2019**, *19* (2), 983–989. <https://doi.org/10.1021/acs.nanolett.8b04216>.
- (105) Tan, B. H.; An, H.; Ohl, C.-D. Identifying Surface-Attached Nanobubbles. *Curr. Opin. Colloid Interface Sci.* **2021**, *53*, 101429. <https://doi.org/10.1016/j.cocis.2021.101429>.
- (106) Chen, J.; Zhou, K.; Wang, Y.; Gao, J.; Yuan, T.; Pang, J.; Tang, S.; Chen, H. Y.; Wang, W. Measuring the Activation Energy Barrier for the Nucleation of Single Nanosized Vapor Bubbles. *Proc. Natl. Acad. Sci. U. S. A.* **2019**, *116* (26), 12678–12683. <https://doi.org/10.1073/pnas.1903259116>.
- (107) Zhou, K.; Yuan, T.; Su, H.; Wang, W. Accessing the Spatiotemporal Heterogeneities of Single Nanocatalysts by Optically Imaging Gas Nanobubbles. *Curr. Opin. Colloid Interface Sci.* **2021**, *55*, 101465. <https://doi.org/10.1016/j.cocis.2021.101465>.
- (108) Hao, R.; Fan, Y.; Anderson, T. J.; Zhang, B. Imaging Single Nanobubbles of H₂ and O₂ during the Overall Water Electrolysis with Single-Molecule Fluorescence Microscopy. *Anal. Chem.* **2020**, *92* (5), 3682–3688. <https://doi.org/10.1021/acs.analchem.9b04793>.
- (109) Xu, S.; Yu, X.; Chen, Z.; Zeng, Y.; Guo, L.; Li, L.; Luo, F.; Wang, J.; Qiu, B.; Lin, Z. Real-Time Visualization of the Single-Nanoparticle Electrocatalytic Hydrogen Generation Process and Activity under Dark Field Microscopy. *Anal. Chem.* **2020**, *92*

- (13), 9016–9023. <https://doi.org/10.1021/acs.analchem.0c01129>.
- (110) Wang, J.; Zhang, L.; Xie, J.; Weizmann, Y.; Li, D.; Li, J. Single Particle Hopping as an Indicator for Evaluating Electrocatalysts. *Nano Lett.* **2022**, 0–24. <https://doi.org/10.1021/acs.nanolett.2c01631>.
- (111) Chen, S.; Yin, C.; Huang, Z.; Chen, J.; Zheng, Y.; Chen, J.; Yang, S.; Su, Y.; Fang, Y. Plasmonic Imaging the Catalysis of Single Graphene Sheets – The Edge Effect. *Carbon N. Y.* **2022**, *191*, 333–339. <https://doi.org/10.1016/j.carbon.2022.02.007>.
- (112) Li, S.; Du, Y.; He, T.; Shen, Y.; Bai, C.; Ning, F.; Hu, X.; Wang, W.; Xi, S.; Zhou, X. Nanobubbles: An Effective Way to Study Gas-Generating Catalysis on a Single Nanoparticle. *J. Am. Chem. Soc.* **2017**, *139* (40), 14277–14284. <https://doi.org/10.1021/jacs.7b08523>.
- (113) Ma, C.; Wei, H.-F.; Wang, M.-X.; Wu, S.; Chang, Y.-C.; Zhang, J.; Jiang, L.-P.; Zhu, W.; Chen, Z.; Lin, Y. Hydrogen Evolution Reaction Monitored by Electrochemiluminescence Blinking at Single-Nanoparticle Level. *Nano Lett.* **2020**, *20* (7), 5008–5016. <https://doi.org/10.1021/acs.nanolett.0c01129>.
- (114) Wang, Y.; Chen, J.; Jiang, Y.; Wang, X.; Wang, W. Label-Free Optical Imaging of the Dynamic Stick-Slip and Migration of Single Sub-100-Nm Surface Nanobubbles: A Superlocalization Approach. *Anal. Chem.* **2019**, *91* (7), 4665–4671. <https://doi.org/10.1021/acs.analchem.9b00022>.
- (115) Wang, H.; He, T.; Du, Y.; Wang, W.; Shen, Y.; Li, S.; Zhou, X.; Yang, F. Evolution of Single Nanobubbles through Multi-State Dynamics. *Chinese Chem. Lett.* **2020**, *31* (9), 2442–2446. <https://doi.org/https://doi.org/10.1016/j.ccllet.2020.03.049>.
- (116) Noël, J.-M.; Lemineur, J.-F. Optical Microscopy to Study Single Nanoparticles Electrochemistry: From Reaction to Motion. *Curr. Opin. Electrochem.* **2021**, *25*, 100647. <https://doi.org/10.1016/j.coelec.2020.100647>.
- (117) Pendergast, A. D.; Renault, C.; Dick, J. E. Correlated Optical-Electrochemical Measurements Reveal Bidirectional Current Steps for Graphene Nanoplatelet Collisions at Ultramicroelectrodes. *Anal. Chem.* **2021**, *93* (5), 2898–2906. <https://doi.org/10.1021/acs.analchem.0c04409>.
- (118) Brasiliense, V.; Clausmeyer, J.; Berto, P.; Tessier, G.; Combellas, C.; Schuhmann, W.; Kanoufi, F. Monitoring Cobalt-Oxide Single Particle Electrochemistry with Subdiffraction Accuracy. *Anal. Chem.* **2018**, *90* (12), 7341–7348. <https://doi.org/10.1021/acs.analchem.8b00649>.
- (119) Wonner, K.; Evers, M. V.; Tschulik, K. Simultaneous Opto- and Spectro-

- Electrochemistry: Reactions of Individual Nanoparticles Uncovered by Dark-Field Microscopy. *J. Am. Chem. Soc.* **2018**, *140* (40), 12658–12661. <https://doi.org/10.1021/jacs.8b02367>.
- (120) Hill, C. M.; Pan, S. A Dark-Field Scattering Spectroelectrochemical Technique for Tracking the Electrodeposition of Single Silver Nanoparticles. *J. Am. Chem. Soc.* **2013**, *135* (46), 17250–17253. <https://doi.org/10.1021/ja4075387>.
- (121) Hill, C. M.; Clayton, D. A.; Pan, S. Combined Optical and Electrochemical Methods for Studying Electrochemistry at the Single Molecule and Single Particle Level: Recent Progress and Perspectives. *Phys. Chem. Chem. Phys.* **2013**, *15* (48), 20797. <https://doi.org/10.1039/c3cp52756e>.
- (122) Mefford, J. T.; Akbashev, A. R.; Kang, M.; Bentley, C. L.; Gent, W. E.; Deng, H. D.; Alsem, D. H.; Yu, Y. S.; Salmon, N. J.; Shapiro, D. A.; Unwin, P. R.; Chueh, W. C. Correlative Operando Microscopy of Oxygen Evolution Electrocatalysts. *Nature* **2021**, *593* (7857), 67–73. <https://doi.org/10.1038/s41586-021-03454-x>.
- (123) Lee, B.; Yoon, S.; Lee, J. W.; Kim, Y.; Chang, J.; Yun, J.; Ro, J. C.; Lee, J. S.; Lee, J. H. Statistical Characterization of the Morphologies of Nanoparticles through Machine Learning Based Electron Microscopy Image Analysis. *ACS Nano* **2020**, *14* (12), 17125–17133. <https://doi.org/10.1021/acsnano.0c06809>.
- (124) Shiratori, K.; Bishop, L. D. C.; Ostovar, B.; Baiyasi, R.; Cai, Y. Y.; Rossky, P. J.; Landes, C. F.; Link, S. Machine-Learned Decision Trees for Predicting Gold Nanorod Sizes from Spectra. *J. Phys. Chem. C* **2021**, *125* (35), 19353–19361. <https://doi.org/10.1021/acs.jpcc.1c03937>.
- (125) Jany, B. R.; Janas, A.; Krok, F. Retrieving the Quantitative Chemical Information at Nanoscale from Scanning Electron Microscope Energy Dispersive X-Ray Measurements by Machine Learning. *Nano Lett.* **2017**, *17* (11), 6520–6525. <https://doi.org/10.1021/acs.nanolett.7b01789>.
- (126) Daviddi, E.; Gonos, K. L.; Colburn, A. W.; Bentley, C. L.; Unwin, P. R. Scanning Electrochemical Cell Microscopy (SECCM) Chronopotentiometry: Development and Applications in Electroanalysis and Electrocatalysis. *Anal. Chem.* **2019**, *91* (14), 9229–9237. <https://doi.org/10.1021/acs.analchem.9b02091>.
- (127) Zhu, C.; Huang, K.; Siepser, N. P.; Baker, L. A. Scanning Ion Conductance Microscopy. *Chem. Rev.* **2021**, *121* (19), 11726–11768. <https://doi.org/10.1021/acs.chemrev.0c00962>.
- (128) Feng, H.; Xu, X.; Du, Y.; Dou, S. X. Application of Scanning Tunneling Microscopy

- in Electrocatalysis and Electrochemistry. *Electrochem. Energy Rev.* **2021**, *4* (2), 249–268. <https://doi.org/10.1007/s41918-020-00074-3>.
- (129) Unwin, P. Concluding Remarks: Next Generation Nanoelectrochemistry - next Generation Nanoelectrochemists. *Faraday Discuss.* **2022**, *233*, 374–391. <https://doi.org/10.1039/d2fd00020b>.
- (130) Turing, A. Computer Machinery and Intelligence. *Psychol. Philosophy* **1950**, *236*, 433–460.
- (131) Kumar, M.; Sood, I. Review on Artificial Intelligence Techniques. *Proc. 4th Int. Conf. Auton. Robot. Agents* **2009**, *7* (7), 1363–1367. <https://doi.org/10.1109/ICARA.2000.4804025>.
- (132) Zhou, J.; Huang, B.; Yan, Z.; Bünzli, J. C. G. Emerging Role of Machine Learning in Light-Matter Interaction. *Light Sci. Appl.* **2019**, *8* (1). <https://doi.org/10.1038/s41377-019-0192-4>.
- (133) Mistry, A.; Franco, A. A.; Cooper, S. J.; Roberts, S. A.; Viswanathan, V. How Machine Learning Will Revolutionize Electrochemical Sciences. *ACS Energy Lett.* **2021**, *6* (4), 1422–1431. <https://doi.org/10.1021/acseenergylett.1c00194>.
- (134) George, J.; Hautier, G. Chemist versus Machine: Traditional Knowledge versus Machine Learning Techniques. *Trends Chem.* **2021**, *3* (2), 86–95. <https://doi.org/10.1016/j.trechm.2020.10.007>.
- (135) Jiang, Z.; Li, J.; Yang, Y.; Mu, L.; Wei, C.; Yu, X.; Zhao, K.; Cloetens, P.; Lin, F.; Liu, Y.; Pianetta, P. Machine-Learning-Revealed Statistics of the Particle-Carbon/Binder Detachment in Lithium-Ion Battery Cathodes. *Nat. Commun.* **2020**. <https://doi.org/10.1038/s41467-020-16233-5>.
- (136) Rosen, E. M.; Silverman, D. C. Corrosion Prediction from Polarization Scans Using an Artificial Neural Network Integrated with an Expert System. *Corrosion* **1992**, *48* (9), 734–745. <https://doi.org/10.5006/1.3315994>.
- (137) Trasatti, S. P.; Mazza, F. Crevice Corrosion: A Neural Network Approach. *Br. Corros. J.* **1996**, *31* (2), 105–112. <https://doi.org/10.1179/bcj.1996.31.2.105>.
- (138) Lastres, E.; De Armas, G.; Catasús, M.; Alpízar, J.; García, L.; Cerdà, V. Use of Neural Networks in Solving Interferences Caused by Formation of Intermetallic Compounds in Anodic Stripping Voltammetry. *Electroanalysis* **1997**, *9* (3), 251–254. <https://doi.org/10.1002/elan.1140090313>.
- (139) Raj, R. A.; Parthiban, T.; Artificial, I.; Anns, T. Artificial Neural Network Applications in Electrochemistry - a Review. **1999**, *5* (12), 552–555.

- (140) Talaie, A.; Romagnoli, J. A. An Integrated Artificial Neural Network/Polymer-Based PH Sensor: A New Engineering Perspective to Conducting Polymer Technology. *Synth. Met.* **1996**, *82* (3), 231–235. [https://doi.org/10.1016/S0379-6779\(96\)03797-6](https://doi.org/10.1016/S0379-6779(96)03797-6).
- (141) Kennedy, G. F.; Zhang, J.; Bond, A. M. Automatically Identifying Electrode Reaction Mechanisms Using Deep Neural Networks. *Anal. Chem.* **2019**, *91* (19), 12220–12227. <https://doi.org/10.1021/acs.analchem.9b01891>.
- (142) Chen, H.; Kätelhön, E.; Le, H.; Compton, R. G. Use of Artificial Intelligence in Electrode Reaction Mechanism Studies: Predicting Voltammograms and Analyzing the Dissociative CE Reaction at a Hemispherical Electrode. *Anal. Chem.* **2021**, *93* (39), 13360–13372. <https://doi.org/10.1021/acs.analchem.1c03154>.
- (143) Ye, J. J.; Lin, C. H.; Huang, X. J. Analyzing the Anodic Stripping Square Wave Voltammetry of Heavy Metal Ions via Machine Learning: Information beyond a Single Voltammetric Peak. *J. Electroanal. Chem.* **2020**, *872*, 113934. <https://doi.org/10.1016/j.jelechem.2020.113934>.
- (144) Hoar, B. B.; Zhang, W.; Xu, S.; Deeba, R.; Costentin, C.; Gu, Q.; Liu, C. Electrochemical Mechanistic Analysis from Cyclic Voltammograms Based on Deep Learning. *ACS Meas. Sci. Au* **2022**. <https://doi.org/10.1021/acsmeasuresciau.2c00045>.
- (145) Wagner, F. H.; Dalagnol, R.; Tarabalka, Y.; Segantine, T. Y. F.; Thomé, R.; Hirye, M. C. M. U-Net-Id, an Instance Segmentation Model for Building Extraction from Satellite Images-Case Study in the Joanopolis City, Brazil. *Remote Sens.* **2020**, *12* (10), 1–14. <https://doi.org/10.3390/rs12101544>.
- (146) Xu, H.; Zhu, J.; Finegan, D. P.; Zhao, H.; Lu, X.; Li, W.; Hoffman, N.; Bertei, A.; Shearing, P.; Bazant, M. Z. Guiding the Design of Heterogeneous Electrode Microstructures for Li-Ion Batteries : Microscopic Imaging , Predictive Modeling , and Machine Learning. **2021**, *2003908*, 1–34. <https://doi.org/10.1002/aenm.202003908>.
- (147) Nehme, E.; Freedman, D.; Gordon, R.; Ferdman, B.; Weiss, L. E.; Alalouf, O.; Naor, T.; Orange, R.; Michaeli, T.; Shechtman, Y. DeepSTORM3D: Dense 3D Localization Microscopy and PSF Design by Deep Learning. *Nat. Methods* **2020**, *17* (7), 734–740. <https://doi.org/10.1038/s41592-020-0853-5>.
- (148) Pfaff, S.; Larsson, A.; Orlov, D.; Harlow, G. S.; Abbondanza, G.; Linpé, W.; Rämisch, L.; Gericke, S. M.; Zetterberg, J.; Lundgren, E. Operando Reflectance Microscopy on Polycrystalline Surfaces in Thermal Catalysis, Electrocatalysis, and Corrosion. *ACS Appl. Mater. Interfaces* **2021**, *13* (16), 19530–19540. <https://doi.org/10.1021/acsami.1c04961>.

- (149) Su, Z.; Decencière, E.; Nguyen, T. T.; El-Amiry, K.; De Andrade, V.; Franco, A. A.; Demortière, A. Artificial Neural Network Approach for Multiphase Segmentation of Battery Electrode Nano-CT Images. *npj Comput. Mater.* **2022**, *8* (1). <https://doi.org/10.1038/s41524-022-00709-7>.
- (150) Lombardo, T.; Duquesnoy, M.; El-Bouysidy, H.; Årén, F.; Gallo-Bueno, A.; Jørgensen, P. B.; Bhowmik, A.; Demortière, A.; Ayerbe, E.; Alcaide, F.; Reynaud, M.; Carrasco, J.; Grimaud, A.; Zhang, C.; Vegge, T.; Johansson, P.; Franco, A. A. Artificial Intelligence Applied to Battery Research: Hype or Reality? *Chem. Rev.* **2021**. <https://doi.org/10.1021/acs.chemrev.1c00108>.
- (151) Sun, C.; Ko, S. J.; Jung, S.; Wang, C.; Lee, D.; Kim, J. G.; Kim, Y. Visualization of Electrochemical Behavior in Carbon Steel Assisted by Machine Learning. *Appl. Surf. Sci.* **2021**, *563* (June), 150412. <https://doi.org/10.1016/j.apsusc.2021.150412>.
- (152) Nash, W.; Zheng, L.; Birbilis, N. Deep Learning Corrosion Detection with Confidence. *npj Mater. Degrad.* **2022**, *6* (1), 1–13. <https://doi.org/10.1038/s41529-022-00232-6>.
- (153) Eremin, D. B.; Galushko, A. S.; Boiko, D. A.; Pentsak, E. O.; Chistyakov, I. V.; Ananikov, V. P. Toward Totally Defined Nanocatalysis: Deep Learning Reveals the Extraordinary Activity of Single Pd/C Particles. *J. Am. Chem. Soc.* **2022**, *144* (13), 6071–6079. <https://doi.org/10.1021/jacs.2c01283>.
- (154) Midtvedt, B.; Helgadottir, S.; Argun, A.; Pineda, J.; Midtvedt, D.; Volpe, G. Quantitative Digital Microscopy with Deep Learning. *Appl. Phys. Rev.* **2021**, *8* (1), 1–22. <https://doi.org/10.1063/5.0034891>.
- (155) Jadhav, Y.; Farimani, A. B. Dominant Motion Identification of Multi-Particle System Using Deep Learning from Video. **2021**, 1–15.
- (156) Mitchell, S.; Parés, F.; Faust Akl, D.; Collins, S. M.; Kepaptsoglou, D. M.; Ramasse, Q. M.; Garcia-Gasulla, D.; Pérez-Ramírez, J.; López, N. Automated Image Analysis for Single-Atom Detection in Catalytic Materials by Transmission Electron Microscopy. *J. Am. Chem. Soc.* **2022**. <https://doi.org/10.1021/jacs.1c12466>.
- (157) Furnival, T.; Leary, R. K.; Tyo, E. C.; Vajda, S.; Ramasse, Q. M.; Thomas, J. M.; Bristowe, P. D.; Midgley, P. A. Anomalous Diffusion of Single Metal Atoms on a Graphene Oxide Support. *Chem. Phys. Lett.* **2017**, *683*, 370–374. <https://doi.org/10.1016/j.cplett.2017.04.071>.
- (158) Zhang, T.; Li, S.; Du, Y.; He, T.; Shen, Y.; Bai, C.; Huang, Y.; Zhou, X. Revealing the Activity Distribution of a Single Nanocatalyst by Locating Single Nanobubbles with Super-Resolution Microscopy. *J. Phys. Chem. Lett.* **2018**, *9* (18), 5630–5635.

- <https://doi.org/10.1021/acs.jpcclett.8b02302>.
- (159) Zwaschka, G.; Nahalka, I.; Marchioro, A.; Tong, Y.; Tong, Y.; Roke, S.; Campen, R. K.; Campen, R. K. Imaging the Heterogeneity of the Oxygen Evolution Reaction on Gold Electrodes Operando: Activity Is Highly Local. *ACS Catal.* **2020**, *10* (11), 6084–6093. <https://doi.org/10.1021/acscatal.0c01177>.
- (160) Vogt, H. The Quantities Affecting the Bubble Coverage of Gas-Evolving Electrodes. *Electrochim. Acta* **2017**, *235*, 495–499. <https://doi.org/10.1016/j.electacta.2017.03.116>.
- (161) Attard, P. The Stability of Nanobubbles. *Eur. Phys. J. Spec. Top.* **2014**, *223* (5), 893–914. <https://doi.org/10.1140/epjst/e2013-01817-0>.
- (162) Tan, B. H.; An, H.; Ohl, C. D. Stability of Surface and Bulk Nanobubbles. *Current Opinion in Colloid and Interface Science*. Elsevier Ltd 2021, p 101428. <https://doi.org/10.1016/j.cocis.2021.101428>.
- (163) Mita, M.; Matsushima, H.; Ueda, M.; Ito, H. In-Situ High-Speed Atomic Force Microscopy Observation of Dynamic Nanobubbles during Water Electrolysis. *J. Colloid Interface Sci.* **2022**, *614*, 389–395. <https://doi.org/10.1016/j.jcis.2022.01.089>.
- (164) Karim, W.; Spreafico, C.; Kleibert, A.; Gobrecht, J.; Vandevondele, J.; Ekinici, Y.; Van Bokhoven, J. A. Catalyst Support Effects on Hydrogen Spillover. *Nature* **2017**, *541* (7635), 68–71. <https://doi.org/10.1038/nature20782>.
- (165) Wang, W. Imaging the Chemical Activity of Single Nanoparticles with Optical Microscopy. *Chem. Soc. Rev.* **2018**, *47* (7), 2485–2508. <https://doi.org/10.1039/c7cs00451f>.
- (166) Jing, C.; Reichert, J. Nanoscale Electrochemistry in the “Dark-Field.” *Curr. Opin. Electrochem.* **2017**, *6* (1), 10–16. <https://doi.org/10.1016/j.coelec.2017.06.008>.
- (167) Collins, S. S. E.; Cittadini, M.; Pecharromán, C.; Martucci, A.; Mulvaney, P. Hydrogen Spillover between Single Gold Nanorods and Metal Oxide Supports: A Surface Plasmon Spectroscopy Study. *ACS Nano* **2015**, *9* (8), 7846–7856. <https://doi.org/10.1021/acs.nano.5b02970>.
- (168) Georgescu, N. S.; Robinson, D. A.; White, H. S. Effect of Nonuniform Mass Transport on Nanobubble Nucleation at Individual Pt Nanoparticles. *J. Phys. Chem. C* **2021**, *125* (36), 19724–19732. <https://doi.org/10.1021/acs.jpcc.1c05020>.
- (169) Sevenler, D.; Avci, O.; Ünlü, M. S. Quantitative Interferometric Reflectance Imaging for the Detection and Measurement of Biological Nanoparticles. *Biomed. Opt. Express* **2017**, *8* (6), 2976. <https://doi.org/10.1364/BOE.8.002976>.
- (170) Hassel, A. W.; Lohregel, M. M. The Scanning Droplet Cell and Its Application to

- Structured Nanometer Oxide Films on Aluminium. *Electrochim. Acta* **1997**, *42* (20–22), 3327–3333. [https://doi.org/10.1016/S0013-4686\(97\)00184-9](https://doi.org/10.1016/S0013-4686(97)00184-9).
- (171) Güell, A. G.; Lai, S. C. S.; McKelvey, K.; Snowden, M. E.; Unwin, P. R. Scanning Electrochemical Cell Microscopy: A Versatile Technique for Nanoscale Electrochemistry and Functional Imaging Neil Ebejer¹. *Annu. Rev. Anal. Chem.* **2013**, *6* (1), 329–351. <https://doi.org/10.1146/annurev-anchem-062012-092650>.
- (172) Chen, Q.; Luo, L.; Faraji, H.; Feldberg, S. W.; White, H. S. Electrochemical Measurements of Single H₂ Nanobubble Nucleation and Stability at Pt Nanoelectrodes. *J. Phys. Chem. Lett.* **2014**, *5* (20), 3539–3544. <https://doi.org/10.1021/jz501898r>.
- (173) Epstein, P. S.; Plesset, M. S. On the Stability of Gas Bubbles in Liquid Gas Solutions. *J. Chem. Phys.* **1951**, *19* (2), 256. <https://doi.org/10.1063/1.1748182>.
- (174) Davies, T. J.; Compton, R. G. The Cyclic and Linear Sweep Voltammetry of Regular and Random Arrays of Microdisc Electrodes: Theory. *J. Electroanal. Chem.* **2005**, *585* (1), 63–82. <https://doi.org/10.1016/j.jelechem.2005.07.022>.
- (175) Henstridge, M. C.; Compton, R. G. Mass Transport to Micro- and Nanoelectrodes and Their Arrays: A Review. *Chem. Rec.* **2012**, *12* (1), 63–71. <https://doi.org/10.1002/tcr.201100032>.
- (176) Lohse, D.; Zhang, X. Surface Nanobubbles and Nanodroplets. *Rev. Mod. Phys.* **2015**, *87* (3), 981–1035. <https://doi.org/10.1103/RevModPhys.87.981>.
- (177) Lohse, D.; Zhang, X. Pinning and Gas Oversaturation Imply Stable Single Surface Nanobubbles. *Phys. Rev. E - Stat. Nonlinear, Soft Matter Phys.* **2015**, *91* (3), 1–5. <https://doi.org/10.1103/PhysRevE.91.031003>.
- (178) Yang, S.; Tsai, P.; Kooij, E. S.; Prosperetti, A.; Zandvliet, H. J. W.; Lohse, D. Electrolytically Generated Nanobubbles on Highly Orientated Pyrolytic Graphite Surfaces. *Langmuir* **2009**, *25* (3), 1466–1474. <https://doi.org/10.1021/la8027513>.
- (179) Brenner, M. P.; Lohse, D. Dynamic Equilibrium Mechanism for Surface Nanobubble Stabilization. *Phys. Rev. Lett.* **2008**, *101* (21), 1–4. <https://doi.org/10.1103/PhysRevLett.101.214505>.
- (180) Edwards, M. A.; White, H. S.; Ren, H. Voltammetric Determination of the Stochastic Formation Rate and Geometry of Individual H₂, N₂, and O₂ Bubble Nuclei. *ACS Nano* **2019**, *13* (6), 6330–6340. <https://doi.org/10.1021/acsnano.9b01015>.
- (181) Liu, Y.; Jin, C.; Liu, Y.; Ruiz, K. H.; Ren, H.; Fan, Y.; White, H. S.; Chen, Q. Visualization and Quantification of Electrochemical H₂ Bubble Nucleation at Pt, Au, and MoS₂ Substrates. *ACS Sensors* **2021**, *6* (2), 355–363.

<https://doi.org/10.1021/acssensors.0c00913>.

- (182) Chen, Q.; Luo, L. Correlation between Gas Bubble Formation and Hydrogen Evolution Reaction Kinetics at Nanoelectrodes. *Langmuir* **2018**, *34* (15), 4554–4559. <https://doi.org/10.1021/acs.langmuir.8b00435>.
- (183) Chen, Q.; Luo, L.; White, H. S. Electrochemical Generation of a Hydrogen Bubble at a Recessed Platinum Nanopore Electrode. *Langmuir* **2015**, *31* (15), 4573–4581. <https://doi.org/10.1021/acs.langmuir.5b00234>.
- (184) Wang, Y.; Gordon, E.; Ren, H. Mapping the Nucleation of H₂ Bubbles on Polycrystalline Pt via Scanning Electrochemical Cell Microscopy. *J. Phys. Chem. Lett.* **2019**, *10* (14), 3887–3892. <https://doi.org/10.1021/acs.jpcclett.9b01414>.
- (185) German, S. R.; Edwards, M. A.; Chen, Q.; White, H. S. Laplace Pressure of Individual H₂ Nanobubbles from Pressure-Addition Electrochemistry. *Nano Lett.* **2016**, *16* (10), 6691–6694. <https://doi.org/10.1021/acs.nanolett.6b03590>.
- (186) Zhang, L.; Zhang, Y.; Zhang, X.; Li, Z.; Shen, G.; Ye, M.; Fan, C.; Fang, H.; Hu, J. Electrochemically Controlled Formation and Growth of Hydrogen Nanobubbles. *Langmuir* **2006**, *22* (19), 8109–8113. <https://doi.org/10.1021/la060859f>.
- (187) Ustarroz, J.; Ornelas, I. M.; Zhang, G.; Perry, D.; Kang, M.; Bentley, C. L.; Walker, M.; Unwin, P. R. Mobility and Poisoning of Mass-Selected Platinum Nanoclusters during the Oxygen Reduction Reaction. *ACS Catal.* **2018**, *8* (8), 6775–6790. <https://doi.org/10.1021/acscatal.8b00553>.
- (188) Kong, L.; Mayorga-Martinez, C. C.; Guan, J.; Pumera, M. Photocatalytic Micromotors Activated by UV to Visible Light for Environmental Remediation, Micropumps, Reversible Assembly, Transportation, and Biomimicry. *Small* **2020**, *16* (27), 1–14. <https://doi.org/10.1002/sml.201903179>.
- (189) Gibbs, J. G.; Zhao, Y. P. Autonomously Motile Catalytic Nanomotors by Bubble Propulsion. *Appl. Phys. Lett.* **2009**, *94* (16). <https://doi.org/10.1063/1.3122346>.
- (190) Gao, W.; Feng, X.; Pei, A.; Gu, Y.; Li, J.; Wang, J. Seawater-Driven Magnesium Based Janus Micromotors for Environmental Remediation. *Nanoscale* **2013**, *5* (11), 4696–4700. <https://doi.org/10.1039/c3nr01458d>.
- (191) Chen, X.; Maljusch, A.; Rincón, R. A.; Battistel, A.; Bandarenka, A. S.; Schuhmann, W. Local Visualization of Catalytic Activity at Gas Evolving Electrodes Using Frequency-Dependent Scanning Electrochemical Microscopy. *Chem. Commun.* **2014**, *50* (87), 13250–13253. <https://doi.org/10.1039/c4cc06100d>.
- (192) Zeradjanin, A. R.; Ventosa, E.; Bondarenko, A. S.; Schuhmann, W. Evaluation of the

- Catalytic Performance of Gas-Evolving Electrodes Using Local Electrochemical Noise Measurements. *ChemSusChem* **2012**, *5* (10), 1905–1911. <https://doi.org/10.1002/cssc.201200262>.
- (193) Bentley, C. L.; Edmondson, J.; Meloni, G. N.; Perry, D.; Shkirskiy, V.; Unwin, P. R. Nanoscale Electrochemical Mapping. *Anal. Chem.* **2019**, *91* (1), 84–108. <https://doi.org/10.1021/acs.analchem.8b05235>.
- (194) Bentley, C. L.; Kang, M.; Unwin, P. R. Nanoscale Surface Structure-Activity in Electrochemistry and Electrocatalysis. *J. Am. Chem. Soc.* **2019**, *141* (6), 2179–2193. <https://doi.org/10.1021/jacs.8b09828>.
- (195) Armstrong, N. R.; Lin, A. W. C.; Fujihira, M.; Kuwana, T. Electrochemical and Surface Characteristics of Tin Oxide and Indium Oxide Electrodes. *Anal. Chem.* **1976**, *48* (4), 741–750. <https://doi.org/10.1021/ac60368a035>.
- (196) Bierwagen, O. Indium Oxide - A Transparent, Wide-Band Gap Semiconductor for (Opto)Electronic Applications. *Semicond. Sci. Technol.* **2015**, *30* (2). <https://doi.org/10.1088/0268-1242/30/2/024001>.
- (197) Batchelor-Mcauley, C.; Martinez-Marrades, A.; Tschulik, K.; Patel, A. N.; Combellas, C.; Kanoufi, F.; Tessier, G.; Compton, R. G. Simultaneous Electrochemical and 3D Optical Imaging of Silver Nanoparticle Oxidation. *Chem. Phys. Lett.* **2014**, *597*, 20–25. <https://doi.org/10.1016/j.cplett.2014.02.007>.
- (198) Dick, J. E.; Renault, C.; Kim, B.-K.; Bard, A. J. Simultaneous Detection of Single Attoliter Droplet Collisions by Electrochemical and Electrogenenerated Chemiluminescent Responses. *Angew. Chemie Int. Ed.* **2014**, *53* (44), 11859–11862. <https://doi.org/10.1002/anie.201407937>.
- (199) Brasiliense, V.; Berto, P.; Combellas, C.; Tessier, G.; Kanoufi, F. Electrochemistry of Single Nanodomains Revealed by Three-Dimensional Holographic Microscopy. *Acc. Chem. Res.* **2016**, *49* (9), 2049–2057. <https://doi.org/10.1021/acs.accounts.6b00335>.
- (200) Byers, C. P.; Zhang, H.; Swearer, D. F.; Yorulmaz, M.; Hoener, B. S.; Huang, D.; Hoggard, A.; Chang, W. S.; Mulvaney, P.; Ringe, E.; Halas, N. J.; Nordlander, P.; Link, S.; Landes, C. F. From Tunable Core-Shell Nanoparticles to Plasmonic Drawbridges: Active Control of Nanoparticle Optical Properties. *Sci. Adv.* **2015**, *1* (11), 1–10. <https://doi.org/10.1126/sciadv.1500988>.
- (201) Chen, H.; Liu, T.; Wang, B.; Liu, Z.; Li, Y.; Zhao, Q.; Wang, N.; He, H.; Liu, H.; Guo, Z. Highly Efficient Charge Collection in Dye-Sensitized Solar Cells Based on Nanocomposite Photoanode Filled with Indium-Tin Oxide Interlayer. *Adv. Compos.*

- Hybrid Mater.* **2018**, *1* (2), 356–363. <https://doi.org/10.1007/s42114-018-0035-4>.
- (202) Mashkov, O.; Körfer, J.; Eigen, A.; Yousefi-Amin, A. A.; Killilea, N.; Barabash, A.; Sytnyk, M.; Khansur, N.; Halik, M.; Webber, K. G.; Heiss, W. Effect of Ligand Treatment on the Tuning of Infrared Plasmonic Indium Tin Oxide Nanocrystal Electrochromic Devices. *Adv. Eng. Mater.* **2020**, *22* (9), 1–7. <https://doi.org/10.1002/adem.202000112>.
- (203) Zhang, B.; Xu, G.; Tan, S.; Liu, C. Effects of Indium-Doped Tin Oxide Film on Electrochromic Properties under Lithium Ion Guidance. *Opt. Mater. (Amst)*. **2020**, *101* (February), 109756. <https://doi.org/10.1016/j.optmat.2020.109756>.
- (204) Chhina, H.; Campbell, S.; Kesler, O. An Oxidation-Resistant Indium Tin Oxide Catalyst Support for Proton Exchange Membrane Fuel Cells. *J. Power Sources* **2006**, *161* (2), 893–900. <https://doi.org/10.1016/j.jpowsour.2006.05.014>.
- (205) Escudero-Escribano, M.; Verdaguier-Casadevall, A.; Malacrida, P.; Grønbjerg, U.; Knudsen, B. P.; Jepsen, A. K.; Rossmeisl, J.; Stephens, I. E. L.; Chorkendorff, I. Pt 5Gd as a Highly Active and Stable Catalyst for Oxygen Electroreduction. *J. Am. Chem. Soc.* **2012**, *134* (40), 16476–16479. <https://doi.org/10.1021/ja306348d>.
- (206) Zhang, H.; Zhou, W.; Du, Y.; Yang, P.; Wang, C. One-Step Electrodeposition of Platinum Nanoflowers and Their High Efficient Catalytic Activity for Methanol Electro-Oxidation. *Electrochem. commun.* **2010**, *12* (7), 882–885. <https://doi.org/10.1016/j.elecom.2010.04.011>.
- (207) Matveeva, E. Electrochemistry of the Indium-Tin Oxide Electrode in 1 M NaOH Electrolyte. *J. Electrochem. Soc.* **2005**, *152* (9), H138. <https://doi.org/10.1149/1.1984348>.
- (208) Huang, C. A.; Li, K. C.; Tu, G. C.; Wang, W. S. The Electrochemical Behavior of Tin-Doped Indium Oxide during Reduction in 0.3 M Hydrochloric Acid. *Electrochim. Acta* **2003**, *48* (24), 3599–3605. [https://doi.org/10.1016/S0013-4686\(03\)00480-8](https://doi.org/10.1016/S0013-4686(03)00480-8).
- (209) Liu, L.; Yellinek, S.; Valdinger, I.; Donval, A.; Mandler, D. Important Implications of the Electrochemical Reduction of ITO. *Electrochim. Acta* **2015**, *176*, 1374–1381. <https://doi.org/10.1016/j.electacta.2015.07.129>.
- (210) Senthilkumar, M.; Mathiyarasu, J.; Joseph, J.; Phani, K. L. N.; Yegnaraman, V. Electrochemical Instability of Indium Tin Oxide (ITO) Glass in Acidic PH Range during Cathodic Polarization. *Mater. Chem. Phys.* **2008**, *108* (2–3), 403–407. <https://doi.org/10.1016/j.matchemphys.2007.10.030>.
- (211) Geiger, S.; Kasian, O.; Mingers, A. M.; Mayrhofer, K. J. J.; Cherevko, S. Stability

- Limits of Tin-Based Electrocatalyst Supports. *Sci. Rep.* **2017**, *7* (1), 3–9. <https://doi.org/10.1038/s41598-017-04079-9>.
- (212) Sundaresan, V.; Cutri, A. R.; Metro, J.; Madukoma, C. S.; Shrout, J. D.; Hoffman, A. J.; Willets, K. A.; Bohn, P. W. Potential Dependent Spectroelectrochemistry of Electrofluorogenic Dyes on Indium-tin Oxide. *Electrochem. Sci. Adv.* **2021**, No. May, 1–9. <https://doi.org/10.1002/elsa.202100094>.
- (213) Wahab, O. J.; Kang, M.; Meloni, G. N.; Daviddi, E.; Unwin, P. R. Nanoscale Visualization of Electrochemical Activity at Indium Tin Oxide Electrodes. *Anal. Chem.* **2022**, *94* (11), 4729–4736. <https://doi.org/10.1021/acs.analchem.1c05168>.
- (214) Molina, N. Y.; Pungsrissai, T.; Dell, Z. J. O.; Paranzino, B.; Willets, K. A. The Hidden Role of the Supporting Electrode for Creating Heterogeneity in Single Entity Electrochemistry. **2022**, *19122*. <https://doi.org/10.1002/celc.202200245>.
- (215) van den Meerakker, J. E. A. M.; Baarslag, P. C.; Scholten, M. On the Mechanism of ITO Etching in Halogen Acids: The Influence of Oxidizing Agents. *J. Electrochem. Soc.* **1995**, *142* (7), 2321–2325. <https://doi.org/10.1149/1.2044294>.
- (216) Li, S.; Tian, M.; Gao, Q.; Wang, M.; Li, T.; Hu, Q.; Li, X.; Wu, Y. Nanometre-Thin Indium Tin Oxide for Advanced High-Performance Electronics. *Nat. Mater.* **2019**, *18* (10), 1091–1097. <https://doi.org/10.1038/s41563-019-0455-8>.
- (217) Spada, E. R.; De Paula, F. R.; Plá Cid, C. C.; Candiotti, G.; Faria, R. M.; Sartorelli, M. L. Role of Acidic and Basic Electrolytes on the Structure and Morphology of Cathodically Reduced Indium Tin Oxide (ITO) Substrates. *Electrochim. Acta* **2013**, *108*, 520–524. <https://doi.org/10.1016/j.electacta.2013.06.077>.
- (218) Shen, S.; Zhang, X.; Mubeen, S.; Soriaga, M. P.; Stickney, J. L. Optimization of the Nucleation-Site Density for the Electrodeposition of Cadmium Sulfide on Indium-Tin-Oxide. *Electrochim. Acta* **2019**, *316*, 105–112. <https://doi.org/10.1016/j.electacta.2019.05.120>.
- (219) German, S. R.; Edwards, M. A.; Ren, H.; White, H. S. Critical Nuclei Size, Rate, and Activation Energy of H₂ Gas Nucleation. *J. Am. Chem. Soc.* **2018**, *140* (11), 4047–4053. <https://doi.org/10.1021/jacs.7b13457>.
- (220) Ustarroz, J.; Hammons, J. A.; Altantzis, T.; Hubin, A.; Bals, S.; Terryn, H. A Generalized Electrochemical Aggregative Growth Mechanism. *J. Am. Chem. Soc.* **2013**, *135* (31), 11550–11561. <https://doi.org/10.1021/ja402598k>.
- (221) Gökçeli, G.; Karatepe, N. Investigation of Hydrogen Post-Treatment Effect on Surface and Optoelectronic Properties of Indium Tin Oxide Thin Films. *J. Alloys Compd.* **2021**,

851. <https://doi.org/10.1016/j.jallcom.2020.156861>.
- (222) Bouden, S.; Dahi, A.; Hauquier, F.; Randriamahazaka, H.; Ghilane, J. Multifunctional Indium Tin Oxide Electrode Generated by Unusual Surface Modification. *Sci. Rep.* **2016**, *6* (November), 1–9. <https://doi.org/10.1038/srep36708>.
- (223) Cornut, R.; Lefrou, C. New Analytical Approximation of Feedback Approach Curves with a Microdisk SECM Tip and Irreversible Kinetic Reaction at the Substrate. *J. Electroanal. Chem.* **2008**, *621* (2), 178–184. <https://doi.org/10.1016/j.jelechem.2007.09.021>.
- (224) Park, K.-S.; Choi, Y.-J.; Kang, J.-G.; Sung, Y.-M.; Park, J.-G. The Effect of the Concentration and Oxidation State of Sn on the Structural and Electrical Properties of Indium Tin Oxide Nanowires. *Nanotechnology* **2011**, *22* (28), 285712. <https://doi.org/10.1088/0957-4484/22/28/285712>.
- (225) Zach, M. P.; Penner, R. M. Nanocrystalline Nickel Nanoparticles. *Adv. Mater.* **2000**, *12* (12), 878–883. [https://doi.org/10.1002/1521-4095\(200006\)12:12<878::AID-ADMA878>3.0.CO;2-X](https://doi.org/10.1002/1521-4095(200006)12:12<878::AID-ADMA878>3.0.CO;2-X).
- (226) Ritzert, N. L.; Moffat, T. P. Ultramicroelectrode Studies of Self-Terminated Nickel Electrodeposition and Nickel Hydroxide Formation upon Water Reduction. *J. Phys. Chem. C* **2016**, *120* (48), 27478–27489. <https://doi.org/10.1021/acs.jpcc.6b10006>.
- (227) Wang, R.; Bertocci, U.; Tan, H.; Bendersky, L. A.; Moffat, T. P. Self-Terminated Electrodeposition of Ni, Co, and Fe Ultrathin Films. *J. Phys. Chem. C* **2016**, *120* (29), 16228–16237. <https://doi.org/10.1021/acs.jpcc.6b01901>.
- (228) Clausmeyer, J.; Masa, J.; Ventosa, E.; Öhl, D.; Schuhmann, W. Nanoelectrodes Reveal the Electrochemistry of Single Nickelhydroxide Nanoparticles. *Chem. Commun.* **2016**, *52* (11), 2408–2411. <https://doi.org/10.1039/C5CC08796A>.
- (229) Mernissi Cherigui, E. A.; Sentosun, K.; Bouckenooge, P.; Vanrompay, H.; Bals, S.; Terryn, H.; Ustarroz, J. Comprehensive Study of the Electrodeposition of Nickel Nanostructures from Deep Eutectic Solvents: Self-Limiting Growth by Electrolysis of Residual Water. *J. Phys. Chem. C* **2017**, *121* (17), 9337–9347. <https://doi.org/10.1021/acs.jpcc.7b01104>.
- (230) Danilovic, N.; Subbaraman, R.; Strmcnik, D.; Chang, K. C.; Paulikas, A. P.; Stamenkovic, V. R.; Markovic, N. M. Enhancing the Alkaline Hydrogen Evolution Reaction Activity through the Bifunctionality of Ni(OH)₂/Metal Catalysts. *Angew. Chemie - Int. Ed.* **2012**, *51* (50), 12495–12498. <https://doi.org/10.1002/anie.201204842>.

- (231) Chhetri, M.; Sultan, S.; Rao, C. N. R. Electrocatalytic Hydrogen Evolution Reaction Activity Comparable to Platinum Exhibited by the Ni/Ni(OH)₂/Graphite Electrode. *Proc. Natl. Acad. Sci. U. S. A.* **2017**, *114* (34), 8986–8990. <https://doi.org/10.1073/pnas.1710443114>.
- (232) Liu, Y.; Gokcen, D.; Bertocci, U.; Moffat, T. P. Self-Terminating Growth of Platinum Films by Electrochemical Deposition. *Science* (80-.). **2012**, *338* (6112), 1327–1330. <https://doi.org/10.1126/science.1228925>.
- (233) Bagheri, F.; Mosivand, S. Ball-like Nickel Hydroxide Nanoparticles: Electro-Synthesis, Characterization, and Application. *Mater. Today Commun.* **2021**, *26* (September 2020), 101714. <https://doi.org/10.1016/j.mtcomm.2020.101714>.
- (234) Smith, J. G.; Yang, Q.; Jain, P. K. Identification of a Critical Intermediate in Galvanic Exchange Reactions by Single-Nanoparticle-Resolved Kinetics. *Angew. Chemie - Int. Ed.* **2014**, *53* (11), 2867–2872. <https://doi.org/10.1002/anie.201309307>.
- (235) Wilson, A. J.; Devasia, D.; Jain, P. K. Nanoscale Optical Imaging in Chemistry. *Chem. Soc. Rev.* **2020**, *49* (16), 6087–6112. <https://doi.org/10.1039/D0CS00338G>.
- (236) Yu, R.-J.; Ying, Y.-L.; Gao, R.; Long, Y.-T. Confined Nanopipette Sensing: From Single Molecules, Single Nanoparticles, to Single Cells. *Angew. Chemie Int. Ed.* **2019**, *58* (12), 3706–3714. <https://doi.org/https://doi.org/10.1002/anie.201803229>.
- (237) McKelvey, K.; German, S. R.; Zhang, Y.; White, H. S.; Edwards, M. A. Nanopipettes as a Tool for Single Nanoparticle Electrochemistry. *Curr. Opin. Electrochem.* **2017**, *6* (1), 4–9. <https://doi.org/10.1016/j.coelec.2017.06.006>.
- (238) Lai, S. C. S.; Lazenby, R. A.; Kirkman, P. M.; Unwin, P. R. Nucleation, Aggregative Growth and Detachment of Metal Nanoparticles during Electrodeposition at Electrode Surfaces. *Chem. Sci.* **2015**, *6* (2), 1126–1138. <https://doi.org/10.1039/C4SC02792B>.
- (239) Kim, Y.-R.; Lai, S. C. S.; McKelvey, K.; Zhang, G.; Perry, D.; Miller, T. S.; Unwin, P. R. Nucleation and Aggregative Growth of Palladium Nanoparticles on Carbon Electrodes: Experiment and Kinetic Model. *J. Phys. Chem. C* **2015**, *119* (30), 17389–17397. <https://doi.org/10.1021/acs.jpcc.5b03513>.
- (240) Ustarroz, J. Current Atomic-Level Understanding of Electrochemical Nucleation and Growth on Low-Energy Surfaces. *Curr. Opin. Electrochem.* **2020**, *19*, 144–152. <https://doi.org/10.1016/j.coelec.2019.12.001>.
- (241) Momotenko, D.; Page, A.; Adobes-Vidal, M.; Unwin, P. R. Write–Read 3D Patterning with a Dual-Channel Nanopipette. *ACS Nano* **2016**, *10* (9), 8871–8878. <https://doi.org/10.1021/acsnano.6b04761>.

- (242) Hengsteler, J.; Mandal, B.; van Nisselroy, C.; Lau, G. P. S.; Schlotter, T.; Zambelli, T.; Momotenko, D. Bringing Electrochemical Three-Dimensional Printing to the Nanoscale. *Nano Lett.* **2021**, *21* (21), 9093–9101. <https://doi.org/10.1021/acs.nanolett.1c02847>.
- (243) Daryadel, S.; Behroozfar, A.; Minary-Jolandan, M. Toward Control of Microstructure in Microscale Additive Manufacturing of Copper Using Localized Electrodeposition. *Adv. Eng. Mater.* **2019**, *21* (1), 1800946. <https://doi.org/10.1002/adem.201800946>.
- (244) Daryadel, S.; Behroozfar, A.; Morsali, S. R.; Moreno, S.; Baniasadi, M.; Bykova, J.; Bernal, R. A.; Minary-Jolandan, M. Localized Pulsed Electrodeposition Process for Three-Dimensional Printing of Nanotwinned Metallic Nanostructures. *Nano Lett.* **2018**, *18* (1), 208–214. <https://doi.org/10.1021/acs.nanolett.7b03930>.
- (245) Ustarroz, J.; Kang, M.; Bullions, E.; Unwin, P. R. Impact and Oxidation of Single Silver Nanoparticles at Electrode Surfaces: One Shot versus Multiple Events. *Chem. Sci.* **2017**, *8* (3), 1841–1853. <https://doi.org/10.1039/C6SC04483B>.
- (246) Kleijn, S. E. F.; Lai, S. C. S.; Miller, T. S.; Yanson, A. I.; Koper, M. T. M.; Unwin, P. R. Landing and Catalytic Characterization of Individual Nanoparticles on Electrode Surfaces. *J. Am. Chem. Soc.* **2012**, *134* (45), 18558–18561. <https://doi.org/10.1021/ja309220m>.
- (247) Güell, A. G.; Cuharuc, A. S.; Kim, Y. R.; Zhang, G.; Tan, S. Y.; Ebejer, N.; Unwin, P. R. Redox-Dependent Spatially Resolved Electrochemistry at Graphene and Graphite Step Edges. *ACS Nano* **2015**, *9* (4), 3558–3571. <https://doi.org/10.1021/acs.nano.5b00550>.
- (248) Hill, J. W.; Hill, C. M. Directly Visualizing Carrier Transport and Recombination at Individual Defects within 2D Semiconductors. *Chem. Sci.* **2021**, *12* (14), 5102–5112. <https://doi.org/10.1039/D0SC07033E>.
- (249) Brunet Cabré, M.; Paiva, A. E.; Velický, M.; Colavita, P. E.; McKelvey, K. Electrochemical Kinetics as a Function of Transition Metal Dichalcogenide Thickness. *Electrochim. Acta* **2021**, *393*, 139027. <https://doi.org/10.1016/j.electacta.2021.139027>.
- (250) Takahashi, Y.; Kobayashi, Y.; Wang, Z.; Ito, Y.; Ota, M.; Ida, H.; Kumatani, A.; Miyazawa, K.; Fujita, T.; Shiku, H.; Korchev, Y. E.; Miyata, Y.; Fukuma, T.; Chen, M.; Matsue, T. High-Resolution Electrochemical Mapping of the Hydrogen Evolution Reaction on Transition-Metal Dichalcogenide Nanosheets. *Angew. Chemie* **2020**, *132* (9), 3629–3636. <https://doi.org/10.1002/ange.201912863>.
- (251) Güell, A. G.; Meadows, K. E.; Dudin, P. V.; Ebejer, N.; Macpherson, J. V.; Unwin, P.

- R. Mapping Nanoscale Electrochemistry of Individual Single-Walled Carbon Nanotubes. *Nano Lett.* **2014**, *14* (1), 220–224. <https://doi.org/10.1021/nl403752e>.
- (252) Byers, J. C.; Güell, A. G.; Unwin, P. R. Nanoscale Electrocatalysis: Visualizing Oxygen Reduction at Pristine, Kinked, and Oxidized Sites on Individual Carbon Nanotubes. *J. Am. Chem. Soc.* **2014**, *136* (32), 11252–11255. <https://doi.org/10.1021/ja505708y>.
- (253) Mariano, R. G.; Kang, M.; Wahab, O. J.; McPherson, I. J.; Rabinowitz, J. A.; Unwin, P. R.; Kanan, M. W. Microstructural Origin of Locally Enhanced CO₂ Electroreduction Activity on Gold. *Nat. Mater.* **2021**, *20* (7), 1000–1006. <https://doi.org/10.1038/s41563-021-00958-9>.
- (254) Aaronson, B. D. B.; Chen, C. H.; Li, H.; Koper, M. T. M.; Lai, S. C. S.; Unwin, P. R. Pseudo-Single-Crystal Electrochemistry on Polycrystalline Electrodes: Visualizing Activity at Grains and Grain Boundaries on Platinum for the Fe²⁺/Fe³⁺ Redox Reaction. *J. Am. Chem. Soc.* **2013**, *135* (10), 3873–3880. <https://doi.org/10.1021/ja310632k>.
- (255) Wang, Y.; Gordon, E.; Ren, H. Mapping the Potential of Zero Charge and Electrocatalytic Activity of Metal-Electrolyte Interface via a Grain-by-Grain Approach. *Anal. Chem.* **2020**, *92* (3), 2859–2865. <https://doi.org/10.1021/acs.analchem.9b05502>.
- (256) Tao, B.; Yule, L. C.; Daviddi, E.; Bentley, C. L.; Unwin, P. R. Correlative Electrochemical Microscopy of Li-Ion (De)Intercalation at a Series of Individual LiMn₂O₄ Particles. *Angew. Chemie* **2019**, *131* (14), 4654–4659. <https://doi.org/10.1002/ange.201814505>.
- (257) Lai, S. C. S.; Dudin, P. V.; MacPherson, J. V.; Unwin, P. R. Visualizing Zeptomole (Electro)Catalysis at Single Nanoparticles within an Ensemble. *J. Am. Chem. Soc.* **2011**, *133* (28), 10744–10747. <https://doi.org/10.1021/ja203955b>.
- (258) Choi, M.; Siepser, N. P.; Jeong, S.; Wang, Y.; Jagdale, G.; Ye, X.; Baker, L. A. Probing Single-Particle Electrocatalytic Activity at Facet-Controlled Gold Nanocrystals. *Nano Lett.* **2020**, *20* (2), 1233–1239. <https://doi.org/10.1021/acs.nanolett.9b04640>.
- (259) Bentley, C. L. Scanning Electrochemical Cell Microscopy for the Study of (Nano)Particle Electrochemistry: From the Sub-particle to Ensemble Level. *Electrochem. Sci. Adv.* **2022**, *2* (3), 1–18. <https://doi.org/10.1002/elsa.202100081>.
- (260) Saha, P.; Rahman, M. M.; Hill, C. M. Borohydride Oxidation Electrocatalysis at Individual, Shape-controlled Au Nanoparticles. *Electrochem. Sci. Adv.* **2021**, No. May,

- 1–10. <https://doi.org/10.1002/elsa.202100120>.
- (261) Hao, R.; Fan, Y.; Zhang, B. Imaging Dynamic Collision and Oxidation of Single Silver Nanoparticles at the Electrode/Solution Interface. *J. Am. Chem. Soc.* **2017**, *139* (35), 12274–12282. <https://doi.org/10.1021/jacs.7b06431>.
- (262) Sandmann, G.; Dietz, H.; Plieth, W. Preparation of Silver Nanoparticles on ITO Surfaces by a Double-Pulse Method. *J. Electroanal. Chem.* **2000**, *491* (1–2), 78–86. [https://doi.org/10.1016/S0022-0728\(00\)00301-6](https://doi.org/10.1016/S0022-0728(00)00301-6).
- (263) Ueda, M.; Dietz, H.; Anders, A.; Knepe, H.; Meixner, A.; Plieth, W. Double-Pulse Technique as an Electrochemical Tool for Controlling the Preparation of Metallic Nanoparticles. *Electrochim. Acta* **2002**, *48* (4), 377–386. [https://doi.org/10.1016/S0013-4686\(02\)00683-7](https://doi.org/10.1016/S0013-4686(02)00683-7).
- (264) Harbron, E. J.; Barbara, P. F. The Poisson Distribution and Single-Molecule Spectroscopy. An Undergraduate Analytical Laboratory Experiment. *J. Chem. Educ.* **2002**, *79* (2), 211. <https://doi.org/10.1021/ed079p211>.
- (265) Hussein, H. E. M.; Maurer, R. J.; Amari, H.; Peters, J. J. P.; Meng, L.; Beanland, R.; Newton, M. E.; Macpherson, J. V. Tracking Metal Electrodeposition Dynamics from Nucleation and Growth of a Single Atom to a Crystalline Nanoparticle. *ACS Nano* **2018**, *12* (7), 7388–7396. <https://doi.org/10.1021/acsnano.8b04089>.
- (266) Liu, T.; Liu, S.; Jiang, W.; Wang, W. Tracking Sub-Nanometer Shift in the Scattering Centroid of Single Gold Nanorods during Electrochemical Charging. *ACS Nano* **2019**, *13* (6), 6279–6286. <https://doi.org/10.1021/acsnano.8b09636>.
- (267) Snowden, M. E.; Güell, A. G.; Lai, S. C. S.; McKelvey, K.; Ebejer, N.; Oconnell, M. A.; Colburn, A. W.; Unwin, P. R. Scanning Electrochemical Cell Microscopy: Theory and Experiment for Quantitative High Resolution Spatially-Resolved Voltammetry and Simultaneous Ion-Conductance Measurements. *Anal. Chem.* **2012**, *84* (5), 2483–2491. <https://doi.org/10.1021/ac203195h>.
- (268) Bentley, C. L.; Kang, M.; Maddar, F. M.; Li, F.; Walker, M.; Zhang, J.; Unwin, P. R. Electrochemical Maps and Movies of the Hydrogen Evolution Reaction on Natural Crystals of Molybdenite (MoS₂): Basal vs. Edge Plane Activity. *Chem. Sci.* **2017**, *8* (9), 6583–6593. <https://doi.org/10.1039/C7SC02545A>.
- (269) Güell, A. G.; Ebejer, N.; Snowden, M. E.; McKelvey, K.; Macpherson, J. V.; Unwin, P. R. Quantitative Nanoscale Visualization of Heterogeneous Electron Transfer Rates in 2D Carbon Nanotube Networks. *Proc. Natl. Acad. Sci. U. S. A.* **2012**, *109* (29), 11487–11492. <https://doi.org/10.1073/pnas.1203671109>.

- (270) Daviddi, E.; Chen, Z.; Beam Massani, B.; Lee, J.; Bentley, C. L.; Unwin, P. R.; Ratcliff, E. L. Nanoscale Visualization and Multiscale Electrochemical Analysis of Conductive Polymer Electrodes. *ACS Nano* **2019**. <https://doi.org/10.1021/acsnano.9b06302>.
- (271) Lai, S. C. S.; Patel, A. N.; McKelvey, K.; Unwin, P. R. Definitive Evidence for Fast Electron Transfer at Pristine Basal Plane Graphite from High-Resolution Electrochemical Imaging. *Angew. Chemie - Int. Ed.* **2012**, *51* (22), 5405–5408. <https://doi.org/10.1002/anie.201200564>.
- (272) Yule, L. C.; Shkirskiy, V.; Aarons, J.; West, G.; Bentley, C. L.; Shollock, B. A.; Unwin, P. R. Nanoscale Active Sites for the Hydrogen Evolution Reaction on Low Carbon Steel. *J. Phys. Chem. C* **2019**, *123* (39), 24146–24155. <https://doi.org/10.1021/acs.jpcc.9b07216>.
- (273) Kirkman, P. M.; Güell, A. G.; Cuharuc, A. S.; Unwin, P. R. Spatial and Temporal Control of the Diazonium Modification of Sp² Carbon Surfaces. *J. Am. Chem. Soc.* **2014**, *136* (1), 36–39. <https://doi.org/10.1021/ja410467e>.
- (274) Zhang, G.; Kirkman, P. M.; Patel, A. N.; Cuharuc, A. S.; McKelvey, K.; Unwin, P. R. Molecular Functionalization of Graphite Surfaces: Basal Plane versus Step Edge Electrochemical Activity. *J. Am. Chem. Soc.* **2014**, *136* (32), 11444–11451. <https://doi.org/10.1021/ja505266d>.
- (275) Patel, A. N.; McKelvey, K.; Unwin, P. R. Nanoscale Electrochemical Patterning Reveals the Active Sites for Catechol Oxidation at Graphite Surfaces. *J. Am. Chem. Soc.* **2012**, *134* (50), 20246–20249. <https://doi.org/10.1021/ja3095894>.
- (276) Oseland, E. E.; Ayres, Z. J.; Basile, A.; Haddleton, D. M.; Wilson, P.; Unwin, P. R. Surface Patterning of Polyacrylamide Gel Using Scanning Electrochemical Cell Microscopy (SECCM). *Chem. Commun.* **2016**, *52* (64), 9929–9932. <https://doi.org/10.1039/C6CC05153G>.
- (277) McKelvey, K.; O’Connell, M. A.; Unwin, P. R. Meniscus Confined Fabrication of Multidimensional Conducting Polymer Nanostructures with Scanning Electrochemical Cell Microscopy (SECCM). *Chem. Commun.* **2013**, *49* (29), 2986–2988. <https://doi.org/10.1039/c3cc00104k>.
- (278) Parker, A. S.; Al Botros, R.; Kinnear, S. L.; Snowden, M. E.; McKelvey, K.; Ashcroft, A. T.; Carvell, M.; Joiner, A.; Peruffo, M.; Philpotts, C.; Unwin, P. R. Combinatorial Localized Dissolution Analysis: Application to Acid-Induced Dissolution of Dental Enamel and the Effect of Surface Treatments. *J. Colloid Interface Sci.* **2016**, *476*, 94–

102. <https://doi.org/10.1016/j.jcis.2016.05.018>.
- (279) Kinnear, S. L.; McKelvey, K.; Snowden, M. E.; Peruffo, M.; Colburn, A. W.; Unwin, P. R. Dual-Barrel Conductance Micropipet as a New Approach to the Study of Ionic Crystal Dissolution Kinetics. *Langmuir* **2013**, *29* (50), 15565–15572. <https://doi.org/10.1021/la403630u>.
- (280) Chen, C. H.; Meadows, K. E.; Cuharuc, A.; Lai, S. C. S.; Unwin, P. R. High Resolution Mapping of Oxygen Reduction Reaction Kinetics at Polycrystalline Platinum Electrodes. *Phys. Chem. Chem. Phys.* **2014**, *16* (34), 18545–18552. <https://doi.org/10.1039/c4cp01511h>.
- (281) Wang, H.; Shan, X.; Chen, H. Y.; Tao, N. Pauli Repulsion-Induced Expansion and Electromechanical Properties of Graphene. *Nano Lett.* **2017**, *17* (1), 236–241. <https://doi.org/10.1021/acs.nanolett.6b03955>.
- (282) Lippmann, G. Relations Entre Les Phénomènes Électriques et Capillaires. *Ann. Chim. Phys.* **1875**, *5*, 494–549.
- (283) Quinn, A.; Sedev, R.; Ralston, J. Influence of the Electrical Double Layer in Electrowetting. *J. Phys. Chem. B* **2003**, *107* (5), 1163–1169. <https://doi.org/10.1021/jp0216326>.
- (284) Quinn, A.; Sedev, R.; Ralston, J. Contact Angle Saturation in Electrowetting. *J. Phys. Chem. B* **2005**, *109* (13), 6268–6275. <https://doi.org/10.1021/jp040478f>.
- (285) Qiu, Y.; Ren, H.; Edwards, M. A.; Gao, R.; Barman, K.; White, H. S. Electrochemical Generation of Individual Nanobubbles Comprising H₂, D₂, and HD. *Langmuir* **2020**, *36* (22), 6073–6078. <https://doi.org/10.1021/acs.langmuir.0c00232>.
- (286) Morse, J. W.; Arvidson, R. S.; Lüttge, A. Calcium Carbonate Formation and Dissolution. *Chemical Reviews*. February 2007, pp 342–381. <https://doi.org/10.1021/cr050358j>.
- (287) Meldrum, F. C.; O’Shaughnessy, C. Crystallization in Confinement. *Advanced Materials*. August 2020, p 2001068. <https://doi.org/10.1002/adma.202001068>.
- (288) Gebauer, D.; Völkel, A.; Cölfen, H. Stable Prenucleation Calcium Carbonate Clusters. *Science (80-.)*. **2008**, *322* (5909), 1819–1822. <https://doi.org/10.1126/science.1164271>.
- (289) Smeets, P. J. M.; Finney, A. R.; Habraken, W. J. E. M.; Nudelman, F.; Friedrich, H.; Laven, J.; De Yoreo, J. J.; Rodger, P. M.; Sommerdijk, N. A. J. M. A Classical View on Nonclassical Nucleation. *Proc. Natl. Acad. Sci.* **2017**, *114* (38), E7882–E7890. <https://doi.org/10.1073/pnas.1700342114>.
- (290) Sebastiani, F.; Wolf, S. L. P.; Born, B.; Luong, T. Q.; Cölfen, H.; Gebauer, D.;

- Havenith, M. Water Dynamics from THz Spectroscopy Reveal the Locus of a Liquid-Liquid Binodal Limit in Aqueous CaCO₃ Solutions. *Angew. Chemie Int. Ed.* **2017**, *56* (2), 490–495. <https://doi.org/10.1002/anie.201610554>.
- (291) Gabrielli, C.; Maurin, G.; Poindessous, G.; Rosset, R. Nucleation and Growth of Calcium Carbonate by an Electrochemical Scaling Process. *J. Cryst. Growth* **1999**, *200* (1–2), 236–250. [https://doi.org/10.1016/S0022-0248\(98\)01261-5](https://doi.org/10.1016/S0022-0248(98)01261-5).
- (292) Blount, B.; Kilner, K.; Hu, H.; Gohmann, D.; Gordon, E.; Wang, Y.; Ren, H. Electrochemically Induced Nucleation of a Nanoscopic Ionic Solid. *J. Phys. Chem. C* **2020**, *124* (31), 17413–17417. <https://doi.org/10.1021/acs.jpcc.0c05009>.
- (293) Oloye, O.; O'Mullane, A. P. Electrochemical Capture and Storage of CO₂ as Calcium Carbonate. *ChemSusChem* **2021**, *14* (7), 1767–1775. <https://doi.org/10.1002/cssc.202100134>.
- (294) Lui, F. H. Y.; Wang, Y.; Yao, Y.; Mobbs, R. J.; Pogson, R. E.; Koshy, P.; Lucien, F. P.; Zhou, D.; Sorrell, C. C. Quiescent Mineralisation for Free-Standing Mineral Microfilms with a Hybrid Structure. *J. Colloid Interface Sci.* **2021**, *604*, 327–339. <https://doi.org/10.1016/j.jcis.2021.06.171>.
- (295) Farhadi Khouzani, M.; Chevrier, D. M.; Güttlein, P.; Hauser, K.; Zhang, P.; Hedin, N.; Gebauer, D. Disordered Amorphous Calcium Carbonate from Direct Precipitation. *CrystEngComm* **2015**, *17* (26), 4842–4849. <https://doi.org/10.1039/C5CE00720H>.
- (296) Rudd, N. C.; Cannan, S.; Bitziou, E.; Ciani, I.; Whitworth, A. L.; Unwin, P. R. Fluorescence Confocal Laser Scanning Microscopy as a Probe of PH Gradients in Electrode Reactions and Surface Activity. *Anal. Chem.* **2005**, *77* (19), 6205–6217. <https://doi.org/10.1021/ac050800y>.
- (297) Parkhurst, D. L.; Appelo, C. a. J. Description of Input and Examples for PHREEQC Version 3 — A Computer Program for Speciation, Batch-Reaction, One-Dimensional Transport, and Inverse Geochemical Calculations. In *U.S. Geological Survey Techniques and Methods, book 6, chapter A43*; U.S. Geological Survey Techniques and Methods, 2013; p 497.
- (298) Mahamdeh, M.; Howard, J. Implementation of Interference Reflection Microscopy for Label-Free, High-Speed Imaging of Microtubules. *J. Vis. Exp.* **2019**, *2019* (150), 1–8. <https://doi.org/10.3791/59520>.
- (299) Crocker, J. C.; Grier, D. G. Methods of Digital Video Microscopy for Colloidal Studies. *J. Colloid Interface Sci.* **1996**. <https://doi.org/10.1006/jcis.1996.0217>.
- (300) Savitzky, A.; Golay, M. J. E. Smoothing and Differentiation. *Anal. Chem.* **1964**, *36* (8),

1627–1639.

- (301) Li, G.; Mao, J.; Saqib, M.; Hao, R. Operando Optoelectrochemical Analysis of Single Zinc Dendrites with a Reflective Nanopore Electrode. *Chem. – An Asian J.* **2022**. <https://doi.org/10.1002/asia.202200824>.
- (302) Boniface, A.; Mounaix, M.; Blochet, B.; de Aguiar, H. B.; Quéré, F.; Gigan, S. Spectrally Resolved Point-Spread-Function Engineering Using a Complex Medium. *Opt. Express* **2021**, 29 (6), 8985. <https://doi.org/10.1364/oe.403578>.
-